

# 2D calculations for atoms and ions in strong magnetic fields of white dwarfs and neutron stars

## DISSERTATION

Von der Fakultät Mathematik und Physik der Universität Stuttgart  
zur Erlangung der Würde eines Doktors der Naturwissenschaften  
(Dr. rer. nat.) genehmigte Abhandlung

Vorgelegt von

Christoph Schimeczek

aus München

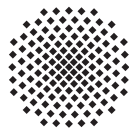
Hauptberichter:

Prof. Dr. Günter Wunner

Mitberichter:

Junior Prof. Dr. Maria Fyta

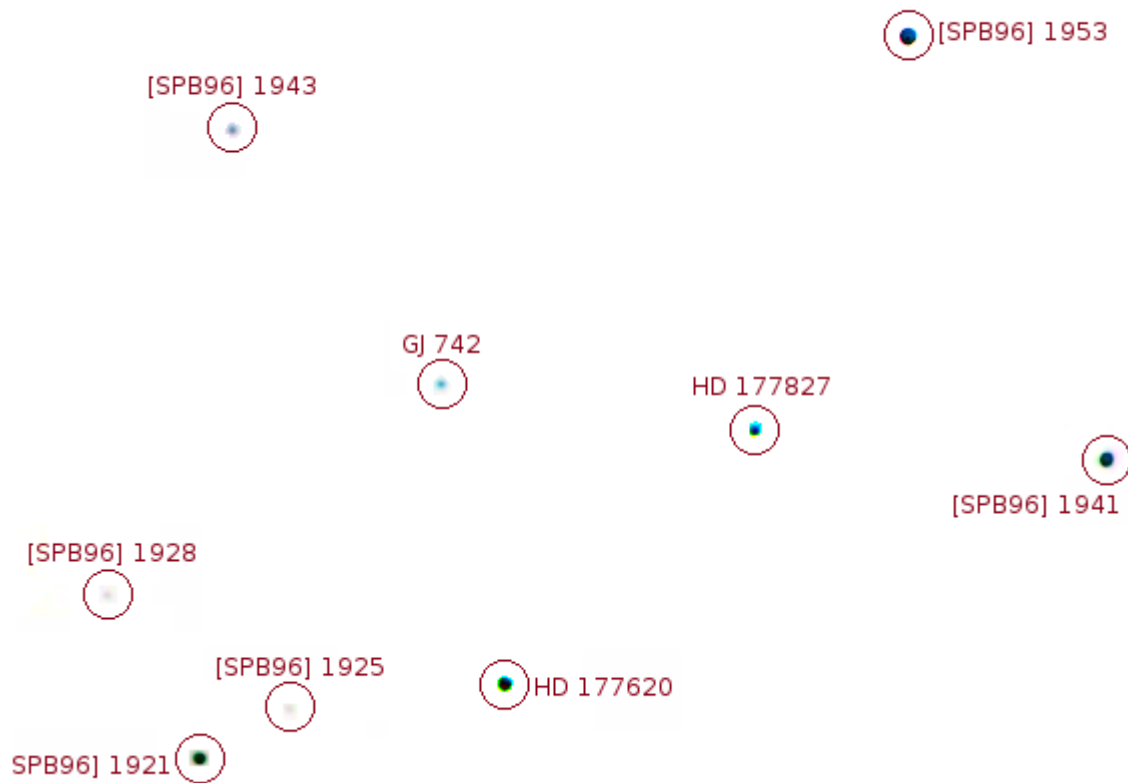
Tag der mündlichen Prüfung: 24.01.2014



1. Institut für Theoretische Physik der Universität Stuttgart

2014





False-color image of the magnetic white dwarf GJ 742, also known as GRW+70°8247, among other stars in constellation Draco. The area on display is about  $16 \times 12$  square arcminutes. I made the observations for this image on Oct 24 2013 in Fellbach using a small Newton reflector telescope and a modified web cam. The bright stars HD177620 and HD177827 with apparent magnitudes 7.9 and 8.9 (see Ref. [1]) served as reference stars for tracking. GJ 742 has an apparent magnitude of 13.2 and elaborate image processing was necessary to uncover the star with this small setup.

- Telescope: Skywatcher Explorer 150 PDS on EQ 5 mount
- Camera: Philips ToUCam PCVC 740K
- Exposure: 15 000 color images at 5 frames per second, 50 min total exposure
- Image Processing: Images demosaicked using *AviRaw*, stacked 30% of the images with highest quality using *AviStack* after subtracting a 10 min averaged dark-frame, color histogram adapted and noise reduced with *Fitswork*, colors inverted and labels added using *GIMP*.



# Contents

<b>Nomenclature</b>	<b>11</b>
List of symbols . . . . .	12
<b>Abstract</b>	<b>13</b>
<b>Inhaltsangabe</b>	<b>15</b>
<b>1 Introduction</b>	<b>17</b>
1.1 Motivation . . . . .	17
1.2 Framework of this thesis . . . . .	19
1.3 Acknowledgements . . . . .	20
<b>2 Hydrogen in magnetic fields of arbitrary strength</b>	<b>21</b>
2.1 Setting . . . . .	21
2.2 Expansion of the wave function . . . . .	23
2.2.1 Ansätze . . . . .	23
2.2.2 Method of solution . . . . .	24
2.2.3 Applicability of the expansions . . . . .	26
2.2.4 Finite element basis . . . . .	28
2.3 Automated magnetic field strength variation . . . . .	31
2.4 Transitions . . . . .	34
2.5 Results . . . . .	35
2.5.1 Energy values . . . . .	35
2.5.2 Transition wavelengths . . . . .	38
2.5.3 Wave functions . . . . .	43
2.5.4 Dipole strengths and oscillator strengths . . . . .	46
2.5.5 Improved spectral plots . . . . .	56
<b>3 Many-electron systems in neutron star magnetic fields: General considerations</b>	<b>61</b>
3.1 Setting . . . . .	61
3.2 Expansion of the single-particle wave functions . . . . .	64
3.3 Error estimates for the slim expansions . . . . .	67
3.3.1 Tightly-bound states . . . . .	68
3.3.2 Hydrogen-like states . . . . .	69

<b>4</b>	<b>The accelerated doubly self-consistent Hartree-Fock-Roothaan method</b>	<b>71</b>
4.1	Hartree-Fock-Roothaan equations . . . . .	71
4.1.1	Equations for the $B$ -spline coefficients . . . . .	72
4.1.2	Equations for the Landau expansion coefficients . . . . .	73
4.2	Solution method . . . . .	74
4.3	Transitions . . . . .	76
4.4	Procedural optimizations . . . . .	78
4.4.1	Speed boost . . . . .	78
4.4.2	Enhanced convergence . . . . .	79
<b>5</b>	<b>The full 2D Landau-Hartree-Fock-Roothaan method</b>	<b>81</b>
5.1	2D Hartree-Fock-Roothaan equations . . . . .	81
5.2	Interaction cutoff and renormalization . . . . .	82
5.2.1	Procedure . . . . .	82
5.2.2	Thorough error analysis . . . . .	85
5.3	The 2DLHFR program . . . . .	92
5.3.1	Workload distribution . . . . .	93
5.4	Transitions . . . . .	94
<b>6</b>	<b>Results</b>	<b>95</b>
6.1	Other methods in the literature . . . . .	95
6.2	Energy values . . . . .	96
6.3	Transition strengths and energies . . . . .	105
6.4	Ground state configurations . . . . .	109
6.4.1	Ground state regimes . . . . .	110
6.4.2	Qualitative analysis . . . . .	110
6.4.3	Complete data set of ground state configurations . . . . .	116
	<b>Conclusion and outlook</b>	<b>125</b>
	<b>Zusammenfassung in deutscher Sprache</b>	<b>129</b>
	<b>A Atomic units</b>	<b>145</b>
	<b>B Landau averaged potentials</b>	<b>147</b>
	<b>Bibliography</b>	<b>151</b>
	<b>Danksagung</b>	<b>161</b>
	<b>Lebenslauf</b>	<b>163</b>

# List of Figures

1.1	Spectrum of a magnetic white dwarf . . . . .	17
1.2	Spectrum of a neutron star . . . . .	18
2.1	Convergence ranges of expansions . . . . .	27
2.2	Accessible field strengths with spherical expansion . . . . .	28
2.3	Expansion orders at different field strengths . . . . .	29
2.4	Contour plot of the state $(-2,+10)$ . . . . .	30
2.5	Structure of the energy function . . . . .	32
2.6	Data point placement . . . . .	32
2.7	Scheme of AMV procedure . . . . .	33
2.8	Spin-down energy values $n \leq 5$ . . . . .	36
2.9	Symmetry subspace $m = 0, \pi_z = -$ . . . . .	37
2.10	Symmetry subspace $m = 1, \pi_z = +$ . . . . .	37
2.11	Qualitative behavior of transition energies . . . . .	42
2.12	Lyman series . . . . .	43
2.13	Balmer series . . . . .	44
2.14	Wave function evolution . . . . .	45
2.15	Wave functions at avoided crossings . . . . .	45
2.16	Precision of data point interpolation . . . . .	47
2.17	Qualitative behavior of transition strengths . . . . .	48
2.18	Cancellation of dipole integral . . . . .	54
2.19	Oscillator strengths at avoided crossing . . . . .	55
2.20	Signatures of avoided crossings . . . . .	55
2.21	High resolution dipole strength . . . . .	56
2.22	Lyman series weighted . . . . .	57
2.23	Balmer series weighted . . . . .	58
2.24	Lyman to Brackett series . . . . .	59
2.25	Combined line data . . . . .	60
3.1	Different longitudinal wave function extensions . . . . .	65
3.2	Errors from expansions: tightly-bound states . . . . .	69
3.3	Errors from expansions: hydrogen-like states . . . . .	70
4.1	Scheme of the HFFER II program . . . . .	76
4.2	Speedup factor of the HFFER II implementation . . . . .	79
4.3	Frustrated convergence . . . . .	80

*List of Figures*

---

5.1	Energies and calculation times over minimal occupation threshold . . . . .	84
5.2	Re-evaluated energies via the SQMC method . . . . .	86
5.3	Helium: different states and their energy errors due to interaction cutoff .	87
5.4	Energy errors and the magnetic field strength: malign states . . . . .	88
5.5	Energy errors and magnetic field strength: benign states . . . . .	89
5.6	Energy errors and atomic numbers . . . . .	90
5.7	Convergence of the 2DLHFR ansatz . . . . .	91
5.8	Scheme of the 2DLHFR program . . . . .	92
6.1	2DLHFR vs. full CI transitions: energy values . . . . .	106
6.2	2DLHFR vs. full CI transitions: dipole strengths . . . . .	107
6.3	Ground state crossings of neutral neon . . . . .	111
6.4	Ground state crossings of neutral chlorine . . . . .	112
B.1	Example effective electron-core potential . . . . .	148
B.2	Transformed potentials . . . . .	149



# List of Tables

2.1	Binding energies of the states $(0,+1)$ and $(0,+2)$ . . . . .	39
2.2	Binding energies of the states $(0,-1)$ and $(0,-2)$ . . . . .	40
2.3	Binding energies of the states $(-1,+1)$ and $(-2,+1)$ . . . . .	41
2.4	Energies and dipole strengths for tb-tb transitions . . . . .	49
2.5	Table 2.4 continued . . . . .	50
2.6	Energies and dipole strengths for transitions . . . . .	51
2.7	Table 2.6 continued . . . . .	52
6.1	Binding energies of the helium state $0^01^0$ . . . . .	97
6.2	Binding energies of the helium state $0^02^0$ . . . . .	98
6.3	Binding energies of the helium state $0^00^1$ . . . . .	98
6.4	Binding energies of the complex helium state $0^01^1$ . . . . .	99
6.5	Binding energies of the complex helium state $0^03^0$ . . . . .	99
6.6	Indices corresponding to electronic configurations . . . . .	100
6.7	Ground state binding energies at $B = 10^7$ T of neutral helium to silicon .	101
6.8	Ground state binding energies at $B = 5 \times 10^7$ T of neutral helium to iron	102
6.9	Ground state binding energies at $B = 10^8$ T of neutral helium to iron . .	103
6.10	Ground state binding energies at $B = 5 \times 10^8$ T of neutral helium to iron	104
6.11	Energies and dipole strengths of the transition $0^00^2$ to $0^00^1$ . . . . .	105
6.12	Energies and dipole strengths of the transition $0^01^0$ to $0^01^1$ . . . . .	106
6.13	Energies and oscillator strengths of tb-hl transitions in neutral carbon . .	108
6.14	2DLHFR ground state transitions to full spin polarization . . . . .	113
6.15	FPDQMC ground state transitions to full spin polarization . . . . .	113
6.16	2DLHFR transitions to the high-field ground state . . . . .	115
6.17	FPDQMC transitions to the high-field ground state . . . . .	115
6.18	Ground state crossings for $Z = 2 \dots 21$ and $N = 2 \dots 4$ . . . . .	117
6.19	Ground state crossings for $Z = 7 \dots 12$ and $N = 4$ . . . . .	117
6.20	Ground state crossings for $Z = 5 \dots 21$ and $N = 4 \dots 5$ . . . . .	118
6.21	Ground state crossings for $Z = 6, 7$ and $N = 6$ . . . . .	118
6.22	Ground state crossings for $Z = 7 \dots 21$ and $N = 6 \dots 9$ . . . . .	119
6.23	Ground state crossings for $Z = 11, 12, 16 \dots 21$ and $N = 8, 9$ . . . . .	120
6.24	Ground state crossings for $Z = 10, 11, 13$ and $N = 9, 10$ . . . . .	120
6.25	Ground state crossings for $Z = 11 \dots 21$ and $N = 9 \dots 11$ . . . . .	120
6.26	Ground state crossings for $Z = 16$ and $N = 10$ . . . . .	120
6.27	Ground state crossings for $Z = 12 \dots 21$ and $N = 10 \dots 13$ . . . . .	121

*List of Tables*

---

6.28	Ground state crossings for $Z = 16 \dots 20$ and $N = 12 \dots$	121
6.29	Ground state crossings for $Z = 14 \dots 21$ and $N = 12 \dots 15 \dots$	122
6.30	Ground state crossings for $Z = 16, 18, 19, 21$ and $N = 13 \dots 15 \dots$	122
6.31	Ground state crossings for $Z = 16 \dots 18, 20, 21$ and $N = 14 \dots 16 \dots$	122
6.32	Ground state crossings for $Z = 17 \dots 20$ and $N = 15 \dots 17 \dots$	123
6.33	Ground state crossings for $Z = 18 \dots 21$ and $N = 15 \dots 17 \dots$	123
6.34	Ground state crossings for $Z = 18 \dots 21$ and $N = 17 \dots 20 \dots$	123
6.35	Ground state crossings for $Z = 21$ and $N = 21 \dots$	123
A.1	Units and constants in atomic Rydberg units	145

# Nomenclature

2DLHFR ...	two-dimensional Landau-Hartree-Fock-Roothaan method
FPDQMC ..	fixed-phase diffusion quantum Monte Carlo method
HFFEM ...	Hartree-Fock finite element method
HFFER II ..	accelerated Hartree-Fock finite element Roothaan method
HFFER ....	Hartree-Fock finite element Roothaan method
SQMC .....	simple quantum Monte Carlo method
a.u. ....	atomic Rydberg units
AMV .....	automated magnetic field strength variation
CI .....	configuration interaction
FSP .....	full spin polarization
HFGS .....	high-field ground state
HFR .....	Hartree-Fock-Roothaan
hl .....	hydrogen-like
mfs .....	magnetic field strength
MPI .....	Message Passing Interface
MWD .....	magnetic white dwarf
NS .....	neutron star
PSP .....	partial spin polarization
QMC .....	quantum Monte Carlo
RAM .....	random-access memory
SDSS .....	Sloan Digital Sky Survey
tb .....	tightly-bound

## List of symbols

$Z$	atomic number	$N_L$	last included Landau channel
$N$	number of electrons	$N_{\text{int}}^i$	last interacting Landau channel
$B$	magnetic flux density	$t_{\text{min}}$	minimal Landau occupation
$\beta$	mfs parameter	$\xi^i$	interaction renormalization factor
$\beta_Z$	charge-scaled mfs parameter	$q_{\text{eff}}^i$	screened effective core charge
$m$	magnetic quantum number	$x_{\text{max}}$	basis width
$m'$	negative of $m$	$k$	$B$ -spline order
$m_s$	spin $z$ -projection	$\alpha$	$B$ -spline coefficient
$\pi_z$	$z$ -parity	$t_n^i$	Landau channel occupation
$l$	angular momentum	$\delta E$	relative energy difference
$n$	Landau quantum number	$E$	energy
$\nu$	single-particle excitation	$\hat{H}$	Hamiltonian
$\nu_a$	asymptotic excitation number	$F$	Fock matrix
$\nu'$	longitudinal node number	$S$	overlap matrix
$M$	total magnetic quantum number	$V$	electron-core potential
$\Pi_z$	total wave function $z$ -parity	$U$	direct interaction potential
$S_z$	total spin $z$ -projection	$A$	exchange interaction potential
$\nu^*$	total excitation number	$\epsilon_{\text{int}}$	energy convergence criterion
$\psi$	single-particle wave function	$\epsilon_{\text{prec}}$	absolute energy precision
$\Psi$	many-particle wave function	$\epsilon_{\text{conv}}$	precision of energy interpolation
$P(z)$	longitudinal orbital component	$\Delta E$	transition energy
$Y_{lm}$	spherical harmonic	$\lambda$	wavelength
$\Phi$	Landau orbital	$f$	oscillator strength
$B$	$B$ -spline	$d$	dipole strength
$l_{\text{max}}$	last included angular momentum	$p^q$	dipole matrix element
$\mu_{\text{max}}$	number of $B$ -splines	$q$	polarization index
$N_{\text{fem}}$	number of finite elements	$\beta_Z^{\text{Tr}}$	transition field strength
$\eta_p$	parallelization efficiency	$f(r)$	radial orbital component
$\{x_i\}$	$B$ -spline node sequence		

# Abstract

The following work is devoted to the description of atoms and ions in strong magnetic fields as they can occur in the vicinity of magnetic white dwarfs and neutron stars. The ultimate goal of this work is the contribution to an understanding of unique absorption features detected in the spectra of such stars. One natural explanation for these features are atomic absorptions in the stars' strongly magnetized atmospheres. Models for the atmospheres of magnetic white dwarfs and corresponding spectra have already been applied with great success to observed data, and absorption features of the light elements hydrogen and helium were identified. A comparable success in the modeling of neutron star atmospheres has still to be accomplished. This is related to the extreme conditions in neutron star atmospheres, namely very high temperatures, magnetic fields, and particle densities. Also, the progenitors of neutron stars produce heavy elements up to iron, which are likely to contribute to the composition of the neutron star atmosphere. The poor knowledge of atomic data of heavier elements in strong magnetic fields hampers the further understanding of neutron star emission spectra.

In this work we present reliable and fast programs that are capable of creating a large database for atomic states and transitions in a wide range of the magnetic field strength. Based upon previous work we implemented a two-dimensional Hartree-Fock-Roothaan method that overcomes former restrictions, namely the adiabatic approximation and the Landau orbital product ansatz. This software suite allows for a precise description of atomic wave functions and energy values in an extended range of magnetic field strengths. Additionally, the programs are capable of calculating atomic transition energies and strengths. During the development of these programs we focused on automated data production and processing, and paid special attention to program reliability and execution speed. The results for the hydrogen atom presented in this work have already proven useful in the context of an astrophysical application, and improve current atmosphere model calculations of magnetic white dwarfs. Further, our results enhance the understanding of atomic energy spectra at neutron star magnetic fields. The wave functions and energy values calculated in this thesis serve as a starting point for other methods, e.g. the fixed-phase diffusion quantum Monte Carlo method, as well as for photoionization calculations of atoms in strong magnetic fields.



# Inhaltsangabe

Die nachstehende Arbeit befasst sich mit Atomen und Ionen in Magnetfeldern solcher Stärke wie sie auf den Oberflächen von magnetischen weißen Zwergen und Neutronensternen vorkommen können. Unser Ziel ist zum Verständnis von bis dato unverstandenen Absorptionsmerkmalen in den Spektren dieser Sterne beizutragen. Als Ursache dieser Merkmale kommt unter anderem die Absorption von Licht durch die Atome der Sternatmosphäre in Betracht. Für weiße Zwerge konnten bereits mehrfach Modellierungen der Sternatmosphäre und der zugehörigen Sternspektren durchgeführt werden, sodass den beobachteten Spektren erfolgreich Absorptionen der leichten Elemente Wasserstoff und Helium zugeordnet werden konnten. Dies ist mit letzter Gewissheit für Neutronensterne noch nicht gelungen, nicht zuletzt deshalb, weil ein umfassendes Verständnis atomarer Zustände in starken Magnetfeldern, insbesondere auch der schwereren Elemente bis Eisen, welche als Fusionsprodukte des Vorgängersterns die atomare Zusammensetzung der Sternatmosphäre bestimmen können, zwingende Voraussetzung für eine solche Modellierung ist. Bisher liegen jedoch kaum atomare Daten für Elemente schwerer als Helium unter solchen Bedingungen vor.

In dieser Arbeit wird eine zuverlässige und schnelle Methode präsentiert, die den Aufbau einer Datenbank von atomaren Zuständen und Übergängen in einem weiten Wertebereich der Magnetfeldstärke ermöglicht. Basierend auf Erkenntnissen vorheriger Untersuchungen wurde ein zweidimensionales Hartree-Fock-Roothaan-Verfahren implementiert. Bisherige Näherungen zur Beschreibung der Wellenfunktionen, wie die adiabatische Näherung und der Produktansatz für Landauorbitale wurden überwunden. Die erstellte Programmsuite ermöglicht eine genaue Beschreibung der atomaren Wellenfunktionen und Energiewerte in einem großen Bereich der Magnetfeldstärke und erlaubt des Weiteren die Berechnung von atomaren Übergängen. Besonderes Augenmerk lag bei der Entwicklung der Programme auf Stabilität und Geschwindigkeit, sodass eine automatisierte Gewinnung und Verarbeitung der atomaren Daten möglich wird. Die hier vorgestellten Ergebnisse fanden zum einen bereits im Rahmen aktueller astrophysikalischen Studien zur Verbesserung der Atmosphärenmodelle weißer Zwerge Verwendung, und leisten zum anderen einen wesentlichen Beitrag zum Verständnis von atomaren Zuständen bei Neutronensternmagnetfeldstärken. Des Weiteren dienen die im Rahmen dieser Arbeit berechneten Wellenfunktionen und Energiewerte als Ausgangspunkt für weiterführende Verfahren, wie zum Beispiel der Fixed-Phase Diffusions-Quanten-Monte-Carlo Methode, sowie Berechnungen zur Photoionisation in starken Magnetfeldern.





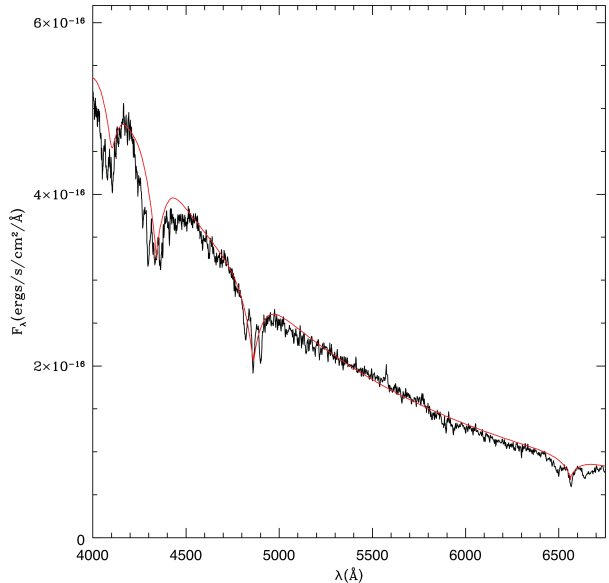
# 1 Introduction

## 1.1 Motivation

The effects of strong magnetic fields found in magnetic white dwarfs (MWD) and neutron stars (NS) on atoms in their atmospheres have been subject to research activities for several decades - but still many questions remain unanswered. A reason for this slow progress is that even the simple hydrogen atom cannot be described analytically in a magnetic field [2], but has to be addressed with full numerical methods (see, e.g. Ref. [3–6]) at field strengths beyond the perturbative Zeeman regime. Ruder et al. [7] were the first to publish extensive amounts of energy levels for the lowest 38 hydrogen states, as well as corresponding transition energies and oscillator strengths over the full range of the magnetic field strength from  $B = 0$  T to  $B \approx 5 \cdot 10^8$  T. Later, Kravchenko et al. [8, 9] and Stubbins et al. [10] presented new ansätze allowing the calculation of hydrogen levels with up to 15 or 30 digits precision over a wide range of magnetic field strengths, but they showed results for a few low-lying levels only. A fully relativistic description of the problem was first presented by Lindgren and Virtamo [11] and in more detail by Chen and Goldman [12].

The calculated atomic data allowed to understand the absorption features of hydrogen atmospheres of MWDs, which did not fit models without magnetic fields. A contemporary example for such a mismatch is displayed in Fig. 1.1, which was taken from Ref.

**Fig. 1.1:** Spectrum of the magnetic white dwarf SDSS J111010.50+600141.44 with inadequate fit of a model without magnetic field (red curve), taken from Kepler et al. [13] (Fig. 1). Courtesy of Monthly Notices of the Royal Astronomical Society.



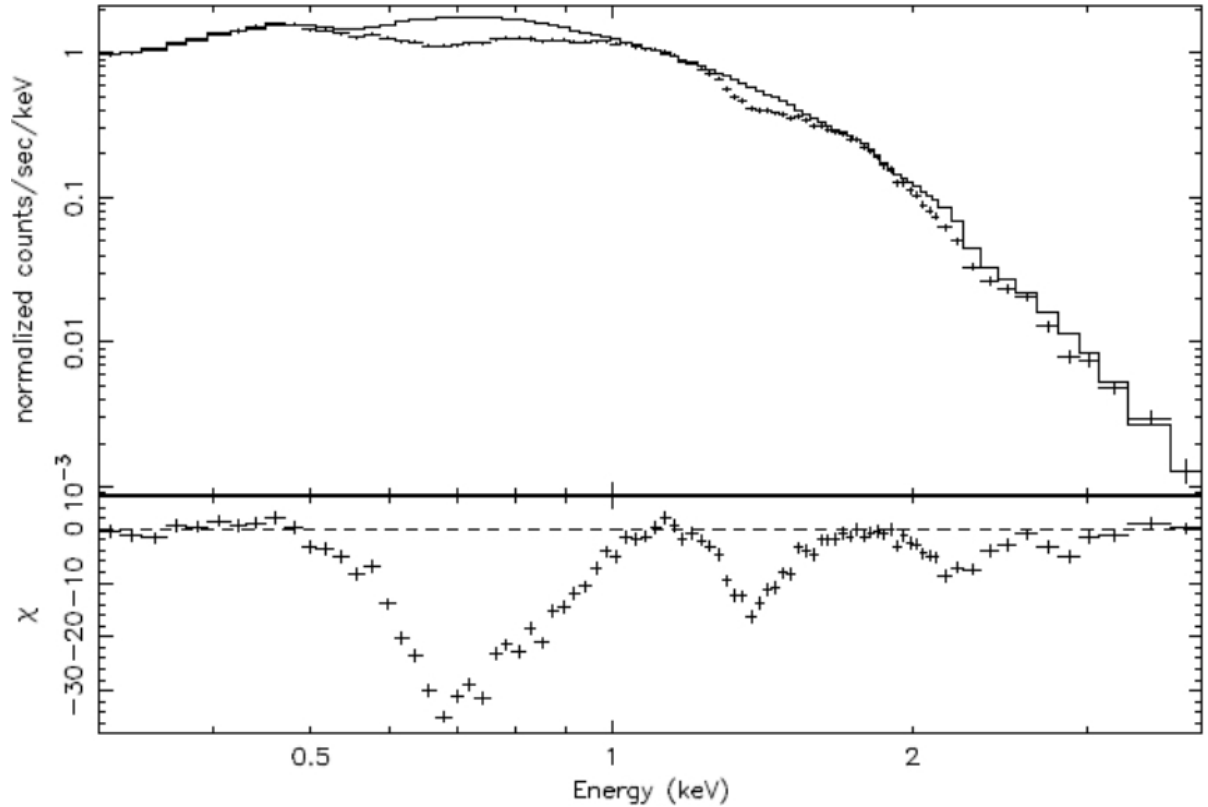


**Fig. 1.2:** X-ray absorption spectrum of 1E 1207.4-5209 by *XMM-Newton* with continuum blackbody fit from Bignami et al. [21], by courtesy of Giovanni Bignami. Notice the broad absorption features at roughly 0.7 keV and 1.4 keV, which could be caused by cyclotron lines similar to those found by Trümper et al. [22], and, more recently, Hambaryan et al. [23]. Alternatively, these features could stem from atomic absorptions as suggested by Mori et al. [24].

[13]. It shows the spectrum of a MWD along with an inappropriate zero-magnetic-field fit. Including magnetic fields into their considerations, Angel et al. [14], Jordan [15] and Friedrich et al. [16] analyzed the spectrum of GRW+70°8247 and were able to explain absorption line positions and shapes. We give a false-color image of this star, that is also referred to as GJ 742, on the cover. More recently, Euchner et al. [17–19] have developed a method allowing the reconstruction of magnetic field topologies including magnetic dipole and quadrupole components. This method was used by Külebi et al. [20] to analyze several MWD spectra observed in the Sloan Digital Sky Survey (SDSS). To predict surface gravities of MWDs with magnetic fields below 2 MG, Kepler et al. [13] requested precise hydrogen line data for states up to the principal quantum number  $n = 10$ . A part of this work is committed to satisfy this need by extending previous hydrogen data sets with highest reasonable precision.

In contrast to the latest success in modeling MWD spectra, Lattimer et al. [25] indicated that models of magnetized NS atmospheres that include absorptions by atoms

heavier than hydrogen “are still in a state of infancy”. Several reasons for this situation can be found: Firstly, the solution of multi-electron atomic problems in the strong magnetic fields of NSs with field strengths up to  $B = 10^{11}$  T is quite elaborate and no comprehensive analysis of all atoms and ions at relevant magnetic field strengths could be completed yet. So far, merely helium was analyzed thoroughly by Becken et al. [26–29], Jones et al. [30, 31] and others [7, 32–38]. Lithium was studied by Wang et al. [39] and Al-Hujaj et al. [40], while the last group also presented results for beryllium [41]. A more general analysis of heavier elements was carried out by Mori et al. [24, 42], Engel et al. [43], Bücheler et al. [44] and Meyer et al. [45] as well as Boblest [46], who calculated ground state energies for elements up to iron at four different magnetic field strengths.

A second reason for the slow progress of NS atmosphere modeling is connected to the atmospheric conditions on a NS surface featuring high temperatures and mass densities up to  $k_B T_{\text{eff}} = 200$  eV and  $100 \text{ g/cm}^3$ , respectively (see Miller [47]). Those are expected to significantly change the NS spectra via ionization and pressure effects, such as volume restrictions and electric microfields (see, e.g. Mori et al. [24]). Finally, the relatively poor quality of observed NS spectra further complicates their analysis. Figure 1.2 from Bignami et al. [21] shows a spectrum of the NS 1E 1207.4-5209 as well as deviations from a blackbody fit. The poor spectral resolution hampers the identification of finer absorption features, suggested by Mereghetti et al. [48] and Sanwal et al. [49]. The combination of a high resolution spectrum with a proper atmosphere model allows to fit the gravitational redshift parameter of a NS, which in turn restricts its nuclear matter equation of state [50]. Ho et al. [51] performed such an analysis for a NS with weak magnetic fields. A similar analysis of NSs with strong magnetic fields will be an important future step to understand these fascinating objects, that exist on the verge of gravitational collapse.

## 1.2 Framework of this thesis

This work is devoted to the fast and reliable calculation of states and energies of atoms and ions from hydrogen to iron at magnetic field strengths relevant for MWDs and NSs. Chapter 2 deals with the description of single-particle wave functions in magnetic fields of arbitrary strength. There we present results for the hydrogen states as well as corresponding transition energies and oscillator strengths. In Chap. 3, we lay the foundation for the treatment of many-electron systems in strong magnetic fields. The following two Chaps. 4 and 5 describe the accelerated doubly self-consistent Hartree-Fock-Roothaan method and the 2D Landau-Hartree-Fock-Roothaan method, respectively. Whereas the first of these methods is based on forerunner models by Klews [52, 53] and Engel [43, 54], the latter was newly developed to gain access to lower magnetic field strengths and, more importantly, to improve the precision of the results. In Chap. 6 we discuss the results obtained by both methods, in particular the magnetic field strength dependent ground state configurations of atoms and ions.

## 1.3 Acknowledgements

A large number of calculations contributing to this work were performed on the infrastructure of the bwGrid [55].

## 2 Hydrogen in magnetic fields of arbitrary strength

A significant fraction of white dwarfs (estimates range from 2% to 30% [56]) is considered to have magnetic fields of such a strength that a significant influence on their spectra is expected to be observable. Magnetic fields detected so far on hydrogen-rich white dwarfs range from about 10 T to  $10^5$  T (see [13] and references therein). Neutron stars, however, have magnetic fields of much higher strength, ranging up to  $10^{11}$  T [57]. Some of them possibly possess a hydrogen atmosphere [23]. Therefore, a detailed analysis of the hydrogen problem at arbitrary field strengths is highly desirable. Extensive theoretical work has already been performed over the past decades, and we chose to follow Ruder et al. [7] for the presentations in this chapter.

### 2.1 Setting

The non-relativistic Hamiltonian describing an electron in a Coulomb potential of charge  $Z = 1$  and a uniform magnetic field  $\mathbf{B} = B\mathbf{e}_z$  reads

$$\hat{H} = -\Delta + 2\beta m + \beta^2 \rho^2 + 4\beta m_s - \frac{2}{|\mathbf{r}|}, \quad (2.1)$$

where atomic Rydberg units (see Appx. A) are used. Here, the magnetic field strength  $\beta = B/B_0$  is measured in units of the reference magnetic field strength  $B_0 \approx 4.7 \times 10^5$  T, where  $m$  and  $m_s$  represent the magnetic quantum number and the  $z$ -projection of the spin, respectively. Also, the symmetric gauge  $\mathbf{A}(\mathbf{r}) = \frac{1}{2}\mathbf{B} \times \mathbf{r}$  is used. In contrast to the Hamiltonian without a magnetic field,  $\hat{H}$  in Eq. (2.1) has cylindrical instead of spherical symmetry and the angular momentum  $l$  is no longer a good quantum number. Therefore, the only good quantum numbers left are parity with respect to the  $z$ -axis  $\pi_z$ , the magnetic quantum number  $m$  and the spin projection  $m_s$ . These quantum numbers define a symmetry subspace and states within one such subspace can be labeled according to their excitation level  $\nu$ . Throughout this chapter the notation  $(m, \pi_z, \nu, \{\uparrow\})$  will be used to identify states at any magnetic field strength (mfs). The spin alignment will be omitted if the spin points down, and for the sake of brevity we will only give the sign of the  $z$ -parity, being  $+$  or  $-$ . The mfs may also be given in units of MG =  $10^2$  T, in accordance with astronomical literature. For convenience we adopt an electron spin  $g$ -factor of 2. Higher order corrections are only relevant when transitions between different

spin-states are considered. Even then, changes to our results are marginal, whereas the choice  $g = 2$  facilitates the comparison of results to the literature [26].

The Hamiltonian (2.1) is equivalent to the problem of a non-moving hydrogen atom with infinite proton mass  $m_p$  in a magnetic field. It is convenient to stick to this simplification, as results for energies  $E$ , wave functions  $\psi$  and transition dipole strengths  $d$  with finite and infinite proton mass are related via (see Pavlov-Verevkin et al. [58] and Refs. [7, 26])

$$\psi(m_p, \beta, \mathbf{r}) = \lambda_m^{-3/2} \psi(m_p \rightarrow \infty, \beta \lambda_m^2, \mathbf{r}/\lambda_m), \quad (2.2)$$

$$E(m_p, \beta) = \lambda_m^{-1} E(m_p \rightarrow \infty, \beta \lambda_m^2) - 4\beta(m + m_s)(\lambda_m - 1), \text{ and} \quad (2.3)$$

$$d_{\text{if}}^q(m_p, \beta) = \lambda_m^2 d_{\text{if}}^q(m_p \rightarrow \infty, \beta \lambda_m^2), \quad (2.4)$$

with  $\lambda_m = (1 + m_e/m_p)$ , the electron to proton mass ratio  $m_e/m_p$  and the polarization index  $q$  (see Sec. 2.4). While the second term in Eq. (2.3) features the proton's cyclotron energy, which causes significant energy shifts at higher magnetic field strengths [59], the first term treats the reduced mass effect, which is of the order of magnitude  $m_e/m_p$  independent of  $\beta$ . If spin-flip transitions are not addressed, the energy shift  $4\beta m_s(\lambda_m - 1)$  from the spin term may as well be omitted, as all states with the same spin are affected in the same way. In the following we restrict ourselves to the calculation of states with magnetic quantum numbers  $m \leq 0$  and  $m_s = -1/2$  without loss of generality, since one can obtain the energy values for states with positive  $m$  or spin-up states by adding  $4\beta|m|$  or  $4\beta$ , respectively. Accordingly, wave functions for states with  $m > 0$  or with their spin pointing up correspond to their negative quantum number counterparts, differing only in the spin part of the eigenfunction or the angular momentum  $z$ -projection, respectively.

Methods for solving the moving hydrogen system in constant magnetic fields were presented e.g. by Potekhin [60] or Lozovik et al. [61]. For a moving atom the wave function symmetries are reduced even further and full three-dimensional calculations become necessary. The same applies when additional electric fields are present. Vincke et al. [62] studied both cases for the hydrogen atom using canonical transformations to account for the center of mass motion and presented variational calculations. Faßbinder et al. [63] investigated wavelength shifts for a limited number of hydrogen transitions and electric field strengths. Garcke et al. [64] presented a sparse grid method to calculate energies and eigenvalues of hydrogen and helium in magnetic and electric fields. More recently, Guan [65] applied pseudo-spectral discretization techniques to investigate both energy values and oscillator strengths of the Balmer transitions in crossed electric and magnetic fields. A comprehensive investigation of the hydrogen states and transitions in crossed electric and magnetic fields of arbitrary strength and orientation is still not available in the literature but absolutely essential to fully understand the shapes and positions of absorption lines in the spectra of MWDs and NSs, and are therefore currently investigated by Kersting at this institute.

The Hamiltonian (2.1) does also not include relativistic effects. This may seem inappropriate, especially in the region of very strong magnetic fields above the quantum critical field strength  $B_{\text{crit}} \approx 4.4 \times 10^9$  T, where the electron cyclotron energy equals the

rest energy of the electron. However, studies by Lindgren et al. [11] showed, that the shape of the wave functions perpendicular to the magnetic field as well as the transverse energy contributions are the same in the relativistic and non-relativistic theory. Thus, as long as the Coulomb binding energies are below the electron's rest energy, no significant relativistic corrections can be expected for bound states (see also Harding et al. [66]). These conclusions are backed up by numerical results of Lindgren et al. [11], Chen et al. [12] and Poszwa et al. [67], who find that relative corrections on the binding energies are smaller than  $10^{-5}$ , at any mfs below  $B_{\text{crit}}$ .

## 2.2 Expansion of the wave function

In previous work several different types of expansions were used for the hydrogen wave functions, including, e.g., anisotropic 2D Gaussians [26], power series for radial and angular functions [8], or formulations in parabolic coordinates [10]. To exploit the symmetries and different characteristics of the Hamiltonian (2.1) at different magnetic field strengths, we applied a number of different expansions for the wave functions  $\psi$ .

### 2.2.1 Ansätze

In weak magnetic fields  $\beta \ll 1$ , the Coulomb interaction dominates over the magnetic field, which then can be treated as a perturbation. Therefore, an expansion using spherical harmonics  $Y_{lm}$  (see e.g. Refs. [7, 68])

$$\psi(\mathbf{r}) = \sum_l^{l_{\max}} \frac{1}{r} f_l(r) Y_{lm}(\vartheta, \phi) \quad (2.5)$$

seems natural, and was thus also employed quite recently by Zhao et al. [6]. We adopt the *spherical expansion* (2.5) and use  $B$ -splines  $B_\mu$  [69] with coefficients  $\alpha_{l\mu}$  on a finite element grid for  $f_l(r) = \sum_\mu \alpha_{l\mu} B_\mu(r)$  to expand the radial components  $f_l(r)$  for each angular momentum  $l$  of the wave function. At high field strengths  $\beta \gtrsim 1$ , however, the magnetic-field effects dominate and the nucleus's Coulomb forces become a perturbation for the electron's motion perpendicular to the direction of the magnetic field. In this limit the wave function is best described using Landau orbitals  $\Phi_{nm}$  (see, e.g. Ref. [70]), which solve the Schrödinger equation of a charged particle in a magnetic field. Exploiting this Landau-orbital structure of the wave functions [7] we arrive at

$$\psi(\mathbf{r}) = \sum_{n=0}^{N_L} P_n(z) \Phi_{nm}(\rho, \phi), \quad (2.6)$$

where  $N_L$  denotes the last included Landau channel. Again, we use  $B$ -splines to describe the longitudinal components  $P_n(z) = \sum_\mu \alpha_{n\mu} B_\mu(z)$  of the *Landau expansion* (2.6). Both two-dimensional expansions in Eqs. (2.5) and (2.6) are in principle complete for wave functions with a sharp magnetic quantum number  $m$ .

At field strengths  $\beta > 1$ , the longitudinal components  $P_n(z)$  of each  $n$  become similar in shape [43] and differ only with respect to their magnitude. Thus, they can be merged into a single longitudinal wave function component  $P(z)$  with different weights  $t_n$  for the Landau channels, resulting in a *product ansatz* for the wave function

$$\psi(\mathbf{r}) = P(z)\Phi(\rho, \phi) = \sum_{\mu} \alpha_{\mu} B_{\mu}(z) \sum_n t_n \Phi_{nm}(\rho, \phi), \quad (2.7)$$

which was already applied by Engel et al. [43, 54]. In even stronger magnetic fields  $\beta \gg 1$ , the contributions of the higher Landau channels diminish, and the well-known *adiabatic expansion*

$$\psi(\mathbf{r}) = \sum_{\mu} \alpha_{\mu} B_{\mu}(z) \Phi_{0m}(\rho, \phi) \quad (2.8)$$

becomes valid. There, only the contributions of the lowest Landau channel are taken into account. Due to its simple nature it has been used widely in the past (see, e.g. Refs. [7, 52, 53]). The latter two expansions (2.7) and (2.8) are not used for the calculation of hydrogen results, but will be important for the calculations concerning many-electron atoms in the following chapters.

In contrast to the previous expansions, which exploited the structure of the wave functions in the limit of vanishing or very strong magnetic fields, the ansatz presented by Wang et al. [5]

$$\psi(\mathbf{r}) = \frac{e^{im\phi}}{\sqrt{2\pi}} \sum_{\mu\nu} \alpha_{\mu\nu} B_{\mu}(\rho) B_{\nu}(z), \quad (2.9)$$

relies only on the cylindrical symmetry of  $\hat{H}$  and expands both, the  $\rho$  and  $z$  components, using  $B$ -splines. Being a rather numerical approach, this *2D finite element expansion* appears to be somehow uninspired, but, as we will see in Sec. 2.2.3, profit can be taken from its flexibility.

## 2.2.2 Method of solution

For each of the Eqs. (2.5), (2.6) and (2.9) we expand the Hamiltonian (2.1) and obtain the Hamiltonian matrices. As  $B$ -splines form a non-orthonormal basis set, the expansions of the wave functions yield additional overlap matrices. The Hamiltonian matrices of the



spherical, Landau, and 2D finite element expansion take, in that order, the form

$$H_{l\mu l'\nu} = \int_0^\infty B_\mu(r) \left[ \delta_{ll'} \left( \frac{l(l+1)}{r^2} - \frac{\partial^2}{\partial r^2} - \frac{2}{r} + 2\beta m + 4\beta m_s \right) + V_m^{ll'}(r) \right] B_\nu(r) dr, \quad (2.10)$$

$$H_{n\mu n'\nu} = \int_0^\infty B_\mu(z) \left[ \delta_{nn'} \left( 4n\beta - \frac{\partial^2}{\partial z^2} \right) + V_m^{nn'}(z) \right] B_\nu(z) dz, \quad (2.11)$$

$$H_{\mu\nu\chi\xi} = \int_0^\infty \int_0^\infty B_\mu(\rho) B_\nu(z) \hat{H} B_\chi(\rho) B_\xi(z) \rho d\rho dz. \quad (2.12)$$

Please note that the spin- and magnetic energy components in Eq. (2.11) are included in the Landau energy term  $4n\beta$  for  $m_s = -1/2$  and negative  $m$ . For positive magnetic quantum numbers or spin projection, an energy shift must be added. In the energy functionals (2.10) and (2.11) the originally three-dimensional integrals have been reduced to one-dimensional integrals with the help of effective potentials (cf. Ref. [7]). Those are defined as

$$V_m^{ll'}(r) = \frac{2}{3} \beta^2 r^2 \left[ \delta_{ll'} - \left( \frac{2l+1}{2l'+1} \right)^{\frac{1}{2}} (l0, 20|l'0)(lm, 20|l'm) \right], \quad (2.13)$$

$$V_m^{nn'}(z) = -2 \int \frac{\Phi_{nm}^*(\mathbf{r}^\perp) \Phi_{n'm}(\mathbf{r}^\perp)}{|\mathbf{r}|} d\mathbf{r}^\perp, \quad (2.14)$$

and utilize Clebsch–Gordan coefficients or effective Landau potentials, respectively. The calculation of  $V_m^{nn'}$  can be highly non-trivial (cf. Refs. [7, 71]). The reduction to a one-dimensional integration is not possible for the 2D finite element energy functional (2.12), but the conservation of the magnetic quantum number allows at least for a trivial solution of the  $\varphi$ -integration.

The orthonormality of the spherical harmonics and Landau orbitals reduces the overlap matrices

$$S_{l\mu l'\nu} = \delta_{ll'} \int_0^\infty B_\mu(r) B_\nu(r) dr, \quad (2.15)$$

$$S_{n\mu n'\nu} = \delta_{nn'} \int_0^\infty B_\mu(z) B_\nu(z) dz, \quad (2.16)$$

$$S_{\mu\nu\chi\xi} = \int_0^\infty \int_0^\infty B_\mu(\rho) B_\nu(z) B_\chi(\rho) B_\xi(z) \rho d\rho dz, \quad (2.17)$$

of the spherical and Landau expansion to one-dimensional integrals. Due to the  $z$ -parity of the wave functions we can omit the integration for  $z < 0$  in all formulae above, as the

corresponding factor of two cancels in the Hamilton and overlap matrices. With these matrices the Schrödinger equation becomes a generalized eigenvalue problem of the form

$$\sum_{a\mu} \alpha_{a\mu} H_{a\mu b\nu} = \varepsilon \sum_{a\mu} \alpha_{a\mu} S_{a\mu b\nu}, \quad (2.18)$$

which can be solved numerically. Here, the indices  $(a, b)$  can be replaced by either  $(l, l')$ ,  $(n, n')$ , or  $(\chi, \xi)$  to retrieve the proper form corresponding to each of the three expansions. Independently of the applied expansion, we search for the eigenstate-coefficients  $\alpha_{a\mu}$  and energy eigenvalues  $\varepsilon$  of the generalized eigenvalue problem. Since this is a two-dimensional problem, the matrices can grow substantially large (up to  $8000 \times 8000$  entries), and remain quite dense as several percent of the entries are different from zero. An efficient method solving such large problems is therefore imperative — we use the LAPACK [72] routine 'DSYGVX'. LAPACK offers many different routines to solve symmetric definite generalized eigenvalue problems. Several test calculations proved that this routine is the most efficient one in our case.

Despite the similarities of the implementations, the spherical and Landau expansions differ significantly from the more general 2D finite element ansatz, where the calculation of both the overlap and Hamiltonian matrices involves integrals of higher dimension. Additionally, we expect higher expansion orders for the 2D  $B$ -spline expansion compared to the spherical one at low magnetic fields, or compared to the Landau expansion at high magnetic fields. On the other hand, the convergence of those expansions is not assured in the intermediate regime, which is also called the “chaotic regime” (see e.g. Refs. [7, 73]), where magnetic and Coulomb interactions are comparable in strength. To ensure that our computations converge in a wide range of  $\beta$  we enabled our programs to include up to  $N_L = 70$  Landau channels or 100 angular momenta. The latter corresponds to  $l_{\max} = 200$  as the  $z$ -parity of the spherical harmonics is given by  $(-1)^{l-m}$ , thus only odd or even angular momenta contribute to the problem.

### 2.2.3 Applicability of the expansions

The spherical and Landau expansions naturally require the dominance of the corresponding wave function symmetry and are thus restricted to a certain range of the mfs. The following considerations give rough estimates for the field strength  $\beta_c$ , where we expect a change of symmetry, depending on the principal quantum number  $n$  of a state: The diamagnetic term  $\beta^2 \rho^2$  in the Hamiltonian (2.1) has cylindrical symmetry, whereas the other terms have spherical symmetry. Therefore, we expect a change of symmetry if the cylindrically symmetric energy contributions ( $\sim \beta^2 n^4$ ) outweigh the spherically symmetric ones ( $1/n^2$ ). As a result we find the dependence

$$\beta_c \sim n^{-3}. \quad (2.19)$$

A different but equally justifiable estimate compares the binding length of a state ( $r \sim n^2$ ) to the Larmor radius  $a_L \sim 1/\sqrt{\beta}$ , resulting in the relation

$$\beta_c \sim n^{-4}. \quad (2.20)$$

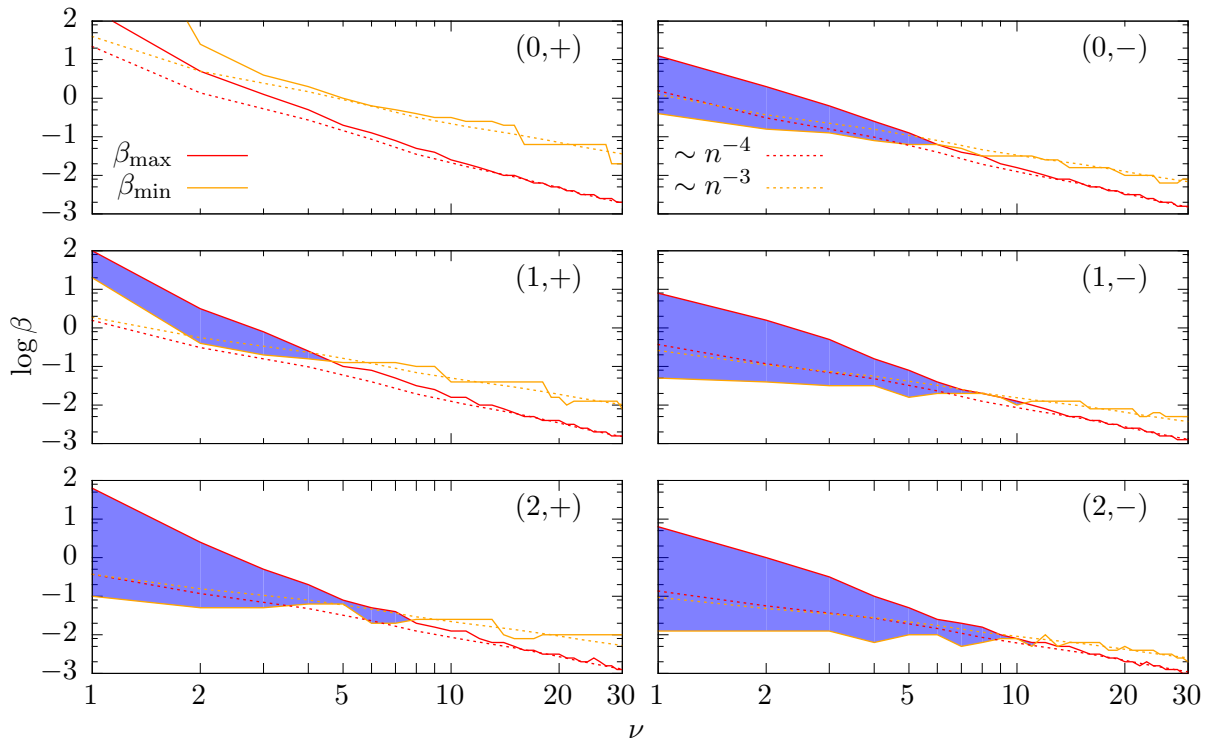


**Fig. 2.1:** Log-log plot of the *minimal*  $\beta$  (yellow line), at which the Landau expansion, depending on the excitation number  $\nu$ , still reaches an absolute energy precision of  $10^{-5}$  Ry, with the maximum number of expansion terms fixed to  $N_L = 30$ . Red lines correspond to the *maximum*  $\beta$ , at which the spherical expansion met the same energy precision with  $l_{\max} = 100$ . Labels in the right corner denote the symmetry subspace. Dotted lines are power law estimates proportional to  $\sim n^{-4}$  (red) or  $\sim n^{-3}$  (orange). The correspondence to the principal quantum numbers  $n$  can be found in Ref. [74]. Blue filled regions mark the ranges where both expansions converge. Lines serve as a guide to the eye.

In addition there is another estimate in the literature [7], which compares the diamagnetic energy to the energy difference between principal quantum numbers, which yields  $\beta_c \sim n^{-3.5}$ .

To understand which estimate is best we applied both of the two expansions in question and performed a vast set of calculations for the states  $(\{0, -1, -2\}, \pm, \leq 30)$  at several field strengths. In Fig. 2.1, we show for each of the states the minimal and maximal  $\beta$ , where we could reach convergence to a certain energy precision while using a fixed maximum expansion order. To speed up the calculations we did not use our maximum possible expansion orders stated above, and in turn reduced the desired energy precision. We also plot in Fig. 2.1 the power law estimates for the change of symmetry field strengths  $\beta_c \sim n^{-4}$  and  $\beta_c \sim n^{-3}$ . As we can see, *both* estimates have their justification: Whereas  $\beta_c \sim n^{-3}$  indicates at which  $\beta$  the Landau expansion becomes feasible,  $\beta_c \sim n^{-4}$  indicates the field strength at which the spherical expansion becomes inadequate. The two different powers of the two estimates already hint at the existence of a

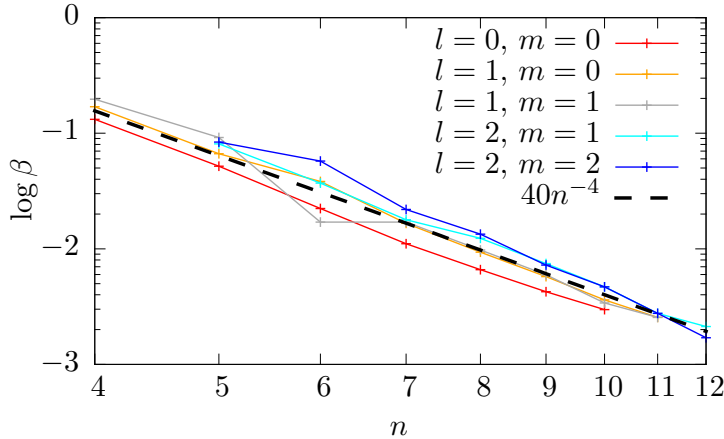


**Fig. 2.2:** Maximum magnetic field strength  $\beta$  that could be reached maintaining an energy precision of  $10^{-6}$  Ry using the spherical expansion (2.5) ( $l_{\max} = 100$ ), as a function of the principal quantum number  $n$ . The states are labeled according to their low-field quantum numbers  $n$ ,  $l$ , and  $m$ . The dashed black line is an average of individual fits. Lines serve as a guide to the eye.

third regime, where none of the two expansions is appropriate. This is also demonstrated by the blue filled regions in Fig. 2.1, which indicate ranges of  $\beta$ , where both expansions converged. Many states, especially those of the symmetry subspace  $(0, +)$  and those with higher  $\nu$ , show a “convergence gap” at intermediate field strengths, where none of the two expansions reaches the desired precision. This gap, which corresponds to the intermediate, chaotic regime, spans a wider range of mfs for higher  $\nu$ . These estimates for  $\beta_c$  also hold for a higher energy precision, as is demonstrated in Fig. 2.2. There we show the maximum  $\beta$  for which we could reach convergence with the spherical expansion at a desired energy precision of  $10^{-6}$  Ry. Here we used the zero-field quantum numbers  $n, l, m$  to denote the states.

So far we have only utilized about half of the maximum possible order for both expansions. Still, even with the maximum order for both expansions we cannot enforce convergence for higher excited states in the intermediate regime, as it is shown in Fig. 2.3. There, the number of terms in the spherical expansion diverges at  $\beta = 3 \times 10^{-3}$ , but the convergence of the Landau expansion does not set in before  $\beta = 5 \times 10^{-1}$ . As a remedy, we apply the flexible 2D  $B$ -spline expansion, whose number of finite elements in  $\rho$ -direction is shown in the same figure. Please note, that this number  $\mu_{\max}$  is almost constant over the whole range of displayed  $\beta$  values, especially in the intermediate mfs region. At very low or very high  $\beta$  the numerical effort is — compared to the two symmetry-adapted expansions — only moderately larger. This flexibility of the 2D finite element expansion convinced us to use this ansatz at all field strengths. Additionally, this allows for an easy comparison of the results at different  $\beta$ , which otherwise would have been handicapped if different wave function expansions were used. For these reasons all further discussions and results in this chapter are based on the 2D finite element expansion.

## 2.2.4 Finite element basis

The efficiency of the  $B$ -spline expansion (2.9) strongly depends on the employed finite element bases. Each of them — in  $\rho$  and  $z$  direction — is characterized by its node

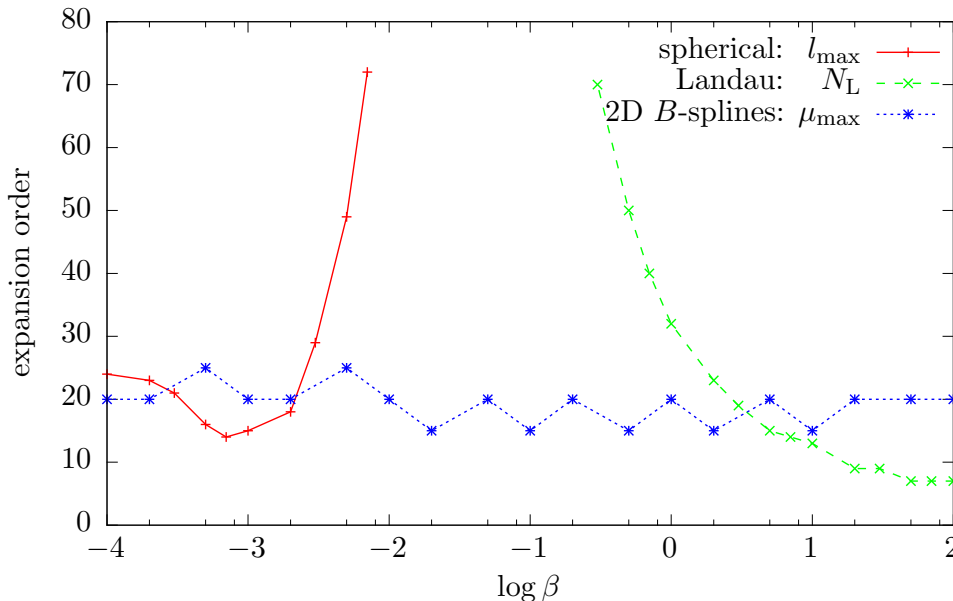


**Fig. 2.3:** Expansion orders of programs utilizing the three expansions (2.5) “spherical”, (2.6) “Landau” and (2.9) “2D  $B$ -splines” as a function of  $\beta$  for the state ( $m = 0$ ,  $\pi_z = +$ ,  $\nu = 20$ ). The expansion orders are chosen to reach an energy precision of  $10^{-7}$  Ry. The minimum in the expansion order of the spherical ansatz at  $\beta \approx 7 \times 10^{-4}$  is due to the first anticrossing with the state  $(0,+,21)$ , causing significant changes of the wave function. Lines serve as a guide to the eye.

sequence  $\{x_i\}$  and the  $B$ -spline order  $k$ . It is an important task to find a proper node sequence and to minimize the energy error arising from the expansion. For the construction of a node sequence we need to know the domain of definition  $[0, x_{\max}]$  and the number of finite elements  $N_{\text{fem}}$ . Then, we distribute the nodes from 0 to  $x_{\max}$ , while the spacing between the nodes increases linearly (cf. [53]). We found this to be much more efficient than an equidistant node distribution or such with a quadratic finite element widening. Both parameters  $x_{\max}$  and  $N_{\text{fem}}$  are chosen independently for both directions  $\rho$  and  $z$ .

The cutoff length  $x_{\max}$ , which corresponds to the outermost sampling point of the wave function, has a strong influence on the precision of the results. If  $x_{\max}$  is chosen too small, a significant part of the wave function’s tail is neglected. Thus, the wave function will be overestimated at the sampled points due to renormalization. This results in an overestimation of the binding energy. On the other hand, choosing  $x_{\max}$  too large increases the number of finite elements needed to accurately sample the wave function and therefore increases the computing time considerably. Our goal is to find an optimal cutoff length  $x_{\max}$ , which reduces the calculation effort to a minimum, but maintains the demanded precision. This is quite a challenging task, as wave functions of excited states may have complex spatial probability distributions and undergo drastic changes in the regime of intermediately strong field strengths.

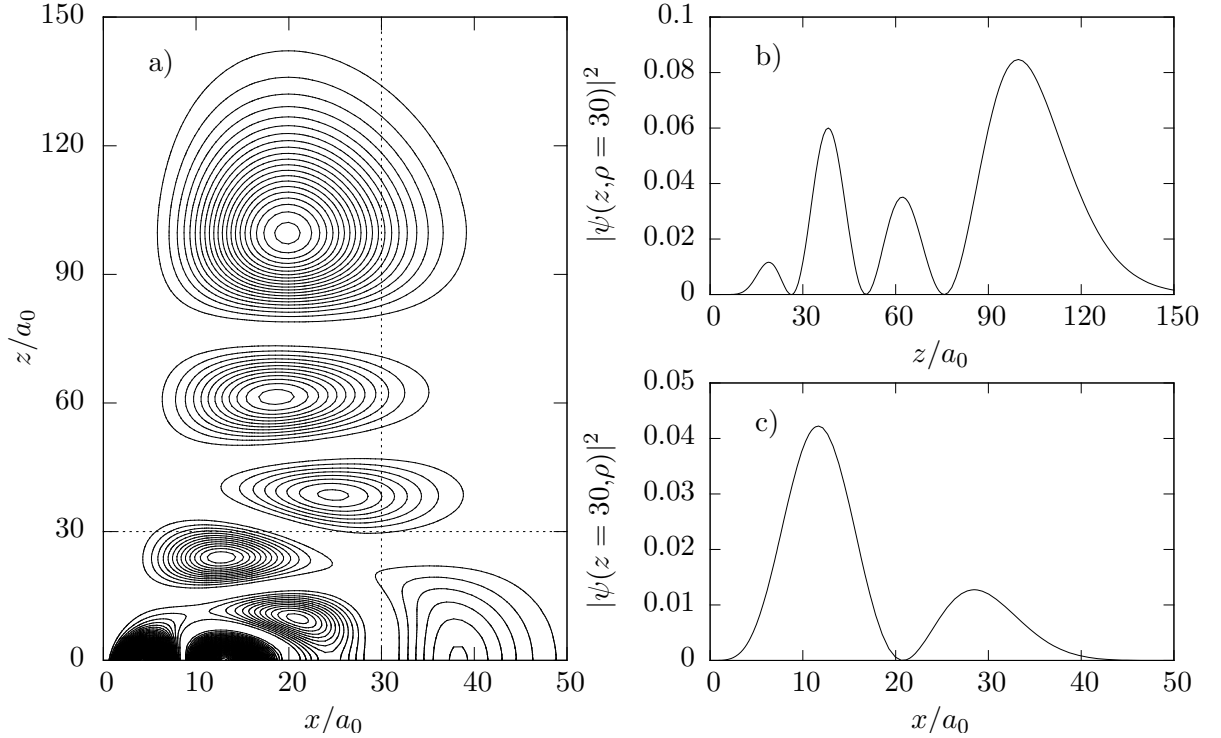


**Fig. 2.4:** a) Contour plot of the squared spatial probability distribution of the state  $(-2, +, 10)$  at a magnetic field strength of  $\beta = 5 \times 10^{-3}$ . Lines are drawn every 5 per mill relative to the squared maximum of the wave function. In b) a slice cut parallel to the  $z$ -axis at  $\rho = 30$ , in c) parallel to the  $\rho$ -axis at  $z = 30$  is shown (see dashed lines in a)).

An example for such a wave function is presented in Fig. 2.4, which shows a visualization of the spatial probability distribution of the state  $(-2, +, 10)$  at an intermediate mfs, as well as slices parallel to the  $\rho$  and  $z$  axes. In search for a good estimate of  $x_{\max}$  we analyze several of these wave function slices, determine the position where their absolute value has finally dropped to  $10^{-6}$  of the total wave function's maximum absolute value, and assume this to be the slices' optimal width. This cutoff criterion was found to be appropriate for all investigated states during intensive calculations. If the absolute value of the wave function slice has not decayed sufficiently far at the current edge of the basis, an improved basis width is obtained from an extrapolation of the wave function assuming an exponential decay in its outer regions.

Having analyzed all slices we carefully adjust the basis widths. The new width is given by the maximum of the estimated optimal widths of all slices in that direction. We then iteratively optimize  $x_{\max}$ . To dampen a possible oscillatory behavior of  $x_{\max}$  during these iterations we restrict changes of  $x_{\max}$  to 20%. Oscillations can arise as the  $B$ -spline basis is not complete and a change of the node sequence always induces (small) changes of the wave function. Due to the lower node density in the outer regions of the domain of definition the wave function's decay behavior is especially sensitive to changes of the node sequence. The dependence of the wave function on the finite element basis

also hampers an extrapolation of  $x_{\max}$  if the width is chosen too small. Therefore, we do not stop this iteration as long as the suggested basis width exceeds the current one. The adaption of  $x_{\max}$  stops only in case the suggested width is up to 20% smaller than the current width.

Now that we have found a suitable domain of definition, we have to optimize the number of finite elements  $N_{\text{fem}}$ . Appropriate initial values can be obtained using previously calculated results at similar magnetic field strengths. If such results are not available, the initial values have to be guessed. We then increase  $N_{\text{fem}}$  in steps of 5 and monitor the convergence of the resulting energies. If energies of two consecutive steps differ less than a convergence threshold  $\epsilon_{\text{conv}}$ , we stop to increase  $N_{\text{fem}}$  and use the last obtained result.

The energy convergence behavior for  $N_{\text{fem}} \rightarrow \infty$  strongly depends on the mfs, the state in question, and the basis' node sequence. The exact remaining energy error caused by the basis at a given  $N_{\text{fem}}$  and  $x_{\max}$  is not known. Still, we determined a reasonable error estimate in an empirical way by comparing hundreds of results at various magnetic field strengths and for several states from our calculations to those from Ruder et al. [7] and Kravchenko et al. [8] (see Sec. 2.5), as well as to our own results obtained with other programs using a spherical (2.5) or Landau (2.6) expansion, where applicable. The remaining energy difference of our results to the more precise ones was in all cases much smaller than ten times the convergence threshold  $\epsilon_{\text{conv}}$ . Therefore, we can safely choose  $\epsilon_{\text{prec}} > 10 \cdot \epsilon_{\text{conv}}$ .

To take account of the complex structure of the wave functions we vary the number of finite elements separately, but not independently, for both directions. If  $N_{\text{fem}}^p$  is changed, the energy has to be checked again for convergence of  $N_{\text{fem}}^z$  — and vice versa, until the finite element bases of both directions converge simultaneously. This powerful method allows us to quickly calculate virtually any hydrogen state with reasonable precision at any mfs. As  $\beta$  is a continuous parameter we need to carefully select the field strengths at which those calculations shall be performed. Afterwards we can interpolate the energy values for arbitrary field strengths with sufficiently high precision.

## 2.3 Automated magnetic field strength variation

The intermediate field strength regime sets another challenge besides the problem of symmetry dominance discussed before. Anticrossings [75] of states within the same symmetry subspace cause substantial changes to the states' electronic structure and the corresponding energy eigenvalues on a relatively short interval of the mfs. The number of avoided crossings increases with the excitation level of a state, as can be seen in Fig. 2.5. There, we present the energy as a function of the mfs given in MG of a low-lying state (orange), which is rather smooth, and that of a highly excited state (blue), showing several anticrossing edges.

A thorough analysis of the energy functions cannot be efficient for all states, when fixed equidistant or exponential distributions of the data points are chosen, as shown in Fig.

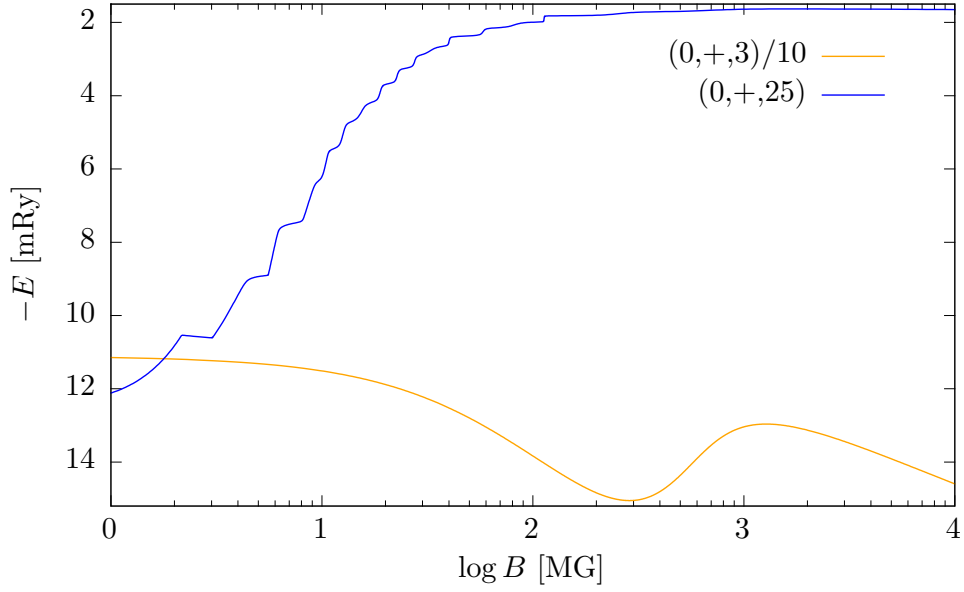


**Fig. 2.5:** Comparison of the energies for the states  $(0,+3)$  and  $(0,+25)$  as a function of the magnetic field strength. Values of the lower state are divided by ten for convenience. The energy function of the lower state (orange) shows no remarkable features, whereas the highly excited state (blue) has several features arising from avoided crossings with other states of its symmetry subspace.

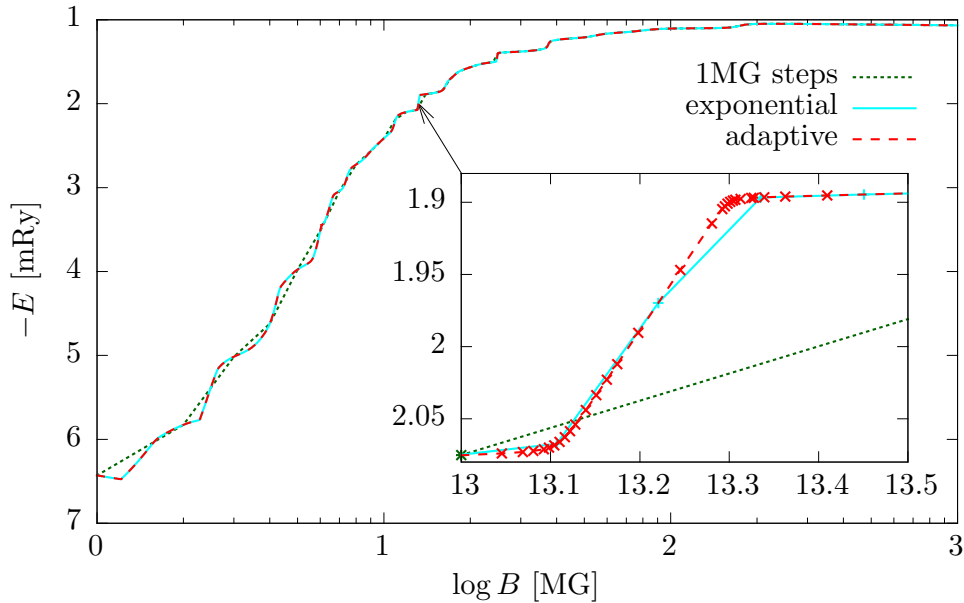


**Fig. 2.6:** Calculations for the state  $(-1,-30)$  at magnetic field strengths typical for MWDs. 1000 data points are distributed equidistantly in steps of 1 MG (dotted green), 267 exponentially (solid cyan), and 793 according to the adaptive AMV (dashed red). The inset provides a detailed view on the distinct edge of the energy function at 13 MG.



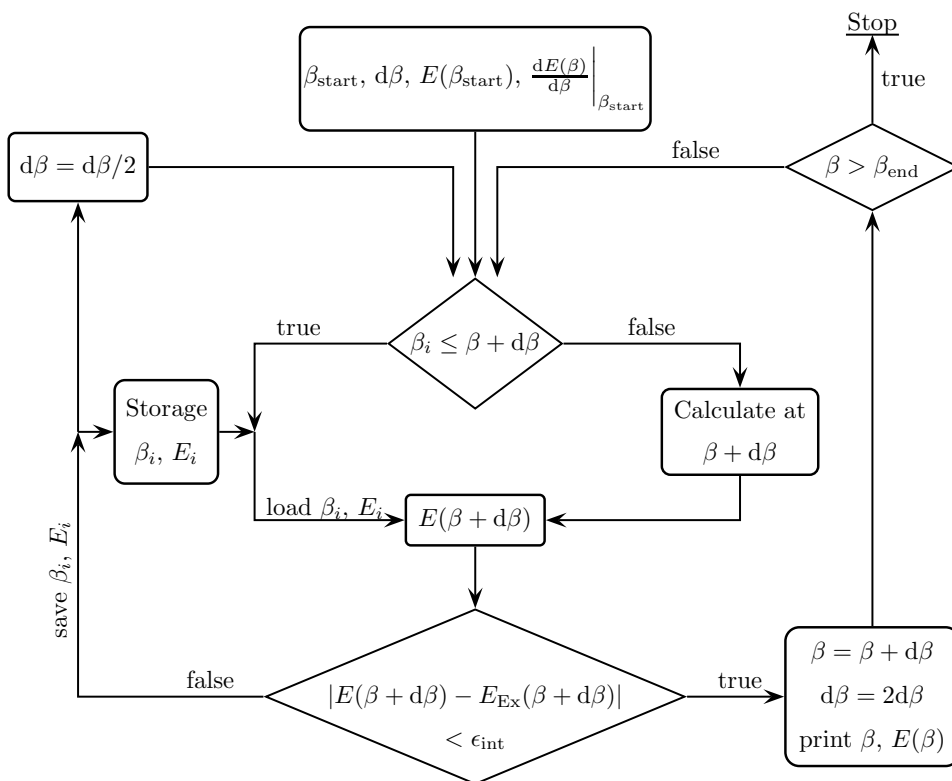


**Fig. 2.7:** Scheme of the automated magnetic field variation procedure (for details see text).

2.6. There we show calculations for a rather complex state  $(-1, -, 30)$  with different data point distributions, and we apply a linear interpolation between the calculated results. The linear data point distribution is not precise enough in the range of 1 MG to about 15 MG — whereas beyond 300 MG the number of points exceeds the sufficient sample density, wasting 700 data points in a rather featureless region of the energy function. The exponential data point distribution yields quite good results, but an adaptive method reproduces the true energy function in better detail, as can be seen from the inset.

This automated magnetic field strength variation method (AMV) adapts the step width  $d\beta$  during the analysis of the energy over field strength function. The step width is determined in such a way that a linear interpolation between the data points deviates from the true result only within an acceptable interpolation error margin  $\epsilon_{\text{int}}$ , which should be larger than the working precision  $\epsilon_{\text{prec}}$ . We chose  $\epsilon_{\text{int}} > 10 \cdot \epsilon_{\text{prec}}$ , which results in the following final hierarchy of precision parameters

$$\epsilon_{\text{int}} > 10 \cdot \epsilon_{\text{prec}} > 100 \cdot \epsilon_{\text{conv}} \quad , \quad (2.21)$$

ensuring a minimum precision of  $\epsilon_{\text{int}}$  for interpolated energies at any mfs. This method requires a minimal number of data points, while ensuring a high data point density in regions rich of features and sparse data point placement where the energy function evolves almost linearly.

Figure 2.7 shows a scheme of the AMV procedure described below. We begin at  $\beta = \beta_{\text{start}} = 0$ . In each step, we try to extrapolate linearly the next energy value at  $\beta' = \beta + d\beta$ . At  $\beta = 0$ , both the precise value of the energy function  $E(\beta = 0)$  as well as its gradient are known: The energy is of course  $1/n^2 \text{Ry}$  with the principal quantum number  $n$ , whereas the linear Zeeman effect  $dE/d\beta = 2m + 4m_s$  determines the gradient. We then perform a full calculation for  $E(\beta')$  and compare the result to the extrapolated value  $E_{\text{Ex}}$ . If deviations are smaller than  $\epsilon_{\text{int}}$  we accept this data point, and are now able to interpolate any energy value between  $\beta$  and  $\beta'$ . Subsequently, we update the true gradient, which is calculated using  $E(\beta)$  and  $E(\beta')$ , as well as the field strength  $\beta \leftarrow \beta'$  and the last accepted energy data point  $E(\beta) \leftarrow E(\beta')$ . Then we try to extrapolate again. Each time the extrapolation succeeds, i.e. the interpolated value deviates from the result of a full calculation at this field strength by less than the desired precision, we double the field strength step  $d\beta$  for subsequent calculations. Each time the extrapolation fails, the current  $d\beta$  is halved and the data point is not accepted, but the correct one is stored as  $(\beta_i, E_i)$  for later use. If an equal or larger field strength is addressed, results of the full calculation can be loaded from storage directly, which saves a considerable amount of computation time. One can, of course, also start at  $\beta_{\text{start}} > 0$  if one provides the program with the correct energy value and gradient corresponding to the starting field strength.

## 2.4 Transitions

Transition energies and oscillator strengths are key components in the analysis of spectra, the only observable quantity of distant stars. The dimensionless oscillator strength  $f$  and the dipole strength  $d$  of a transition from an initial state (i) to a final state (f) can be acquired using the known relations (see Ref. [7])

$$f = \Delta E_{\text{if}} d_{\text{if}}^q, \quad d_{\text{if}}^q = |p_{\text{if}}^q|^2, \quad (2.22)$$

with the energy difference  $\Delta E_{\text{if}} = E_f - E_i$  given in Rydberg units and the magnetic quantum number difference  $q = \Delta m = m_f - m_i$  between final and initial state. The dipole matrix element  $p_{\text{if}}^q$  is calculated using the spherical harmonic  $Y_{1,q}$

$$p_{\text{if}}^q = \left\langle \psi_f \left| \sqrt{\frac{4\pi}{3}} r Y_{1,q}(\theta, \phi) \right| \psi_i \right\rangle, \quad (2.23)$$

with the radial component  $r$  of the position vector given in atomic units. Using the spatial component of our wave function expansion (2.9)

$$\psi(\rho, z) = \sum_{\mu\nu} \alpha_{\mu\nu} B_\mu(\rho) B_\nu(z), \quad (2.24)$$

the dipole matrix elements become

$$p_{if}^0 = 2 \int_0^\infty \int_0^\infty \psi_f(\rho, z) z \psi_i(\rho, z) \rho d\rho dz, \quad (2.25)$$

$$p_{if}^{\pm 1} = \pm \sqrt{2} \int_0^\infty \int_0^\infty \psi_f(\rho, z) \rho \psi_i(\rho, z) \rho d\rho dz. \quad (2.26)$$

Again we use the  $z$ -parity to reduce the  $z$ -integration to the semi-finite interval  $[0, \infty]$  and obtain the original value by a multiplication with 2. In this dipole approximation the three possible values of  $q$  are connected to the polarization of the photon, namely

$$q = \begin{cases} 0, & \text{linear polarization} \\ \pm 1, & \text{circular polarization.} \end{cases} \quad (2.27)$$

## 2.5 Results

The most complete analysis of the hydrogen atomic energy levels in the literature [7] features the 38 lowest states at up to 120 data points in the range of  $\beta = 10^{-4} \dots 10^3$ . The precision of modern high-resolution spectroscopy however sets the demand for even more data especially for higher excitation levels, to fully describe absorption features in the atmosphere of hydrogen-rich magnetic white dwarfs [13]. A spectroscopic resolution of about 1 Å at wavelengths of  $10^4$  Å by the SDSS [76] is roughly equivalent to an energy precision of  $10^{-5}$  Ry for the transitions and thus the atomic state energies. The results presented here were calculated using a precision of  $\epsilon_{\text{prec}} = 10^{-7}$  Ry, excelling the spectroscopic precision by far. The analyses in this section focus on the magnetic field strengths relevant for the interpretation of MWD spectra ( $B = 1 \dots 10^3$  MG), although all results were calculated up to neutron star field strengths of  $\beta = 10^3$ .

### 2.5.1 Energy values

In Fig. 2.8 we present the energy spectrum of the hydrogen atom as a function of the mfs. To retain a clear arrangement, only the spin-down states with  $n \leq 5$  were plotted. The blue labels (A-D) mark groups of states with different high-field behavior:

- A. The “tightly-bound” (tb) states have the lowest energy in the spectrum at  $\beta \gtrsim 1$ . Their wave functions are nodeless in  $z$ -direction and their energies would diverge logarithmically towards  $-\infty$  without the finite nuclear mass corrections from equation (2.3). Considering these corrections, only the ground state ( $m = 0$ ) retains this behavior, whereas the other tightly-bound state energies diverge at very large  $\beta$ .
- B. These curves correspond to the “hydrogen-like” (hl) states with  $m = 0$ . For infinitely strong fields they converge again towards the Rydberg series (red bars). This can be

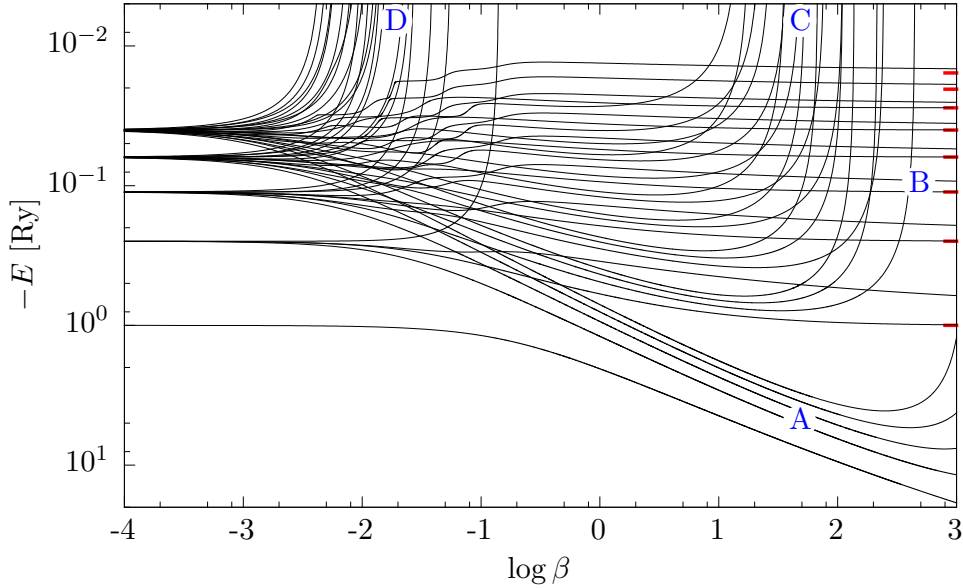


**Fig. 2.8:** Energy as a function of  $\beta$  of the spin-down states with principal quantum number up to  $n = 5$ , including finite nuclear mass corrections. Red bars mark the Rydberg energy series. The labels (A-D) are explained in the text.

explained by the fact that the potential and the wave functions become effectively one-dimensional coulombic in this limit [77].

- C. HI-states with  $m < 0$  become auto-ionizing as the finite nuclear mass correction causes a linear energy shift to all energies of states  $m \neq 0$ . Without this correction, these energies would also converge towards the Rydberg series at large  $\beta$ .
- D. States with positive  $m$  become auto-ionizing at lower field strengths due to the term  $2\beta m$  in the Hamiltonian (2.1). In the same way, this applies to spin-up states (not plotted), which are energetically shifted by  $4\beta m_s$ .

In the following graphs 2.9 and 2.10 we combine only energy levels of the same symmetry subspace into one figure. Their energy functions are not allowed to cross, which enables us to obtain clearer images. The two figures show the lowest 30 states of the symmetry subspaces  $(0,-)$  and  $(-1,+)$  in a smaller section of the field strength. Colors facilitate the tracking of the energy levels even at the narrowest anticrossings. In combination with the other energy functions of a given symmetry subspace the peculiar edges of the single energy functions shown in the previous graphs 2.5 and 2.6 are now a logical consequence of anticrossing cascades.

The comparison with results of other groups poses a further test for the precision of our own results. As it is common in the literature, we do not include finite nuclear mass corrections here. Table 2.1 contains a comparison of our energy values for the states  $(0,+1)$  and  $(0,+2)$  to the high precision results of Kravchenko et al. [8]. This comparison confirms that we have indeed reached the targeted accuracy of seven digits in

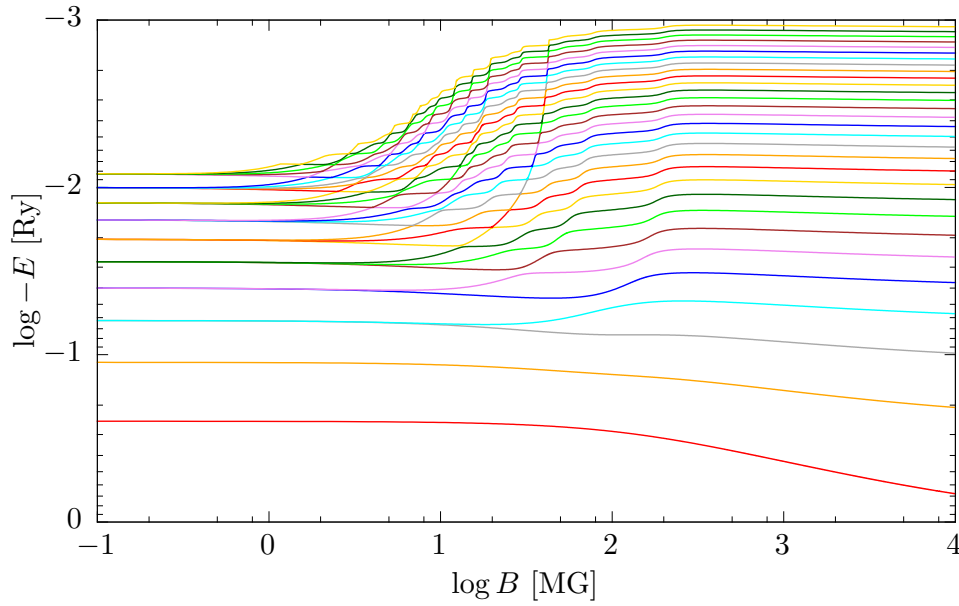


**Fig. 2.9:** Energy  $E$  as a function of the magnetic field  $B$  for the lowest 30 states in the symmetry subspace  $(0, -)$  including finite nuclear mass corrections, which stay small due to the magnetic quantum number  $m = 0$ .

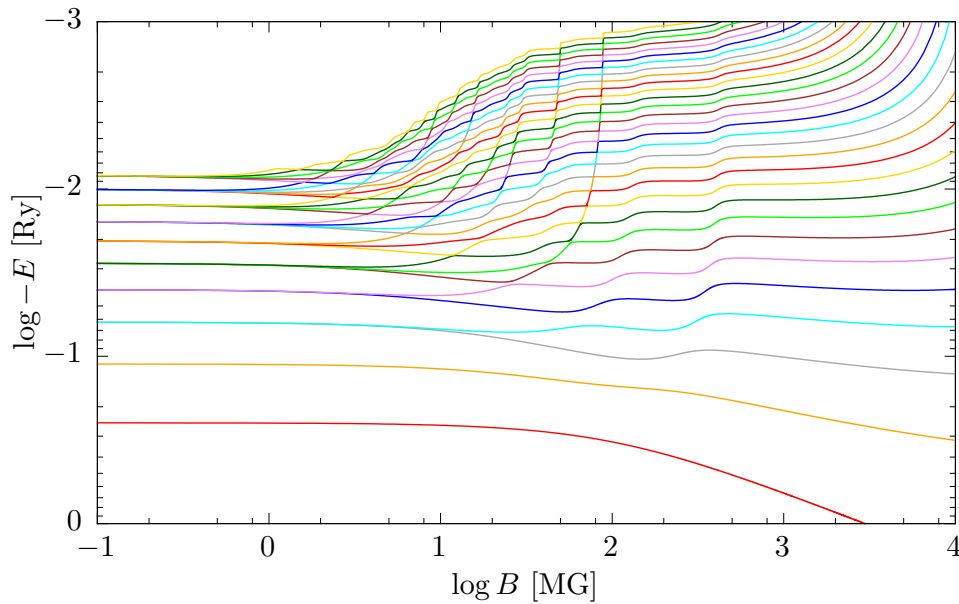


**Fig. 2.10:** Same as in Fig. 2.9 for symmetry subspace  $(-1, +)$ . The second term of the nuclear mass correction formula (2.3) causes the divergence of the state energies at large  $B$ .

all of our calculations. We also note that the precision of the results of Ref. [8] decreases at high  $\beta$ , whereas we maintain our accuracy without difficulty. Table 2.1 also contains values obtained by Wang et al. [5], who, similar to us, used a two-dimensional finite element expansion with  $B$ -splines. In contrast to us, they did not adapt the number of finite elements for each calculation but only changed the node sequences. Therefore, a closer inspection of their results for the state  $(0,+1)$  yields that the corresponding precision is significantly reduced from roughly 10 significant digits at low  $\beta$  to about 6 significant digits at  $\beta = 10^3$ . Compared to our findings their results at  $\beta = 5 \times 10^3$  are even reduced to 5 significant digits. A similar loss of precision is found for their results of the state  $(0,+2)$ .

We compare our results to the data of the same references in Tab. 2.2, which contains results for the two hydrogen-like states  $(0,-1)$  and  $(0,-2)$ . Again, we can confirm to have reached our targeted energy precision, whereas the precision of the results in Refs. [5, 8] decreases with rising  $\beta$ . For some high values of  $\beta$  they do not give results at all. In Tab. 2.3 we compare our data for the tightly-bound states  $(-1,+1)$  and  $(-2,+1)$  to those of Refs. [8] and [6]. The latter used a spherical expansion and  $B$ -splines. Similar to Wang et al. [5] they did not change the number of finite elements but instead adapted the  $B$ -spline order and node sequence to enhance their precision in the radial direction. They included up to about  $l_{\max} = 100$  angular momenta to achieve convergence. As we already have discussed in detail in Sec. 2.2.3, a spherical ansatz can, at high  $\beta$ , only provide high precision results for a very limited number of low-lying states. Surprisingly, the results of Ref. [6] match those of Ref. [8] up to the last digit. Our own results also match those of Ref. [8] within our desired accuracy.

With the precision of our energy values established we can now investigate transition energies and wavelengths. We therefore computed the energy eigenvalues of the lowest 30 states of each of the ten symmetry subspaces ( $m = 0 \dots -4, \pi_z = \pm$ ) at  $\beta = 0 \dots 10^3$ . With the data at hand we will now analyze the magnetic field effects on transition wavelengths in the following section.

## 2.5.2 Transition wavelengths

We use a simple notation, which separates the quantum numbers of initial and final state with a colon  $(m_i, \pi_{z_i}, \nu_i) : (m_f, \pi_{z_f}, \nu_f)$  to denote the transitions. The spin quantum number can again be dropped since we restrict ourselves to those dipole transitions, where no spin-flip occurs.

Figure 2.11 shows the most important effects of the magnetic field on transition wavelengths  $\lambda$  using the example of six transitions from the Balmer series. Please note that the ordinate denotes the mfs in accordance to the representation in the literature. In the Zeeman regime, each line of the series splits into three components — one for each type of the allowed dipole transitions  $\Delta m = 0$  (red, orange),  $\Delta m = -1$  (green, violet) &  $\Delta m = +1$  (blue, cyan). Regarding the solid curves (without finite nuclear mass corrections), the red one corresponds to a transition between two hydrogen-like states, which have a finite energy difference both in the low-field and high-field limit, resulting

**Tab. 2.1:** Binding energies in Rydberg atomic units of the states  $(0, +, 1)$  and  $(0, +, 2)$  at different  $\beta$  in comparison to results from Kravchenko et al. [8] and Wang et al. [5].

$\beta$	$(0, +, 1)$			$(0, +, 2)$		
	this work	Ref. [8]	Ref. [5]	this work	Ref. [8]	Ref. [5]
$1 \times 10^{-4}$	1.0002000	1.000199980000	1.0001999800	0.2501997	0.250199720000	0.25019971
$2 \times 10^{-4}$	1.0003999	1.000399920000	—	0.2503989	0.250398880008	—
$5 \times 10^{-4}$	1.0009995	1.000999500000	—	0.2509930	0.250993000318	0.25099300
$1 \times 10^{-3}$	1.0019980	1.001998000008	1.1001998000	0.2519720	0.251972005096	0.25197200
$2 \times 10^{-3}$	1.0039920	1.003992000142	—	0.2538881	0.253888081394	—
$5 \times 10^{-3}$	1.0099500	1.009950005518	—	0.2593031	0.259303142716	0.25930312
$1 \times 10^{-2}$	1.0198001	1.019800088178	1.0198000878	0.2672484	0.267248355070	0.26724835
$2 \times 10^{-2}$	1.0392014	1.039201403538	—	0.2794797	0.279479649158	0.27947964
$5 \times 10^{-2}$	1.0950530	1.095052960802	—	0.2961783	0.296178311580	0.29617830
$1 \times 10^{-1}$	1.1807631	1.180763130070	1.1807631235	0.2979734	0.297973356396	0.29797334
$2 \times 10^{-1}$	1.3292108	1.329210759736	—	0.2983327	0.298332695696	0.29833268
$5 \times 10^{-1}$	1.6623378	1.662337793466	1.6623377850	0.3209380	0.320937965268	0.32093795
$1 \times 10^0$	2.0444278	2.044427815330	2.0444278053	0.3478894	0.347889411946	0.34788939
$2 \times 10^0$	2.5615960	2.561596032104	2.5615960169	0.3776929	0.377692927400	0.37769290
$5 \times 10^0$	3.4955943	3.495594327428	3.4955942951	0.4179037	0.417903658090	0.41790363
$1 \times 10^1$	4.4307970	4.430797030866	4.4307969687	0.4476842	0.4476842536	0.44768422
$2 \times 10^1$	5.6020596	5.602059649556	5.6020594559	0.4763985	0.4763985456	0.47639850
$5 \times 10^1$	7.5796084	7.579608472610	7.5796079443	0.5123631	0.5123631406	0.51236192
$1 \times 10^2$	9.4542902	9.454290221374	9.4542886885	0.5379364	0.5379364	0.53793620
$2 \times 10^2$	11.7033023	11.703302325664	11.70329920	0.5620594	0.5620594	0.56205587
$5 \times 10^2$	15.3248465	15.324846495510	15.32483814	0.5917149	0.591714	0.59171424
$1 \times 10^3$	18.6095301	18.609530165540	18.60951488	0.6124825	—	0.61248116
$2 \times 10^3$	22.4082904	22.408290413206	—	0.6318565	—	—
$5 \times 10^3$	28.2819371	—	28.2816839	0.6554214	—	—

Tab. 2.2: Same as in Tab. 2.1 for the states  $(0, -, 1)$  and  $(0, -, 2)$ .

$\beta$	$(0, -, 1)$		$(0, -, 2)$	
	this work	Ref. [8]	this work	Ref. [8]
$1 \times 10^{-4}$	0.2501999	0.250199880000	0.1113104	0.1113103912
$2 \times 10^{-4}$	0.2503995	0.250399520002	0.1115082	0.1115082312
$5 \times 10^{-4}$	0.2509970	0.250997000084	0.1120931	0.1120931182
$1 \times 10^{-3}$	0.2519880	0.251988001344	0.1130392	0.1130392236
$2 \times 10^{-3}$	0.2539520	0.253952021470	0.1148249	0.1148248914
$5 \times 10^{-3}$	0.2597008	0.259700831666	0.1193757	0.1193757400
$1 \times 10^{-2}$	0.2688129	0.268812931962	0.1247571	0.1247571238
$2 \times 10^{-2}$	0.2853874	0.285387419480	0.1308128	0.1308127600
$5 \times 10^{-2}$	0.3248201	0.324820156798	0.1397834	0.1397833808
$1 \times 10^{-1}$	0.3703681	0.370368082136	0.1498509	0.1498509108
$2 \times 10^{-1}$	0.4285310	0.428531003988	0.1624457	0.1624457130
$5 \times 10^{-1}$	0.5200132	0.520013231888	0.1804490	0.1804490226
$1 \times 10^0$	0.5954219	0.595421944770	0.1937092	0.1937092020
$2 \times 10^0$	0.6713915	0.671391457342	0.2059013	0.2059013320
$5 \times 10^0$	0.7652997	0.765299696612	0.2196912	0.2196912068
$1 \times 10^1$	0.8267555	0.82675546	0.2281022	0.22810222
$2 \times 10^1$	0.8774676	0.87746760	0.2347463	0.23474628
$5 \times 10^1$	0.9272355	0.92723552	0.2410508	0.24105082
$1 \times 10^2$	0.9530640	0.9530640	0.2442537	—
$2 \times 10^2$	0.9707261	0.9707260	0.2464227	—
$5 \times 10^2$	0.9849900	0.9849900	0.2481656	—
$1 \times 10^3$	0.9911896	—	0.2489221	—
				Ref. [5]
				0.11131039
				—
				0.11209312
				0.11306976
				—
				0.11937573
				0.12475712
				0.13081275
				0.13978337
				0.14985090
				0.16244568
				0.18044898
				0.19370916
				0.20590129
				0.21969114



**Tab. 2.3:** Binding energies in Rydberg atomic units of the tightly-bound states  $(-1, +, 1)$  and  $(-2, +, 1)$  at different  $\beta$  in comparison to results from Kravchenko et al. [8] and Zhao et al. [6].

$\beta$	$(-1, +, 1)$			$(-2, +, 1)$		
	this work	Ref. [8]	Ref. [6]	this work	Ref. [8]	Ref. [6]
$1 \times 10^{-4}$	0.2503998	0.250399760000	0.250399760000	0.1117100	0.111710031126	0.111710031126
$2 \times 10^{-4}$	0.2507990	0.250799040006	—	0.1123068	0.112306791348	0.112306791348
$5 \times 10^{-4}$	0.2519940	0.251994000232	0.251994000232	0.1140841	0.114084120350	0.114084120350
$1 \times 10^{-3}$	0.2539760	0.253976003710	0.253976003710	0.1170033	0.117003258404	0.117003258404
$2 \times 10^{-3}$	0.2579041	0.257904059260	—	0.1226814	0.122681435522	0.122681435522
$5 \times 10^{-3}$	0.2694023	0.269402288354	0.269402288354	0.1384944	0.138494366806	0.138494366806
$1 \times 10^{-2}$	0.2876352	0.287635220694	0.287635220694	0.1613717	0.161371748792	0.161371748792
$2 \times 10^{-2}$	0.3208951	0.320895070818	—	0.1982491	0.198249060540	0.198249060540
$5 \times 10^{-2}$	0.4016913	0.401691344746	0.401691344746	0.2756790	0.275679030924	0.275679030924
$1 \times 10^{-1}$	0.5010782	0.501078203430	0.501078203430	0.3626412	0.362641213032	0.362641213032
$2 \times 10^{-1}$	0.6427096	0.642709562360	—	0.4819653	0.481965274112	0.481965274112
$5 \times 10^{-1}$	0.9131941	0.913194116848	0.913194116848	0.7060960	0.706096050298	0.706096050298
$1 \times 10^0$	1.1992255	1.199225547204	1.199225547204	0.9423439	0.9423438614	0.9423438614
$2 \times 10^0$	1.5756505	1.575650544060	—	1.2540185	1.2540184504	1.2540184504
$5 \times 10^0$	2.2508447	2.250844683680	2.250844683680	1.8164295	1.8164295510	1.8164295510
$1 \times 10^1$	2.9310171	2.931017091090	2.931017091090	2.3872664	2.3872663600	2.3872663600
$2 \times 10^1$	3.7921651	3.792165064852	—	3.1153981	3.1153981400	3.1153981400
$5 \times 10^1$	5.2695213	5.269521330598	5.269521330598	4.3763345	4.3763344800	4.3763344800
$1 \times 10^2$	6.6942905	6.69429046	—	5.6040001	5.60400006	5.60400006
$2 \times 10^2$	8.4302566	8.43025656	—	7.1124256	7.11242556	7.11242556
$5 \times 10^2$	11.2768422	11.27684216	—	9.6102214	9.61022134	9.61022134

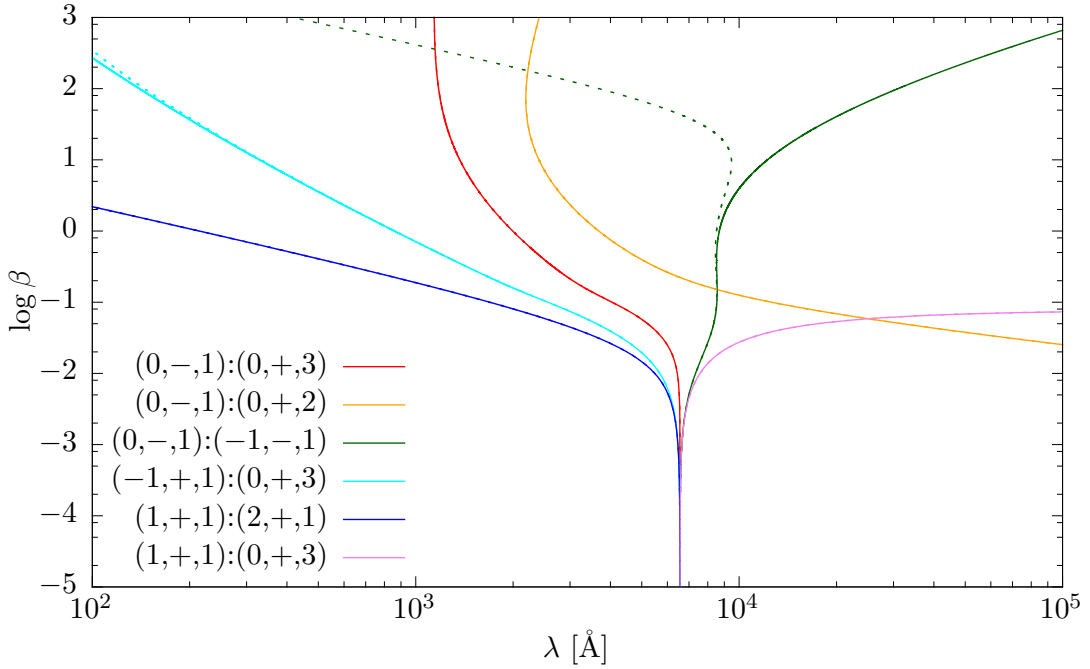


**Fig. 2.11:** Six transition lines from the Balmer series with different qualitative behavior under variation of  $\beta$ . Solid curves correspond to wavelengths  $\lambda$  calculated without finite nuclear mass corrections. Dotted curves in corresponding colors include these corrections for each of the six transitions.

in finite wavelengths at all magnetic field strengths. The orange curve stems also from two hydrogen-like states, but their energy values coincide in the low-field limit, causing large wavelengths in this limit:  $\lambda \rightarrow \infty$  at  $\beta \rightarrow 0$ . The opposite situation is represented by the solid green curve, where initial and final state become energetically degenerate in the high-field limit, i.e.  $\lambda \rightarrow \infty$  for  $\beta \rightarrow \infty$ .

If the initial state is tightly-bound, its binding energy diverges logarithmically with  $\beta$  and corresponding wavelengths converge towards zero (cyan curve). Energies of  $\Delta m = +1$  transitions to states with  $m > 0$  grow linearly in  $\beta$ , and the corresponding wavelengths show a fast convergence towards zero (blue curve), whereas all wavelengths from  $\Delta m = -1$  transitions with initial states having  $m > 0$  diverge at intermediate magnetic field strengths (violet curve). Both effects arise from the linear  $4\beta m$  energy shift of states with positive magnetic quantum number.

If one takes into account the finite mass of the nucleus (dotted curves), energies of states with  $m < 0$  are also shifted, but only by  $4(m_e/m_p)\beta m$ . This much smaller shift, due to the prefactor corresponding to the electron-nucleus mass ratio, still has significant effects on the transition wavelengths at higher magnetic field strengths  $\beta \gtrsim 10$ : Wavelengths of  $\Delta m = +1$  transitions diverge at some field strength due to energetic crossings of initial and final states, whereas those of  $\Delta m = -1$  transitions converge towards zero (dotted green curve). Solely  $\Delta m = 0$  transitions may converge to a finite

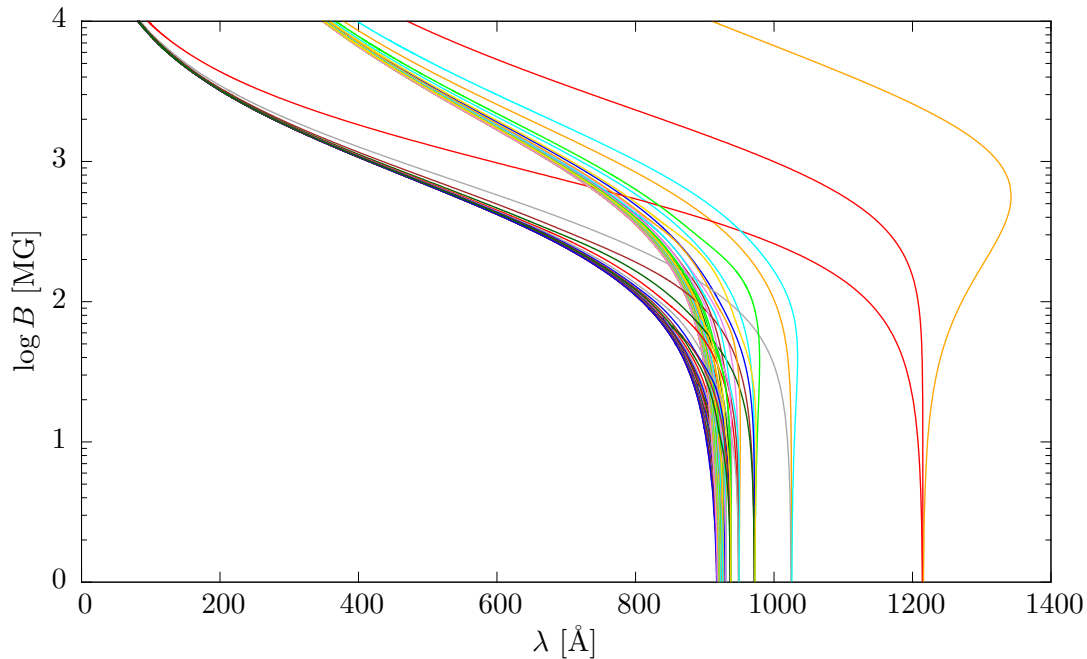


**Fig. 2.12:** Magnetic field strength as a function of the wavelength of the first 90 transitions from  $(0,+1)$  to  $(0,-,1 \dots 30)$ ,  $(1,+1 \dots 30)$ , and  $(-1,+1 \dots 30)$  in the Lyman series. The lines emerge from the field-free Lyman transitions up to principal quantum numbers  $n = 10$ .

value. Nonetheless, further analyses in this chapter do not include finite nuclear mass corrections as the focus will be on magnetic field strengths relevant for MWDs and thus below  $\beta = 1$ . With this in mind we turn to Figs. 2.12 and 2.13, which show the wavelengths of transitions of the Lyman and Balmer series at magnetic field strengths in the range  $B = 1 \dots 10^4$  MG. The Lyman series corresponds to transitions from the ground state  $(0,+1)$ , whose energy diverges,  $E \rightarrow -\infty$  in the limit  $B \rightarrow \infty$ . Therefore, all lines in Fig. 2.12 converge towards  $\lambda = 0$  at high magnetic field strengths, as the transition wavelength (given in  $\text{\AA}$ ) is inversely proportional to the transition energy  $\delta E$ , which is expressed by the relation  $\lambda = \gamma_{\text{AE}}/\delta E$ , with  $\delta E$  given in Rydberg units and  $\gamma_{\text{AE}} \approx 911$ .

The more complex behavior of the transitions in Fig. 2.13 can be explained with the four different initial states  $(0,+2)$ ,  $(0,-,1)$ ,  $(-1,+1)$ ,  $(1,+1)$  of the Balmer series. One has positive  $m$ , one is a tightly-bound state, and the other two are hydrogen-like states. Thus, all of the different lines discussed in Fig. 2.11 can be observed.

### 2.5.3 Wave functions

So far we have only investigated the effects of the magnetic field on the energy spectrum of the Hamiltonian and on transition wavelengths. In the next step we will analyze the wave functions at different  $\beta$ .

Figure 2.14 a) shows the energy  $E(\beta)$  of three low-lying states. Figure 2.14 b) to d)

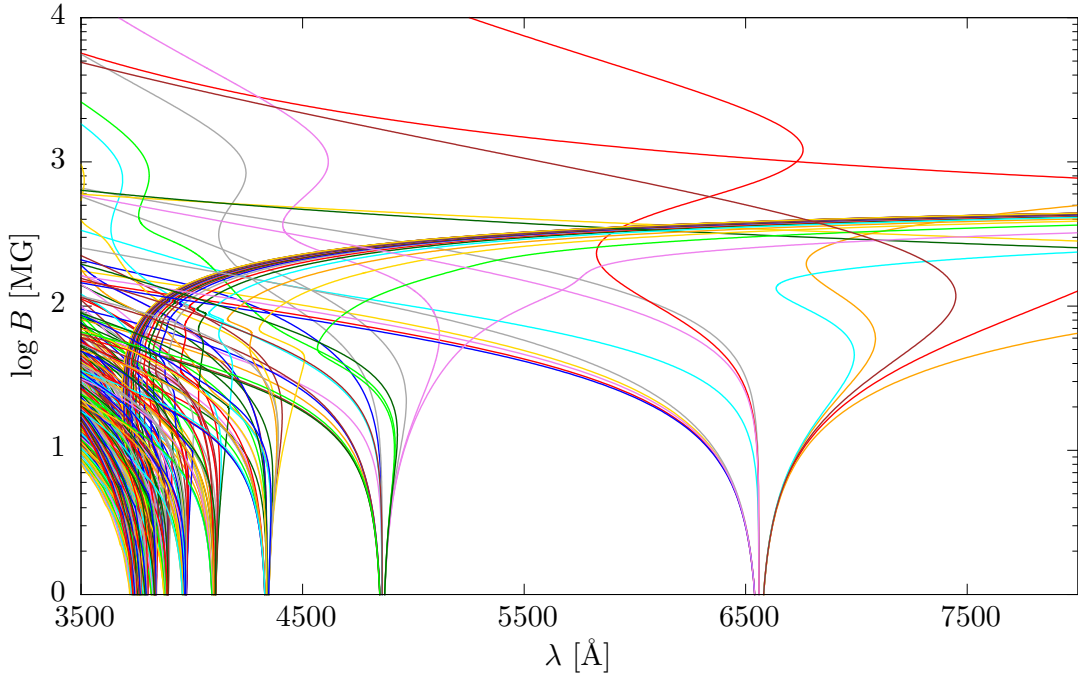


**Fig. 2.13:** Magnetic field strength as a function of the wavelength of the first 325 transitions from the Balmer series, which emerge from the field-free Balmer transitions up to principal quantum numbers  $n = 10$ .

present the corresponding wave function slices along the  $z$ -axis. Each color corresponds to one state: Red lines represent the tb ground state  $(0,+1)$  and the green/orange ones the first hl state with positive  $(0,+2)$  or negative  $(0,-,1)$   $z$ -parity. In the low-field limit given in Fig. 2.14 b) one can easily recognize the radial solutions of the hydrogen atom, which are still approximate solutions to the Hamiltonian (2.1) at  $\beta \approx 10^{-4}$ . Figure 2.14 c) depicts the wave functions at an intermediate field strength: The  $z$  wave function slice of the hl state with  $\pi_z = +$  (green) has already changed significantly. In the high-field limit, depicted in Fig. 2.14 c), the wave functions of the hl states with positive (green) and negative (orange)  $z$ -parity become very similar. This almost degeneracy of the wave functions is caused by the one-dimensional high-field limit of the potential term in the Hamiltonian (2.1)

$$V(\mathbf{r}) = -\frac{2}{|\mathbf{r}|} \xrightarrow{\beta \rightarrow \infty} -\frac{2}{|z|}. \quad (2.28)$$

In this limit, states with quantum numbers  $\{(m,-,\nu_a), (m,+,\nu_a + 1)\}$  form pairs with identical spatial probability distributions, and their wave functions differ only with respect to their  $z$ -parity. This degeneracy extends even over different magnetic quantum numbers. Without finite nuclear mass correction, the energy values become degenerate for  $\beta \rightarrow \infty$  as well and approach  $E_{\nu_a} = 1/\nu_a^2$ .

While the wave functions vary slowly with  $\beta$  at high field strengths, they show severe changes on a rather short interval of the mfs close to avoided crossings. Figure 2.15

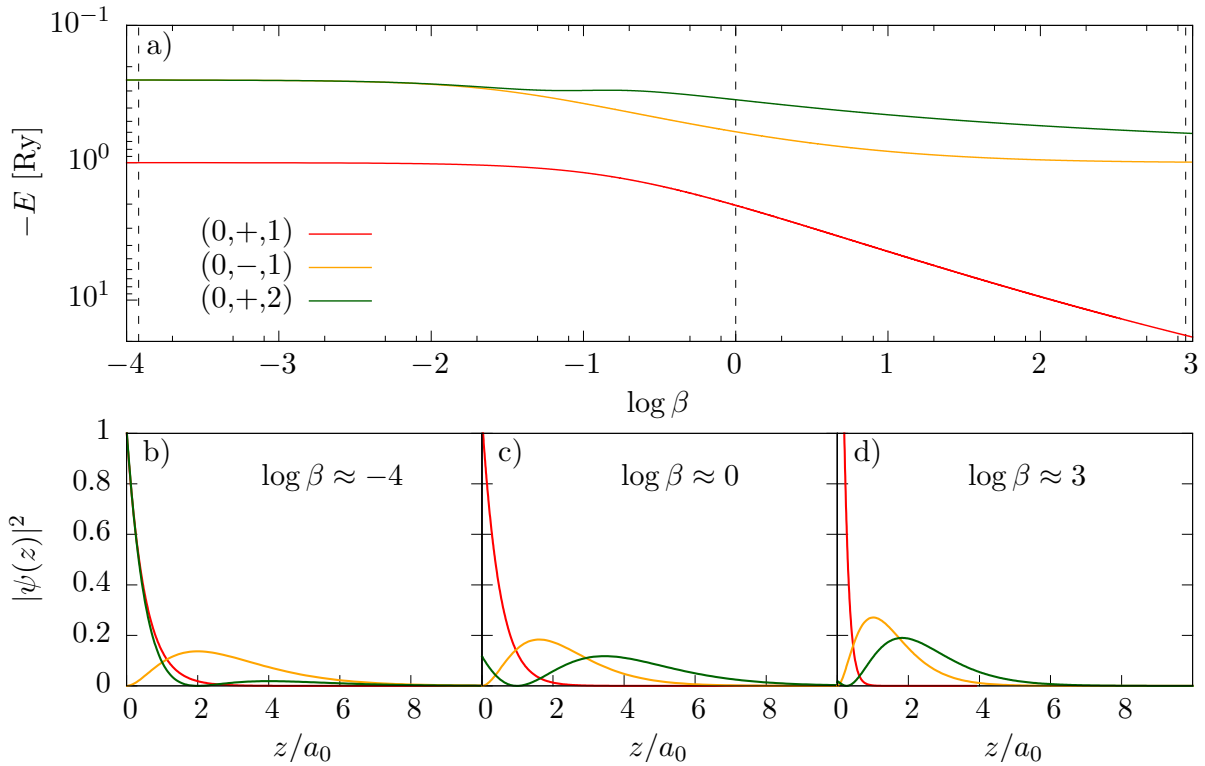


**Fig. 2.14:** Top panel: Energy vs.  $\beta$  of the three lowest states with  $m = 0$ . Bottom panels: Wave function slices along the  $z$ -axis of these three states at low, intermediate and high magnetic field strength. The integrals of the presented wave function slices were normalized to 1 for convenience.

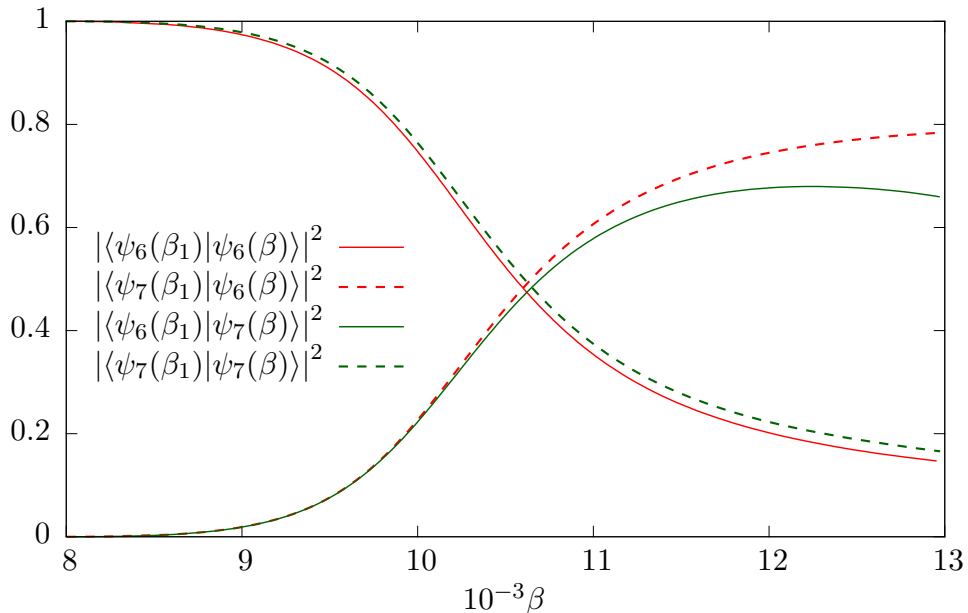


**Fig. 2.15:** Projections of the states  $(0,+,6) \hat{=} |\psi_6\rangle$  and  $(0,+,7) \hat{=} |\psi_7\rangle$  at different  $\beta$  near their first avoided crossing onto their wave functions at  $\beta_1 = 8 \times 10^{-3}$ .

shows the projection coefficients of the two states  $(0,+6)$  and  $(0,+7)$  next to their first avoided crossing onto a basis of the same two states at a fixed mfs of  $\beta_1 = 8 \times 10^{-3}$ . Solid [broken] lines correspond to the basis states  $(0,+6)|_{\beta_1}$  [ $(0,+7)|_{\beta_1}$ ] and green [red] colors denote the projected state  $(0,+6)$  [ $(0,+7)$ ]. A mutual exchange of the wave function shape of the two states can be seen from the increased portion of the cross-projections represented by the solid green and broken red line. The decrease of the cross projection  $|\langle \psi_6(\beta_1) | \psi_7(\beta) \rangle|^2$  at higher  $\beta$  can be explained with a further anticrossing of the states  $(0,+7)$  and  $(0,+8)$ , which occurs near  $\beta = 14 \times 10^{-3}$ . The sum of both projections of each state  $(0,+6)$  [ $(0,+7)$ ] is larger than 95% [85%] at all field strengths shown. This illustrates that in the vicinity of anticrossings the wave functions of the states involved mix, and contributions of other states are rather unimportant.

### 2.5.4 Dipole strengths and oscillator strengths

With an understanding of the wave functions and how their shapes change under the influence of a magnetic field, we can monitor its effects on the dipole strength  $d$  of the transitions. The corrections due to the finite nuclear mass to the wave functions (2.2) and dipole strengths (2.4) are small at any mfs. They cause no qualitative difference to the dipole strengths and are thus omitted again.

Before we explore the physical nature of the dipole strengths, a technical problem regarding their calculation has to be discussed. The wave functions in Eqs. (2.25) and (2.26) of initial and final state of course have to correspond to the same mfs. However, our AMV selects the magnetic field strengths individually for each state, and the situation where data for initial and final state exist at the same  $\beta$ , is a rare exception. A conceptually simple remedy for this situation would be to calculate all states at the same field strengths, but this is opposed to the idea of the AMV and would lead to a very large overhead of calculations.

Instead we make use of the fact that the wave functions vary continuously with  $\beta$  even at avoided crossings, and further assume that a change of the wave function of a state comes along with a change of the state's energy value. Under this assumption the field strength selection of the AMV is also appropriate for the calculation of dipole strengths. The above assumption is true up to quite high field strengths. At very strong fields, however, the energy values of all hl states with  $m \leq 0$  converge to a finite value, as calculations are performed without nuclear mass corrections (compare Fig. 2.9), but the  $(\rho - \phi)$  wave functions still change as they converge towards the Landau state  $\Phi_{n=0,m}$ , whose extension in  $\rho$ -direction declines proportional to  $1/\sqrt{\beta}$ . This leads to comparatively large differences in the field strengths corresponding to the initial and final state, but causes only a negligible error of the dipole strengths for  $\beta < 10^3$ .

Therefore, we apply a linear interpolation scheme for the calculation of a transition's dipole strength: For each field strength  $\beta^i$ , where the initial state was calculated at, we search the nearest lower  $\beta_1^f$  and higher  $\beta_2^f$  field strength, where results exist for the final state. We then calculate the dipole strengths for both final states with the initial one according to Eq. (2.25) or (2.26), and interpolate  $d$  to identical field strengths  $\beta^f = \beta^i$ .

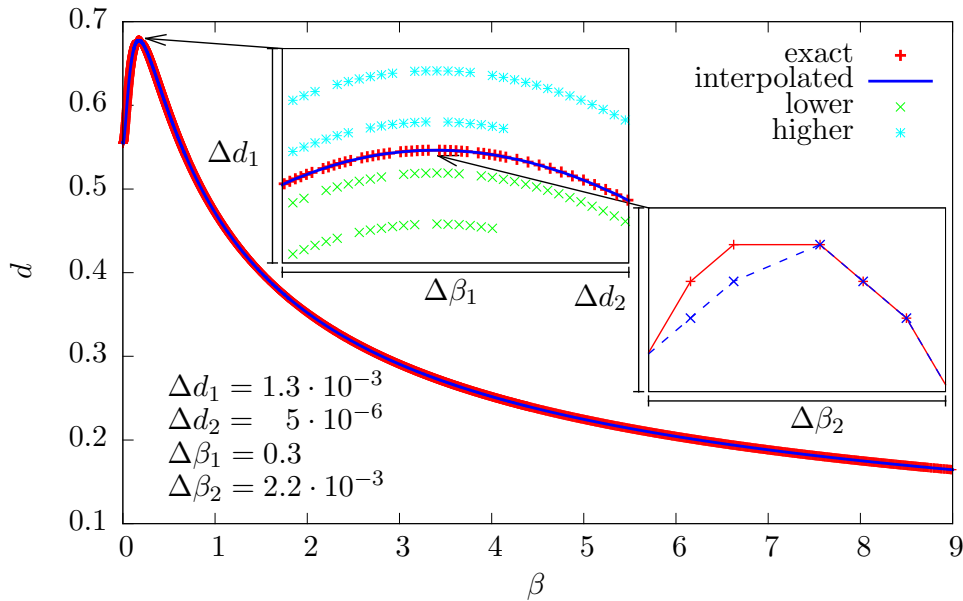


**Fig. 2.16:** Dipole strength  $d$  of the transition  $(0,+1):(0,-,1)$  as a function of  $\beta$ . The interpolated results (blue) deviate only in the seventh digit (second inset) from the values without interpolation (red). Also shown are the dipole strengths obtained with wave functions corresponding to lower (green) and higher (cyan) field strengths. Lines serve as a guide to the eye. (Note that the values of  $d$  alternate as  $\beta$  increases.)

After handling all field strengths of the initial state, we proceed with the field strengths of the final state in the same manner and afterwards join the results of both calculations. This ensures that changes of the wave functions of both states are dealt with adequately.

Figure 2.16 shows the interpolated results (blue line) and the intermediary results needed for interpolation. Green points correspond to results from  $\beta^f < \beta^i$  and cyan ones to  $\beta^f > \beta^i$ . For comparison we also calculated both states at the same field strengths to obtain dipole strengths without the need of any interpolation (red crosses), which we labeled “exact”. The excellent agreement of both the interpolated and non-interpolated values of the dipole strength proves that this method works well and that it is possible to retrieve accurate dipole strengths using the AMV for data point distribution.

The most convincing proof for the accuracy of our results comes from the comparison with the literature. In Tabs. 2.4 – 2.7 we compare energies and dipole strengths of important transitions with results taken from Baye et al. [78], who used a Lagrange-mesh method and spherical or semi-parabolic coordinates. For this comparison we again assume an infinite nuclear mass. We show 10 tb-tb transitions from  $(0,+1):(-1,+1)$  to  $(-9,+1):(-10,+1)$  in Tabs. 2.4 and 2.5 and again find that our energy precision is as high as we expected: 7 digits. Some energy values of Ref. [78] at  $\beta = 500$  differ from ours in Tab. 2.5. It must be noted, however, that the precision of the results in Ref. [78] rapidly decreases at high field strengths. Our dipole strengths agree with the results of Ref. [78] by at least 8 digits. This is positively surprising, as we rely only on the energy

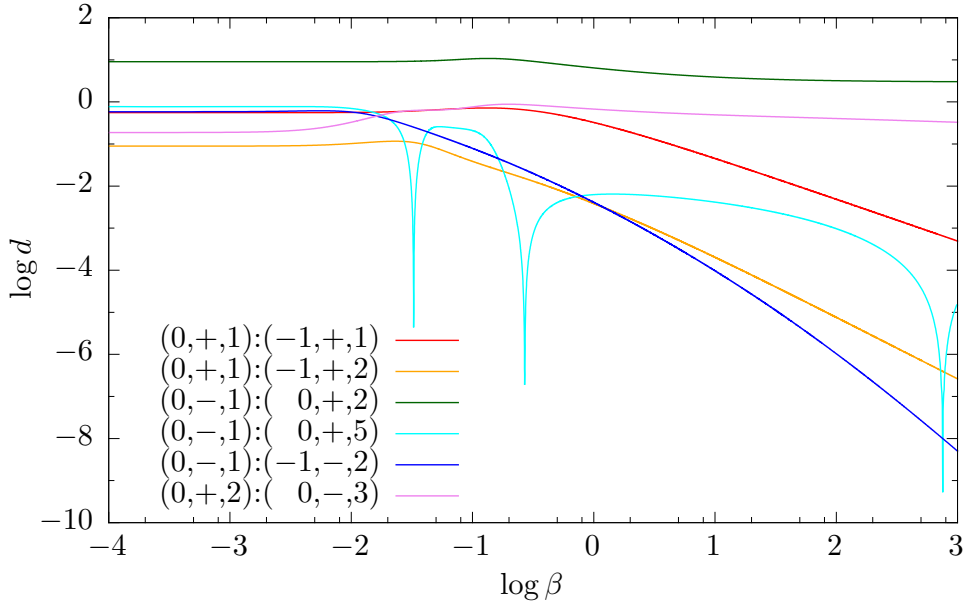


**Fig. 2.17:** Dipole strengths  $d$  as a function of  $\beta$  of six transitions in the Lyman and Balmer series. They correspond to the field-free transitions  $1s_0:2p_{-1}$  (red),  $1s_0:3p_{-1}$  (orange),  $2p_0:2s_0$  (green),  $2p_0:4d_0$  (cyan),  $2p_0:4d_{-1}$  (blue) and  $2s_0:4f_0$  (violet).

values to check the convergence of our calculations.

We also compare to results of Ref. [78] in Tabs. 2.6 and 2.7 and, in the latter one, additionally to values of Forster et al. [79], who published the most complete data set for hydrogen transitions in the literature so far. Their data include finite nuclear mass corrections except for dipole strengths, thus we restrict ourselves to the comparison of dipole strengths with Ref. [79]. They did not present data for states with principal quantum number  $n > 3$ , thus no results of Ref. [79] are shown in Tab. 2.7. The transitions shown in both tables are of the type  $tb-hl$  or  $hl-hl$  and are part of the Lyman, Balmer, Paschen, or Brackett series.

As found previously, our energy values deviate only in the case of high magnetic fields, i.e.  $\beta = (50, 500)$  from the energies given in the literature. Please note that for most states in Ref. [78] no results are presented at  $\beta = 500$ , presumably due to convergence problems. The dipole strengths do not agree as perfect as in the previous tables, but we still find most states to have 7-8 significant digits in common with the values from Ref. [78]. Deviations are larger in rare cases only and are limited to high field strengths again, where Ref. [78] suffers from a reduced energy precision as well. The comparison with Ref. [79] shows a 3 digit accordance in all results. The reduced accuracy is due to the fact that those calculations were performed using truncated spherical or Landau expansions, and therefore are only approximate. All comparisons demonstrate that we have reached an excellent accuracy, not only for the energy values but also for the dipole strengths of the transitions.

After this technical excursion and comparison with the literature, we can now focus



**Tab. 2.4:** Energies  $\Delta E$  and dipole strengths  $d$  in Rydberg atomic units for tb-tb transitions at high  $\beta$  compared to results of Baye et al. [78].

transition	$\beta$	$\Delta E$		$d$	
		this work	Ref. [78]	this work	Ref. [78]
$(0, +, 1): (-1, +, 1)$	0.5	0.7491437	0.7491436766184	0.501548538	0.5015485403
	5	1.2447496	1.244749643740	0.0858207408	0.085820740633
	50	2.3100871	2.3100871420	0.0095906859	0.009590685913
	500	4.0480043	4.048004334	0.0009847157	0.000984715683
$(-1, +, 1): (-2, +, 1)$	0.5	0.2070981	0.2070980665482	1.6257462598	1.625746259709
	5	0.4344152	0.4344151326806	0.1900476417	0.190047641716
	50	0.8931868	0.89318683468	0.0197197002	0.019719700164
	500	1.6666208	1.666620774	0.0019901842	0.001990184250
$(-2, +, 1): (-3, +, 1)$	0.5	0.1061581	0.1061581093086	2.6937746178	2.693774614343
	5	0.2408911	0.2408911847390	0.2918350349	0.291835034653
	50	0.5163217	0.51632165674	0.0297727575	0.029772757547
	500	0.9934801	0.99348012	0.0029923515	0.002992351487
$(-3, +, 1): (-4, +, 1)$	0.5	0.0675620	0.0675619985856	3.7339389430	3.733938912828
	5	0.1594855	0.1594854970340	0.3928736119	0.392873611786
	50	0.3503001	0.350300169462	0.0398031538	0.039803153811
	500	0.6877212	0.68772108	0.0039935558	0.003993555797
$(-4, +, 1): (-5, +, 1)$	0.5	0.0479903	0.0479903346252	4.7610248616	4.761024874987
	5	0.1160647	0.1160646343654	0.4935743088	0.493574308548
	50	0.2592639	0.259263875392	0.0498234242	0.049823424158
	500	0.5166204	0.51662082	0.0049943386	0.004994338592

Tab. 2.5: Same as in Tab. 2.5.

transition	$\beta$	$\Delta E$		$d$	
		this work	Ref. [78]	this work	Ref. [78]
(-5,+1):(-6,+1)	0.5	0.0364341	0.0364340808404	5.7808773687	5.780877372661
	5	0.0895997	0.0895997130168	0.594089110	0.594089109541
	50	0.2027038	0.20270375298	0.0598381731	0.059838173063
(-6,+1):(-7,+1)	500	0.4086942	0.40869364	0.0059948959	0.00599489585
	0.5	0.0289251	0.0289251519534	6.7962493128	6.796249321741
	5	0.0720204	0.0720203995592	0.6944887016	0.694488701441
(-7,+1):(-8,+1)	50	0.1645873	0.16458736470	0.0698495286	0.069849528609
	500	0.3350801	0.3350814	0.0069953169	0.00699531692
	0.5	0.0237135	0.0237134872722	7.8086200700	7.80862013370
(-8,+1):(-9,+1)	5	0.0596180	0.059617997502	0.7948109926	0.794810992722
	50	0.1373856	0.1373855808	0.0798586247	0.079858624721
	500	0.2820181	0.2820170	0.0079956487	0.00799564864
(-9,+1):(-10,+1)	0.5	0.0199174	0.0199174080016	8.8188637127	8.81886369967
	5	0.0504685	0.050468516186	0.8950783904	0.895078390800
	50	0.1171277	0.1171276474	0.0898661273	0.089866127402
(-9,+1):(-10,+1)	500	0.2421633	0.2421658	0.0089959183	0.0089959184
	0.5	0.0170485	0.0170485088226	9.8275337063	9.8275336917
	5	0.0434824	0.043482362916	0.9953051121	0.995305112192
(-9,+1):(-10,+1)	50	0.1015351	0.1015351488	0.0998724566	0.099872456665
	500	0.2112586	0.2112566	0.0099961429	0.0099961429

**Tab. 2.6:** Energies  $\Delta E$  and dipole strengths  $d$  in Rydberg atomic units for transitions at high  $\beta$  compared to results of Baye et al. [78] and Forster et al. [79].

transition	$\beta$	$\Delta E$		$d$		
		this work	Ref. [78]	this work	Ref. [78]	Ref. [79]
$(0,+1):(0,-,1)$	0.5	1.1423246	1.1423245615790	0.5901316089	0.59013161498	0.5902
	5	2.7302946	2.7302946308172	0.2246670349	0.2246670334	0.2252
$(0,-,1):(0,+,2)$	50	6.6523729	6.6523729439898	0.0621460120	0.0621460109	0.06217
	500	14.3398565	14.3398570529642	0.0158531753	0.01585325	0.01585
$(-1,+,-,1):(0,+,2)$	0.5	0.1990752	0.1990752666196	7.9694837072	7.9694836333	7.944
	5	0.3473961	0.347396038526	4.3715764996	4.3715765681	4.371
$(-1,+,-,1):(0,+,2)$	50	0.4148724	0.41487238846	3.3171608053	3.31716083	3.317
	500	0.3932751	0.393318	3.054854835	3.055609	3.055
$(-1,+,-,1):(0,+,2)$	0.5	0.5922561	0.5922561515806	0.0854715825	0.08547157589	0.08129
	5	1.8329411	1.83294102560	0.0012965569	0.0012965574214	0.001290
$(-1,+,-,1):(-1,+,1)$	50	4.7571582	4.7571581900	0.000032168	0.000032168265	0.00003318
	500	10.6851273	10.685170	0.000009848	0.000009853305	0.000009846
$(-1,+,-,1):(0,-,1)$	0.5	0.5000594	0.50005938912638	1.7275501912	1.727550194	1.728
	5	1.5729323	1.5729323040730	0.4772969856	0.477296986	0.4773
$(-1,+,-,1):(0,-,1)$	50	4.3837790	4.3837790458	0.1222156237	0.122215623	0.1222
	0.5	0.1068785	0.1068785041660	0.8703732787	0.8703732714	0.8704
$(-1,+,-,1):(0,-,1)$	5	0.0873873	0.087387317002	0.0981570787	0.098157077652	0.09816
	50	0.0414932	0.0414932442	0.0099813979	0.009981397847	0.009981
$(-1,+,-,1):(0,+,2)$	0.5	0.0699795	0.0699794756	0.8189677854	0.818967796	0.8190
	5	0.0533006	0.053300668730	0.0959952311	0.0959952296538	0.09601
$(-1,+,-,1):(0,+,2)$	50	0.0428578	0.04285778	0.0098677543	0.009867754	0.009868
	0.5	1.4113793	1.4113793038	0.0082376074	0.00823760725	0.008238
$(-1,+,-,1):(0,+,2)$	5	3.1309913	3.13099133810	0.0005187584	0.0005187584226	0.0005169
	50	7.1101031	7.11010312	0.0000207508	0.00002075083	0.00002073
$(-1,+,-,1):(-2,+,1)$	0.5	0.4551375	0.4551375606	0.0294804058	0.02948040627	0.02948
	5	1.4518265	1.45182656162962	0.0007164006	0.0007164006011	0.0007161
$(-1,+,-,1):(-2,+,1)$	50	3.9068292	3.90682914	0.0000211632	0.000021163182	0.00002116
	0.5	0.1621762	0.16217623808070	10.6799990883	10.679999056	10.68
$(-1,+,-,1):(-2,+,1)$	5	0.3133094	0.31330939024004	5.0827007631	5.0827007537	5.083
	50	0.4162370	0.416237028	3.4851901912	3.4851901	3.485

**Tab. 2.7:** Energies  $\Delta E$  and dipole strengths  $d$  in Rydberg atomic units for transitions at high  $\beta$  compared to results of Baye et al. [78].

transition	$\beta$	$\Delta E$		$d$	
		this work	Ref. [78]	this work	Ref. [78]
(-2,-,1):(-2,+,1)	0.5	0.3461527	0.34615270934706	2.6261074153	2.6261074103
	5	1.1915152	1.191515217472	0.6735775630	0.673577564
(-2,-,1):(-1,-,1)	50	3.5208175	3.5208174680	0.1694470246	0.169447025
	0.5	0.0531914	0.0531913867690	1.8734114524	1.8734114506
(-2,-,1):(-1,-,1)	5	0.0529981	0.0529980460832	0.1980555125	0.198055512058
	50	0.0302253	0.0302252578	0.0199774636	0.019977463603
(-2,+,2):(-1,+,2)	0.5	0.0278627	0.0278626883564	1.8893737464	1.8893737425
	5	0.0260014	0.0260014316	0.1973477142	0.197347713627
(-2,+,2):(-1,+,2)	50	0.0222445	0.0222458	0.0199126876	0.019912691
	0.5	0.6900983	0.6900983155632	0.0078113897	0.00781138940
(-2,+,2):(-1,+,1)	5	1.9122431	1.9122431258	0.0004166955	0.0004166954691
	50	4.8222605	4.8222618	0.0000161847	0.00001618473
(-2,+,2):(-3,+,1)	0.5	0.3768421	0.3768421397066	0.0171736445	0.01717364
	5	1.2369368	1.2369368084	0.0005168126	0.0005168126918
(-2,+,2):(-3,+,1)	50	3.4127520	3.4127532	0.0000164132	0.00001641326
	0.5	0.1368475	0.13684753966790	12.9601817835	12.960181745
(-2,+,2):(-2,-,1)	5	0.2863127	0.286312774618	5.6785287950	5.678528757859
	50	0.4082562	0.40825624	3.6318264550	3.631829

on the physical interpretation of the  $d(\beta)$  functions. Six characteristic ones are shown in Fig. 2.17. All of them are significantly strong in the low-field limit, but  $\Delta m = \pm 1$  transitions are suppressed for  $\beta \gg 1$ . This holds for all types of states involved in such transitions — tb-tb (red), hl-hl (blue) or tb-hl (orange) — and can easily be understood by looking at the high-field limits of the dipole matrix elements (cf. Refs. [7, 54]) in adiabatic approximation

$$p_{\text{if}}^0 = 2 \int_0^{\infty} P_{\text{f}}(z) z P_{\text{i}}(z) dz, \quad (2.29)$$

$$p_{\text{if}}^{+1} = -\sqrt{|m_{\text{i}}|/\beta} \int_0^{\infty} P_{\text{f}}(z) P_{\text{i}}(z) dz, \quad (2.30)$$

$$p_{\text{if}}^{-1} = \sqrt{|m_{\text{f}}|/\beta} \int_0^{\infty} P_{\text{f}}(z) P_{\text{i}}(z) dz, \quad (2.31)$$

where the wave functions are a product of the lowest Landau level  $\Phi_{0m}$  and a longitudinal wave function  $P(z)$  (see Sec. 2.2.1). We already mentioned that this approximation is only valid for very large field strengths  $\beta \gg 1$ , but this condition is easily fulfilled on the right side of Fig. 2.17. Equations (2.30) and (2.31) include the prefactor  $1/\sqrt{\beta}$ , which stems from the ever decreasing size of the wave functions perpendicular to the magnetic field at such field strengths. This also explains the reduction of the dipole strengths at large  $\beta$  for tb-tb transitions (red curve). Additionally, wave functions  $P(z)$  of hl-states with different excitation numbers become approximately orthogonal, reducing the  $z$ -overlap in (2.30) and (2.31), as can be seen by the rapid decay of the corresponding hl-hl dipole strength (blue curve). On the other hand, tb-hl transitions suffer from the extreme differences in the  $z$ -wave functions' elongation, and the suppression of the dipole strength (orange curve) is apparent. This also effects tb-hl transitions with  $\Delta m = 0$ .

The remaining lines in Fig. 2.17 correspond to hl-hl  $\Delta m = 0$  transitions. The green curve represents a transition between two states that converge to the same energy at infinite field strength. The corresponding wave functions become almost degenerate, differing only in  $z$ -parity and thus the dipole integral (2.25) becomes large. Transitions from low-energy states possessing an even  $z$ -parity to high-energy states with odd  $z$ -parity also do not vanish at large  $\beta$  (violet). However, if the low-energy state has odd  $z$ -parity, the dipole strength will show features even at high  $\beta$  (cyan curve  $\beta \approx 750$ ). These features are not caused by extensive changes of the wave functions, but are cancellation effects that can easily be explained by examining Fig. 2.18.

There we have plotted slices along the  $z$ -axis of the wave functions corresponding to the states  $(0, -, 1)$  and  $(0, +, 5)$  at  $\beta \approx 754$ , where the dipole strength of the transition between these states is strongly suppressed. Figure 2.18 shows the integrand (dotted orange line) of the dipole strength integral presented in Eq. (2.29). The areas below this function (relative to the dashed green base line) almost cancel out each other due to

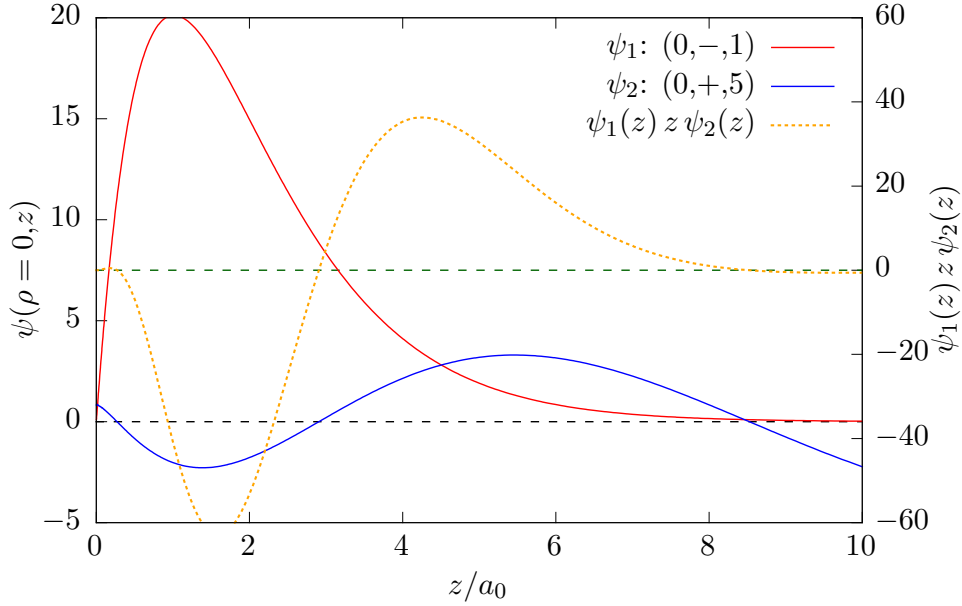


**Fig. 2.18:** Wave function slices (solid lines) at  $\rho = 0$  of the states  $(0,-,1)$  and  $(0,+,5)$  at  $\beta \approx 754$ . The dotted orange line shows the integrand of both wave functions and the  $z$ -value. Dashed: Base lines of the left and right vertical axes, corresponding to the wave functions and the integrand, respectively.

the position of the nodes of the higher-excited wave function (blue), and the integral in (2.29) almost vanishes. Such cancellation effects are also predicted for heavier elements and bound-free transitions [80].

The two other dips of the cyan line in Fig. 2.17 at intermediate  $\beta$  are related to avoided crossings of the state  $(0,+,5)$  with the neighboring states  $(0,+,4)$  and  $(0,+,6)$ . There, a change of the dipole strength is not surprising, as the wave functions of states participating in an avoided crossing undergo changes (see Fig. 2.15).

A more detailed view on an avoided crossing is presented in Fig. 2.19, which shows the energy  $E(\beta)$  (dashed lines) close to the avoided crossing of the states  $(0,+,6)$  and  $(0,+,7)$  that were already shown in Fig. 2.15. The solid lines depict the oscillator strengths  $f$  of transitions from the lower state  $(0,-,1)$  to these two states. The mixing of wave functions of the two upper states causes a suppression of the transition  $(0,-,1):(0,+,7)$  (orange) and enhances the other transition  $(0,-,1):(0,+,6)$  (red), whereas the sum of both oscillator strengths (green line) is almost constant.

Highly excited states pass through many avoided crossings in the region of intermediate field strengths, and the oscillator strengths (and dipole strengths) of associated transitions typically undergo a cascade of suppression and reinforcement, as can be seen in Fig. 2.20. There, the blue line represents the dipole strength of the transition  $(0,+,1):(0,-,10)$  as a function of  $\beta$ . Dashed lines indicate the positions of avoided crossings of the state  $(0,-,10)$ , coinciding with either particularly low or high dipole strengths.

An impressive demonstration for both the efficiency of our dipole strength calculation

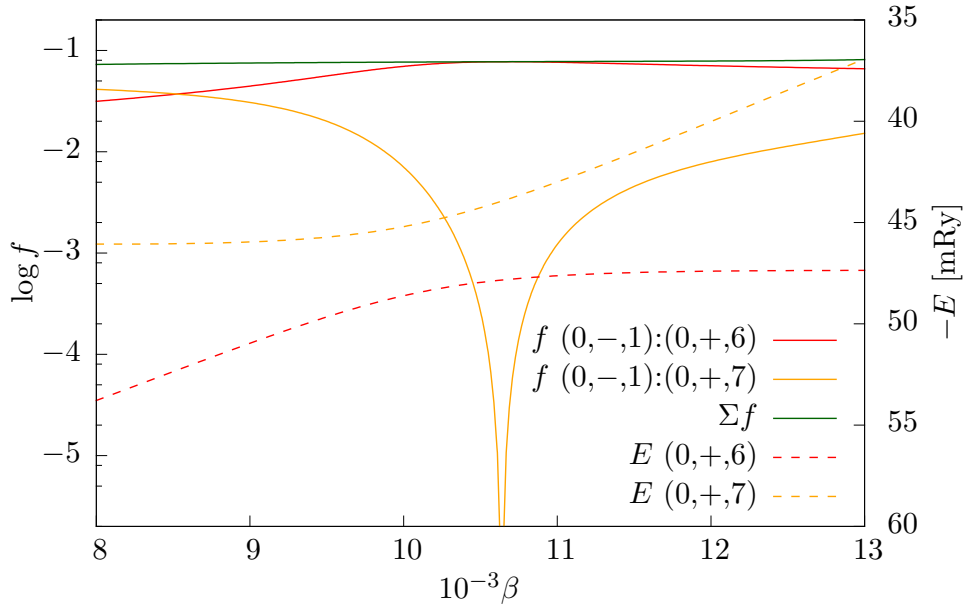


**Fig. 2.19:** Dashed lines: Energies of the states  $(0,+6)$  and  $(0,+7)$  as a function of  $\beta$  near their first avoided crossing. Solid lines: Oscillator strengths  $f$  of transitions with these states and  $(0,-1)$  in corresponding colors. The green line represents the sum of both oscillator strengths.

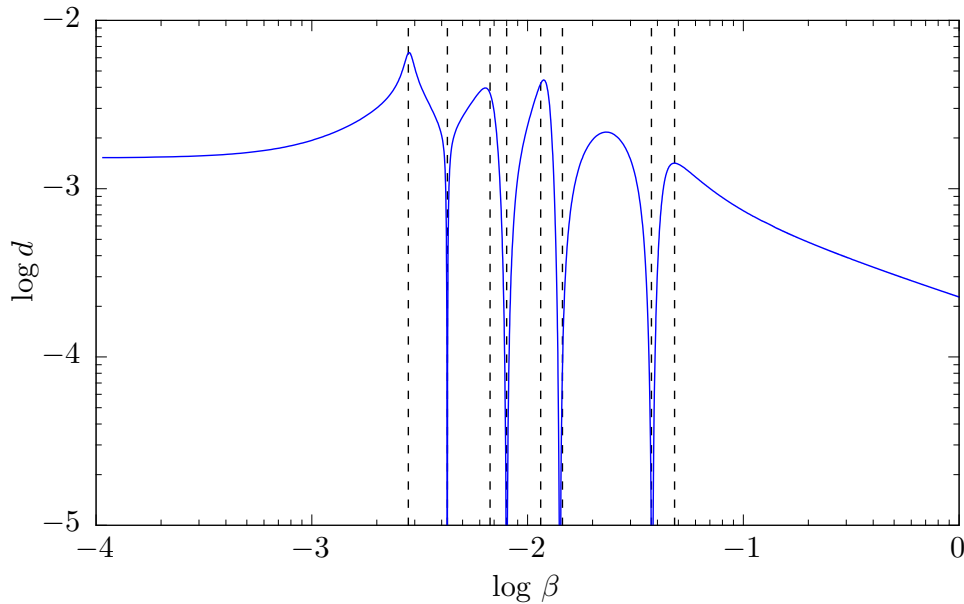


**Fig. 2.20:** Dipole strength  $d$  of the transition  $(0,+1):(0,-10)$  as a function of  $\beta$ . Field strengths corresponding to avoided crossings of the upper state are marked by dashed black lines.

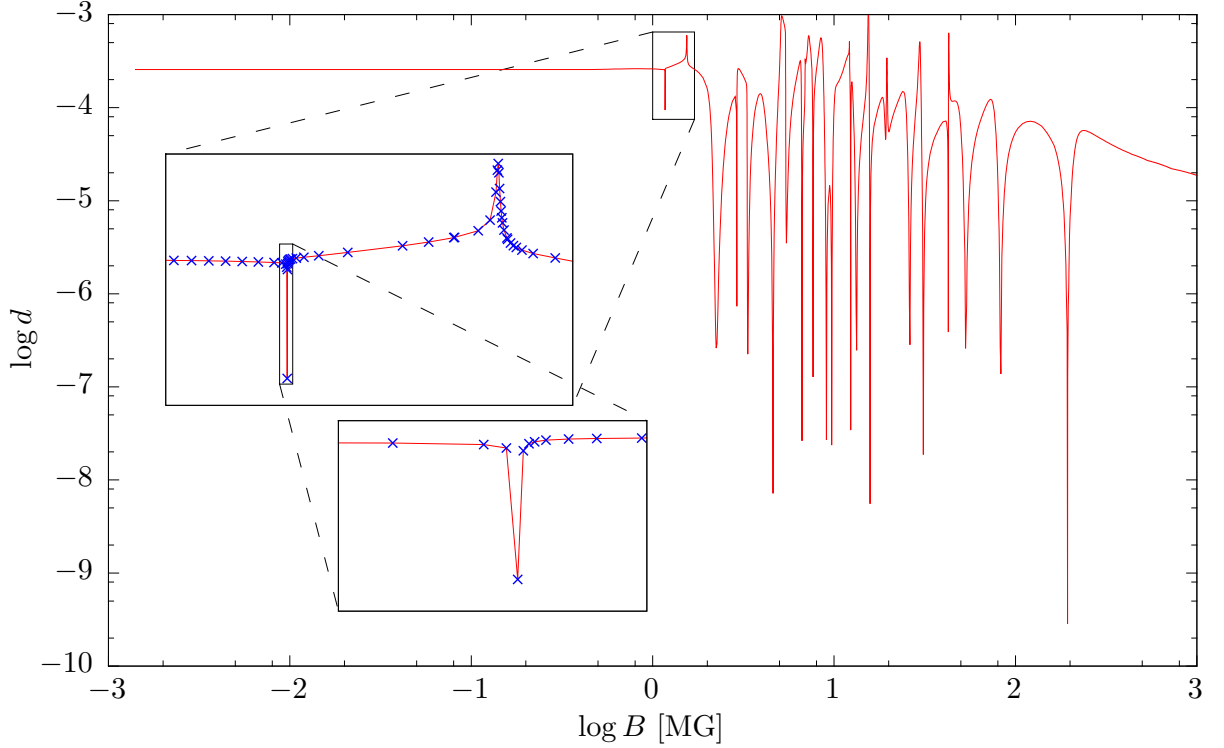


**Fig. 2.21:** Dipole strength  $d$  of the transition  $(0,+1):(0,-,30)$  as a function of  $B$ . The upper state passes through several avoided crossings, causing the complex structure of the graph. Insets show a detailed view of the first, very small-banded anticrossings, with data points in blue.

scheme and the AMV data point selection algorithm can be seen in Fig. 2.21, which shows the dipole strength of the transition from the ground state to a highly excited state with many avoided crossings. There, even the smallest features of the dipole strength function  $d(\beta)$  can be resolved, as is shown by the insets.

### 2.5.5 Improved spectral plots

The high line density at lower wavelengths in the  $\lambda$  vs.  $B$  plots 2.12 and 2.13 can hamper the identification of possible absorption features. For the higher Paschen and Brackett series, numerous lines that differ only marginally in wavelength exist, and this problem is aggravated. The combination of both wavelengths and line strengths into a single plot improves clarity and allows for a fast identification of the important line features at any  $B$ . As oscillator strengths obey sum rules and can be converted to absorption cross sections (see, e.g. Ref. [81]) we use these quantities to represent the line strengths.

To obtain a reasonable visualization we divide the plot area into small picture elements  $(\lambda, \beta)$  and add up the oscillator strengths of the transitions that cross this pixel. We linearly interpolate values for wavelengths and oscillator strengths and thereby bridge



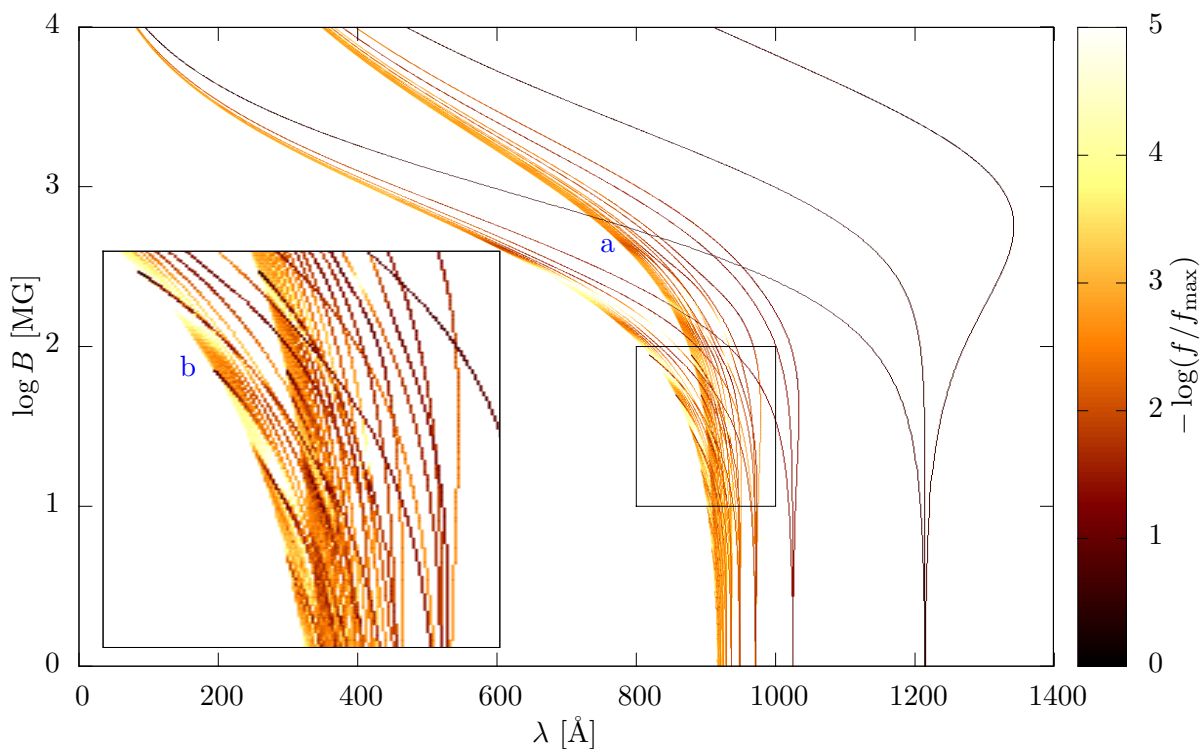


**Fig. 2.22:** Transition lines and oscillator strengths of the Lyman series as in Fig. 2.12. Line colors correspond to the oscillator strength of the transitions relative to the highest value in the plot. A detailed view on the boxed region of intermediate field strengths is provided in the inset.

gaps between transition data points. If multiple data points of a single transition correspond to the same pixel, we average these dipole strengths before adding them to the sum. Finally, we assign colors to the sum of oscillator strengths of each pixel relative to the maximum value in the selected plot range. Dark colors represent high values of  $f$ , or strong transitions, and light colors show low values of  $f$  or weak transitions, respectively.

Figure 2.22 shows the Lyman series in the same range of wavelengths and magnetic field strengths as in Fig. 2.12, but with line colors according to the oscillator strength of the transitions. One can clearly see that transitions from lower excited states (originating from  $\text{Ly}\alpha$  and  $\text{Ly}\beta$ ) have higher oscillator strengths than the transitions from higher excited states, which are roughly three orders of magnitude weaker. These transitions from higher excited states form bands, where one can observe the signatures of anticrossings: alternating regions of the field strength with stronger and weaker oscillator strengths (dark and light stripes). The dark red stripe in the central band close to the label “a” is caused by broad anticrossings with strong coupling between the excited states, whereas the thin dark red line near label “b” in the inset stems from narrow anticrossings with rather weak coupling. Without closer inspection, signatures from such narrow anticrossings could be mistaken as single, but very strong transitions. Instead, they refer to transitions from different states, connected in a sequence of anticrossings.

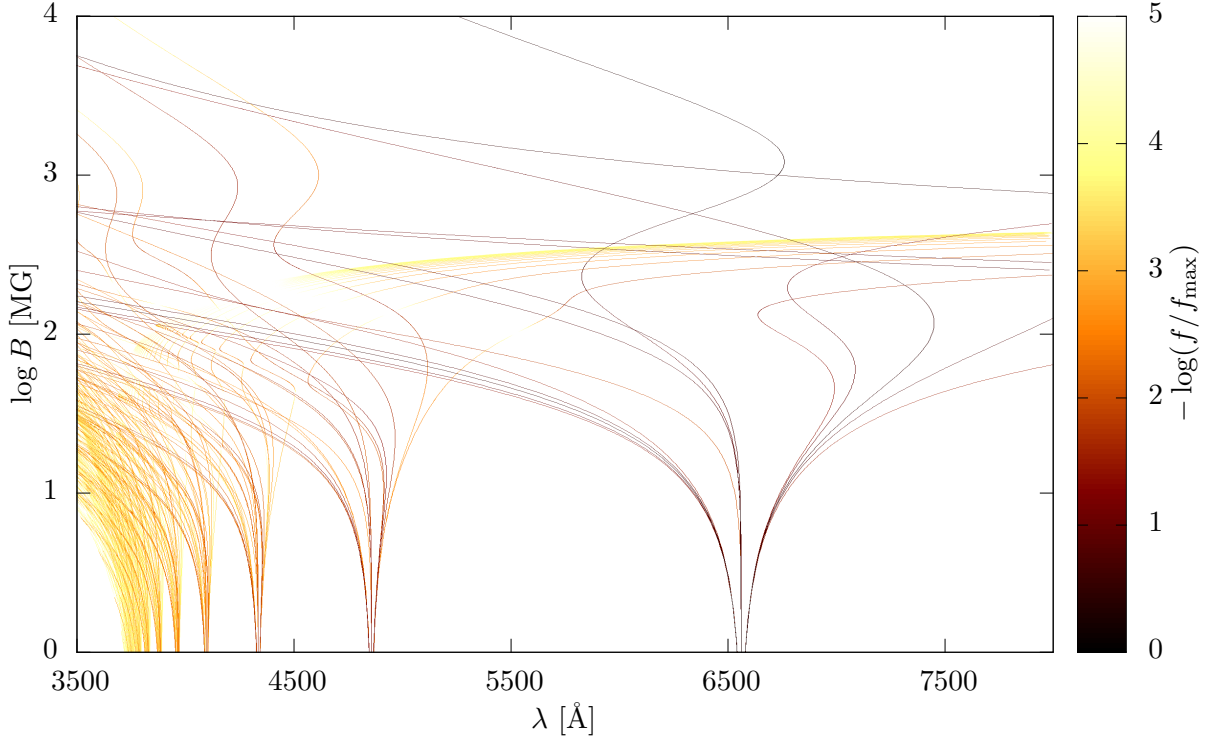


**Fig. 2.23:** Transition lines of the Balmer series as in Fig. 2.13.

This explains the abrupt end of the strong signature next to label “b”: We only included the lowest 30 states of each symmetry subspace into our calculations, thus the further course of this anticrossing sequence through higher excitation levels is not represented here. Still, an abrupt end of these anticrossing resonances at wavelengths corresponding to the ionization energy is expected: Figures 2.9 and 2.10 in Sec. 2.5.1 show that the anticrossings are concentrated in an ever-diminishing interval  $\delta\beta \rightarrow 0$  of the mfs with rising excitation level  $\nu \rightarrow \infty$ . Thus, we do not expect a recognizable influence of the anticrossings on the spectrum of bound-free transitions.

In Fig. 2.23 we present the Balmer series in the same manner as in the previous picture, and in the same parameter ranges as in Fig. 2.13. The bunch of higher excited lines below 4000 Å and between 10 MG and 100 MG are clearly weaker than the H $\alpha$  and H $\beta$  lines (beginning near 6500 Å and 4800 Å), which dominate in oscillator strength over the entire range of  $\beta$ .

An overview of the strongest transitions from the Lyman, Balmer, Paschen and Brackett series is displayed in Fig. 2.24. The combination of the series into a single plot suggests thermal weighting for the initial states, which is why we multiply the oscillator strengths with a Boltzmann weight

$$w = e^{-(E_i - E_g)/(k_B T)}, \quad (2.32)$$

corresponding to the energies  $E_i$  and  $E_g$  of the initial and ground state. We selected an exemplary effective temperature of 20,000 K, which is a reasonable choice for MWDs

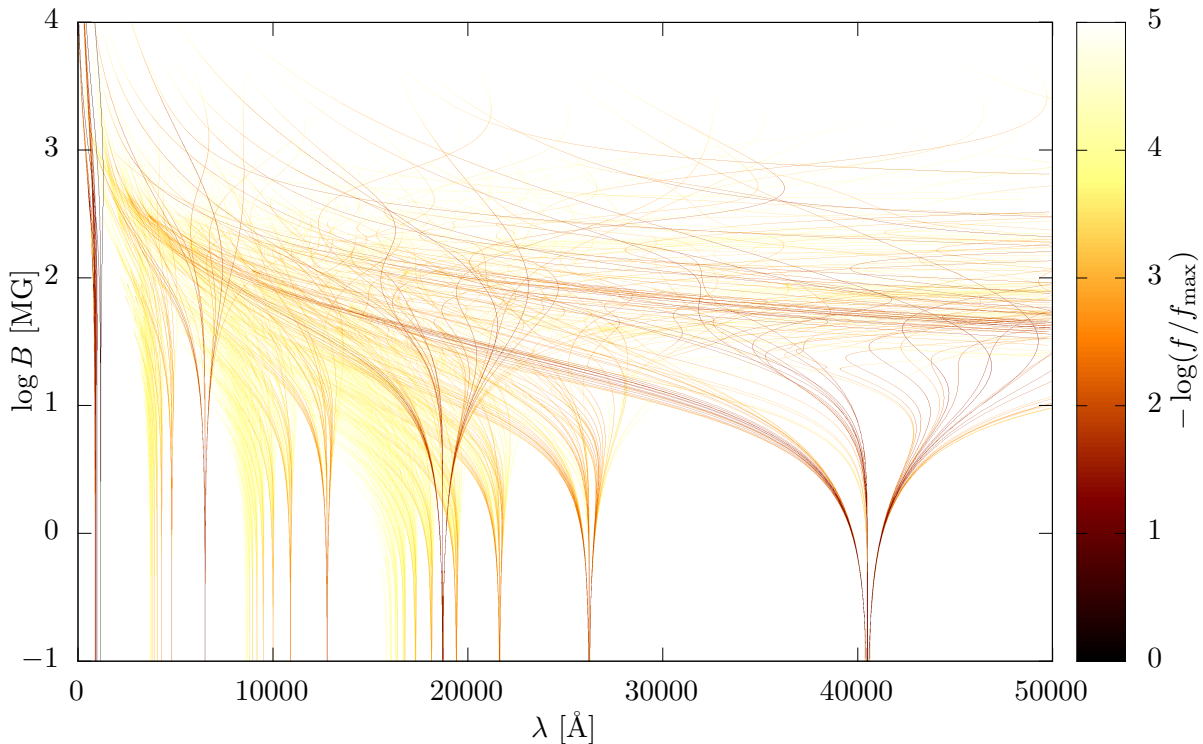


**Fig. 2.24:** Transition lines of the Lyman, Balmer, Paschen and Brackett series including thermal weighting for  $T = 20,000$  K. The line colors correspond to the oscillator strengths.

(cf. [13]). Despite this Boltzmann factor, even the lines from the Brackett series stay clearly visible and quite intense up to intermediate field strengths, due to the rather high thermal energy compared to the excitation energy of the initial states. At larger field strengths, the effects of thermal excitation become visible: all transitions but those from the ground state (Lyman series) fade out, which is easily understood when we remember the diverging ground state energy at large  $B$ .

In a last step we focus again on the wavelengths accessible in the SDSS observations. In Fig. 2.25 we include not only the Balmer series but also the transitions from higher series presented in the previous figure. There we can see that at mfs between 10 MG and 250 MG a broad band of transitions from the Paschen and Brackett series crosses this window of wavelengths, some of them with non-negligible oscillator strengths. Still, it is unlikely that those lines contribute significantly to the spectrum of a MWD. The almost horizontal alignment of the lines implies that the transition wavelengths strongly depend on the mfs. However, the mfs is not constant on the surface of a white dwarf, but varies, at least by a factor of two if one assumes a pure magnetic dipole configuration (see also Ref. [20]). Therefore, single transitions of this band will not contribute to the spectrum with narrow absorption features, as it is expected for stationary line components (see Refs. [7, 16]). Instead, different suppression effects on parts of the spectrum may occur depending on the considered magnetic field strengths, e.g. at  $B_{\max} = 50$  MG

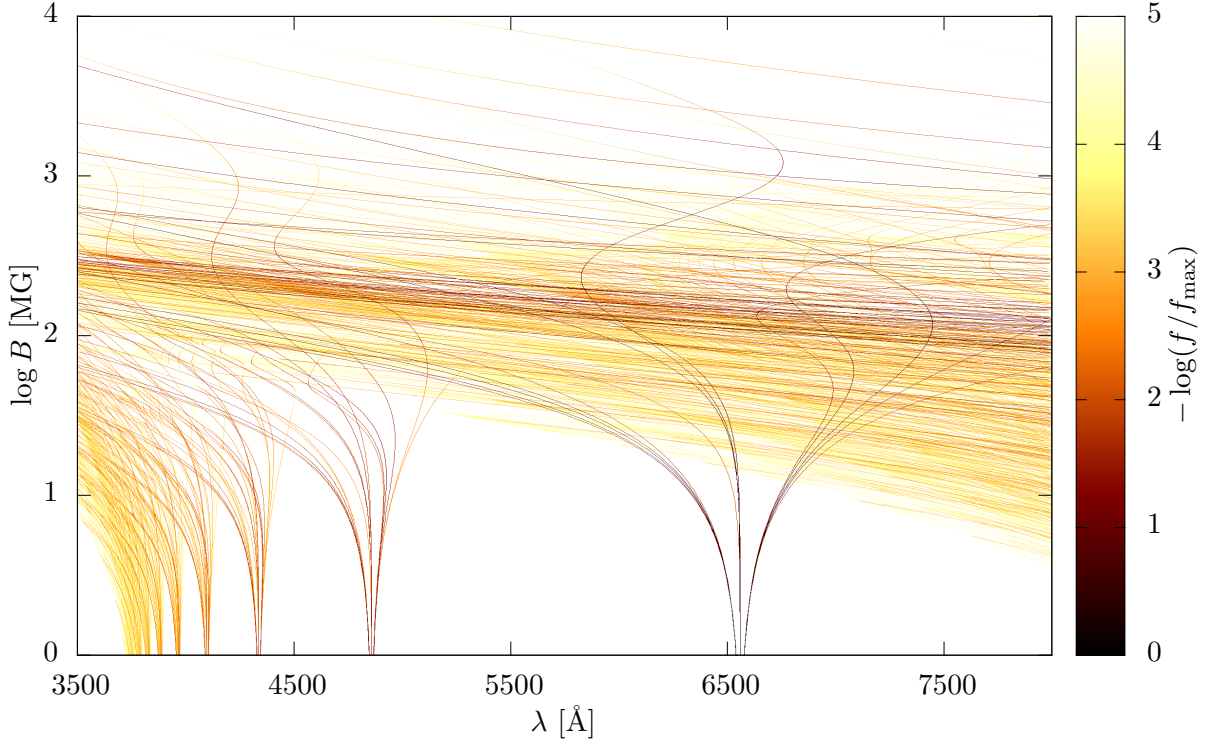


**Fig. 2.25:** Same as is Fig. 2.24, but restricted to the parameter ranges from Fig. 2.13.

a suppression of the spectral intensity for wavelengths beyond 6000 Å can be expected.

At this point we have to leave further analyses of MWD spectra to experts, who model MWD atmospheres including details such as higher magnetic multipoles, inclinations of the magnetic, rotation and viewing axes, temperature distributions, the surface gravity and much more (see Refs. [17–19]). Külebi et al. already applied their methods to the spectra of MWDs from the SDSS [20, 82] using the previously available atomic data sets. The atomic data obtained in this work were already brought to use by Kepler et al. [83], who found evidence for a more complex than dipolar surface distribution of the magnetic field of a MWD with a hydrogen atmosphere.

# 3 Many-electron systems in neutron star magnetic fields: General considerations

In the previous chapter we analyzed the hydrogen atom in magnetic fields of arbitrary strength. In the following chapters we will discuss heavier atoms and ions from helium to iron. The first part lays the foundation for this discussion as we address the general properties of multi-electron atoms in neutron star magnetic fields and investigate proper wave function expansions, whereas subsequent chapters will focus on methods and results. While we only had to consider a core charge  $Z = 1$  in the case of hydrogen, we now concentrate on values of  $Z$  in the range of  $2 \dots 26$ . Therefore, we define the reference magnetic field strength  $B_Z = Z^2 B_0$  to match that  $B$ , where the electron's Larmor radius equals the *charge-scaled* Bohr radius. This allows us to define an extended, charge-scaled magnetic field strength parameter  $\beta_Z = B/B_Z = \beta/Z^2$ . In the following we will only consider strong fields  $\beta_Z \gtrsim 0.1$ , which are relevant for the understanding of X-ray emission spectra of strongly magnetized neutron stars.

## 3.1 Setting

We stick to the assumption that relativistic effects can be neglected. This is justified, as relativistic corrections from solving directly the Dirac equation [12] are expected to be much smaller than intrinsic Hartree-Fock errors. Hence, we consider the non-relativistic Hamiltonian of a non-moving atom or ion with  $N$  electrons in a uniform magnetic field pointing in  $z$ -direction using atomic units and cylindrical coordinates

$$\begin{aligned} \hat{H} = & \sum_{i=1}^N - \left( \frac{\partial^2}{\partial \rho_i^2} + \frac{1}{\rho_i} \frac{\partial}{\partial \rho_i} + \frac{1}{\rho_i^2} \frac{\partial^2}{\partial \phi_i^2} + \frac{\partial^2}{\partial z_i^2} \right) + 2\beta m_i + \beta^2 \rho_i^2 \\ & + \sum_{i=1}^N 4\beta m_s^i - \frac{2Z}{|\mathbf{r}_i|} + \sum_{\substack{i=1 \\ j=i+1}}^N \frac{2}{|\mathbf{r}_i - \mathbf{r}_j|} = \sum_{i=1}^N \hat{h}^i + \sum_{\substack{i=1 \\ j=i+1}}^N \hat{w}^{(i,j)}, \end{aligned} \quad (3.1)$$

which can be described as a sum of single-particle operators  $\hat{h}^i$  for each electron  $i$  and two-particle operators  $\hat{w}^{(i,j)}$  for each pair of electrons  $(i, j)$ . Again, we assumed a nucleus of infinite mass, but unlike in the case of hydrogen no exact scaling relations exist to a Hamiltonian of finite nuclear mass. Using the pseudo separation of the Hamiltonian

of Schmelcher et al. [84], Becken et al. [26] introduced an approximative energy scaling law, similar to the one of the hydrogenic case (2.3), by taking into account the dominant part of the finite nuclear mass corrections

$$E(m_{\text{nuc}}, \beta) = \mu E(m_{\text{nuc}} \rightarrow \infty, \beta/\mu^2) - 4\beta(M + S_z)m_e/m_{\text{nuc}}, \quad (3.2)$$

where  $m_{\text{nuc}}$  represents the core mass and  $\mu = m_{\text{nuc}}/(m_{\text{nuc}} + m_e)$ . The total magnetic and spin-projection quantum numbers  $M$  and  $S_z$  are explained below. This scaling law ignores contributions from the mass polarization terms (see Ref. [85]), which contribute to the energy functional by coupling two pairs of wave functions with different magnetic quantum numbers  $(m_i, m'_i)$  and  $(m_j, m'_j)$  with  $|m_{i,j} - m'_{i,j}| = 1$ . These terms break the cylindrical symmetry of the single-particle wave functions, and their treatment would require three-dimensional calculations. As all other terms of the energy functional preserve the cylindrical symmetry, i.e. they induce no coupling between different  $m$ , we expect the energy and wave function corrections due to the mass polarization terms to be very small and neglect them, as was also done in Ref. [85].

The finite mass corrections caused by the spin term in the scaling law (3.2) may be omitted if spin-flip transitions are ignored. Generally, this scaling law applies only to systems with a vanishing generalized momentum perpendicular to the magnetic field and to uncharged atomic systems. According to Becken [85] no good scaling laws can be found for charged atomic systems, i.e.  $Z \neq N$ , as the components of the generalized momentum operator do not commute [7]. In this case the internal and external motions of an atomic system are coupled, i.e. the electronic motion couples to the center of mass motion.

In order to solve the Schrödinger-equation corresponding to  $\hat{H}$  we construct the total wave function  $\Psi$  from a Slater-determinant (Hartree-Fock approximation) as

$$\Psi(\mathbf{x}^1, \dots, \mathbf{x}^N) = \frac{1}{\sqrt{N!}} \begin{vmatrix} \varphi^1(\mathbf{x}^1) & \varphi^1(\mathbf{x}^2) & \dots & \varphi^1(\mathbf{x}^N) \\ \varphi^2(\mathbf{x}^1) & \varphi^2(\mathbf{x}^2) & \dots & \varphi^2(\mathbf{x}^N) \\ \vdots & \vdots & \ddots & \vdots \\ \varphi^N(\mathbf{x}^1) & \varphi^N(\mathbf{x}^2) & \dots & \varphi^N(\mathbf{x}^N) \end{vmatrix}, \quad (3.3)$$

with single-particle spin orbitals  $\varphi^i(\mathbf{x})$  of each electron  $i$ , which are products of a spatial part  $\psi^i(\mathbf{r})$  and a spin function  $\chi^i(s)$ , with  $\mathbf{x} = (\mathbf{r}, s)$ . We remark that for the Hamiltonian (3.1), which lacks spin-orbit or spin-spin coupling, this *standard* Hartree-Fock ansatz leads to the same Hartree-Fock equations as an ansatz with two Slater-determinants, which are combined in a Hartree product

$$\Psi = \Psi_{\downarrow}(\mathbf{x})\Psi_{\uparrow}(\mathbf{x}), \quad (3.4)$$

one for all spin-up electrons  $\Psi_{\uparrow}$ , and one for all spin-down electrons  $\Psi_{\downarrow}$ . This other ansatz corresponds to the same symmetry subspace [86] and is commonly used in Monte Carlo calculations [46, 86, 87].

In multi-electron problems only the quantum numbers of the total wave function are conserved, namely the total magnetic quantum number  $M$ , the total  $z$ -parity  $\Pi_z$ , the total-spin projection  $S_z$ , and the total (squared) spin  $S^2$ . As we apply no restrictions to the wave function of paired electrons which feature identical quantum numbers but different spin orientation, we use an unrestricted Hartree-Fock ansatz. In general, this method does not give exact eigenfunctions of  $S^2$  [88] and our results may be contaminated with other spin states. This is not the case if all spins are aligned parallelly — the common spin configuration in strong magnetic fields. In the few cases where we deal with spin-paired orbitals we do not find a significant influence of the spin contamination on our results for the energy.

The quantum numbers of a total wave function, which is set up in the Hartree-Fock approximation (3.3), are connected to the corresponding single-particle quantum numbers via the relations

$$M = \sum_i^N m_i, \quad \Pi_z = \prod_i^N \pi_z^i, \quad S_z = \sum_i^N m_s^i. \quad (3.5)$$

The last quantum number to identify a state, the excitation number, cannot be constructed from the single-particle quantum numbers. However, in order to compare states that are denoted by total quantum numbers, e.g. results of diffusion quantum Monte Carlo [45, 46, 89] or configuration interaction (CI) [26, 40, 41] methods, which both act in full configuration space, we need to know about their correspondence to the Hartree-Fock states. This is a drawback of the Hartree-Fock method as extensive calculations can be necessary to find such correspondences. In case we compare to results of quantum Monte Carlo or CI calculations we label the states using the notation  $\{-M, \Pi_z, -S_z, \nu^*\}$ , where  $\nu^* = 1, 2, \dots$  denotes the excitation level within the corresponding many-particle symmetry subspace.

In accordance to previous work (e.g. Ref. [7]) we will define a shorter notation of the single-electron states, joining the excitation number  $\nu$  and the  $z$ -parity  $\pi_z = \pm 1$  using  $\nu' = 2\nu - (3 + \pi_z)/2$ . Here,  $\nu'$  corresponds to the number of longitudinal wave function nodes in the limit of strong magnetic fields. Further, we use the *negative* of the magnetic quantum number  $m' = -m$ , since we found that positive magnetic quantum numbers do not lead to truly bound states at the magnetic field strengths we consider. This allows us to label an orbital with only two numbers and a spin orientation, which we write in the form  $(m')_{\{\uparrow\}}^{\nu'}$ . The spin orientation is omitted in the spin-down case, as we already did in the hydrogen notation. The many-particle states can be represented by concatenating the single-orbital identifiers. As an example for this notation we use the ground state configurations of the helium atom at low or high magnetic field strengths  $(m' = 0, \nu' = 0, m_s = -\frac{1}{2})(m' = 0, \nu' = 0, m_s = +\frac{1}{2})$  and  $(m' = 0, \nu' = 0, m_s = -\frac{1}{2})(m' = 1, \nu' = 0, m_s = -\frac{1}{2})$ , respectively, which contract to  $0^0 0^0_{\uparrow}$  and  $0^0 1^0$ .

Even this short representation of multi-particle configurations is rather inexpedient if many electrons are involved, hence we additionally introduce a high-field notation, inspired by Ivanov et al. [90]: In the limit of very strong magnetic fields (again neglecting

the finite nuclear mass), the tightly-bound states ( $\nu' = 0$ ) are the lowest-lying orbitals. Therefore, in the ground state the  $N$  electrons occupy only these orbitals, beginning at  $m' = 0$  up to  $m' = N - 1$

$$\underline{0}_N = 0^0 1^0 2^0 \dots (N - 1)^0, \quad (3.6)$$

which is called the high-field ground state (HFGS) configuration. If some electrons  $X$  differ from this configuration, we use the high-field notation for the  $N - X$  HFGS-conform electrons and concatenate the quantum numbers of the deviating  $X$  electrons. This allows for a very compact labeling of many-electron configurations at large field strengths, e.g. the ground state of an iron atom at  $B = 5 \times 10^7$  T can be written as  $\underline{0}_{19} 0^0_{\uparrow} 0^1 1^1 2^1 3^1 4^1 0^2$ .

## 3.2 Expansion of the single-particle wave functions

As we restrict ourselves to strong magnetic fields it is reasonable to utilize Landau states in describing single-particle wave functions. In Sec. 2.2.1 we already introduced a general expansion of the Landau type (2.6), which has only been applied to the hydrogenic problem (see, e.g. Ref. [7]) so far. By contrast, the two simpler Landau expansions given in Eqs. (2.7) and (2.8) were used in the past to solve many-electron problems (see Refs. [7, 43, 52–54, 80, 91–94]). These two expansions utilize the approximate decoupling of the fast perpendicular and much slower longitudinal motion of the electrons in the case of very strong fields. In the product ansatz (2.7) [54, 91, 92], which is reasonable at  $\beta_Z \geq 1$ , the perpendicular component is constructed by a superposition of Landau states with a Landau channel occupation vector  $\mathbf{t}$ , whereas for very strong fields  $\beta_Z \gg 1$  the adiabatic expansion (2.8) [52, 53] can be employed, which uses only the lowest Landau state.

In any case we expand the longitudinal component  $P(z)$  of the  $i$ th electronic orbital with the help of  $B$ -splines [54] on finite elements, i.e.

$$P^i(z) = \sum_{\mu} \alpha_{\mu}^i B_{\mu}^i(z). \quad (3.7)$$

We already used this expansion in the previous chapter. However, it is a task of much higher complexity to find an efficient  $B$ -spline basis for multi-electron systems than it is for a single electron: The effort of calculating the interaction terms for each pair of electrons ( $i, j$ ) rises proportional to  $x^4$ , where  $x$  represents the number of expansion elements (either the number of  $B$ -splines or included Landau channels). Additionally, the number of electron pairs rises  $\sim N^2$ . Thus, the workload for the evaluation of many-particle terms always dominates over those for evaluating the single-particle terms, which rise proportional to  $x^2$ . Therefore, an algorithm that just increases the finite element number until a desired precision is reached, similar to our solution in the hydrogen case, would be very slow, and therefore not appropriate. Instead, we need to find  $B$ -spline



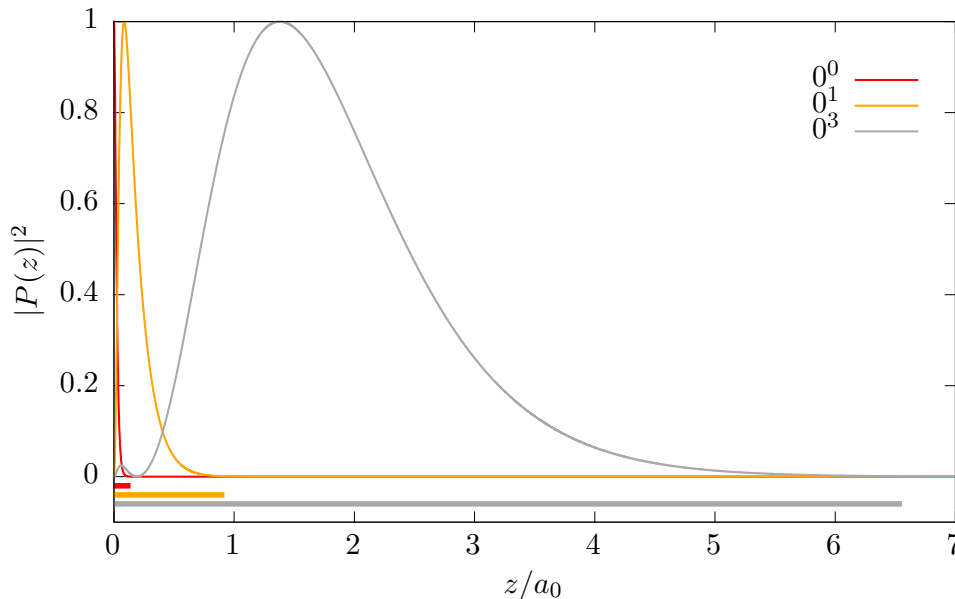


**Fig. 3.1:** Single-particle longitudinal wave functions  $0^0$ ,  $0^2$  and  $0^3$  of an iron state at  $\beta = 2500$ . The maxima were renormalized to 1. At the bottom, bars in corresponding colors indicate the approximate  $z$ -extension of the longitudinal wave functions  $P(z)$ , such that  $|P(z)|^2$  has dropped to about  $5 \times 10^{-4}$  at this value of  $z$ .

bases that use a minimal number of finite elements but guarantee a sufficient precision. The meaning of the word *sufficient* in this context will be discussed later in this chapter.

Additionally, our search for efficient finite element bases is hampered by the different spatial  $z$ -extensions of single-particle wave functions in excited many-electron atoms: The nodeless tb states are localized closely to the nucleus and their  $z$ -extension falls with rising magnetic field strength. In contrast, the hl states may extend far out and their  $z$ -elongation shows a rather weak dependence on  $\beta$ . Thus, for large  $\beta$  hl and tb states may differ significantly with respect to their  $z$ -extension, as can be seen in Fig. 3.1. There we show different single-particle  $z$ -wave functions and extensions of an iron state at high  $\beta$ . The  $z$ -wave function of the hl  $0^3$  single-particle component (grey) is about 50 times as wide as the  $z$ -wave function of the innermost tb component  $0^0$ .

An appropriate description of all single-particle orbitals thus requires a large number of finite elements if one uses a *common* finite element decomposition and, therefore, a common  $B$ -spline basis set. Engel et al. [43, 54] employed such a technique, and their calculations suffered from quite large computational effort if hl orbitals were involved. As a remedy, we use *independent* finite element bases. This allows us to individually select the total number of finite elements  $N_{\text{fem}}$ , the basis width  $z_{\text{max}}$  and the distribution scheme  $\{x\}$  of these elements onto the interval  $[0, z_{\text{max}}]$  for each single-particle orbital. The only parameter that we keep fixed for all particles is the  $B$ -spline order, which we set to  $k = 6$  to obtain reasonably sparse matrices. However, the selection of the other parameters  $z_{\text{max}}$ ,  $N_{\text{fem}}$  and  $\{x^i\}$  for each orbital  $i$  is a less trivial task, which needs

further inspection. We first consider the basis width, as we know about its importance from the hydrogen atom: There, we had to analyze several slices of the two-dimensional wave function in each direction to determine good basis widths, but with either of the Landau expansions given in Eqs. (2.7) and (2.8), only a single  $z$ -wave function needs to be analyzed. Even if one uses the full Landau expansion (2.6) it suffices to analyze the  $z$ -wave function corresponding to the lowest Landau channel as it has always the largest  $z$ -extension. Higher Landau channels correct the wave function with regard to the presence of the Coulomb potential of the nucleus (cusp-like behavior) and thus only at small values of  $z$ . In accordance with Sec. 2.2.4 we adjust  $z_{\max}$  such that the modulus of the wave function has dropped to  $10^{-3}$  of its maximum value at its outmost position. Again, we also accept marginally larger bases, but not smaller ones.

Secondly, we have to decide how many finite elements  $N_{\text{fem}}$  are used. We already mentioned that the single-particle excitation number  $\nu'$  roughly corresponds to the number of nodes of the  $z$ -wave function at large  $\beta$ . To account for the associated oscillations of the wave function we start with a basic number of finite elements but increase their number linearly with  $\nu'$ . A minimum of 10 finite elements and an increase of 5 finite elements per wave function node,

$$N_{\text{fem}} = 5\nu' + 10, \quad (3.8)$$

proved to be most efficient during extensive test calculations. This leads to a significant reduction of deployed finite elements compared to the common basis for all electrons with 70 finite elements that was used in Ref. [91].

Thirdly, a suitable distribution  $\{x\}$  of finite elements in the range  $[0, z_{\max}]$  must be chosen. We found a combination of equidistant and quadratically widening element borders most efficient. The electron's wave function oscillates in the classically allowed area of the mean-field potential, therefore we use an equidistant node distribution in this range to account for this oscillatory structure. We identify this area using the  $z$ -position of the largest maximum of the wave function's modulus, which is associated with the classical turning point. Beyond this point, in the classically forbidden regime, we can expect an exponential decline of the wave function and therefore spread the finite elements using a quadratic widening. We distribute the finite elements depending on the excitation level  $\nu'$  and use the following scheme: Let  $z_1$  be the largest maximum of the  $z$ -wave function's modulus  $|P(z)|$  and  $\nu'$  the approximate number of longitudinal nodes. Then the interval  $[0, z_1]$  is divided into  $a = (N_{\text{fem}} + 1)(1 - \frac{1}{\nu'+1})$  (integer part) equidistant element borders. The remaining interval  $[z_1, z_{\max}]$ , in which the wave function decays exponentially, is divided into the remaining  $b = (N_{\text{fem}} + 1)\frac{1}{\nu'+1}$  (integer part) quadratically widening element borders. This ensures a growing fraction of equidistantly distributed elements with rising excitation level and allows for a good description of the oscillatory behavior of the wave function out to the last maximum of its modulus.

It must be noted that for some very exotic electronic configurations, which include several hl single-particle states, our  $B$ -spline bases may not be appropriate. In these rare cases the fundamental structure of the wave function changes and our finite element

distribution algorithm becomes inefficient. We then fall back to an all-quadratic widening of the finite elements. This less subtle method of finite element distribution enables us to proceed with our calculations for such extreme configurations, albeit with a reduced precision of the results.

Since the  $B$ -spline bases introduced above use very few finite elements we call them “slim” bases. With this subtle choice for the finite elements we can face the challenging task of calculating energies and wave functions in many-electron systems. However, before we proceed to this task we have to answer the following questions: What is the size of the additional errors stemming from the slim finite element expansion? What are the other sources of errors in our method and how do these errors compare with those caused by the slim finite element expansion? We answer these questions in the following section.

### 3.3 Error estimates for the slim expansions

It is of utter importance to know about error sources and error sizes of an algorithm one is about to use. The most important error sources of the method presented here are the total wave function ansatz (3.3), the Landau expansions (2.6) – (2.8), and the expansion of the longitudinal wave function components (3.7). We give a short description of these errors and how we can estimate their sizes.

The restriction to a single Slater determinant is also known as the Hartree-Fock approximation and causes the neglect of most electronic correlations, which we refer to as the “correlation error”. This error cannot be overcome by whatever sophisticated single-particle wave function expansion. In order to retrieve an estimate for the correlation error we have to compare our best Hartree-Fock results to those of methods that include all electronic correlations, such as the diffusion quantum Monte Carlo method in magnetic fields [86]. Typical fractions for such neglected correlation energies in Hartree-Fock calculations are in the range of several per mill of the binding energy, depending on the core charge, the magnetic field strength, and the number of electrons. These electronic correlations diminish with increasing  $Z$  and  $\beta$  as the inter-electronic potentials become negligible compared to the electron-core potentials. The lowest relative correlation error found with the help of the fixed-phase diffusion quantum Monte Carlo method (FPDQMC) [45, 95] in an extensive study by Boblest [46] was 0.9‰, for the iron ground state at  $B = 5 \times 10^8$  T. This will serve as our reference value for the minimal relative correlation energy error in the range of  $Z$  and  $\beta$  that we will focus on. We can safely neglect errors of other sources if they are considerably smaller in size than this value.

The longitudinal expansion error is caused by the finite number of  $B$ -splines and finite elements, although strictly speaking an infinite number of basis elements does not necessarily lead to a vanishing expansion error, since the finite element method does not provide a complete set of basis functions. Still, we obtain an estimate for this error by comparing the energies calculated using the slim longitudinal  $B$ -spline basis with those

of a second calculation employing a vastly increased number of finite elements, which is expected to have a negligible remaining finite element expansion error. For the sake of brevity we call this second basis set “fat”, as it features 50 *additional* finite elements. The energy difference between these two calculations is then a reasonable estimate for the error caused by the slim longitudinal expansion.

The Landau expansion error stems from the finite number of Landau channels included in expansions (2.6) and (2.8), and additionally in Eq. (2.7) from the restriction to a product ansatz of the transverse and longitudinal motion. We obtain an estimate for this error by a comparison of the results obtained with the fat longitudinal  $B$ -spline basis to results of the 2D finite element expansion (2.9), which we will refer to as numerically “exact” in this context as we can guarantee an energy precision of  $10^{-7}$  Ry.

In the following section we evaluate the error sizes of longitudinal and Landau expansion errors of all three expansions (2.6), (2.7) and (2.8) for different hydrogen states at various  $\beta$ . If we can show that the slim  $B$ -spline expansion error is smaller than either the correlation energy error or the Landau expansion error we can be sure that we have succeeded in finding a proper longitudinal finite element expansion with a vastly reduced number of finite elements.

### 3.3.1 Tightly-bound states

In Fig. 3.2 we analyze the states  $0^0 \dots 25^0$  and compare the errors attributed to the three different sources explained above. One can see that the longitudinal expansion error is smaller than the correlation error estimate for all quantum numbers  $m'$ , with only one exception at low  $\beta$  and  $m' = 0$ . However, in this exceptional case the Landau expansion error widely exceeds the longitudinal basis error, which is thus irrelevant again. The slim  $B$ -spline expansion errors of the adiabatic and product expansions are very small and are only visible in the upper right plot at  $m' = 1$  and low  $\beta$ . This can be explained by the simplicity of the corresponding Landau expansions: Those feature only a single  $z$ -wave function that can be described excellently by our slim  $B$ -spline bases. By contrast, the full expansion (2.6) combines 31 different  $z$ -wave functions and the quality of their description decreases for higher Landau channels as the  $B$ -spline bases are optimized according to the shape and extension of the lowest Landau channel’s wave function only. Therefore, it is not surprising that the full expansion profits most from an increased number of finite elements. Figure 3.2 also permits a first comparison between the three expansions of the Landau type. The superiority of the full expansion at all magnetic field strengths is obvious, as the errors corresponding to this expansion exceed the correlation error only in the case  $m' = 0$ . The two simpler expansions do not yield such good results for tightly-bound states, but the result quality improves for higher  $\beta$  and also for states of higher  $m'$ . For  $m' \geq 5$  the error of the product ansatz is in the range of, or even below, the correlation error at any displayed field strength. In contrast, the errors stemming from the adiabatic expansion are quite large and can be neglected only at very high  $\beta$  or large  $m'$ . Let us summarize that our chosen set of parameters for the slim longitudinal  $B$ -spline bases yields results of sufficient precision and may be used for the expansion

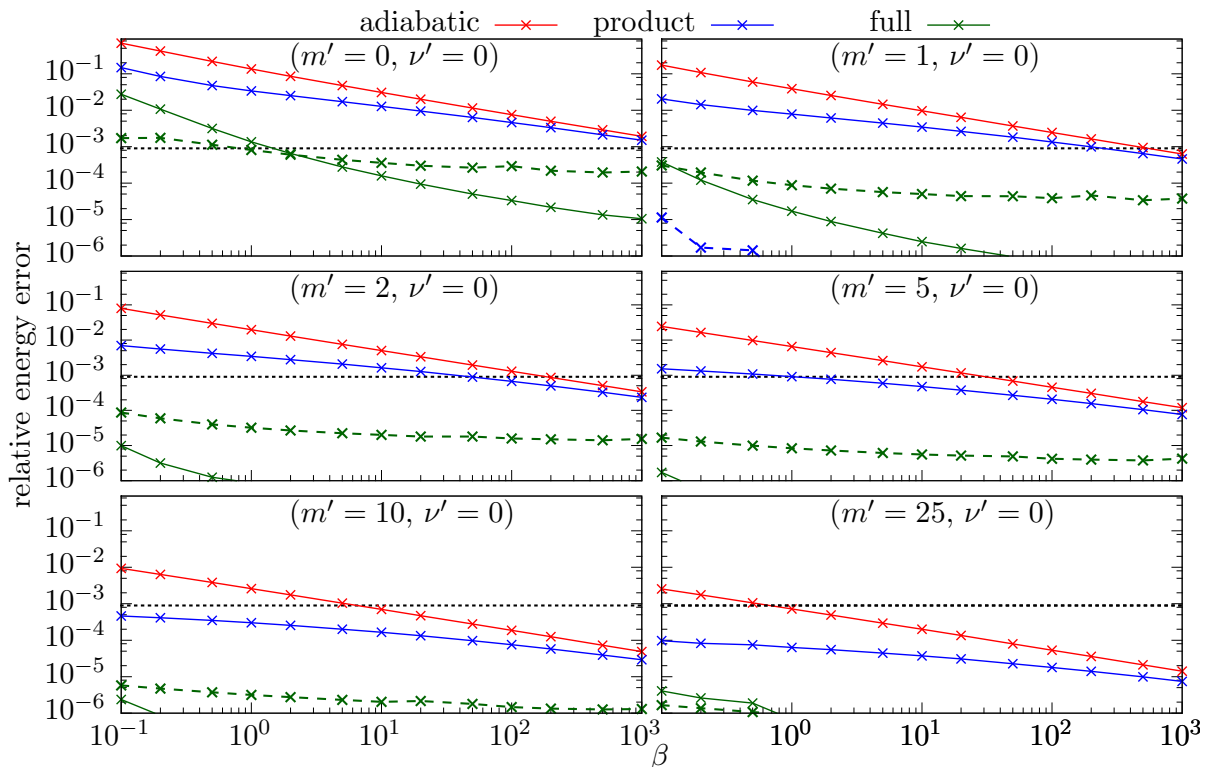


**Fig. 3.2:** Relative energy errors of binding energies of tightly-bound states in dependence of  $\beta$  using different Landau expansions. Line types correspond to the error sources: Landau expansion error (solid) and slim longitudinal expansion error (dashed). An estimate for the correlation error (dotted) was found by a comparison with Monte-Carlo studies (see text). Lines serve as a guide to the eye.

of any tightly-bound state at  $\beta \geq 0.1$ . We have thus demonstrated the usefulness and high accuracy of the slim finite element expansion and proceed to test its capabilities in describing hydrogen-like orbitals.

### 3.3.2 Hydrogen-like states

In Fig. 3.3 we perform a similar analysis, but now for hydrogen-like states with different excitation numbers. These orbitals have, in contrast with tightly-bound ones, rather small binding energies. Accordingly, their contributions do not lead to ground-state configurations at high magnetic fields, but to excited many-particle states. As the FPDQMC method is restricted to low-lying states we have no estimate for the correlation energy errors of highly excited many-particle states and thus we give no correlation error estimate in Fig. 3.3. However, we expect that the relative correlation errors are larger for the hydrogen-like states due to their small overall binding energies. Our first observation is that the energy errors of states with negative  $z$ -parity (odd  $\nu'$ , left column of Fig. 3.3) are significantly smaller than the errors of states with positive  $z$ -parity (even  $\nu'$ , right

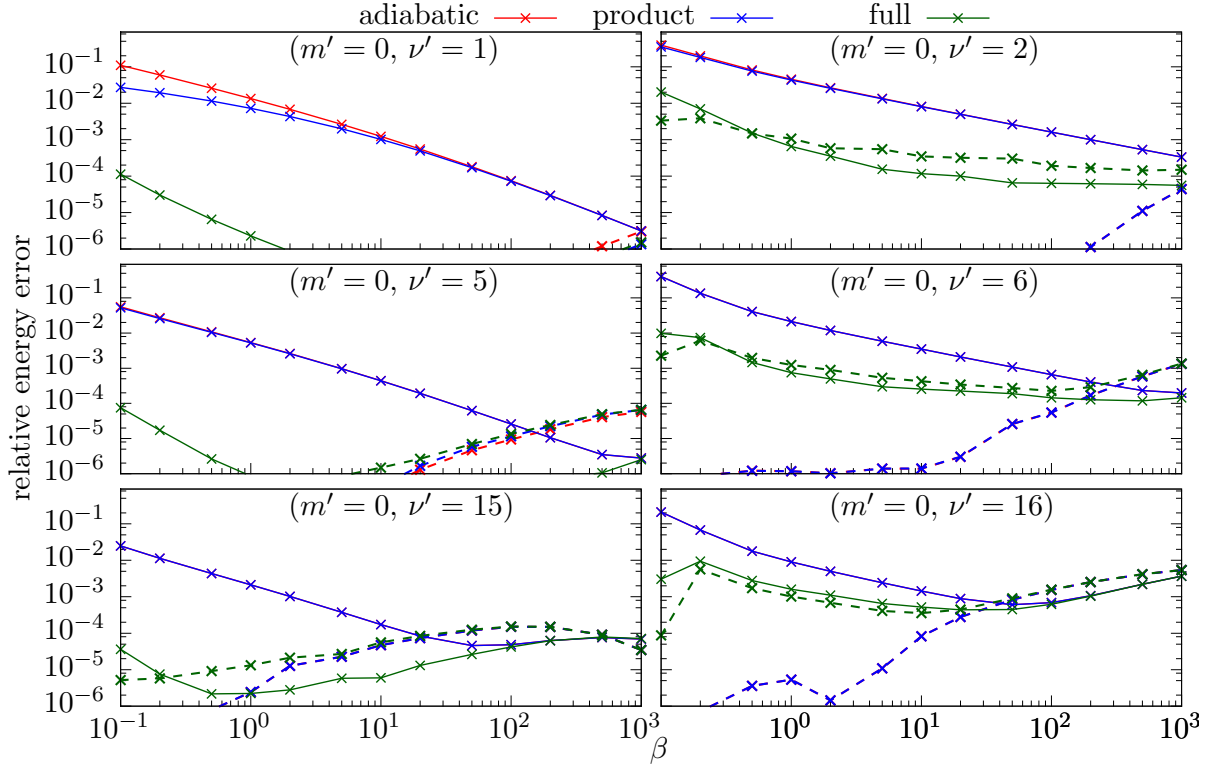


**Fig. 3.3:** Same as in Fig. 3.2, but for hydrogen-like states.

column of Fig. 3.3). This is due to the vanishing probability density at  $z = 0$  of odd states, which reduces the influence of the nucleus. Secondly, both the Landau expansion errors and the longitudinal expansion errors of the adiabatic and product ansätze coincide for higher excitations or magnetic field strengths. There, the additional Landau weights  $\mathbf{t}$  of the product ansatz bring no advantage over the adiabatic expansion, and the contributions of the higher Landau channels vanish for high  $\beta$  and  $\nu'$ . This effectively reduces the product ansatz to an adiabatic expansion and both yield the same results and errors. In this case, we expect only the full Landau expansion to further reduce the energy errors. This is the case for any state shown, similar to our findings in Fig. 3.2.

Thirdly, at large  $\beta$  and for high excitation numbers we see an increase of both the Landau expansion error and the longitudinal expansion error for any of the adiabatic, product or full Landau expansion. The rise of the longitudinal expansion error is caused by the finite integration precision. This is also the case for the Landau expansion errors, which are in fact not caused by the Landau expansions, but by remaining inaccuracies of the fat longitudinal expansion. Note that these errors seem large on a relative scale but are tiny in absolute values due to the extremely weak binding energies of the highly excited states shown here. We conclude that our slim longitudinal single-particle wave function expansion scheme is adequate to describe any orbital of interest with sufficient precision. Thus, we finally progress to the solution of many-particle problems.

# 4 The accelerated doubly self-consistent Hartree-Fock-Roothaan method

After a more general view on multi-electron systems in strong magnetic fields we proceed with the description of methods and their implementations to solve the Schrödinger equation for such systems. Klews [52, 53] developed a self-consistent Hartree-Fock finite-element method for many-electron atoms in very strong magnetic fields. This method uses the adiabatic expansion (2.8) for the single-particle wave functions. In accordance with the literature we call the implementation HFFEM. Later, this method was extended by Engel [43, 54], which resulted in the doubly self-consistent Hartree-Fock-Roothaan method that employs the product ansatz (2.7). The original implementation is called HFFER (Hartree-Fock finite-element Roothaan), whereas the latest implementation of this method by Schimeczek et al. [92] is referred to as HFFER II. This version features several important improvements regarding the runtime and convergence behavior of the program. Although we already know from Sec. 3.3.1 that the product ansatz is inferior to the full Landau expansion (2.6) with respect to precision, its simplicity makes it vastly superior with regard to the calculational effort. It allows scanning many states for their energies, which is useful, for example during ground state analyses or for the calculation of partition functions. Moreover, the wave functions found with this method serve as initial wave functions for the more complex 2D Landau-Hartree-Fock-Roothaan method that will be discussed in Chap. 5. Therefore the results of the HFFER II program are indispensable even if higher precision is needed. For this reason we recapitulate the basics of the doubly self-consistent Hartree-Fock-Roothaan method and explain important procedural optimizations.

## 4.1 Hartree-Fock-Roothaan equations

We start from the Schrödinger equation that corresponds to the Hamiltonian (3.1), insert the Hartree-Fock ansatz (3.3) for the total wave function, and use the expansion (2.7) for the single-electron orbitals. Aiming for equations that can be solved numerically, we vary the energy functional  $\langle \Psi | \hat{H} | \Psi \rangle$  with respect to all  $B$ -spline coefficients  $\alpha_\mu^i$  but frozen Landau weights  $t_n^i$ , or vice versa. This leads to eigenvalue problems for each electron that can be solved with standard numerical routines from the LAPACK [72] software package.

### 4.1.1 Equations for the $B$ -spline coefficients

The variation of the energy functional with respect to all  $B$ -spline coefficients  $\alpha_\mu^i$  but frozen Landau weights  $t_n^i$  leads to  $N$  generalized eigenvalue problems for the  $B$ -spline coefficients

$$\sum_{\mu} F_{\mu\nu}^i \alpha_{\mu}^i = \varepsilon_i \sum_{\mu} S_{\mu\nu}^i \alpha_{\mu}^i, \quad i = 1, \dots, N, \quad (4.1)$$

which we call the ‘‘longitudinal problem’’. On the right-hand side,  $S_{\mu\nu}^i = \int B_{\mu}^i(z) B_{\nu}^i(z) dz$  denotes the overlap matrix between  $B$ -splines of orbital  $i$ . The Fock matrix on the left-hand side of Eq. (4.1) is composed of five terms: the kinetic energy of the longitudinal motion, the spin energy and the Landau energy of the transverse motion, the potential energy in the Coulomb field of the nucleus, and the mean field energies of the direct and the exchange interactions between electrons  $i$  and  $j$ . The terms read, in that order,

$$\text{long } F_{\mu\nu}^i = - \int_{-\infty}^{\infty} B_{\nu}^i(z) \frac{\partial^2}{\partial z^2} B_{\mu}^i(z) dz, \quad (4.2)$$

$$\text{tran } F_{\mu\nu}^i = 4\beta \left[ \left( m_s^i + \frac{1}{2} \right) + \sum_{n=0}^{N_L} n (t_n^i)^2 \right] S_{\mu\nu}^i, \quad (4.3)$$

$$\text{nucl } F_{\mu\nu}^i = \int_{-\infty}^{\infty} B_{\nu}^i(z) B_{\mu}^i(z) V^i(z) dz, \quad (4.4)$$

$$\text{dir } F_{\mu\nu}^i = \sum_{j=1}^N \int_{-\infty}^{\infty} B_{\nu}^i(z_i) B_{\mu}^i(z_i) \int_{-\infty}^{\infty} |P^j(z_j)|^2 U^{ij}(z_i, z_j) dz_j dz_i, \quad (4.5)$$

$$\text{ex } F_{\mu\nu}^i = - \sum_{j=1}^N \delta_{m_s^i, m_s^j} \int_{-\infty}^{\infty} B_{\nu}^i(z_i) P^j(z_i) \int_{-\infty}^{\infty} P^j(z_j) A^{ij}(z_i, z_j) B_{\mu}^i(z_j) dz_j dz_i. \quad (4.6)$$

In Eq. (4.4),  $V^i(z)$  denotes the longitudinal potential of the nucleus, which is defined with the help of effective Landau-averaged Coulomb potentials  $V_{m_i}^{nn'}(z)$

$$V^i(z) = \sum_{n, n'=0}^{N_L} t_n^i t_{n'}^i V_{m_i}^{nn'}(z), \quad (4.7)$$

$$\text{with } V_{m_i}^{nn'}(z) = -2 Z \int \frac{\Phi_{nm_i}^*(\mathbf{r}^{\perp}) \Phi_{n'm_i}(\mathbf{r}^{\perp})}{|\mathbf{r}|} d\mathbf{r}^{\perp}. \quad (4.8)$$

The effective interaction potentials in Eqs. (4.5) and (4.6) explicitly depend on the



Landau expansion coefficients  $\mathbf{t}$  and are given by [43]

$$U^{ij}(z_i, z_j) := \sum_{n_i, n'_i, n_j, n'_j=0}^{N_L} t_{in_i} t_{in'_i} t_{jn_j} t_{jn'_j} U_{m_i m_j}^{n_i n_j n'_i n'_j}(z_i, z_j) \quad \text{and} \quad (4.9)$$

$$A^{ij}(z_i, z_j) := \sum_{n_i, n'_i, n_j, n'_j=0}^{N_L} t_{in_i} t_{in'_i} t_{jn_j} t_{jn'_j} A_{m_i m_j}^{n_i n_j n'_i n'_j}(z_i, z_j) \quad , \quad (4.10)$$

which on their part depend on the effective direct and exchange two-particle potentials between Landau states

$$U_{m_i m_j}^{n_i n_j n'_i n'_j}(z_i, z_j) = 2 \iint \frac{\Phi_{n_i m_i}^*(\mathbf{r}_i^\perp) \Phi_{n_j m_j}^*(\mathbf{r}_j^\perp) \Phi_{n'_i m_i}(\mathbf{r}_i^\perp) \Phi_{n'_j m_j}(\mathbf{r}_j^\perp)}{|\mathbf{r}_i - \mathbf{r}_j|} d\mathbf{r}_i^\perp d\mathbf{r}_j^\perp \quad \text{and} \quad (4.11)$$

$$A_{m_i m_j}^{n_i n_j n'_i n'_j}(z_i, z_j) = 2 \iint \frac{\Phi_{n_i m_i}^*(\mathbf{r}_i^\perp) \Phi_{n_j m_j}^*(\mathbf{r}_j^\perp) \Phi_{n'_i m_i}(\mathbf{r}_j^\perp) \Phi_{n'_j m_j}(\mathbf{r}_i^\perp)}{|\mathbf{r}_i - \mathbf{r}_j|} d\mathbf{r}_i^\perp d\mathbf{r}_j^\perp \quad , \quad (4.12)$$

respectively. The evaluation of the expressions (4.8), (4.11) and (4.12) is highly non-trivial and further information on it is given in Appx. B.

### 4.1.2 Equations for the Landau expansion coefficients

A similar variation of the energy functional with respect to all Landau weights  $t_n^i$  for a fixed set of  $B$ -spline coefficients  $\alpha_\mu^i$ , i.e. for frozen longitudinal wave functions, yields the Hartree-Fock-Roothaan equations for the Landau expansion coefficient vector  $\mathbf{t}$ , i.e. the “transverse problem”. Because of the orthonormality of the Landau states, the corresponding overlap matrices are diagonal, and the equations reduce to ordinary eigenvalue problems,

$$\sum_{n=0}^{N_L} \tilde{F}_{nn'}^i t_n^i = \varepsilon_i t_n^i \quad i = 1, \dots, N. \quad (4.13)$$

The Fock matrix  $\tilde{F}_{nn'}^i$  in Eq. (4.13) is again the sum of five terms, corresponding to the kinetic energy of the longitudinal motion, the Landau and spin energies, the potential energy of the Coulomb interaction with the nucleus, and the mean-field energies of the

direct and exchange electron-electron interactions:

$$\text{long } \tilde{F}_{nn'}^i = -\delta_{nn'} \int_{-\infty}^{\infty} P^i(z) \frac{\partial^2}{\partial z^2} P^i(z) dz, \quad (4.14)$$

$$\text{tran } \tilde{F}_{nn'}^i = 4\beta \left[ \left( m_s^i + \frac{1}{2} \right) + n \delta_{nn'} \right], \quad (4.15)$$

$$\text{nucl } \tilde{F}_{nn'}^i = \int_{-\infty}^{\infty} |P^i(z)|^2 V_{m_i}^{nn'}(z) dz, \quad (4.16)$$

$$\text{dir } \tilde{F}_{nn'}^i = \sum_{j=1}^N \sum_{n_j, n'_j=0}^{N_L} t_{n_j}^j t_{n'_j}^j \int_{-\infty}^{\infty} \int_{-\infty}^{\infty} |P^i(z_i)|^2 |P^j(z_j)|^2 U_{m_i m_j}^{nn_j n' n'_j}(z_i, z_j) dz_i dz_j, \quad (4.17)$$

$$\text{ex } \tilde{F}_{nn'}^i = - \sum_{j=1}^N \delta_{m_s^i, m_s^j} \sum_{n_j, n'_j=0}^{N_L} t_{n_j}^j t_{n'_j}^j \int_{-\infty}^{\infty} \int_{-\infty}^{\infty} P^i(z_i) P^j(z_j) P^j(z_i) P^i(z_j) A_{m_i m_j}^{nn_j n' n'_j}(z_i, z_j) dz_i dz_j. \quad (4.18)$$

The evaluation of all longitudinal integrals, also those in Secs. 4.1.1 and 5.1, can be sped up significantly by making use of the  $z$ -parity. Klews [52] showed that it is sufficient to evaluate the single-particle integrals for the positive interval  $z \in [0, \infty]$  as the integrals are symmetric. For each of the two double integrals corresponding to the effective potentials  $U$  and  $A$ , a single integral must be evaluated on the full interval, due to the relations  $U(z_i, z_j) = U(|z_i - z_j|)$  and  $A(z_i, z_j) = A(|z_i - z_j|)$ . These modifications are implemented in all programs and tools.

## 4.2 Solution method

Due to the electron-electron interaction terms, Eqs. (4.1) and (4.13) each represent  $N$  (generalized) coupled eigenvalue problems that have to be solved iteratively in a self-consistent manner. We add a second layer of iteration to account for the additional coupling of the longitudinal and transverse equations and solve Eqs. (4.1) and (4.13) alternatingly until self-consistency is obtained. The choice of proper initial wave functions such that these iterations show benign convergence behavior is explained in detail in Refs. [91, 92]. There, we presented a method that allows an automatic calculation of initial wave functions, which we briefly recapitulate: We solve the single-electron problem of each electron  $i$  with excitation number  $\nu_i^j$  in adiabatic approximation. In this step we use a reduced core charge

$$q_{\text{eff}}^i = Z - \sum_{\substack{j \neq i \\ \nu_i^j > \nu_j^i}}^N \left[ 1 - \int_0^{\infty} |\Phi_{0m_i}(\rho)|^2 \int_0^{\rho} \sum_{\substack{j \neq i \\ \nu_i^j = \nu_j^i}}^N |\Phi_{0m_j}(\rho')|^2 \rho' d\rho' \rho d\rho \right], \quad (4.19)$$

which takes into account the screening effects by other electrons with excitation levels  $\nu'_j$ . Since we have no knowledge about the wave function's shape until we have conducted first calculations, we cannot use the slim  $B$ -spline basis that we introduced in the last chapter. Instead, we begin with an oversized  $B$ -spline basis with an all-quadratic finite element widening for each electron. As soon as a first rough wave function estimate is available we can apply our slim  $B$ -spline algorithm and adapt the  $B$ -spline bases according to the shape of the wave functions.

In some rare cases, especially when many excited electrons create a complicated configuration, the effective core-charge method to find initial wave functions does not lead to convergence, which is why we implemented a second scheme for this task. There, we iteratively add one electron  $i$  after another to the system. We then fully account for the electronic interactions of those electrons  $j$ , that were added before electron  $i$ , but ignore the reactions of electrons added later. By that means, we keep the wave functions of already placed electrons frozen. The sequence of electrons added to the system must be chosen carefully to suppress large effects on the single-particle wave functions as soon as we account for all interactions again. Thus, we add those electrons first to the system that have large binding energies, namely the tightly-bound states. Their longitudinal motion is dominated by the interaction with the core. Weakly bound or hydrogen-like electrons, however, which are considerably influenced by the electronic interactions, must be added last. Therefore, electrons with low  $\nu'$  are placed first, beginning at low  $m'$ . This method to find initial wave functions is time-consuming, but significantly enhances the chances for convergence.

In Fig. 4.1 we show the program scheme of our implementation HFFER II of the doubly self-consistent Hartree-Fock-Roothaan method. The program proceeds as follows: After specifying the core charge and electronic quantum numbers HFFER II calculates effective core charges according to Eq. (4.19) and finds initial wave functions in adiabatic approximation. These are then used to initialize the longitudinal iterations that solve equations (4.1). The resulting longitudinal wave functions are analyzed for the  $z$ -position of their maximum absolute value. With that position and a newly estimated cutoff length  $z_{\max}$  the finite element distribution  $\{x^i\}$  is optimized and equations (4.1) are solved again. In case no further finite element adaption is needed, the Landau weights  $t_n^i$  are adjusted by solving the transverse problem (4.13). Then, the effective interaction potentials given in Eqs. (4.9) and (4.10) are adapted to the new Landau weights. After this step, the HFFER II program returns to solve the longitudinal problem and remains in this loop until the total energy difference between the longitudinal and transverse results falls below a convergence threshold, which we set to  $10^{-3}$  eV. If either of the two self-consistent steps fails to converge in time or no suitable  $B$ -spline basis can be found, HFFER II restarts the iterations at a different magnetic field strength that is chosen to bisect the  $\beta$ -interval between the last converged and failed calculation. Up to 9 consecutive convergence failures are tolerated before the program terminates empty-handed. If convergence was achieved at a different  $B$ , HFFER II adapts the field strength and uses the data set  $\alpha_\mu^i, t_n^i, \{x^i\}$  of the converged state closest with respect to the magnetic field strength for the new initial wave function. This choice significantly increases the

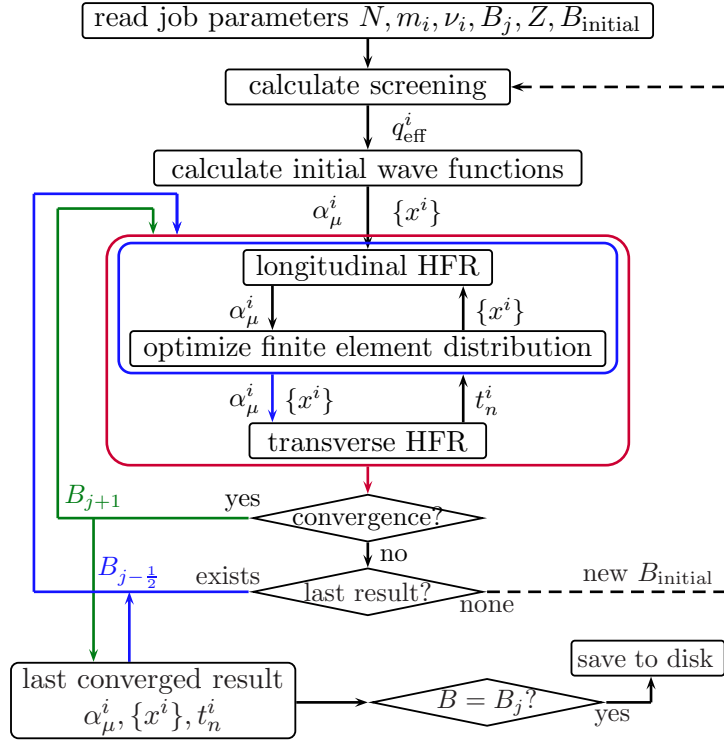


**Fig. 4.1:** Scheme of the HFFER II program course of action (for details see text).

convergence probability. The results for targeted field strengths  $B_j$  that were specified in a separate file, are saved to disk using the special *.aib* file format.

### 4.3 Transitions

The ultimate goal of this work is to provide the atomic raw data needed to model the radiative transfer in the atmospheres of MWDs and NS. Therefore, as in the hydrogen case, we need the dipole strengths, oscillator strengths and energies of the most important bound-bound transitions. Please note that bound-free and free-free transitions are beyond the scope of this work, and can be found in Refs. [80, 93, 94, 96].

We follow Ruder et al. [7] and begin with the dipole matrix element in length form between an initial and final state denoted by indices  $i$  and  $f$ , respectively

$$p_{if}^q = \left\langle \Psi_f \left| \sum_a^N r_a^q \right| \Psi_i \right\rangle. \quad (4.20)$$

Here, the spherical components of the position vector  $r_a^q = \sqrt{\frac{4\pi}{3}} r_a Y_{1,q}(\theta_a, \phi_a)$  are again measured in atomic units, and we have defined  $q = \Delta M = M_f - M_i$ . Since our total

wave functions  $\Psi$  are Slater determinants, Eq. (4.20) can be written in the form

$$p_{\text{if}}^q = \sum_{a,b=1}^N \langle \psi_a^f | r^q | \psi_b^i \rangle M_{a,b}^{\text{if}}, \quad (4.21)$$

(cf. [91]) using the cofactor  $M_{a,b}^{\text{if}}$  of the total overlap matrix

$$S_{ab}^{\text{if}} = \langle \psi_a^f | \psi_b^i \rangle. \quad (4.22)$$

With the dipole matrix element at hand we calculate the dipole and oscillator strengths

$$d_{\text{if}}^q = |p_{\text{if}}^q|^2, \quad (4.23)$$

$$f_{\text{if}}^q = \Delta E_{\text{if}} d_{\text{if}}^q, \quad (4.24)$$

where the energy difference between both states  $\Delta E_{\text{if}}$  is given in atomic units, as well. Equation (4.21) contains integrals between single-particle orbitals, and their evaluation depends on the single-particle wave function expansion. Our wave function expansions use Landau states, and we rely on the expression of  $r_a^q$  in terms of the Landau function ladder operators given in Refs. [7, 54].

We insert the single-particle wave function ansatz (2.7) into the overlap integral (4.22), use the orthonormality of the Landau states and retrieve the following simple expression

$$\langle \psi_a^f | \psi_b^i \rangle = \delta_{m_a, m_b} \delta_{\pi_z^a, \pi_z^b} \delta_{m_s^a, m_s^b} 2 \int_0^\infty P^a(z) P^b(z) dz \sum_{n=0}^{N_L} t_n^a t_n^b, \quad (4.25)$$

where we also used  $\pi_z^a = (-1)^{\nu_a}$ . The dipole integrals in Eq. (4.21) take different forms, depending on their polarization index  $q$  (cf. [54, 91]):

$$\langle \psi_a^f | r^0 | \psi_b^i \rangle = \delta_{m_a, m_b} \delta_{-\pi_z^a, \pi_z^b} \delta_{m_s^a, m_s^b} 2 \int_0^\infty P^a(z) z P^b(z) dz \sum_{n=0}^{N_L} t_n^a t_n^b, \quad (4.26)$$

$$\begin{aligned} \langle \psi_a^f | r^{+1} | \psi_b^i \rangle &= -\delta_{m_a, (m_b+1)} \delta_{\pi_z^a, \pi_z^b} \delta_{m_s^a, m_s^b} \sqrt{\frac{2}{\beta}} \int_0^\infty P^a(z) P^b(z) dz \\ &\times \sum_{n=0}^{N_L} \left[ \sqrt{n+1} t_{(n+1)}^a t_n^b + \sqrt{n-m_b} t_n^a t_n^b \right], \end{aligned} \quad (4.27)$$

$$\begin{aligned} \langle \psi_a^f | r^{-1} | \psi_b^i \rangle &= \delta_{m_a, (m_b-1)} \delta_{\pi_z^a, \pi_z^b} \delta_{m_s^a, m_s^b} \sqrt{\frac{2}{\beta}} \int_0^\infty P^a(z) P^b(z) dz \\ &\times \sum_{n=0}^{N_L} \left[ \sqrt{n} t_{(n-1)}^a t_n^b + \sqrt{n-m_b+1} t_n^a t_n^b \right]. \end{aligned} \quad (4.28)$$

The calculation of transition energies and strengths is not always required, thus it is reasonable to source out this task into a separate program. This program returns the dipole and oscillator strengths along with the transition energy of any two states specified in the *.aib* file format, provided an allowed dipole transition exists.

## 4.4 Procedural optimizations

The HFFER II program is more than a proof of principle. It is intended to perform large-scale analyses of different atomic states at a wide range of magnetic field strengths. Therefore, program speed and reliability are of utter importance. In this section we introduce a series of speed and convergence optimizations which significantly improve the former implementations of the doubly self-consistent Hartree-Fock-Roothaan method by Engel [43, 54] and Schimeczek [91].

### 4.4.1 Speed boost

In Sec. 3.2 we already presented individual *B*-spline bases for each electron, which boost the program speed roughly by a factor of 15 compared to a common finite element decomposition. A second important improvement is the introduction of a flexible parallelization that allows differing numbers of processor cores and electrons. In this case the work is split among the available cores. This enables us to run the program even if fewer processors than electrons are available, for the prize of longer runtimes. In a third step we changed the program structure such that a significant amount of intermediate results is reused in consecutive iterations, especially during the evaluation of the Landau averaged potentials. Also, we precalculated the *adiabatic potentials* (see Appx. B) and load them from binaries as soon as the program starts.

All these steps lead to a tremendous program speedup, depending on the number of electrons, as is shown in Fig. 4.2. The superiority of our new implementation is obvious: Especially for few electrons the speed gain exceeds a factor of 100, but even for 26 electrons our new program is about 70 times as fast as HFFER. No speed up is visible for  $N = 1$ , but the total runtime for single-electron problems is already far below 1 s. Calculations for a single electron are also unimportant as very precise results of the 2D *B*-spline calculations are available. The average speed gain for the whole set of calculations amounts to a formidable factor of about 80. This is lower than the average of all speed-up factors since calculations with few electrons take less time to complete. The full two-dimensional Landau Hartree-Fock-Roothaan (2DLHFR) program, which we will discuss in the next chapter, also profits from this speedup techniques: In the 2DLHFR program we reuse the individually optimized *B*-spline bases of each orbital, which is a first important measure to reduce the large computational costs of this complex method.

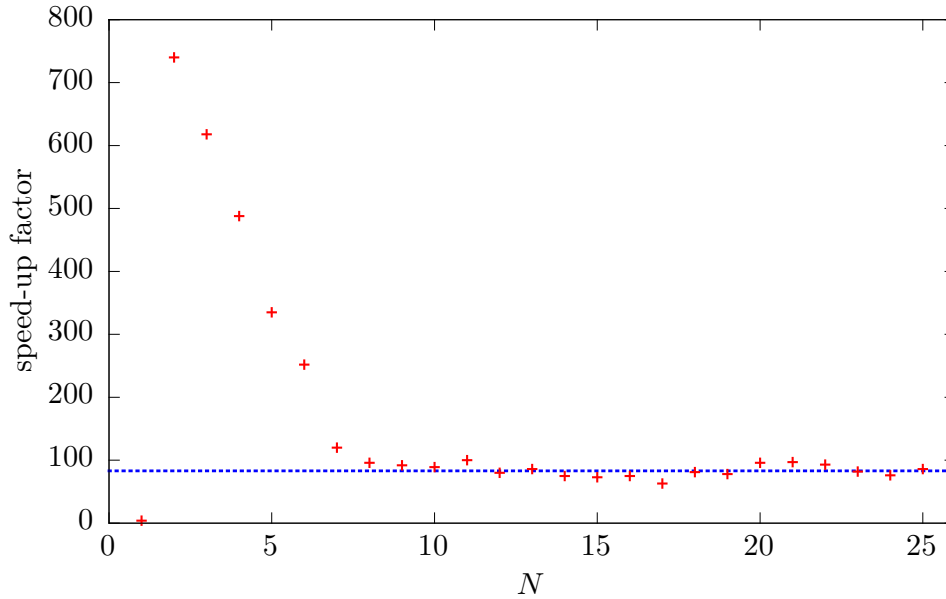


**Fig. 4.2:** Speedup of the HFFER II implementation compared to the previous implementation HFFER by Engel [54]. All calculations were made with high-field ground states of iron ions, gradually increasing the number of electrons  $N$ :  $\underline{0}_1, \dots, \underline{0}_{26}$ . The blue line represents the average speed-up factor of the whole series of calculations, which is  $\approx 83$ .

#### 4.4.2 Enhanced convergence

In Sec. 4.2 we presented a straightforward solution method to the Hartree-Fock-Roothaan (HFR) equations. There, we solved Eq. (4.1) independently and simultaneously for each electron, which is optimal with respect to parallelizability and program speed. However, this method is suboptimal with regard to convergence as we assume a fixed effective potential for each varied wave function, i.e. each electron's wave function is determined under the assumption that the other wave functions do not change during this iteration step. As we vary all wave functions simultaneously we violate this assumption, which can lead to a higher number of necessary iterations until convergence is reached. For some states and initial wave functions this algorithm may even fail to converge at all. States that are especially threatened by convergence failure typically include several weakly-bound orbitals with similar spatial extensions. The spatial proximity of these orbitals causes strong interactions between them, which may, in case of bad initial wave functions, frustrate the convergence to the Hartree-Fock equilibrium state.

If no convergence can be achieved even after a huge amount of iteration steps, we almost always found the algorithm to be trapped in a loop of periodically occurring single-particle wave functions. An example of such a two-step loop with three particles is given by the components a)-c) of Fig. 4.3: In the initial situation a) orbital  $\psi_2$  is driven outwards by the repulsion of electron 1, whereas orbital  $\psi_3$  is attracted due to the core potential. After the first iteration, the repulsion between the orbitals  $\psi_2$  and  $\psi_3$  dominates and both are driven into configuration c), which is similar to the

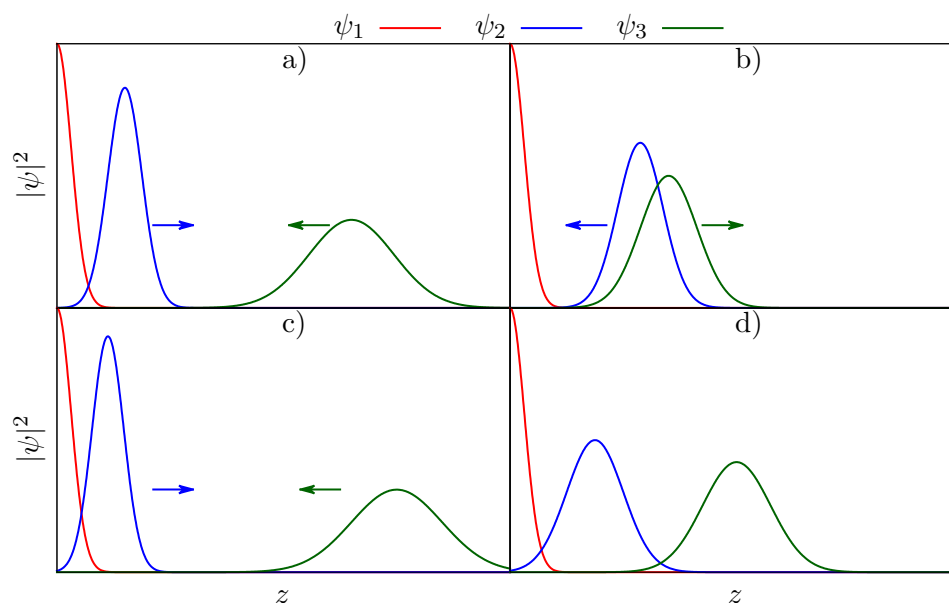


**Fig. 4.3:** Sub figures a)-c): Schematic illustration of non-converging orbitals during periodic Hartree-Fock iterations. The stable solution is depicted in sub-figure d).

initial situation. Eventually, a configuration loop has been created and the equilibrium configuration d) is never reached. We also found more complex loops with a larger number of interacting orbitals or more intermediate steps in each cycle. This is of course not a physical effect but a consequence of the applied Hartree-Fock algorithm.

To counteract infinite configuration loops we set a maximum number of 30 iteration steps in the HFFER II program. If no convergence was reached within these steps, we restart the iterations, but solve the equations in a round-robin<sup>1</sup> manner and update the electronic configuration after each single-electron wave function adaptation. Since each process has to wait for the previous ones to complete they cannot work fully in parallel, and a complete update of all wave functions takes more time than with our previous method. However, this step-by-step algorithm widely enhances our chances to succeed, and in this way convergence could be achieved for every configuration investigated up to date. The implementation of other methods to enhance the convergence probabilities in self-consistent field methods, as for example discussed in Ref. [97], did not prove necessary so far.

<sup>1</sup>Computations are not executed in parallel but one by one.



# 5 The full 2D Landau-Hartree-Fock-Roothaan method

The product ansatz (2.7) of the single-particle orbitals, which is used in the HFFER II program, leads to good results in the case of  $\beta_Z \gtrsim 1$ . The innermost orbitals, however, cannot be described satisfactorily even at these high field strengths, as we showed in Fig. 3.2. To circumvent this problem we make use of the full 2D Landau expansion (2.6) for the single-particle wave functions and assign a different longitudinal wave function  $P_n(z)$  to each Landau channel  $n$ . This expansion in terms of Landau states is complete for cylindrically symmetric wave functions. Hypothetically, we could expand the single-particle orbitals at any magnetic field strength, but as we know from Chap. 2, the Landau expansion converges slowly at low  $\beta$ . Still, as we will see in this chapter, this ansatz extends the range of accessible magnetic field strengths to  $\beta_Z \gtrsim 0.1$ .

## 5.1 2D Hartree-Fock-Roothaan equations

We proceed in the same way as in the last chapter and vary the energy functional with respect to the  $B$ -spline coefficients  $\alpha_{n\nu}^i$  of each electron  $i$ , but this time we obtain two-dimensional Hartree-Fock-Roothaan equations of the form

$$\sum_{n'\mu} F_{n\nu n'\mu}^i \alpha_{n'\mu}^i = \varepsilon_i \sum_{n'\mu} S_{n\nu n'\mu}^i \alpha_{n'\mu}^i. \quad (5.1)$$

$F_{n\nu n'\mu}^i$  and  $S_{n\nu n'\mu}^i$  are the Fock and overlap matrices, respectively. The Fock matrix is constructed from the sum of the longitudinal energy, transverse kinetic plus spin energy, the nuclear potential energy, as well as the direct and exchange electron-electron energy matrices, which read, in that order,

$$\text{long } F_{n\nu n'\mu}^i = -\delta_{n,n'} \int_{-\infty}^{\infty} B_\nu^i(z_i) \frac{\partial^2}{\partial z_i^2} B_\mu^i(z_i) dz_i, \quad (5.2)$$

$$\text{tran } F_{n\nu n'\mu}^i = 4\beta \left( n + m_s^i + \frac{1}{2} \right) \delta_{n,n'} \int_{-\infty}^{\infty} B_\nu^i(z_i) B_\mu^i(z_i) dz_i, \quad (5.3)$$

$$\text{nucl } F_{n\nu n'\mu}^i = \int_{-\infty}^{\infty} B_\nu^i(z_i) V_{m_i}^{nn'}(z_i) B_\mu^i(z_i) dz_i, \quad (5.4)$$

$$\text{dir } F_{nv'n'\mu}^i = \sum_{j=1}^N \frac{1}{\xi^j} \sum_{k,k'}^{N_{\text{int}}^j} \int_{-\infty}^{\infty} B_{\nu}^i(z_i) B_{\mu}^i(z_i) \int_{-\infty}^{\infty} P_k^j(z_j) U_{m_i m_j}^{nn'kk'}(z_i, z_j) P_{k'}^j(z_j) dz_j dz_i, \quad (5.5)$$

$$\text{ex } F_{nv'n'\mu}^i = - \sum_{j=1}^N \delta_{m_s^i, m_s^j} \frac{1}{\xi^j} \sum_{k,k'}^{N_{\text{int}}^j} \int_{-\infty}^{\infty} B_{\nu}^i(z_i) P_k^j(z_i) \int_{-\infty}^{\infty} B_{\mu}^i(z_j) A_{m_i m_j}^{nn'kk'}(z_i, z_j) P_{k'}^j(z_j) dz_j dz_i. \quad (5.6)$$

The Landau-averaged potentials  $V$ ,  $U$  and  $A$  used in the above formulae correspond to those in Eqs. (4.8), (4.11) and (4.12) of the previous section. The overlap matrix  $S$  is given by the expression

$$S_{nv'n'\mu}^i = \delta_{n,n'} \int_{-\infty}^{\infty} B_{\nu}^i(z_i) B_{\mu}^i(z_i) dz_i. \quad (5.7)$$

In Eqs. (5.5) and (5.6) we introduced the interaction cutoff parameters  $N_{\text{int}}^i$  and the renormalization factors  $\xi^j$ , which we explain in the following section.

## 5.2 Interaction cutoff and renormalization

Since we want to reach down into the intermediate regime of magnetic field strengths, we need to account for as many Landau channels as possible to achieve an accurate description of our single-particle wave functions. Therefore, we extended the database of precalculated effective potentials (see Appx. B) in such a way that we may include up to  $N_L + 1 = 31$  Landau channels in our calculations. This extension of the Landau basis comes with two natural drawbacks, both connected with the evaluation of the Fock matrices, especially of the electron interaction terms given in Eqs. (5.5) and (5.6). The number of these terms is roughly proportional to  $N^2 \cdot (N_L)^4$ , so a raise from  $N_L = 7 \rightarrow 30$  increases the calculation times by a factor of about 225. Even more problematic is the fact that the storage of all precalculated potentials  $U$  and  $A$  would require about 500 GB of RAM per processing unit - which is not available on any desktop computer. Thus, we cannot account for more than 8 Landau channels during the calculation of electronic interactions, which corresponds to a memory need of approximately 1.5 GB per processing unit. The alternative, namely the complete evaluation of the effective potentials at runtime, would be extremely slow, and must be ruled out.

### 5.2.1 Procedure

Since we still want to enhance our description of the orbitals we have to overcome these problems and therefore introduce the interaction cutoff parameters  $N_{\text{int}}^i$ . These correspond to the highest Landau channel of electron  $i$  that we account for during the evaluation of the interaction terms in Eqs. (5.5) and (5.6). This means that we evaluate

the kinetic and nuclear potential matrices using the maximum number of Landau channels  $N_L$ , whereas we drop Landau level interaction terms between electrons  $i$  and  $j$  in both Eqs. (5.5) and (5.6) if  $k, k' > N_{\text{int}}^j$  or  $n, n' > N_{\text{int}}^i$ . Due to this disparity between the single-particle and interaction terms we induce a new cutoff error in our energy functional, lower its minimum value and deprive it of its variational nature, since the repulsive electron-electron interactions are not fully taken into account anymore. This loss of repulsive energy contributions can partly be compensated for with the help of renormalization factors

$$\xi^j = \sum_{k=0}^{N_{\text{int}}^j} \int_{-\infty}^{\infty} |P_k^j(z)|^2 dz, \quad (5.8)$$

which boost the interaction terms of the lower Landau channels. We already introduced these factors in Eqs. (5.5) and (5.6). This simplification of the interaction terms is justified as long as the neglected Landau channels have small contributions to a wave function, i.e. while the corresponding renormalization factors are only marginally smaller than 1. We found renormalization factors of  $\xi < 0.95$  already to cause significant deviations in the total energy, which indicates an over-simplification of the corresponding interaction terms. The attentive reader will have recognized that we only renormalize the wave functions of the electrons  $j$ . We do not renormalize the lower Landau level contributions of the orbital  $i$  that is to be varied. If we also renormalized these terms a self-reinforcing process would start: The over-proportional repulsive terms caused by the renormalization of the lower Landau channels  $n \leq N_{\text{int}}$  and the missing repulsive terms for those with  $n > N_{\text{int}}$  cause a slight energetic advantage in favor of the upper Landau channels. Hence, their occupation increases, and with it the renormalization  $1/\xi$ . This results in nonphysically strong contributions of higher Landau channels to the wave function, which we have to avoid.

For the sake of simplicity we could set the new cutoff parameters to  $N_{\text{int}}^i = 7$  for every electron. However, the total computational effort is roughly proportional to  $\sum_{i,j}^N (N_{\text{int}}^i)^2 (N_{\text{int}}^j)^2$ , therefore we can reduce our program runtime significantly if we choose  $N_{\text{int}}^i$  individually for each electron and as low as possible without causing too large additional errors in our resulting wave functions and energies. Since we cannot afford to repeat every calculation in search of acceptable cutoff parameters we need to find a reliable automatic method to determine reasonable cutoff parameters for each orbital. With this need in mind we analyze the Landau level occupation vectors  $t_n^i$  of the wave functions obtained with the HFFER II method. These vectors are an indicator of the importance of higher Landau channel contributions to a set of single-particle orbitals. We define a threshold  $t_{\text{min}}$  and assume that we can safely ignore the interaction terms with those Landau channels, whose squared contributions are below this threshold. The cutoff parameter  $N_{\text{int}}^i$  then corresponds to the last included Landau channel with

$$\left(t_{N_{\text{int}}^i}^i\right)^2 \geq t_{\text{min}}. \quad (5.9)$$

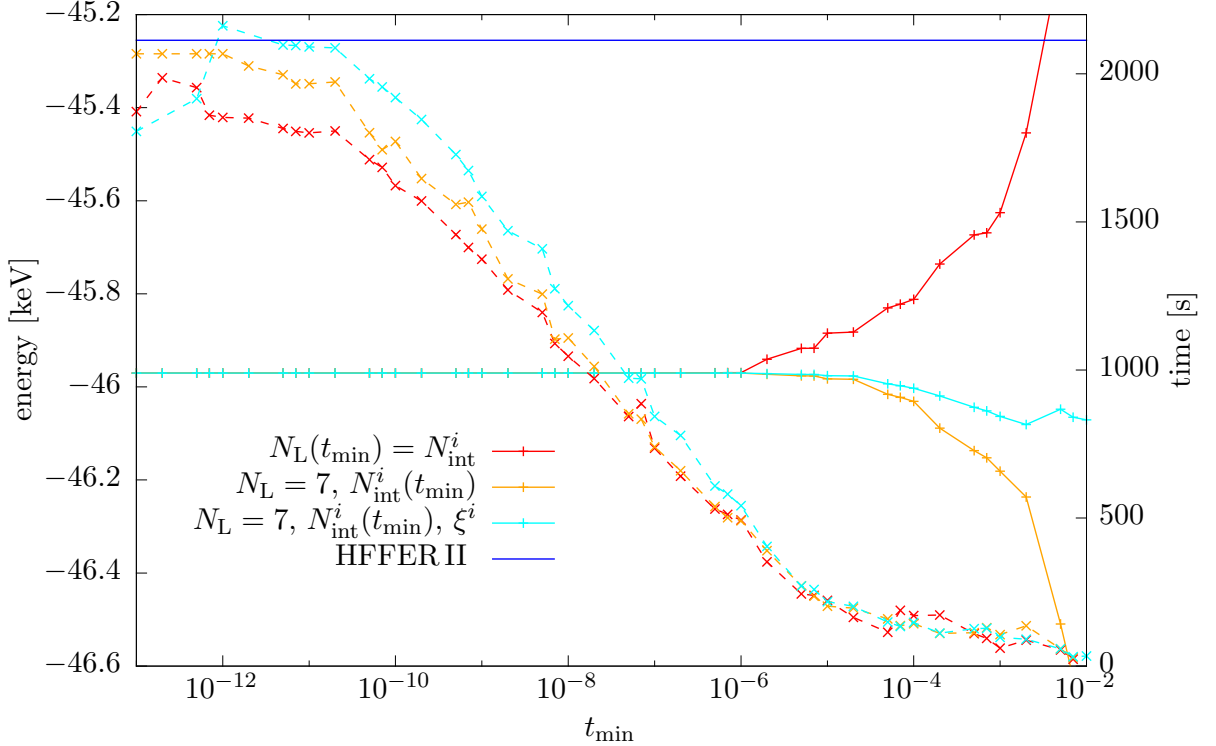


**Fig. 5.1:** Energies (solid) and calculation times (dashed) for the iron state  $0_{21}0^{11}2^13^10^2$  at  $B = 5 \times 10^7$  T in dependence of the minimal occupation threshold  $t_{\min}$ . The results were obtained using three different methods which are explained in the text. Energy results of the methods coincide up to  $t_{\min} \approx 10^{-6}$ . For comparison the energy result of the HFFER II program is also shown. Lines serve as a guide to the eye.

In order to get a qualitative understanding of this threshold and its importance for the variation of the energy functional we show in Fig. 5.1 energy values and calculation times resulting from different  $t_{\min}$ . Here we restricted the overall expansion size to  $N_L = 7$ . In this way we avoid an energy bias caused by neglected higher Landau channel interactions at  $t_{\min} = 0$ , as we correctly include all interactions in this limit. We compare three different approaches: Firstly, we reduce the single-orbital expansion numbers  $N_L$  separately for each electron according to formula (5.9) and set  $N_L = N_{\text{int}}^i$ . This method is still variational as it affects the single-particle and interaction terms in the same way. With increasing  $t_{\min}$  we expect this to result in lower quality wave functions and thus lesser binding energies. However, in Fig. 5.1 up to  $t_{\min} \approx 10^{-6}$  no significant impact on the energy values can be seen (solid red curve), although we already neglect a significant amount of Landau channels. This can be seen from the enormous reduction of calculation time to about 500 s (broken red curve). A detailed inspection of the occupation vectors yields that the outer electrons are well described without the contributions of higher Landau channels, but as soon as the inner electrons ( $m' \leq 5$ ) are affected by the cutoff at  $t_{\min} > 10^{-6}$  the total energy rises quickly.

In our second approach in Fig. 5.1 we reduce the electronic interactions using the cutoff parameters  $N_{\text{int}}^i$ , but keep the overall expansion of all electrons fixed at  $N_L = 7$ . We do not use renormalization factors  $\xi$  to demonstrate the effects of pure reduced interactions. As a result, the energy curve is more stable with respect to  $t_{\text{min}}$ , albeit the lost variationality feigns a vast increase of the binding energy at high  $t_{\text{min}}$ . Adding the renormalization factors  $\xi^i$  in the third approach we further enhance the stability of the energy function to variations of the cutoff parameters  $t_{\text{min}}$ , and partially compensate for the non-physical increase of the binding energy. In fact, with this approach the energies are quite stable up to  $t_{\text{min}} \approx 7 \times 10^{-4}$ . A reasonable choice for  $t_{\text{min}}$ , including a safety margin, could be  $10^{-6}$  in this calculation. For this value of  $t_{\text{min}}$  the calculation times are reduced by a factor of 4, with any of the three approaches.

### 5.2.2 Thorough error analysis

The energy functions presented in Fig. 5.1 were obtained using  $N_L = 7$ , and we were able to double check them in the limit  $t_{\text{min}} \rightarrow 0$ , which effectively included all interaction terms in the calculations. As soon as we extend the Landau expansion to  $N_L = 30$  we are forced to neglect the interaction contributions of Landau channels with  $n > 7$ . This introduces an error into our computations, whose size is hard to estimate as we cannot perform calculations with  $N_{\text{int}}^i \rightarrow 30$ , for the reasons mentioned before. Nonetheless, it is crucial to identify such regions of the state parameter space  $(B, Z, t_{\text{min}}, (m'_i, \nu'_i))$ , where these additional errors are negligible and such regions, where we cannot trust our results. Therefore, we need a second method that can evaluate all interactions correctly and does not rely on pre-calculated effective potentials.

The quantum Monte Carlo (QMC) method is ideally suited for this task. It is able to exactly evaluate the six-dimensional integrals of the electron-electron interactions within statistical error margins. Please note, that we do not want to enhance our results beyond the Hartree-Fock limit by applying a variational or diffusion QMC method, as was done in [45, 46, 89]. These methods work in full configuration space, whereas we stay in the Hartree-Fock approximation and only re-evaluate the approximated two-particle integrals. Therefore, we call the method “simple quantum Monte Carlo” (SQMC) to avoid confusion with the methods presented in other works. It suffices to say that the SQMC method allows us to correctly evaluate *all* two-particle interaction terms in the energy functional as it does not rely on precalculated potentials. Thus, if we feed this method with the wave functions which we obtained from the variation of a slightly modified energy functional we can compute the correct energies corresponding to these modified orbitals.

The relative energy differences  $\delta E$  between the 2DLHFR and the SQMC methods serve as a direct indicator for the applicability of the Landau cutoff and renormalization method. In the following survey, which includes mostly helium-like states, we consider 2DLHFR results with  $\delta E \lesssim 2\%$  to be sufficiently precise, as the lowest relative correlation energy error was found by Boblest [46] to be 3.5% for such states. We start our discussion with Fig. 5.2. There we show the energies of a helium state obtained with

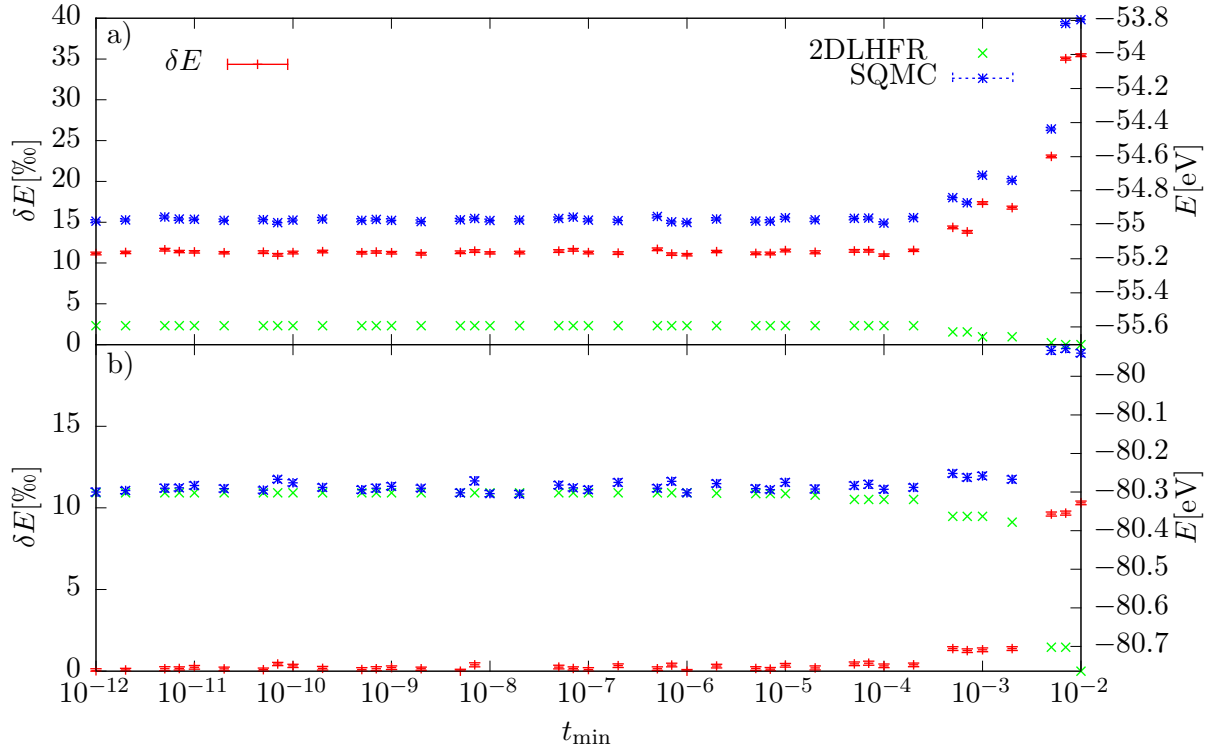


**Fig. 5.2:** Relative energy differences  $\delta E$  (left axis) between the 2DLHFR and SQMC results in dependence of the minimal occupation threshold  $t_{\min}$  for the helium state  $0^0 1$  at a)  $\beta_Z = 0.025$  and b)  $\beta_Z = 0.2$ . The energy results of both methods are also shown (right axis).

the 2DLHFR method using different minimal occupation thresholds, the corresponding SQMC corrected energies and their relative difference  $\delta E$ . Note that the SQMC and  $\delta E$  error bars are caused by the statistical uncertainty of the SQMC method.

In panel a) we chose a very low magnetic field strength of  $\beta_Z = 0.025$ . As a result, we find large contributions of higher Landau channels that are not accounted for in the electronic interaction terms of the 2DLHFR method and even at  $t_{\min} = 10^{-12}$  the 2DLHFR results are about 11% below their true value found by the SQMC method. These deviations are clearly above the desired maximum of 2% and we conclude to have overstretched our ansatz. The deviations become even larger for  $t_{\min} \gtrsim 10^{-4}$  as further important interaction terms are disregarded and the 2DLHFR and SQMC energy values drift apart. In panel b) we kept the electronic configuration but changed the magnetic field strength to  $\beta_Z = 0.2$ . Here, the overall impression is much better: Up to  $t_{\min} = 10^{-4}$  the 2DLHFR and SQMC results agree within the error bars of the SQMC method, and our ansatz works as intended.

The data in Fig. 5.2 show that the magnetic field strength has, as expected, a large influence on the quality of the 2DLHFR results. As this influence may also depend on the electronic configuration, we investigate in Fig. 5.3 states of different symmetry subspaces and keep the magnetic field strength fixed at  $\beta_Z = 0.1$ . In this and subsequent figures

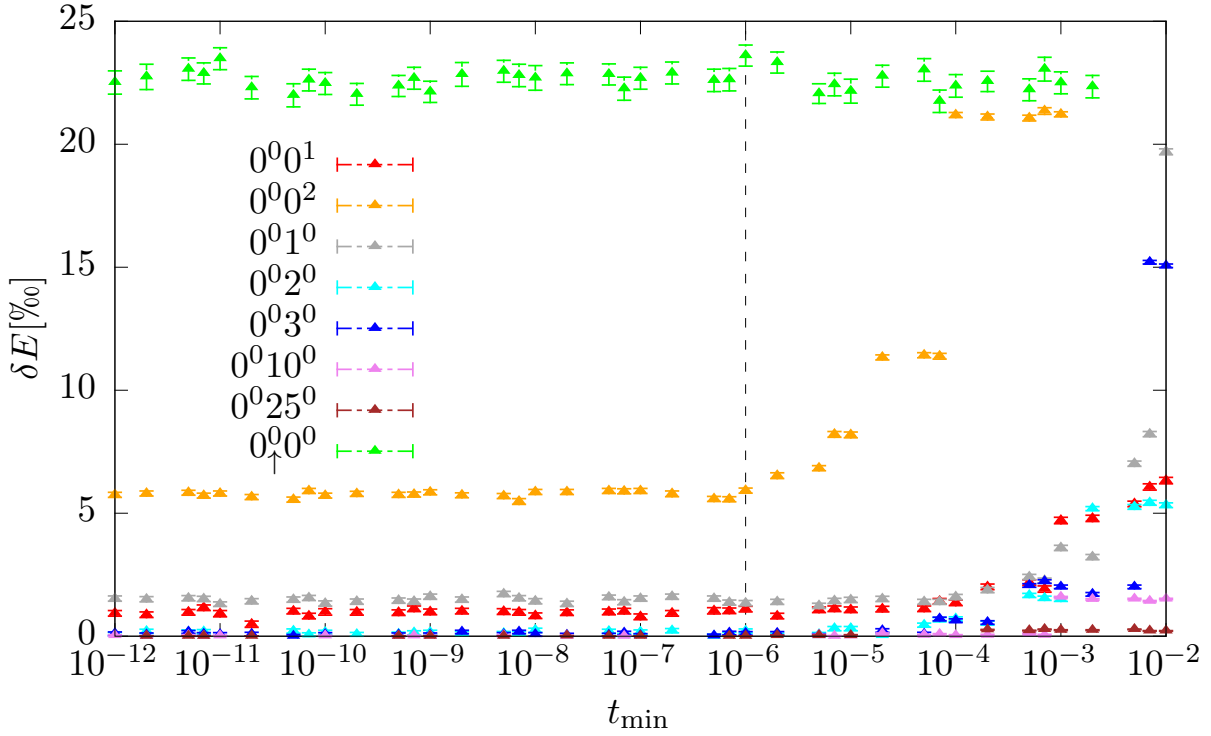


**Fig. 5.3:** Relative energy differences  $\delta E$  between 2DLHFR and SQMC results in dependence of  $t_{\min}$  for different helium states at  $\beta_Z = 0.1$ .

we do not show the energy values of both methods but only their relative difference  $\delta E$ , since the qualitative behavior of both energy functions in dependence on  $t_{\min}$  is identical to those in Fig. 5.2. The worst results, i.e. the largest differences between the 2DLHFR and SQMC energies, correspond to the states  $0^0_↑ 0^0$  and  $0^0 0^2$  with energy differences of approximately 22‰ and 6‰, respectively. This is no surprise, as both states feature two  $m = 0$  orbitals with positive  $z$ -parity: orbitals that are known (see Sec. 2.2.3) to converge slowly within the Landau expansion and thus have large contributions of higher Landau channels. Additionally, in the case of the  $0^0_↑ 0^0$  state, both orbitals are confined to a similar spatial region and thus have strong interactions. The energy differences of the other states given in Fig. 5.3 are remarkably small ( $\delta E < 2‰$ ) and thus tolerable. This figure also shows that we can safely choose  $t_{\min} = 10^{-6}$  without introducing additional errors to any state, as is indicated by the broken line.

Now that we know that the states  $0^0_↑ 0^0$  and  $0^0 0^2$  challenge the Landau cutoff method most, we investigate the accuracy of the results for these states in dependence of the magnetic field strength. Figure 5.4 shows, only for these two states, the relative energy differences  $\delta E$  at several  $\beta$ . In panel a) we show the results for state  $0^0_↑ 0^0$ . There we see that energy deviations smaller than 2‰ are only reached for  $\beta_Z \geq 1$ . By contrast, the results of state  $0^0 0^2$ , shown in panel b), are sufficiently good for  $\beta_Z \geq 0.2$ . For both states we find that no significant additional errors are induced in the energy functional in the 2DLHFR method for the choice  $t_{\min} = 10^{-6}$ , as is indicated by the broken lines.

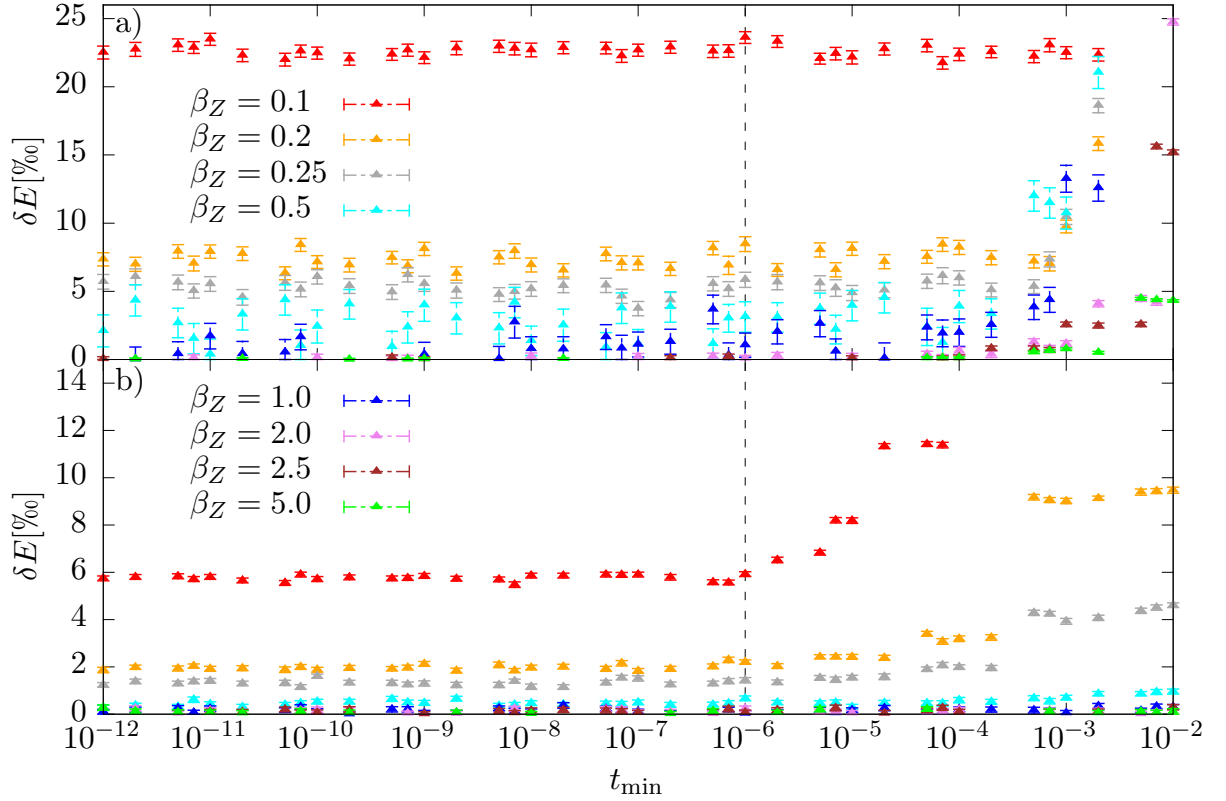


**Fig. 5.4:** Relative energy differences between 2DLHFR and SQMC results in dependence of  $t_{\min}$  for the challenging helium states a)  $0^0_0^0$  and b)  $0^0_0^2$  at several magnetic field strengths. Field strength labels apply in both panels.

In Fig. 5.5 we investigate the magnetic field strength dependence of those states that proved to be less challenging to our method during the analysis of Fig. 5.3. This includes the high-field ground state  $0^0_1^0$  and several single-particle excited states. We find that states with larger spatial separation of the single-particle wave functions, i.e. considerably different  $m'_i$ , lead to very small 2DLHFR energy errors, even at magnetic field strengths as low as  $\beta_Z = 0.025$ . For any state shown, the 2DLHFR interaction cutoff errors are below 2‰ and thus tolerable if  $\beta_Z \geq 0.1$  and  $t_{\min} \leq 5 \times 10^{-5}$ .

We summarize the results for the  $(Z = 2, N = 2)$ -slice of the parameter space: For almost all states and magnetic fields  $\beta_Z \geq 0.1$  our method of reduced electronic interactions leads to negligible energy errors if we keep  $t_{\min} \leq 10^{-6}$ . Only one state is restricted to substantially higher field strengths of  $\beta_Z \geq 1$ , although we would like to point out that even in this case the obtained wave functions were found to be precise enough to serve as guiding functions for the fixed-phase diffusion quantum Monte Carlo implementation of Meyer [45] and Boblest [46].

To complete this analysis we will now investigate the accuracy of the results for a larger number of electrons and thus higher core charges. A larger number of bound electrons obviously increases the complexity of the corresponding atomic problem. Therefore,



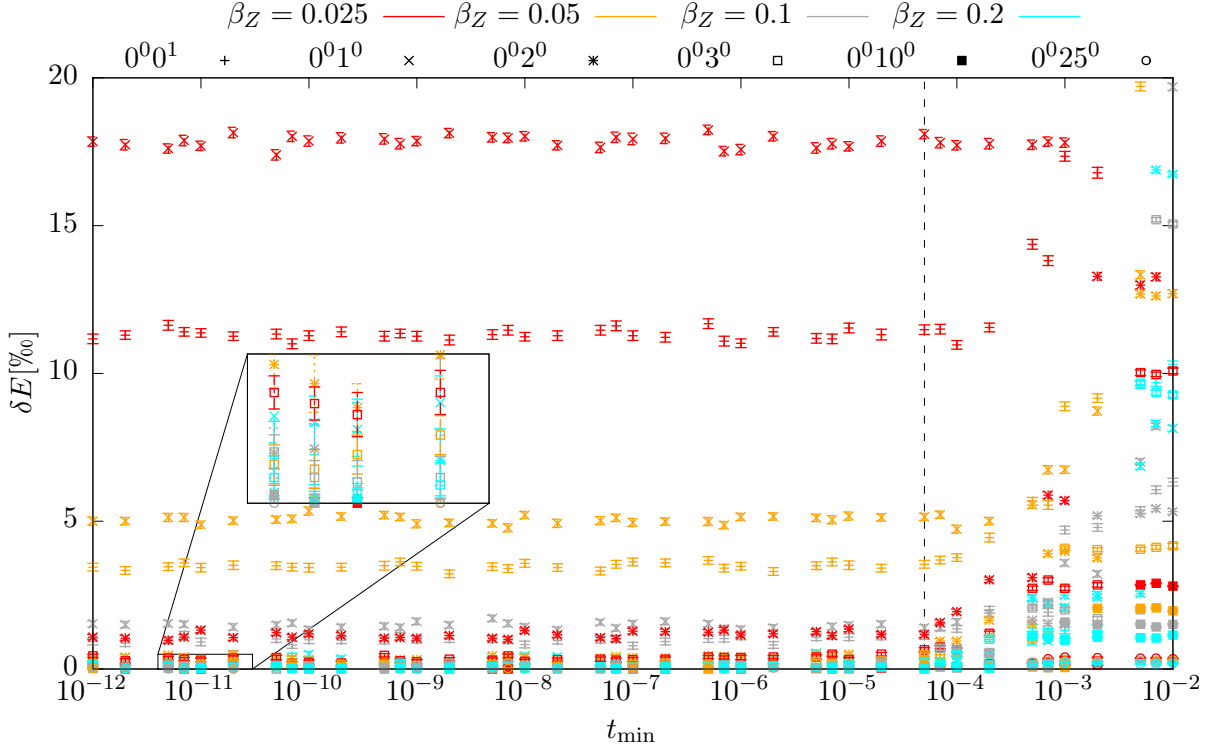


**Fig. 5.5:** Relative energy differences between 2DLHFR and SQMC results in dependence of  $t_{\min}$  of several less challenging helium states (denoted by symbols) for different magnetic field strengths (denoted by colors).

we restrict ourselves to the analysis of the most complex system of core charge  $Z$ , i.e. the non-ionized ones  $Z = N$ . Hydrogen and other elements are known to form several truly bound negative ionic states ( $N > Z$ ) in the presence of a magnetic field (see, e.g. Refs. [98–100]). We do not consider such states here, as negative ions are unlikely to contribute to the atmospheres of NSs or MWDs due to the high effective temperatures on the surface or atmosphere of these objects. In order to simplify the comparison between different atomic systems we will use the high-field ground state electronic configuration  $\underline{0}_Z$  for all calculations. Results for the relative energy errors for  $Z = (2 \dots 10, 26)$  are shown in Fig. 5.6, where each atomic number corresponds to a different color. One can see, that the relative errors  $\delta E$  are reduced with increasing  $Z$ . This effect is caused by two components: On the one hand, if we increase the atomic number,  $Z \rightarrow Z + 1$  and  $N \rightarrow N + 1$ , the additional electron occupies the lowest available tightly-bound orbital ( $m = -Z$ )<sup>0</sup>, which can be described increasingly well by our Landau expansion. Thus, the energy contributions by this additional electron are less susceptible to the expansion cutoff errors. Consequently, the relative amount of energy contributions contaminated by cutoff errors falls with increasing  $Z$ . Secondly, we have observed that additional electrons also reduce the higher Landau channel contributions of the *inner* electrons and we found that their renormalization factors  $\xi^i$  are slightly raised towards unity with

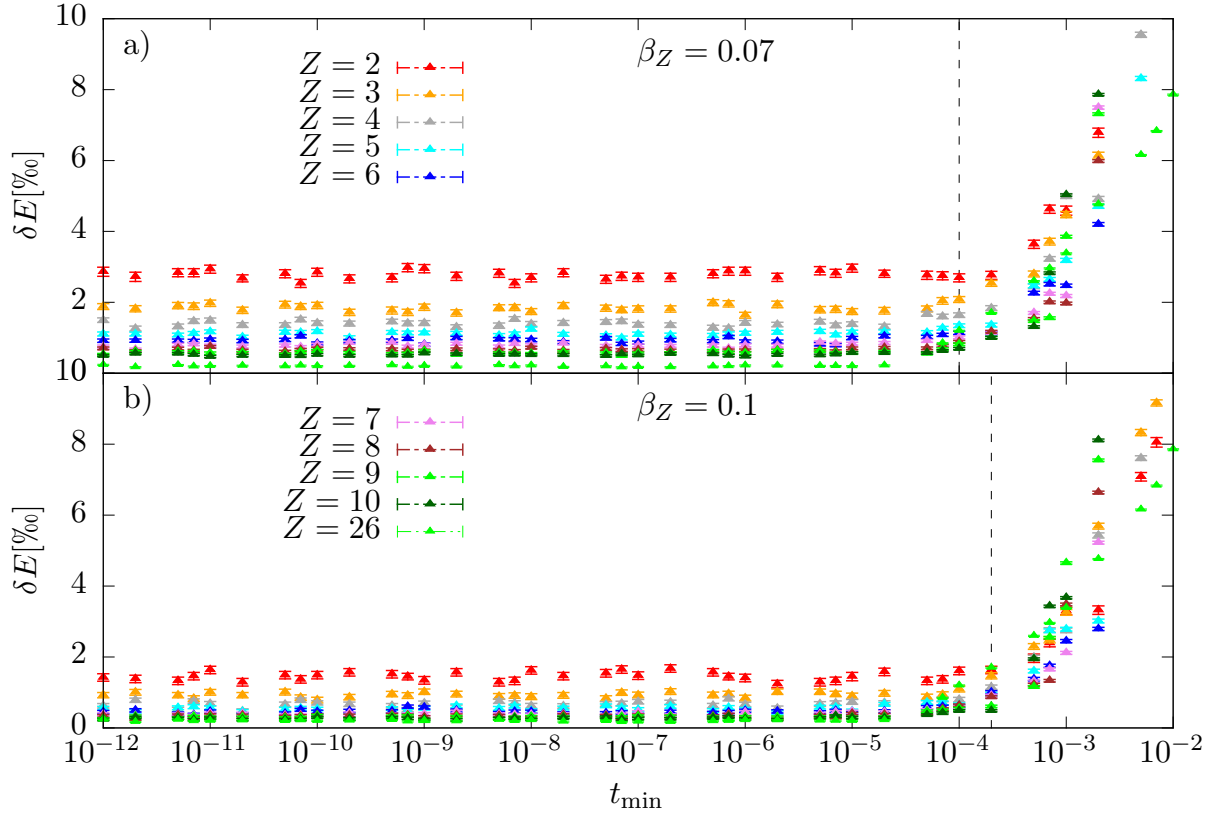


**Fig. 5.6:** Relative energy differences between 2DLHFR and SQMC results in dependence of  $t_{\min}$  for different atoms denoted by their atomic number. The magnetic field strengths were chosen in all calculations such that  $\beta_Z = 0.07$  in a) and  $\beta_Z = 0.1$  in b), respectively. Labels correspond to both subimages.

an increasing number of electrons. We have no definite explanation for this phenomenon but suggest that the larger transverse extension of wave functions associated with higher Landau channels causes a larger overlap with electrons that have higher  $m'$ . Thus the repulsive terms corresponding to higher Landau channels slightly increase with rising  $N$ .

Figure 5.6 a) corresponds to  $\beta_Z = 0.07$ , and one finds that for  $Z = 2$  the relative energy errors are above 2%. Therefore, we consider this magnetic field strength just slightly too low to produce results of sufficient accuracy for all  $Z$ . At  $\beta_Z = 0.1$  in Fig. 5.6 b) all relative energy errors caused by the reduced interactions are below 2% and we find the 2DLHFR method to be sufficiently precise at these magnetic field strengths. The behavior of the functions  $\delta E(t_{\min})$  is almost independent of the system investigated, and we find the reasonable values for  $t_{\min} \approx 10^{-4}$  at  $\beta_Z = 0.07$  and  $t_{\min} \approx 2 \times 10^{-4}$  at  $\beta_Z = 0.1$ , respectively.

With this last study we conclude our extensive error analysis and summarize the results. We have inspected 8 electronic configurations of helium at 20 magnetic field strengths using 44 values for the minimal Landau occupation threshold  $t_{\min}$ . Additionally, we have checked the neutral atoms with  $Z = (2 \dots 10, 26)$ , each at 10 different field

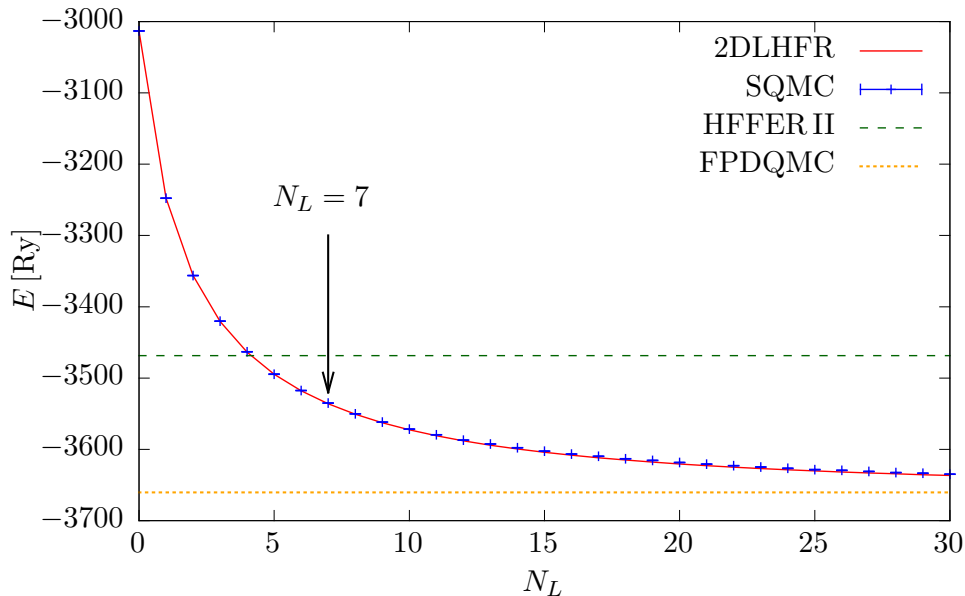


**Fig. 5.7:** Results for the iron ground state  $0_{19}0_{\uparrow}^00^11^12^13^14^10^2$  energy at  $\beta_Z \approx 0.157$  ( $B = 5 \times 10^7$  T) in dependence of the maximum Landau channel number  $N_L$  (2DLHFR). Also shown: The SQMC corrections to the energies, the highly precise FPDQMC result as well as the HFFER II energy. Lines serve as a guide to the eye.

strengths and also 44 values of  $t_{\min}$ , amounting to more than 10,000 2DLHFR calculations. Each result was re-evaluated with the SQMC method. We found that the choice  $t_{\min} = 10^{-6}$  causes only very small additional errors in the total energies for any state, regardless of its atomic number, electronic configuration, or corresponding magnetic field strength, but significantly improves the speed of the calculations. We also found lower limits of  $\beta$  for the applicability of the Landau expansion and interaction cutoff method. These limits slightly depend on the electronic configuration: Only a few states at low  $Z$  are restricted to  $\beta_Z > 0.2$ , or, in one case, to  $\beta_Z \geq 1$ , whereas in all other cases the interaction cutoff energy errors are negligible if  $\beta_Z \geq 0.1$ . For even lower values of  $\beta$  the 2DLHFR method gradually loses precision due to the increasing cutoff errors. Since the Landau expansion also fails to converge with reasonable precision in this range of  $\beta$ , the additional cutoff errors are of no relevance.

Beyond the abstract analyses, Fig. 5.7 shows the energy values of the iron ground state at  $\beta_Z \approx 0.157$  obtained with the 2DLHFR method at different Landau expansion sizes  $N_L$ . One can clearly see that the SQMC corrections stay very small at any  $N_L$ , while the total energy converges to a value only 0.65% above the highly accurate FPDQMC value. Compared with the HFFER II method we have reduced the remaining error in comparison with the highly precise FPDQMC result by a factor of 8 at  $N_L = 30$ . If we restricted the program to the fully variational algorithm and thus to  $N_L = 7$ , we would have reduced the error only by a factor of 1.5, as is indicated by the arrow. This impressively demonstrates the power of the 2DLHFR method and justifies our

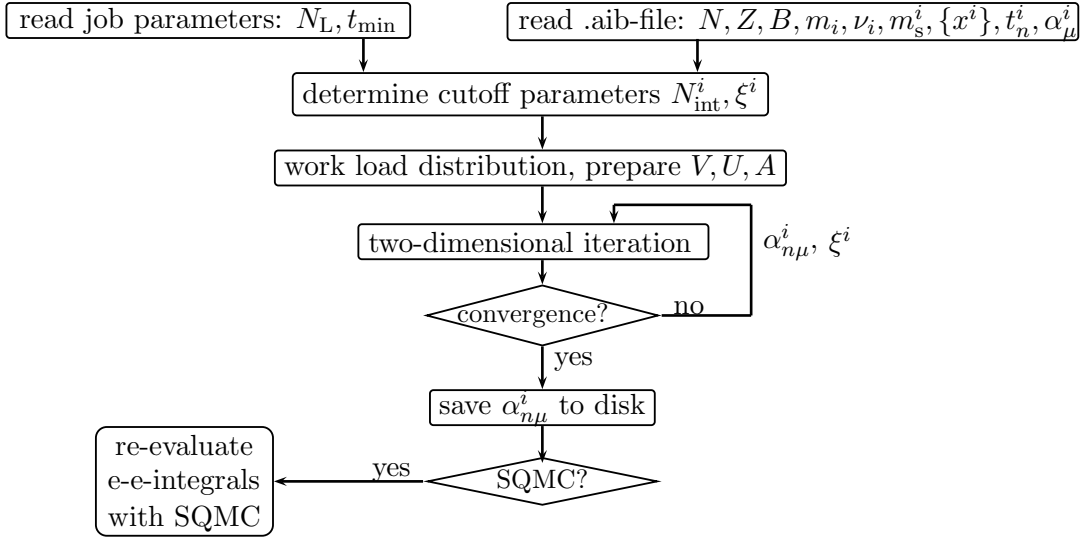


Fig. 5.8: Scheme of the 2DLHFR program and its course of action.

approximations.

### 5.3 The 2DLHFR program

We have discussed all important aspects of the 2D Landau-Hartree-Fock-Roothaan method and will now explain the course of the 2DLHFR-program. A sketch of the most important components is given in Fig. 5.8. We start with the result of HFFER II calculations, which are read from a file in *.aib* format. All necessary parameters are specified in this file, namely the ion  $(Z, N)$ , the magnetic field strength  $B$ , and the single-electron quantum numbers  $m'_i, \nu'_i, m_s^i$ . We adopt the individual  $B$ -spline bases  $\{x^i\}$  that were optimized by the HFFER II program and use the HFFER II wave function results, namely the  $B$ -spline coefficients  $\alpha_\mu^i$  and Landau weights  $t_n^i$ , as initial wave functions for the 2DLHFR method. Additional simulation parameters, e.g.  $N_L$  or  $t_{\min}$ , may be specified in a parameter list that is read from a separate simulation control file. By default, and for all calculations performed in Chap. 6, we use  $N_L = 30$  and  $t_{\min} = 10^{-6}$ .

Before the actual calculations start we analyze the Landau occupation vectors  $t_n^i$  and compare them to the minimal Landau threshold  $t_{\min}$  to set the cutoff parameters  $N_{\text{int}}^i$  and the renormalization factors  $\xi^i$ . The 2DLHFR program is designed to work efficiently with any number of available processors. We achieve this with the help of a workload distribution scheme, which is described in the following section. As soon as each process is informed of its share of work it can load and ready the required effective potentials  $V, U$ , and  $A$  (see also Appx. B). Although this seems to be a lot of overhead, these initialization steps typically take less than one second.

The main part of the 2DLHFR program executes the Hartree-Fock iterations by con-

structuring and solving the generalized eigenvalue problem given in Eq. (5.1) until final convergence is achieved. Typically, it takes 5 to 10 iterations until the total energy difference between the iteration steps drops below our convergence threshold of  $10^{-3}$  eV. If ever no convergence was achieved after 30 steps we switch to the round-robin iteration mode that we introduced for the HFFER II method in Sec. 4.4.2. This ensures a proper convergence behavior. After convergence is reached we write all important data to disk using the special file format *.aclb*. If explicitly demanded, the program may re-evaluate the electronic interaction energies using the SQMC method mentioned above.

### 5.3.1 Workload distribution

The individual  $B$ -spline bases method uses a distinct number of  $B$ -splines to describe each orbital. On the other hand, the interaction cutoff procedure determines for each orbital a distinct number of Landau channels to be included in the calculation of interaction terms. The combination of these two methods causes a reduction of the total amount of calculations that have to be completed during the Hartree-Fock-Roothaan iterations. However, the amount of calculations may strongly vary for different electrons. This fact renders simple work distribution schemes between the processing units, e.g. where each process handles the same number of electrons, inefficient. In our advanced distribution scheme we use a very fine subdivision for the calculation of the interaction matrices, given in Eqs. (5.5) and (5.6), by dividing them into  $(N_{\text{int}}^i + 1) \times (N_{\text{int}}^i + 1)$  sub-matrices. Additionally, we split the sums over  $j$ ,  $k$  and  $k'$  in these sub-matrices to obtain small-sized workload units. We count the number of operations that is needed to build up each split sub-matrix and finally distribute the workload units as evenly as possible among the available processors. As a consequence, each process may contribute to the calculation of several electrons' interaction matrices. Each electron is assigned to a master process which gathers the interaction matrix segments calculated by other processes including itself. Thanks to the MPI standard, the corresponding amount of inter-processor communication can be handled very efficiently and has a negligible share in the total program runtime.

To measure the efficiency  $\eta_p$  of our new parallelization scheme we use the relation

$$\eta_p = \frac{1}{\max(\tau_p)} \frac{1}{p_{\max}} \sum_{p=1}^{p_{\max}} \tau_p, \quad (5.10)$$

where we sum up the individual integration times  $\tau_p$  of each process  $p$  and average over the  $p_{\max}$  processes in total. Then, we divide this average by the integration time of the slowest process, as the other processes have to wait for this one to complete. In this sense maximum parallelization efficiency corresponds to equal integration times on all processing units. We stress that in this way we reached an extraordinary high average parallelization efficiency of  $\eta_p \approx 90\%$ . This value is, within reasonable bounds, almost independent of the ratio of electrons to available processors.

## 5.4 Transitions

The 2DLHFR program can obtain, with high precision, energies and wave functions of many-particle states. Thus we have everything at hand to calculate transition strengths and energies with unprecedented precision. We use the same approach as in Sec. 4.3, but have to account for the different longitudinal wave functions associated with the Landau channels. Therefore, the overlap integral expressions become

$$\langle \psi_a^f | \psi_b^i \rangle = \delta_{m_a, m_b} \delta_{\pi_z^a, \pi_z^b} \delta_{m_s^a, m_s^b} 2 \sum_{n=0}^{N_L} \int_0^\infty P_n^a(z) P_n^b(z) dz, \quad (5.11)$$

and the dipole expressions transform into

$$\langle \psi_a^f | r^0 | \psi_b^i \rangle = \delta_{m_a, m_b} \delta_{-\pi_z^a, \pi_z^b} \delta_{m_s^a, m_s^b} 2 \sum_{n=0}^{N_L} \int_0^\infty P_n^a(z) z P_n^b(z) dz, \quad (5.12)$$

$$\begin{aligned} \langle \psi_a^f | r^{+1} | \psi_b^i \rangle &= -\delta_{m_a, (m_b+1)} \delta_{\pi_z^a, \pi_z^b} \delta_{m_s^a, m_s^b} \sqrt{\frac{2}{\beta}} \times \\ &\sum_{n=0}^{N_L} \left[ \sqrt{n+1} \int_0^\infty P_{(n+1)}^a(z) P_n^b(z) dz + \sqrt{n-m_b} \int_0^\infty P_n^a(z) z P_n^b(z) dz \right], \end{aligned} \quad (5.13)$$

$$\begin{aligned} \langle \psi_a^f | r^{-1} | \psi_b^i \rangle &= \delta_{m_a, (m_b-1)} \delta_{\pi_z^a, \pi_z^b} \delta_{m_s^a, m_s^b} \sqrt{\frac{2}{\beta}} \times \\ &\sum_{n=0}^{N_L} \left[ \sqrt{n} \int_0^\infty P_{(n-1)}^a(z) P_n^b(z) dz + \sqrt{n-m_b+1} \int_0^\infty P_n^a(z) z P_n^b(z) dz \right]. \end{aligned} \quad (5.14)$$

Again, we wrote a small program that calculates oscillator strengths, dipole strengths, and transition energies between states that are specified in files of the *.aclb* format.

We close this chapter with a final remark about our programs: So far, *every* atomic problem posed to the 2DLHFR program converged without human intervention. The high degrees of automation and reliability of both the HFFER II and 2DLHFR programs, in union with their outstanding computational efficiency, make this program combination unique in this area of research. In the following chapter, we will prove that these programs do also excel with respect to result precision.

# 6 Results

In this chapter we compare the results of the HFFER II and 2DLHFR programs to those of a number of other methods. This includes the comparison of energy values as well as transition strengths and energies in Secs. 6.2 and 6.3, respectively. Subsequently, in Sec. 6.4, we investigate the ground state configurations of atoms and ions up to  $Z = 21$  at all magnetic field strengths accessible to our programs.

## 6.1 Other methods in the literature

So far we have only double-checked our results for consistency and used the SQMC routine to find suitable parameters for the reduced electronic interaction method. However, none of our results have been compared to those of other methods, yet. In this section we give a short overview of the methods recently applied in the literature.

The fixed-phase diffusion quantum Monte Carlo (FPDQMC) method was developed by Ortiz et al. [101] and first applied to the study of atoms in magnetic fields by Jones [102]. Starting from an approximate solution of the many-particle Schrödinger equation, called the *trial function*, this method finds an improved estimate for the binding energy by damping contributions of excited eigenfunctions of the Hamiltonian by means of an imaginary time evolution. Therefore, FPDQMC can only find the ground state energy in a given symmetry subspace. This method still contains an approximation as it cannot improve the phase of the trial function. It is thus of high importance that the trial function is similar to the true ground state solution, otherwise this fixed-phase approximation will lead to considerable errors.

Bücheler et al. [44, 89] adopted this approach and worked with trial wave functions of the adiabatic Landau type (2.8), while Meyer [45] and Boblest [46] proceeded to the employment of the advanced Landau trial wave functions specified in the *.aib* or *.aclb* file formats. All FPDQMC results presented in this work are taken from Boblest [46]. In Ref. [30] Jones et al. employed a released-phase correlation function quantum Monte Carlo method, which was originally presented by Ceperley et al. [103], to calculate ground and excited state energies by means of Monte Carlo methods. Recently, Meyer et al. [95] presented a fixed-phase variant of this approach for helium at magnetic field strengths  $\beta_Z \leq 10$ . Due to the intense cooperation with both Sebastian Boblest and Dirk Meyer at this institute, we will present extensive comparisons with their methods. Parts of these comparisons can also be found in Refs. [46, 104, 105].

The Hartree-Fock method is one of the most popular techniques to solve many-particle systems in quantum mechanics. Therefore, several implementations of the unrestricted

Hartree-Fock method for atoms in strong magnetic fields have been created. The crucial criterion for the quality of these implementations is, similar to hydrogen-like systems, the representation of the single-particle wave function. Ivanov et al. [32] used non-uniform 2D grids to describe the orbitals. They investigated several atomic and ionic systems from helium to neon [90, 106–108] and published the corresponding ground state energies over a wide range of the magnetic field strength. Jones et al. [31, 88, 109] focused on the light elements up to carbon and used several different single-particle expansions. They employed either spherical, Landau-type or Slater-type orbitals in order to adapt the expansion to the magnetic field strength dependent shape of the wave function. Thirumalai et al. [38] in turn described the atomic orbitals with the help of a grid-based finite element method and an increased mesh refinement algorithm. This method seems to be quite accurate, albeit very slow. So far they only published results for hydrogen and helium. Mori and Hailey [42] presented a multiconfigurational perturbative, hybrid, Hartree, Hartree-Fock method, which also uses a Landau expansion for the wave function. They solved the Hartree equations for the lowest Landau channel only and considered both, the contributions of higher Landau channels as well as the exchange terms of the Hartree-Fock potentials by means of perturbation theory. This method is not entirely self-consistent and therefore not variational. Additionally, due to the Landau single-particle expansion, it is restricted to  $\beta_Z > 2$ . This group is the only one who also investigated heavier elements up to iron.

The configuration interaction (CI) method is a variational approach that is capable of accounting for those electronic correlations that are neglected in Hartree-Fock calculations. The CI approach combines different many-particle configurations, represented by Slater determinants and preferably of the same symmetry subspace  $\{M, \Pi_z, S_z\}$ , to describe the many-particle wave function. This method can converge to the correct solutions in the limit of an infinite number of configurations included [110] if the single-particle basis set is complete. This advantage comes at the cost of much higher computational effort, which is why CI has only been applied to light elements in strong magnetic fields, so far. Becken [85] used generalized Gaussian-type orbitals to form a single-particle basis and applied a full CI approach. In a series of papers Becken et al. [26–29] investigated helium states and transitions from very low to very strong magnetic fields. With a similar approach Al-Hujaj et al. also presented results for helium [34] and the negative hydrogen ion [99] and then progressed to lithium [40] and beryllium [41]. Wang et al. used a different basis set for the single-particle expansion, namely the Hylleraas-Gaussian basis functions [36], and applied this to the calculation of helium [36, 37] and lithium [111]. Within the frozen core approximation they also investigated lithium [39] and beryllium [112].

## 6.2 Energy values

We start the comparisons with helium, as for this element the most extensive calculations can be found in the literature. In Tabs. 6.1 and 6.2 we compare our energy values for



**Tab. 6.1:** Binding energies in Rydberg units of the helium state  $0^0 1^0 \Leftrightarrow \{1,+,1,1\}$  at different magnetic field strengths calculated with the HFFER II and 2DLHFR methods, compared to results of Boblest [46], Jones et al. [31] and Thirumalai et al. [38]. Numbers in brackets denote the uncertainties in the last digit(s).

$\beta_Z$	HFFER II	2DLHFR	Ref. [46]	Ref. [31]	Ref. [38]
0.1	5.049	5.544	5.6667(3)	5.6602	5.6756
0.2	6.173	6.549	6.6145(2)	6.6032	6.6340(1)
0.5	8.268	8.572	8.6101(1)	8.5960	8.6200(9)
0.7	9.273	9.564	9.5980(1)	9.5822	9.6116(6)
1	10.504	10.784	10.8171(1)	10.8000	10.810(2)
2	13.455	13.722	13.7545(1)	13.7332	13.754(3)
5	18.716	18.969	19.0091(1)	18.9764	19.00(2)
7	21.109	21.357	21.4026(2)	21.3632	21.39(3)
10	23.956	24.197	24.2494(2)	24.2022	24.22(4)
20	30.307	30.736	30.8073(2)	30.7380	—
50	41.438	41.777	41.8902(4)	41.7752	—
70	46.310	46.620	46.7514(5)	46.6132	—
100	51.985	52.265	52.4221(6)	52.2528	—

the helium states  $0_2$  and  $0^0 2^0$  to the results of the 2D Hartree-Fock methods of Jones et al. [31] and Thirumalai et al. [38] as well as to the FPDQMC results of Boblest [46]. We also give our HFFER II results. In comparison with the latter, the improved accuracy of the 2DLHFR results is striking, especially at lower field strengths. There we are able to improve the energy values by up to 9% in the first table. However, at  $\beta_Z = 0.1$  the difference between the 2DLHFR method and the very precise results of Ref. [38] is still about 2%. This changes with increasing field strength. At  $\beta_Z = 10$  the difference between our results and those of Ref. [38] has molten off to 0.1%. With rising  $\beta_Z$  the precision of their results drops, as can be seen from the reduced number of significant digits at  $\beta_Z \geq 5$ . At  $\beta_Z = 50$  we finally outmatch the results of Ref. [31] which are almost as precise as those of Ref. [38], but over a wider span of field strengths. These conclusions hold qualitatively also for Tab. 6.2. There, 2DLHFR outmatches the other Hartree-Fock methods for  $\beta_Z \geq 10$ .

It is, of course, impossible for us to surpass the FPDQMC method in precision, since it uses the 2DLHFR results and improves them. However, the FPDQMC method is inappropriate for the large scale production of results due to its immense computational demands (a factor of about  $10^4$  compared to the 2DLHFR method) and is mainly useful for error estimates. The relative energy difference between both methods reveals the size of the errors stemming from our Landau and finite element expansions as well as the neglected correlations of the Hartree-Fock ansatz. At low  $\beta$  the relative difference to the FPDQMC results is about 2%, mostly due to expansion errors. This difference drops to about 0.3%, which we estimate to be the correlation error, at  $\beta_Z \geq 1$ .

**Tab. 6.2:** Same as in Tab. 6.1 for the helium state  $0^0 2^0 \Leftrightarrow \{2,+,1,1\}$ .

$\beta_Z$	HFFER II	2DLHFR	Ref. [46]	Ref. [31]	Ref. [38]
0.1	4.763	5.245	5.3783(4)	5.3742	5.404(6)
0.2	5.781	6.140	6.2091(3)	6.2010	6.239(3)
0.5	7.667	7.953	7.9908(1)	7.9780	8.00(3)
0.7	8.577	8.849	8.8839(1)	8.8684	8.90(4)
1	9.696	9.957	9.9910(1)	9.9732	9.99(4)
2	12.394	12.642	12.6765(1)	12.6536	12.67(4)
5	17.234	17.469	17.5133(1)	17.4770	17.50(5)
7	19.445	19.674	19.7241(2)	19.6812	19.71(7)
10	22.079	22.302	22.3597(2)	22.3080	22.3(2)
20	27.951	28.406	28.4480(2)	28.3750	—
50	38.330	38.683	38.7795(4)	38.6572	—
70	42.882	43.202	43.3222(5)	43.1908	—
100	48.191	48.478	48.6337(7)	48.4566	—

**Tab. 6.3:** Same as in Tab. 6.1 for the helium state  $0^0 0^1 \Leftrightarrow \{0,-,1,1\}$ . Here we compare with results of Boblest [46] and Becken et al. [26]. Note the use of  $\beta$  instead of  $\beta_Z$  for the magnetic field strength.

$\beta$	HFFER II	2DLHFR	Ref. [46]	Ref. [26]
0.25	4.139	4.747	4.95986(30)	4.960344
0.40	4.653	5.144	5.27674(22)	5.276444
0.50	4.917	5.360	5.46764(20)	5.467626
0.80	5.536	5.901	5.97500(16)	5.974370
1.00	5.869	6.208	6.27064(14)	6.270284
2.50	7.605	7.882	7.91854(10)	7.918470
5.00	9.414	9.668	9.69716(8)	9.697180
10.00	11.758	11.994	12.02330(8)	12.022976
25.00	15.872	16.093	16.11860(10)	16.118932
50.00	19.926	20.135	20.16024(10)	20.159946

**Tab. 6.4:** Same as in Tab. 6.3 for the complex helium state  $0^0 1^1 \Leftrightarrow \{1, -, 1, 1\}$  compared with results of Becken et al. [27].

$\beta$	HFFER II	2DLHFR	FPDQMC	Ref. [27]
0.25	3.997	4.596	4.81470(28)	4.815042
0.40	4.504	4.985	5.11808(22)	5.11801
0.50	4.763	5.197	5.30170(20)	5.301946
0.80	5.370	5.725	5.79190(16)	5.792384
1.00	5.696	6.025	6.08066(16)	6.080608
2.50	7.403	7.673	7.70330(10)	7.703766
5.00	9.200	9.451	9.47466(10)	9.47498
10.00	11.543	11.780	11.80266(8)	11.80422
25.00	15.670	15.895	15.91570(10)	15.918188
50.00	19.741	19.952	19.97522(10)	19.978752

**Tab. 6.5:** Same as in Tab. 6.3 for the complex helium state  $0^0 3^0 \Leftrightarrow \{3, +, 1, 1\}$  compared with results of Becken et al. [28].

$\beta$	HFFER II	2DLHFR	FPDQMC	Ref. [28]
0.25	4.099	4.695	4.91570(28)	4.916486
0.40	4.659	5.138	5.27212(22)	5.272564
0.50	4.949	5.381	5.48762(20)	5.488218
0.80	5.638	5.993	6.06164(16)	6.063034
1.00	6.013	6.342	6.39986(14)	6.401364
2.50	8.009	8.279	8.31570(10)	8.321110
5.00	10.149	10.401	10.43320(10)	10.444804
10.00	12.979	13.217	13.25314(10)	13.273922
25.00	18.033	18.259	18.30340(14)	18.339400
50.00	23.071	23.285	23.34282(20)	23.394850

We remain with helium in Tabs. 6.3, 6.4 and 6.5 and compare our energy values to those of the full CI calculations of Becken et al. [26–28]. We use  $\beta$  instead of  $\beta_Z$  in these tables for convenience. At the lowest field strength on display  $\beta = 0.25$ , which corresponds to  $\beta_Z = 0.0625$ , we see large deviations of about 4.5% in all tables. As we had to expect from the conclusions of Sec. 5.2.2 we have overstretched the 2DLHFR method here. At  $\beta_Z = 0.125$  the relative difference to the CI results has dropped to about 2% in all three tables and our method recovers its precision. Finally, at  $\beta = 5$  ( $\beta_Z = 1.25$ ) our relative errors resemble the correlation errors, which, depending on the electronic configuration, are about 0.2%-0.4%. The CI approach is in principle in a position to yield exact results, whereas the FPDQMC method retains a phase error stemming from the 2DLHFR results. A comparison between the FPDQMC energies

**Tab. 6.6:** Indices corresponding to electronic configurations.

$i$	configuration	$i$	configuration
0	$\underline{0}_N$	4	$\underline{0}_{(N-4)} 0^1 1^1 2^1 3^1$
$\overline{0}$	$\underline{0}_{(N-1)} 0^0_{\uparrow}$	41	$\underline{0}_{(N-4)} 0^1 1^1 2^1 0^2$
1	$\underline{0}_{(N-1)} 0^1_{\uparrow}$	42	$\underline{0}_{(N-4)} 0^1 1^1 0^2 1^2$
$\overline{1}$	$\underline{0}_{(N-2)} 0^0 0^1_{\uparrow}$	$\overline{4}$	$\underline{0}_{(N-5)} 0^0 0^1 1^1 2^1 3^1$
2	$\underline{0}_{(N-2)} 0^1 1^1_{\uparrow}$	$\overline{41}$	$\underline{0}_{(N-5)} 0^0 0^1 1^1 2^1 0^2$
$\overline{2}$	$\underline{0}_{(N-3)} 0^0 0^1 1^1_{\uparrow}$	51	$\underline{0}_{(N-5)} 0^1 1^1 2^1 3^1 0^2$
$\overline{21}$	$\underline{0}_{(N-3)} 0^0 0^1 0^2_{\uparrow}$	52	$\underline{0}_{(N-5)} 0^1 1^1 2^1 0^2 1^2$
3	$\underline{0}_{(N-3)} 0^1 1^1 2^1_{\uparrow}$	$\overline{51}$	$\underline{0}_{(N-6)} 0^0 0^1 1^1 2^1 3^1 0^2$
31	$\underline{0}_{(N-3)} 0^1 1^1 0^2_{\uparrow}$	61	$\underline{0}_{(N-6)} 0^1 1^1 2^1 3^1 4^1 0^2$
$\overline{3}$	$\underline{0}_{(N-4)} 0^0 0^1 1^1 2^1_{\uparrow}$	$\overline{61}$	$\underline{0}_{(N-7)} 0^0 0^1 1^1 2^1 3^1 4^1 0^2$
$\overline{31}$	$\underline{0}_{(N-4)} 0^0 0^1 1^1 0^2_{\uparrow}$	$\overline{62}$	$\underline{0}_{(N-7)} 0^0 0^1 1^1 2^1 3^1 0^2 1^2$
		$\overline{72}$	$\underline{0}_{(N-8)} 0^0 0^1 1^1 2^1 3^1 4^1 0^2 1^2$

obtained from 2DLHFR states and the CI results thus gives an estimate of the 2DLHFR results' phase error. Table 6.3 refers to a state with vanishing phase, hence we expect no phase error. Indeed, here the FPDQMC and CI results are in almost perfect agreement, whereas in Tabs. 6.4 and 6.5, which correspond to complex-valued states, the FPDQMC results never reach the CI quality. In Tab. 6.4 the relative phase error is for all values of  $\beta$  in the range of  $10^{-4}$ . However, in Tab. 6.5 the relative phase error gets as large as 0.2% at large  $\beta$ , which corresponds to about 50% of the relative difference between the 2DLHFR and CI calculations.

The HFFERII and 2DLHFR methods are designed to handle large numbers of electrons. Therefore we switch the focus to heavier elements up to iron. In the literature there are only two publications that investigate elements heavier than carbon: Ivanov et al. [90] (up to  $Z = 10$ ) and, more recently, Mori and Hailey [42] (up to  $Z = 26$ ). It is no trivial task to find the ground state configuration of many-particle systems in strong magnetic fields [105], therefore the investigated electronic configurations are specified in the literature as well. We in turn investigate the ground state configurations and introduce short notations for the different configurations in Tab. 6.6. This notation will be most useful in Sec. 6.4, as well. The first digit in each short notation refers to the number of electrons that are placed in orbitals with  $\nu' \neq 0$ . The remaining electrons are placed in tightly-bound orbitals, i.e.  $\nu' = 0$ , in the high-field ground state configuration. Further digits give the sum of electrons placed in orbitals of even higher  $\nu'$ , e.g. the series of digits 7421 would correspond to 7 orbitals with  $\nu' > 0$ , 4 orbitals with  $\nu' > 1$ , 2 orbitals with  $\nu' > 2$  and 1 orbital with  $\nu' = 4$ . For each  $\nu'$  we occupy the orbitals in the order of rising  $m'$ , starting at  $m' = 0$ . Overlined symbols refer to a spin-flipped configuration, where the outermost tightly-bound orbital is replaced by the  $0^0_{\uparrow}$ -orbital. Such configurations deviate by an additional electron from the high-field ground state

**Tab. 6.7:** Ground state binding energies in Rydberg units at  $B = 10^7$  T of neutral helium to silicon calculated with the HFFERII and 2DLHFR methods and compared to results of FPDQMC calculations of Boblest [46] as well as Hartree-Fock calculations of Ivanov et al. [90] and Mori et al. [42]. Superscripts denote electronic configurations (see Tab. 6.6). Numbers in brackets denote the uncertainties in the last digit(s).

$Z$	$\beta_Z$	HFFERII	2DLHFR	Ref. [46]	Ref. [90]	Ref. [42]
2	5.318	19.13	19.38	19.42776(14)	19.39	19.21
3	2.364	39.07	39.70	39.7824(3)	39.72	39.23
4	1.329	64.80	65.97	66.1171(4)	66.03	65.39
5	0.851	95.89	97.81	98.0428(6)	97.92	97.53
6	0.591	132.07	134.95	135.3104(8)	135.16	136.27
7	0.434	173.10	177.21	177.7634(12)	177.58	—
8	0.332	220.01 <sup>1</sup>	225.94 <sup>1</sup>	226.856(2)	226.56 <sup>1</sup>	—
9	0.263	272.52 <sup>1</sup>	280.51 <sup>1</sup>	281.796(3)	281.47 <sup>1</sup>	—
10	0.213	329.86 <sup>1</sup>	340.38 <sup>1</sup>	342.159(4)	341.83 <sup>1</sup>	—
11	0.176	394.20 <sup>1</sup>	418.13 <sup>1</sup>	422.164(14)	—	—
12	0.148	477.41 <sup>2</sup>	508.23 <sup>2</sup>	513.86(2)	—	—
13	0.126	566.55 <sup>2</sup>	605.37 <sup>2</sup>	612.96(4)	—	—
14	0.109	661.31 <sup>3</sup>	709.66 <sup>3</sup>	719.94(6)	—	—

configuration. For the sake of brevity we may also drop the symbol “0” for the high-field ground state configuration.

This novel notation is tailored to the magnetic field strength regime accessible to us and has three decisive advantages: Firstly, it is very short but unambiguous, as can be seen from Tab. 6.6, where we additionally give the *already shortened* HFGS-notation presented in Sec. 3.1. Secondly, it is independent of the actual number of electrons as it only denotes orbitals deviating from the high-field ground state notation. Thirdly, it indicates at first sight how many electrons deviate from the HFGS configuration and if the full spin polarization is broken.

Tables 6.7, 6.8, 6.9 and 6.10 contain our ground state energies, at four values of  $B$ , obtained with the HFFERII and 2DLHFR methods in comparison to the enhanced results of Boblest [46], as well as to those of Ivanov et al. [90] and Mori and Hailey [42]. Though the magnetic field strength is constant in each table, we give the charge scaled value  $\beta_Z$  in each row as  $\beta_Z$  decreases quadratically with rising  $Z$ . We restrict ourselves to  $Z \leq 14$  in the first table to stay within a regime of  $\beta_Z \gtrsim 0.1$ , but proceed to  $Z = 26$  in the tables thereafter. Throughout all four Tabs. 6.7 – 6.10 one can notice a significant improvement of the results gained by the 2DLHFR method compared to the data obtained with the HFFERII method, especially at low  $\beta_Z$ . But also at  $\beta_Z > 10$  the 2DLHFR method reduces the remaining energy difference between the HFFERII and FPDQMC method by more than 50%. The ground state configuration was found to be the same for the HFFERII and 2DLHFR methods with the exception of  $Z = (21, 22)$

**Tab. 6.8:** Same as in Tab. 6.7 for ground states of neutral helium to iron at  $B = 5 \cdot 10^7$  T. For the superscripts refer to Tab. 6.6.

$Z$	$\beta_Z$	HFFER II	2DLHFR	Ref. [46]	Ref. [90]	Ref. [42]
2	26.590	33.6	33.86	33.9368(3)	33.86	33.6
3	11.818	70.1	70.68	70.8405(6)	70.69	70.0
4	6.647	117.7	118.77	119.0077(7)	118.79	117.6
5	4.254	175.4	177.17	177.4887(8)	177.21	175.7
6	2.954	242.6	245.16	245.5660(10)	245.22	243.1
7	2.171	318.5	322.17	322.7021(13)	322.28	319.9
8	1.662	402.9	407.80	408.4447(13)	407.94	405.5
9	1.313	495.4	501.60	502.4218(17)	501.84	500.0
10	1.064	595.5	603.30	604.3479(18)	603.69	602.5
11	0.879	703.6 <sup>1</sup>	713.46 <sup>1</sup>	714.8493(22)	—	714.3
12	0.739	822.0 <sup>1</sup>	834.03 <sup>1</sup>	835.682(4)	—	838.6 <sup>1</sup>
13	0.629	948.1 <sup>1</sup>	962.61 <sup>1</sup>	964.533(4)	—	973.9 <sup>1</sup>
14	0.543	1081.8 <sup>1</sup>	1099.0 <sup>1</sup>	1101.256(5)	—	1120.6 <sup>2</sup>
15	0.473	1225.1 <sup>2</sup>	1245.6 <sup>2</sup>	1248.356(6)	—	—
16	0.415	1376.2 <sup>2</sup>	1400.1 <sup>2</sup>	1403.384(8)	—	—
17	0.368	1534.6 <sup>2</sup>	1562.3 <sup>2</sup>	1566.104(8)	—	—
18	0.328	1702.4 <sup>3</sup>	1734.5 <sup>3</sup>	1739.008(1)	—	—
19	0.295	1877.5 <sup>3</sup>	1914.2 <sup>3</sup>	1919.484(12)	—	—
20	0.266	2060.2 <sup>4</sup>	2102.1 <sup>4</sup>	2108.32(4)	—	—
21	0.241	2251.3 <sup>4</sup>	2306.6 <sup>51</sup>	2313.72(6)	—	—
22	0.220	2452.0 <sup>51</sup>	2549.0 <sup>51</sup>	2563.26(12)	—	—
23	0.201	2689.8 <sup>51</sup>	2805.6 <sup>51</sup>	2822.02(14)	—	—
24	0.185	2940.4 <sup>51</sup>	3071.9 <sup>51</sup>	3091.4(16)	—	—
25	0.170	3200.0 <sup>61</sup>	3348.7 <sup>61</sup>	3370.9(4)	—	—
26	0.157	3468.5 <sup>61</sup>	3636.6 <sup>61</sup>	3660.4(6)	—	—

in Tab. 6.8. Our 2DLHFR results are in good agreement with those of Ref. [90] with a maximum deviation of about 0.4% in Tab. 6.7.

A comparison with the FPDQMC results to the 2DLHFR values, e.g. for  $B = 5 \cdot 10^8$  T in Tab. 6.10, yields an interesting result: The relative improvement of the FPDQMC method decreases with rising  $Z$  from  $\approx 0.35\%$  at  $Z = 2$  to  $0.09\%$  at  $Z = 26$ . This is somehow counterintuitive as the systems grow more complicated due to the larger number of electrons, and electronic correlations are expected to play an increasingly important role. This effect also occurs at other field strengths but is masked by the growing error of the 2DLHFR's Landau expansion that starts to dominate for  $\beta_Z \leq 1$ . However, the FPDQMC results are not affected as severely by this error in the wave function, and thus the relative energy corrections of FPDQMC to 2DLHFR rise again

**Tab. 6.9:** Same as in Tab. 6.8 at  $B = 10^8$  T. For the superscripts refer to Tab. 6.6.

$Z$	$\beta_Z$	HFFER II	2DLHFR	Ref. [46]	Ref. [90]	Ref. [42]
2	53.180	42.4	42.6	42.7488(6)	42.63	42.4
3	23.635	89.5	90.0	90.2140(10)	89.99	89.2
4	13.295	151.3	152.4	152.6872(12)	152.37	151.1
5	8.509	226.8	228.5	228.9330(12)	228.53	226.7
6	5.909	315.0	317.5	318.020(2)	317.51	315.2
7	4.341	415.0	418.5	419.147(2)	418.55	415.8
8	3.324	526.3	531.0	531.721(3)	531.02	527.4
9	2.626	648.3	654.3	655.200(4)	654.40	650.1
10	2.127	780.5	788.1	789.160(2)	788.24	783.8
11	1.758	922.7	931.9	933.204(3)	—	927.9
12	1.477	1074.4	1085.5	1086.978(4)	—	1083.7
13	1.259	1235.3	1248.5	1250.216(4)	—	1247.5 <sup>1</sup>
14	1.085	1409.6 <sup>1</sup>	1425.6 <sup>1</sup>	1427.764(6)	—	1426.5 <sup>1</sup>
15	0.945	1593.5 <sup>1</sup>	1612.2 <sup>1</sup>	1614.580(6)	—	1616.0 <sup>1</sup>
16	0.831	1786.8 <sup>1</sup>	1808.3 <sup>1</sup>	1811.032(6)	—	1816.7 <sup>2</sup>
17	0.736	1990.9 <sup>2</sup>	2015.9 <sup>2</sup>	2019.118(8)	—	2029.9 <sup>2</sup>
18	0.657	2205.8 <sup>2</sup>	2234.3 <sup>2</sup>	2237.902(8)	—	2261.3 <sup>2</sup>
19	0.589	2429.9 <sup>2</sup>	2462.1 <sup>2</sup>	2466.186(10)	—	2501.6 <sup>2</sup>
20	0.532	2664.1 <sup>3</sup>	2700.7 <sup>3</sup>	2705.37(3)	—	2756.2 <sup>3</sup>
21	0.482	2909.0 <sup>3</sup>	2950.0 <sup>3</sup>	2955.248(3)	—	—
22	0.440	3162.7 <sup>3</sup>	3208.5 <sup>3</sup>	3214.16(4)	—	—
23	0.402	3426.7 <sup>4</sup>	3477.8 <sup>4</sup>	3484.24(4)	—	—
24	0.369	3700.4 <sup>4</sup>	3757.1 <sup>4</sup>	3764.24(6)	—	—
25	0.340	3983.3 <sup>51</sup>	4054.4 <sup>51</sup>	4062.54(8)	—	—
26	0.315	4277.7 <sup>51</sup>	4357.2 <sup>51</sup>	4366.14(10)	—	—

for  $\beta_Z \leq 1$ , as can be seen in Tabs. 6.7 — 6.9. We performed additional computations at  $B = 5 \cdot 10^8$  T to gain a better understanding of this phenomenon. Boblest [46] compared the influence of Jastrow factors and the overall correction in FPDQMC of the energy values for all helium-like ions and several iron ions. The results of his computations show a strongly decreasing influence of the electron-electron Jastrow factor with increasing  $Z$ . One can understand this phenomenon by comparing the relative energy contributions from electron-core and electron-electron interactions: For large values of  $Z$  and in the limit of strong fields the electron-core interactions clearly dominate over the electron-electron interactions, and thus the electronic correlations. The latter two become less important and their relative contributions to the total energy decrease with rising  $Z$  and  $\beta$ .

Compared to the perturbative method of Mori and Hailey [42] we obtain higher binding energies for small nuclear charges  $Z \leq 10$ , but for heavier elements and when  $\beta_Z$  falls

**Tab. 6.10:** Same as in Tab. 6.8 at  $B = 5 \cdot 10^8$  T. For the superscripts refer to Tab. 6.6.

$Z$	$\beta_Z$	HFFER II	2DLHFR	Ref. [46]	Ref. [90]	Ref. [42]
2	265.899	70.6	70.7	70.9782(16)	70.70	70.37
3	118.177	153.2	153.6	154.108(4)	153.56	152.73
4	66.475	264.6	265.5	266.134(4)	265.35	263.57
5	42.544	402.9	404.4	405.210(6)	404.21	402.48
6	29.544	566.5	568.7	569.748(6)	568.53	565.57
7	21.706	754.0	757.2	758.368(8)	756.98	751.96
8	16.619	964.4	968.6	969.962(10)	968.38	962.76
9	13.131	1196.4	1202.0	1203.510(8)	1201.70	1195.38
10	10.636	1449.4	1456.3	1458.144(8)	1456.06	1448.07
11	8.790	1722.3	1730.9	1732.922(10)	—	1720.31
12	7.386	2014.7	2025.1	2027.306(8)	—	2016.51
13	6.293	2325.8	2338.1	2340.490(8)	—	2328.07
14	5.427	2655.0	2669.4	2672.072(8)	—	2657.27
15	4.727	3001.8	3018.4	3021.418(10)	—	3007.2
16	4.155	3365.7	3384.8	3388.112(10)	—	3372.19
17	3.680	3746.3	3768.0	3771.580(14)	—	3753.36
18	3.283	4143.2	4167.7	4171.518(10)	—	4154.88
19	2.946	4555.9	4583.4	4587.51(3)	—	4570.22
20	2.659	4984.3	5014.9	5019.49(2)	—	5000.19
21	2.412	5434.2 <sup>1</sup>	5468.7 <sup>1</sup>	5473.92(4)	—	5452.42 <sup>1</sup>
22	2.198	5901.4 <sup>1</sup>	5939.6 <sup>1</sup>	5945.02(4)	—	5924.14 <sup>1</sup>
23	2.011	6384.3 <sup>1</sup>	6426.3 <sup>1</sup>	6432.08(6)	—	6413.71 <sup>1</sup>
24	1.847	6882.6 <sup>1</sup>	6928.6 <sup>1</sup>	6934.72(6)	—	6927.91 <sup>1</sup>
25	1.702	7401.0 <sup>2</sup>	7451.8 <sup>2</sup>	7458.64(4)	—	7441.74 <sup>1</sup>
26	1.573	7936.3 <sup>2</sup>	7991.7 <sup>2</sup>	7998.84(6)	—	7984.89 <sup>2</sup>

below 1, their results drop far below even the FPDQMC results, with some ground state configurations differing from the ones found by us. We expect that, in this regime, the method presented in Ref. [42] fails to achieve accurate results, as the authors themselves state that its application is limited to  $\beta_Z > 2$ , but they proceed down to  $\beta_Z \approx 0.5$ . We already mentioned that their method is not fully variational and therefore does not necessarily give an upper bound on the energy, in contrast to the HFFER II and FPDQMC methods. At  $\beta_Z \approx 0.5$ , however, our method is above its minimal field strength limit  $\beta_Z \approx 0.1$ , and our results are to be expected very accurate. Electronic configurations including a spin-up orbital were found to form the ground state at  $B = 10^7$  T for elements with nuclear charges  $Z \geq 11$ , and at  $B = 5 \cdot 10^7$  T for heavier elements with nuclear charges  $Z = 22$  to 26. In these cases we obtained an increased estimate for the ground state binding energy of up to 6% in comparison with previous investigations that did not account for such configurations [95].



**Tab. 6.11:** Transition energies  $E$  in Rydberg atomic units and dipole strengths  $d$  of  $\Delta M = 0$  bound-bound transitions from the state  $0^0 0^2$  to the state  $0^0 0^1$  at different magnetic fields compared with results of Becken et al. [29].

$\beta$	$E$			$d$		
	HFFER II	2DLHFR	Ref. [29]	HFFER II	2DLHFR	Ref. [29]
0.25	-0.191	-0.033	-0.051642	7.680	6.165	6.70904
0.4	-0.220	-0.110	-0.129206	6.842	6.385	6.61766
0.5	-0.235	-0.147	-0.166316	6.384	6.157	6.34701
0.8	-0.272	-0.222	-0.23913	5.472	5.362	5.48700
1	-0.294	-0.255	-0.270866	5.066	4.954	5.06134
2.5	-0.382	-0.370	-0.382072	3.798	3.697	3.73113
5	-0.441	-0.432	-0.442282	3.229	3.165	3.16716
10	-0.470	-0.464	-0.47808	2.915	2.874	2.85748
25	-0.478	-0.475	-0.48842	2.750	2.733	2.69282
50	-0.463	-0.462	-0.4738	2.735	2.725	2.67838

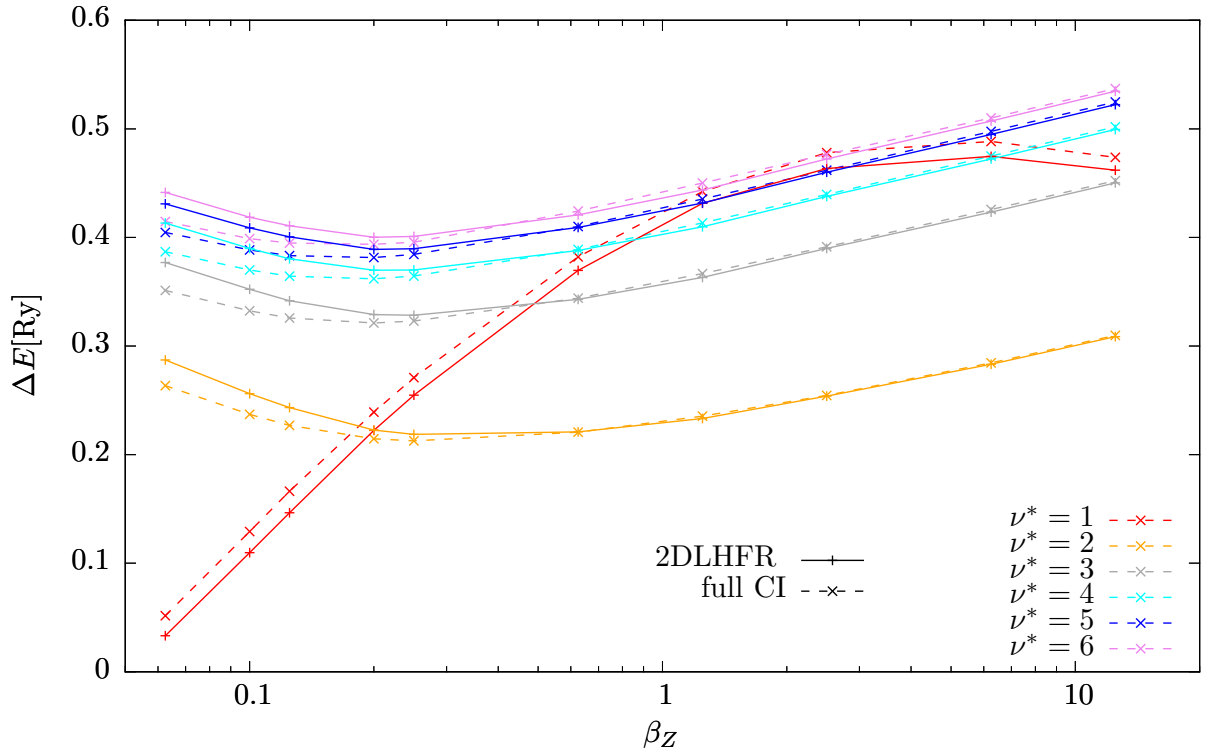
## 6.3 Transition strengths and energies

In this section we focus on transitions, because of their importance for the calculation of absorption spectra. We compare our results for energy differences and dipole strengths for helium transitions with those of the full CI method of Becken et al. [29]. These findings were also published in Ref. [104]. In order to distinguish between our energy and wave function errors we use the dipole strength  $d$  instead of the oscillator strength, which also includes the energy difference between initial and final state, see Eq. (4.24). Becken et al. provide both values. Tables 6.11 and 6.12 give the results of the HFFER II and 2DLHFR programs and those of the full CI ansatz of Becken et al. [29]. In their work they presented a large compendium of electromagnetic transition energies and transition strengths for the helium atom.

At the lowest field strength, which corresponds to  $\beta_Z = 0.0625$  we again overstretch our ansatz. At such low fields the 2DLHFR method induces large errors on both the transition energies and strengths. However, for the states  $0^0 0^2$  and  $0^0 0^1$  shown in Tab. 6.11 the 2DLHFR method is able to reproduce the approach of the two levels towards low  $\beta$  that is found with the full CI method, whereas the HFFER II program does not find this. The large relative deviations between the 2DLHFR and the full CI results are not crucial due to the small absolute values of the transition energies at low  $\beta$ . Gradually increasing the magnetic field strength, our energy differences to Ref. [29] fall below 3% at  $\beta = 5$  in Tab. 6.11. For the states shown in Tab. 6.12, our energy error is below 1% at all field strengths with the exception of  $\beta = 0.25$ . However, the differences in the dipole strength are somewhat larger, ranging from  $-4\%$  to  $+2\%$  in the first table, and  $-2\%$  to  $+5\%$  in the second one for  $\beta > 0.25$ . Still, our dipole strengths are quite

**Tab. 6.12:** Same as in Tab. 6.11, but for the transition from  $0^0 1^0$  to  $0^0 1^1$ .

$\beta$	$E$			$d$		
	HFFER II	2DLHFR	Ref. [29]	HFFER II	2DLHFR	Ref. [29]
0.25	0.426	0.439	0.425002	1.485	1.763	1.88833
0.4	0.544	0.558	0.55323	1.216	1.408	1.43257
0.5	0.617	0.630	0.629066	1.086	1.242	1.24811
0.8	0.801	0.822	0.825168	0.844	0.936	0.92676
1	0.911	0.932	0.937218	0.743	0.815	0.80319
2.5	1.514	1.539	1.54722	0.433	0.458	0.44460
5	2.168	2.193	2.203976	0.284	0.295	0.28280
10	3.035	3.064	3.076902	0.183	0.187	0.17845
25	4.601	4.627	4.650028	0.099	0.101	0.09548
50	6.174	6.195	6.230862	0.061	0.062	0.05868

**Fig. 6.1:** Transition energies  $\Delta E$  of the helium transitions  $\{0,+1,1\}:\{0,-1,\nu^*\}$  over  $\beta_Z$ . The full CI results were taken from Becken [85]. Lines serve as a guide to the eye.

accurate, considering the constraints of our ansatz in comparison to a full CI method. Of course, we can also calculate transitions corresponding to states of higher excitations. We present energies and dipole strengths for the transitions from the lowest state of the

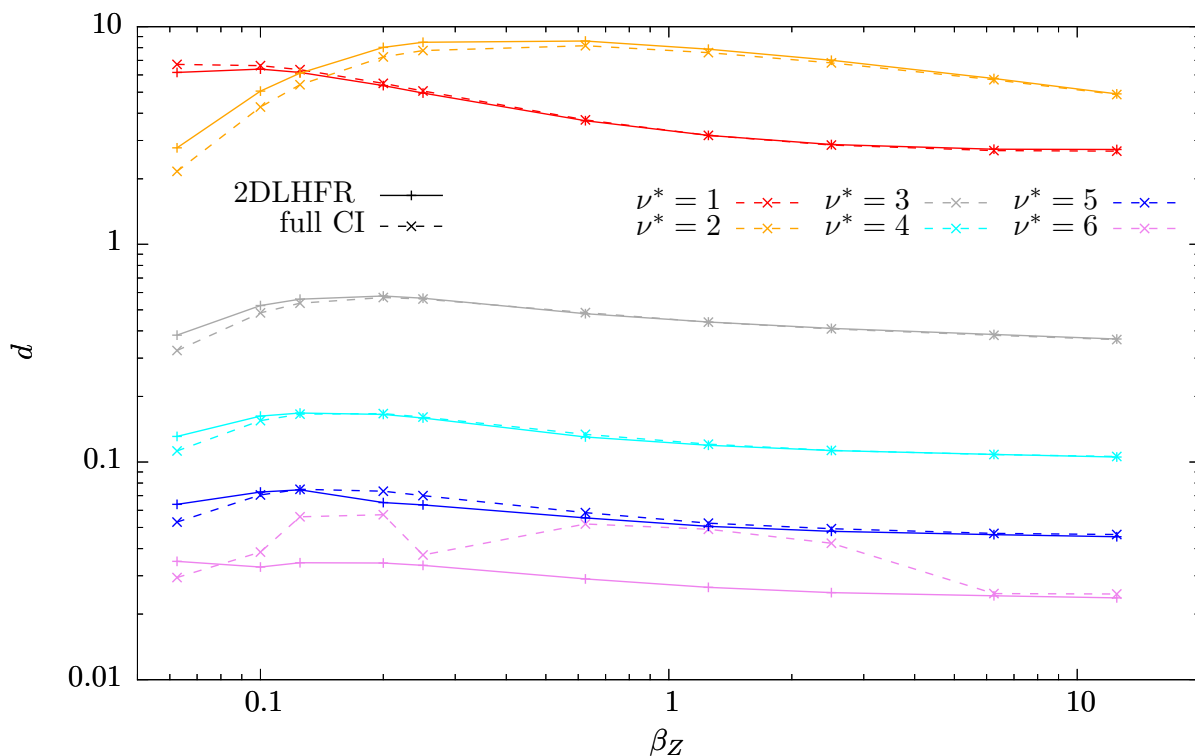


**Fig. 6.2:** Dipole strengths of the helium transitions  $\{0,+1,1\}:\{0,-,1,\nu^*\}$  over  $\beta_Z$ . The full CI results were taken from Becken [85]. Lines serve as a guide to the eye.

symmetry subspace  $\{0,+1\}$  to the six lowest states of the symmetry subspace  $\{0,-,1\}$  in Figs. 6.1 and 6.2, respectively. For comparison the results of Becken [85] are also plotted. The absolute line energies are small, in the range  $E \leq 0.5$  Ry, since initial and final states are quite highly excited. Except for the transition to  $\nu^* = 1$ , the transition energies in Fig. 6.1 quickly converge to the values found with the full CI approach. At  $\beta_Z = 0.625$  the energy results of both methods agree within a relative error  $< 1\%$ . This also applies to the dipole strengths shown in Fig. 6.2, at least for the transitions to the low-lying states  $\nu^* \leq 3$ . For higher values of  $\nu^*$  the 2DLHFR dipole strengths of both methods differ quite significantly for all values of  $\beta$ . In this case the 2DLHFR dipole strength functions  $d(\beta)$  retain their progression, whereas the full CI results seem to fluctuate, especially for the transition to the highest excited state  $\nu^* = 6$ . Since the author of Ref. [85] stated to have experienced convergence problems for higher eigenvalues  $\nu^* > 6$  and due to the smoothness of our dipole strength function  $d(\beta_Z)$ , we trust in the correctness of our results for the transitions to  $\nu^* = 6$ .

The amount of accurate data for transition energies and strengths regarding elements with core charge  $Z > 2$  is very poor in the literature. While Al-Hujaj and Schmelcher [40, 41] published a selection of state energies for lithium and beryllium, they did not present transition strengths. So far, only Mori and Hailey [42] presented tables for transition strengths in heavier elements. We compare our 2DLHFR oscillator strengths

**Tab. 6.13:** Transition energies in eV and oscillator strengths  $\times 10^{-3}$  (in brackets) of  $\Delta M = 0$  bound-bound transitions from electrons ( $m', \nu = 0$ ) of the ground state of neutral carbon to ( $m', \nu = 1$ ) compared to results from Mori and Hailey [42] at  $\beta = 200$  (upper left table),  $\beta = 500$  (upper right table) and  $\beta = 1000$  (lower table).

$m'$	HFFER II	2DLHFR	Ref. [42]	$m'$	HFFER II	2DLHFR	Ref. [42]
0	1024 (42.0)	1051 (45.4)	– (41.0)	0	1370 (12.0)	1394 (12.5)	– (13.0)
1	481 (68.4)	485 (70.4)	– (59.8)	1	671 (27.1)	675 (27.4)	– (22.5)
2	314 (99.9)	315 (101.2)	– (79.7)	2	447 (45.7)	448 (46.0)	– (39.2)
3	233 (135.8)	233 (136.6)	– (114.)	3	335 (67.9)	335 (68.1)	– (61.1)
4	180 (173.2)	180 (173.7)	– (156.)	4	262 (93.0)	262 (93.1)	– (86.3)
5	132 (205.5)	132 (205.8)	– (197.)	5	195 (119.9)	196 (120.0)	– (116.)

$m'$	HFFER II	2DLHFR	Ref. [42]
0	1696 (6.2)	1718 (6.3)	– (5.81)
1	854 (15.5)	858 (15.7)	– (12.8)
2	576 (27.7)	577 (27.8)	– (24.7)
3	435 (42.4)	436 (42.5)	– (37.7)
4	343 (59.9)	344 (59.9)	– (57.2)
5	259 (80.5)	259 (80.5)	– (78.3)

with their results in Tab. 6.13. One can see rather large differences of the oscillator strengths for all transitions, with a maximum difference of 27%. The authors of Ref. [42] mention lacking orthogonality of initial and final state and only calculated the dipole matrix element for the electron that undergoes a transition. This, and different results for the transition energies that influence the oscillator strengths, may explain the large discrepancies. Since we evaluate the dipole integrals within numerical precision and work with perfectly orthogonal states, our results should be more accurate. No transition energies are given in Ref. [42], so we can only compare with the HFFER II transition energies.

The 2DLHFR values are in good agreement with those obtained with the HFFER II method: the largest relative differences in oscillator strength and energy amount to about 7% for the oscillator strengths and 2.6% for the transition energies. These differences correspond to the transition of the innermost electron  $m = 0$  at the lowest magnetic field strength  $\beta = 200$ . We suggest the following explanation: For lower  $\beta$  the initial single-particle (0,0)-state is significantly improved by the 2DLHFR expansion, whereas the final (0,1)-state has a node at  $z = 0$  and thus can be described adequately well by both expansions (2.7) and (2.6). When the error of both the initial and final single electron state is of the same order, even expansion (2.7) proves to be useful and predicts transition energies and oscillator strengths properly, as e.g. in the case of the transitions of  $m = 5$ .

## 6.4 Ground state configurations

The exploration of the ground state configuration of atoms and ions over a wide range of magnetic field strengths is an important step on the way to a complete understanding of their electronic structure in arbitrarily strong magnetic fields. Extensive numerical calculations are required to identify the ground state after a selection of possible ground state configuration candidates has been made with the help of qualitative arguments, cf. the extensive discussion by Ivanov and Schmelcher [90, 107]. Our combination of the very fast HFFER II method and the accurate 2DLHFR method is best suited for this task. With HFFER II we analyze the energies of possible ground state configurations by performing many calculations over a wide range of  $\beta$ . In this way we obtain first estimates for the magnetic field strengths where the ground state configuration changes. Due to the huge number of results that can be obtained with the HFFER II method, we can check all reasonable candidate configurations and make sure not to miss any ground state configuration. We then carefully investigate the HFFER II results and conduct more accurate 2DLHFR calculations for those states that are in reach of the ground state energy for  $\beta$  values close to a possible ground state crossing. A third refinement step can then be performed by the FPDQMC method, as it has been done in Ref. [105].

We determine a precise estimate for the transition field strength  $\beta_Z^{\text{Tr}}$  between two states  $A$  and  $B$  by a linear interpolation of the energy functions  $E(\beta)$  from four  $E(\beta)$ -values in the vicinity of the transition point. We use a very fine grid of 100 field strengths

that are distributed uniformly in  $\log \beta_Z$  between  $\beta_Z = 0.05$  and  $\beta_Z = 5$ . Therefore, a linear interpolation causes only insignificant deviations for the transition field strengths compared to an interpolation of higher order.

### 6.4.1 Ground state regimes

In hydrogen-like systems the ground state is always the lowest state of the  $\{0,+,1/2\}$  subspace. In multi-electron systems, however, the ground state configuration depends on the magnetic field strength. Due to the non-crossing theorem for states of the same symmetry subspace [75], a ground state configuration change corresponds to the crossing of the lowest state of different symmetry subspaces.

Different regimes of ground state configurations in dependence of the magnetic field strength exist. At  $B = 0$  the zero-field ground state configuration and energy is known with very high precision from various investigations in the literature. With rising  $\beta$  changes of the ground state configuration mostly relate to orbitals with positive  $m$  or spin alignment  $m_s = +\frac{1}{2}$ , as the binding energy of those orbitals from energy shifts of  $4m\beta$  and  $4\beta$ . At some value of  $\beta$  no orbital with  $m > 0$  is left to contribute to the ground state configuration and we call this the regime of magnetic polarization. The transition to this regime occurs at  $\beta_Z < 0.1$ . Ivanov et al. [107] found a field strength of  $\beta_Z \approx 7 \times 10^{-3}$  in neutral carbon for the beginning of this regime. Due to the low field strengths we cannot investigate the change to the magnetic polarization regime.

In the regime of magnetic polarization most spin-up orbitals are already eliminated from the ground state configuration, which is called a partial spin polarization (PSP). However, at  $\beta_Z \approx 0.1$  the ground state configuration no longer contains spin-up orbitals and the full spin polarization (FSP) regime is reached. For even larger  $\beta_Z$  one enters the high-field ground state (HFGS) regime: orbitals with  $\nu' > 0$  vanish from the ground state configuration. In this case, all electrons occupy tightly-bound orbitals, corresponding to the lowest-lying orbital with positive  $z$ -parity of each  $m$  (see Eq. (3.6)). The magnetic field strength connected to the onset of the HFGS regime is commonly estimated with the condition  $\beta_Z \gg Z$  [66], although we found this estimate to yield too large values for  $\beta_Z$  for the nuclear core charges we investigated. If one considers the finite nuclear mass corrections given in Eq. (3.2), the energy of orbitals with  $m < 0$  is also affected by a small energy penalty that rises linearly with  $\beta$ . Therefore, another ground state regime exists at very high  $\beta$ , where only orbitals with  $m = 0$  are occupied. Calculations for helium reveal that such ground state configurations are not relevant before  $\beta_Z \approx 3 \times 10^4$  and are therefore not considered here.

### 6.4.2 Qualitative analysis

We have thoroughly investigated the ground state candidates for all atoms and ions with  $2 \leq N \leq Z$  and  $2 \leq Z \leq 21$  in the range of  $\beta_Z \geq 0.05$  with both our HFFER II and 2DLHFR programs. We did not investigate hydrogenic systems since their ground state configuration does not change with  $\beta$  and ground state energies can be obtained for any

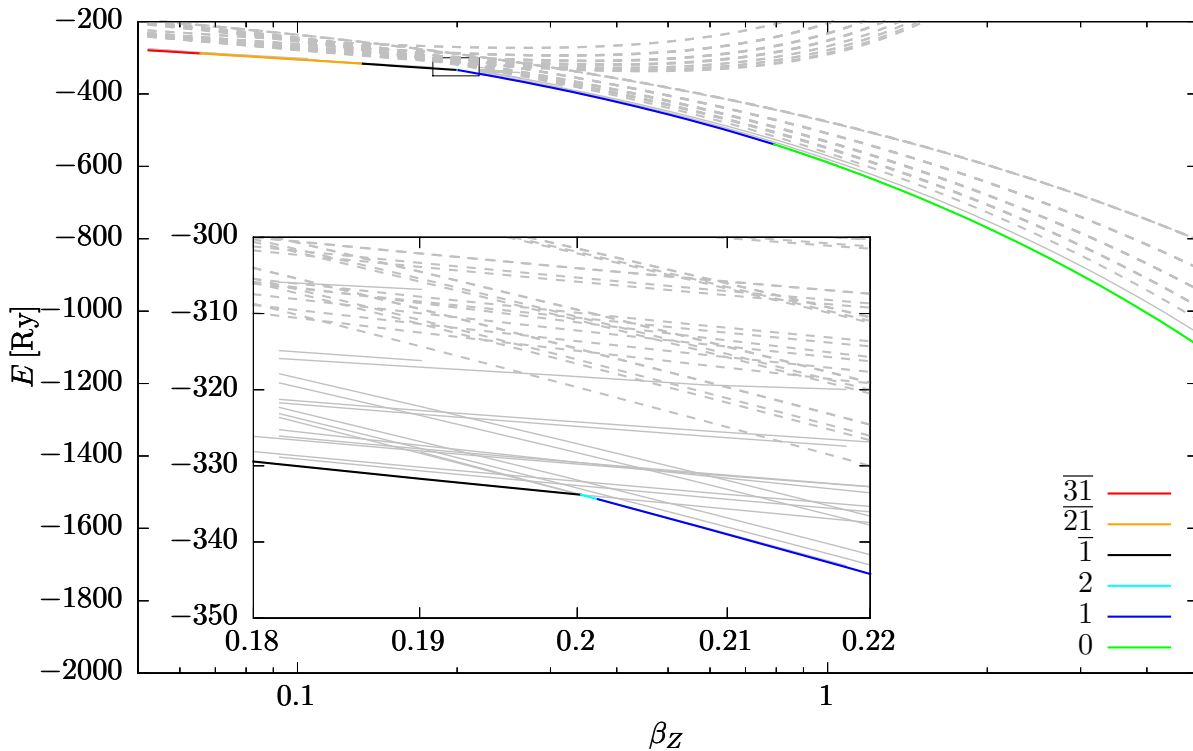


**Fig. 6.3:** Ground state configurations of neutral neon as found with the 2DLHFR program. Solid grey lines correspond to energies of excited states. Dashed grey lines are preliminary results from HFFER II-calculations. Colored lines represent the ground state energy, where the key denotes the electronic configuration using the notation presented in Tab. 6.6.

nuclear core charge via the scaling relations in Eq. (2.3). Our choice for the minimal  $\beta_Z = 0.05$  violates the validity condition  $\beta_Z \geq 0.1$  and our results are to be regarded with care in this region of  $\beta_Z$ . However, it was shown by Boblest [46] that the 2DLHFR wave functions obtained at these field strengths may still serve as trial wave functions for the FPDQMC algorithm, which is capable of compensating for the 2DLHFR errors.

In Fig. 6.3 we present energies as functions of the magnetic field strength of ground and excited states in neutral neon, calculated with the HFFER II and 2DLHFR programs. The most interesting feature of this figure is the tiny segment of the magnetic field strength (from  $\beta_Z = 0.200$  to  $\beta_Z = 0.213$ ) where the configuration 2 (cyan) represents the ground state. This is best viewed in the inset which provides a zoomed view on that region. Boblest et al. [105] have confirmed this finding with their powerful FPDQMC method, whereas Ivanov et al. [90] were not able to identify this ground state configuration, probably because they used considerably less data points. Furthermore, the differences between the HFFER II-results (dashed) and the 2DLHFR-results (solid) in Fig. 6.3 are apparent. It is likewise well recognizable that at low  $\beta$  the HFFER II and 2DLHFR results have a different gradient, indicating the poor performance of the product ansatz (2.7) in this regime of the magnetic field strength. As we use the HFFER II-results to

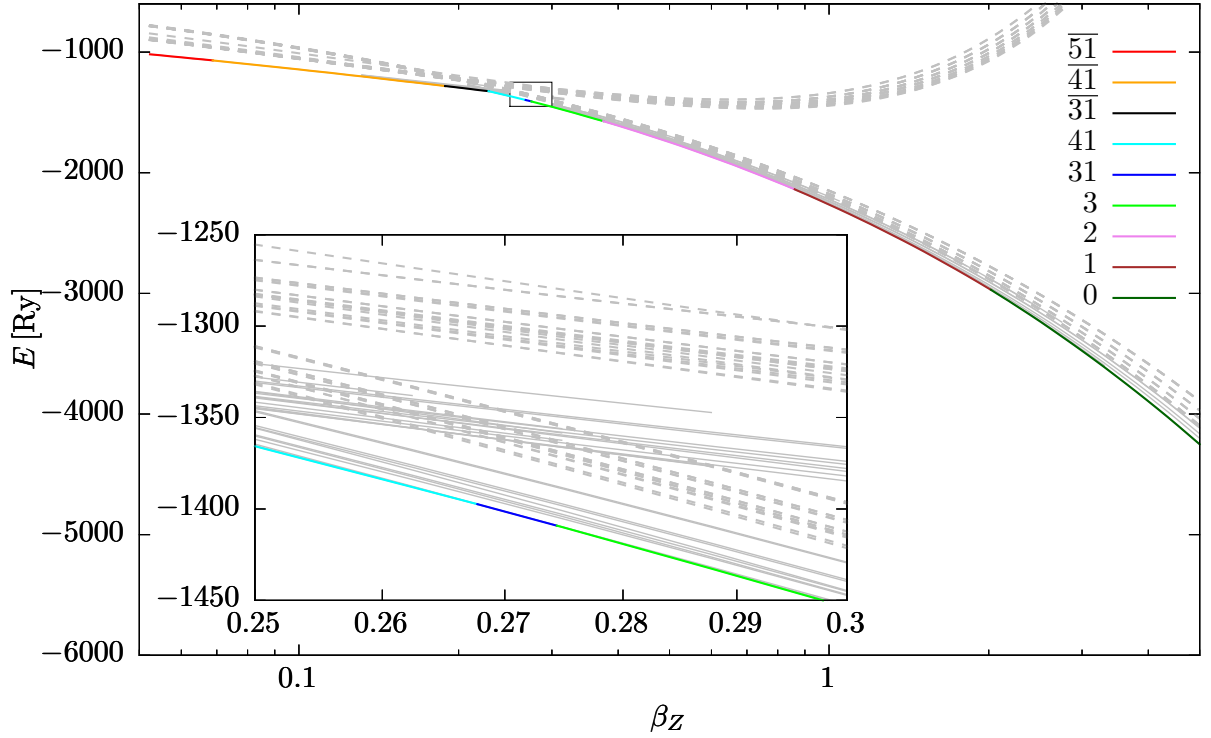


**Fig. 6.4:** Ground state configurations of neutral chlorine as found with the 2DLHFR program. Solid grey lines correspond to energies of excited states. Dashed grey lines are preliminary results from HFFER II-calculations. Colored lines represent the ground state energy, where the key denotes the electronic configuration using the notation presented in Tab. 6.6.

reduce the list of possible ground state candidates and adapt this list individually for each ion and field strength, the 2DLHFR results were not computed at all field strengths. As a consequence there are abruptly terminating 2DLHFR energy functions that can be observed in the inset of Fig. 6.3 at e.g.  $\beta_Z \approx 0.18$  (solid lines).

Another investigation of this type is given in Fig. 6.4, where ground and excited energies for chlorine are shown. This figure is remarkably rich in ground state configuration crossings in the investigated field strength sector. Again, we provide a zoomed view onto the region of  $\beta_Z$  where many ground state crossings occur. In this and the previous figure at  $\beta_Z \gtrsim 0.2$  one can observe the splitting of the energy functions  $E(\beta_Z)$  into two bunches. The one with higher energies corresponds to states with partial spin-polarization that include the  $0_{\uparrow}^0$  orbital. The lower bunch of states is fully spin-polarized. With rising  $\beta_Z$  the ground state features fewer and fewer orbitals with  $\nu' > 0$ , until finally the HFGS configuration 0 is reached at  $\beta_Z \approx 2$ . The large energetic separation of ground and excited states at high magnetic field strengths has a large impact on the atomic partition function. Therefore, the transitions to the PSP and HFGS regimes can be of special interest, as they mark the verge of strong changes in the partition functions.

Boblest et al. [105] analyzed transitions to both regimes for elements with  $2 \leq Z \leq 10$ . We compare our findings for the transitions to the FSP regime in Tab. 6.14 with those



**Tab. 6.14:** Magnetic field strength  $\beta_Z^{\text{Tr}}$  at the ground state crossings from partial to full spin polarization for  $2 \leq Z \leq 10$  and  $2 \leq N \leq Z$  obtained with the 2DLHFR program.

Z	N = 2	N = 3	N = 4	N = 5	N = 6	N = 7	N = 8	N = 9	N = 10
2	0.0923								
3	0.1149	0.1196							
4	0.1270	0.1393	0.1414						
5	0.1343	0.1520	0.1571	0.1584					
6	0.1394	0.1607	0.1682	0.1688	0.1670				
7	0.1430	0.1672	0.1766	0.1766	0.1749	0.1748			
8	0.1458	0.1722	0.1828	0.1825	0.1811	0.1834	0.1845		
9	0.1479	0.1760	0.1879	0.1871	0.1874	0.1905	0.1921	0.1929	
10	0.1496	0.1791	0.1921	0.1911	0.1928	0.1963	0.1985	0.1997	0.2002

**Tab. 6.15:** Magnetic field strength  $\beta_Z^{\text{Tr}}$  at the ground state crossings from partial to full spin polarization for  $2 \leq Z \leq 10$  and  $2 \leq N \leq Z$  as found by the FPDQMC method, taken from Boblest et al. [105]. Numbers in brackets denote statistical uncertainties of the FPDQMC method.

Z	N = 2	N = 3	N = 4	N = 5	N = 6	N = 7	N = 8	N = 9	N = 10
2	0.09393(4)								
3	0.11744(3)	0.12212(3)							
4	0.12993(4)	0.14229(4)	0.14432(4)						
5	0.13763(4)	0.15510(4)	0.16023(4)	0.16129(4)					
6	0.14292(4)	0.16404(4)	0.17145(4)	0.17206(4)	0.17000(3)				
7	0.14675(3)	0.17059(3)	0.17979(3)	0.17993(4)	0.17805(4)	0.17812(4)			
8	0.14960(3)	0.17556(3)	0.18627(3)	0.18600(4)	0.18445(3)	0.18678(4)	0.18781(3)		
9	0.15189(3)	0.17947(4)	0.19137(3)	0.19083(3)	0.19085(3)	0.19388(3)	0.19550(3)	0.19649(4)	
10	0.15372(3)	0.18266(3)	0.19547(3)	0.19472(4)	0.19615(3)	0.19978(3)	0.20191(3)	0.20311(3)	0.20346(3)

calculated by Boblest et al. [105] in Tab. 6.15. The results of both methods agree with a maximum relative difference of 2.8% for the transition field strength  $\beta_Z^{\text{Tr}}$ . A systematic investigation shows that this relative difference rises with  $Z$  but falls with  $N$ , whereas the absolute value of the transition field strength rises with  $Z$  and  $N$ . The latter two findings can be explained excellently using the single-particle orbital picture: One can approximate the ground state crossing field strengths using the energy coincidence field strength of the corresponding hydrogen orbitals. Due to the electronic interactions this picture will only yield a crude estimate and the calculated transition field strengths in many-particle systems are much smaller than found by this rough approximation. However, with rising  $Z$ , electronic interaction energies become negligible in comparison with the electron-core potential and in the limit of infinite nuclear charge the total energy can be approximated by summing the single-particle energies. Thus, ground state crossing field strengths at large  $Z$  rise and slowly approach the value obtained by the single-particle estimate (see Ref. [105]).

The rise of the crossing field strengths with  $N$  is caused by a different effect, which we again explain in the single-particle picture. Ground state changes in the magnetic polarization regime typically correspond to an occupation shift from an orbital found close to the nucleus, whose binding energy is reduced due to an excitation either regarding the spin or  $\nu'$  quantum number, to such an orbital with a larger separation to the core but with adapted spin or lower longitudinal excitation  $\nu'$ , respectively. The binding energy of the latter orbital is affected more by electronic repulsion than the binding energy of the inner orbital. Thus, the more electrons are involved, the larger magnetic fields are necessary to induce ground state crossings. This increase of  $\beta_Z^{\text{Tr}}$  with  $N$  also explains the reduction of the 2DLHFR errors with rising  $N$ : Larger field strengths correspond to smaller errors caused by the employed Landau expansion. In fact, this nature of the ground state crossings even gives an explanation for the finding that the 2DLHFR method typically predicts lower field strengths for the ground state transitions compared to the FPDQMC results. The orbital in spatial proximity to the core is not described as well as the outer orbital by the single-particle Landau expansion. This relative energy shift between the two electronic configurations in the 2DLHFR method corresponds to a smaller predicted  $\beta$  for ground state transitions as found by the FPDQMC method.

In Tabs. 6.16 and 6.17 we compare our magnetic field strengths for the transitions to the HFGS regime with those from Ref. [105]. Although these transitions occur at larger  $\beta_Z$  for most elements, we do not find smaller relative differences between both methods compared with those found for the PSP-FSP change of regime. Instead, the deviations to the FPDQMC results almost reach 4% in the case of neutral carbon. This is caused by the fact that the energy functions  $E(\beta_Z)$  of the configurations 1 and 0 show a very similar gradient and progress almost in parallel. The crossing of these two states corresponds to the beginning of the HFGS regime for all ions with  $N > 4$ . Small differences in those two states' energy may lead to large differences in the predicted crossing field strength and thus the onset of the HFGS regime [46].

**Tab. 6.16:** Magnetic field strength  $\beta_Z^{\text{Tr}}$  at the occurrence of the high-field ground state configuration for  $2 \leq Z \leq 10$  and  $2 \leq N \leq Z$  obtained with the 2DLHFR program.

Z	N = 2	N = 3	N = 4	N = 5	N = 6	N = 7	N = 8	N = 9	N = 10
2	0.0923								
3	0.1149	0.1196							
4	0.1270	0.1393	0.1414						
5	0.1343	0.1520	0.1571	0.1597					
6	0.1394	0.1607	0.1682	0.2019	0.2590				
7	0.1430	0.1672	0.1766	0.2340	0.3108	0.3743			
8	0.1458	0.1722	0.1828	0.2595	0.3517	0.4333	0.5032		
9	0.1479	0.1760	0.1879	0.2792	0.3852	0.4818	0.5699	0.6444	
10	0.1496	0.1791	0.1921	0.2961	0.4101	0.5220	0.6251	0.7166	0.7924

**Tab. 6.17:** Magnetic field strength  $\beta_Z^{\text{Tr}}$  at the occurrence of the high-field ground state configuration for  $2 \leq Z \leq 10$  and  $2 \leq N \leq Z$  as found by the FPDQMC method, taken from Boblest et al. [105]. Numbers in brackets denote statistical uncertainties of the FPDQMC method.

Z	N = 2	N = 3	N = 4	N = 5	N = 6	N = 7	N = 8	N = 9	N = 10
2	0.09393(4)								
3	0.11744(3)	0.12212(3)							
4	0.12993(4)	0.14229(4)	0.14432(4)						
5	0.13763(4)	0.15510(4)	0.16023(4)	0.1657(3)					
6	0.14292(4)	0.16404(4)	0.17145(4)	0.2067(3)	0.2693(4)				
7	0.14675(3)	0.17059(3)	0.17979(3)	0.2378(3)	0.3181(3)	0.3864(4)			
8	0.14960(3)	0.17556(3)	0.18627(3)	0.2622(3)	0.3571(3)	0.4430(3)	0.5172(4)		
9	0.15189(3)	0.17947(4)	0.19137(3)	0.2816(3)	0.3880(3)	0.4894(3)	0.5805(3)	0.6581(6)	
10	0.15372(3)	0.18266(3)	0.19547(3)	0.2971(3)	0.4141(4)	0.5279(3)	0.6335(4)	0.7071(4)	0.8076(4)

### 6.4.3 Complete data set of ground state configurations

In the following we give a compilation of all ground state configurations for atoms and ions with  $2 \leq Z \leq 21$  and  $2 \leq N \leq Z$  at  $\beta_Z \gtrsim 0.05$ . Tables 6.18 to 6.35 present the data in the following manner. The first column denotes the nuclear charge and number of electrons in the format  $Z$ - $N$ . Further columns give the ground state transition field strength  $\beta_Z^{\text{Tr}}$  for the transition from the configuration given in the current column header to the configuration denoted in the column to the right. In the case of the last column, this corresponds to the transition to the HFGS configuration, which is not explicitly mentioned in the tables. Thus, the values of  $\beta_Z$  correspond to the highest field strength where the given configuration is ground state. We merged those ions that show the same ground state configuration sequence with rising  $\beta$  into the same tables. In this way we achieve fully occupied tables and a compact representation of the data. Inside the tables the data are sorted with regard to first  $Z$  and then  $N$ . The tables themselves are approximately sorted according to increasing  $N$ . The number of ground state transitions we found in the investigated region of the magnetic field strength rises, apart from some exceptions, with  $N$ , from 2 different configurations in Tab. 6.18 to 10 configurations in Tab. 6.35. As we have already shown in Figs. 6.3 and 6.4 some configurations have a very small range of  $\beta$  where they form the ground state. An extreme example is found in Tab. 6.27. For  $Z = 14$  and  $N = 13$  the configuration 31 is found to be ground state at  $\beta_Z = 0.2190 \rightarrow 0.2192$ . As our predictions for  $\beta_Z^{\text{Tr}}$  are subject to small errors we suggest to re-investigate such narrow passages of ground state configurations with the more extensive FPDQMC method as well.

For this most complete investigation of ground state configurations at strong magnetic fields we have computed about 970.000 HFFER II-states and additionally 150.000 states with the 2DLHFR program in just about three months on approximately 20 3.2 GHz quad-core processors, the best evidence for the efficiency and reliability of these two programs.

**Tab. 6.18:** Ground state crossings field strengths  $\beta_Z^{\text{Tr}}$  for different ions with  $Z = 2 \dots 21$  and  $N = 2 \dots 4$ . Details see text.

$Z-N$	$\bar{0}$	$Z-N$	$\bar{0}$
2-2	0.0923	11-3	0.1818
3-2	0.1149	12-2	0.1523
3-3	0.1196	12-3	0.1840
4-2	0.1270	13-2	0.1533
4-3	0.1393	13-3	0.1858
4-4	0.1414	14-2	0.1541
5-2	0.1343	14-3	0.1874
5-3	0.1520	15-2	0.1549
5-4	0.1571	15-3	0.1888
6-2	0.1394	16-2	0.1555
6-3	0.1607	16-3	0.1900
6-4	0.1682	17-2	0.1561
7-2	0.1430	17-3	0.1910
7-3	0.1672	18-2	0.1567
8-2	0.1458	18-3	0.1921
8-3	0.1722	19-2	0.1571
9-2	0.1479	19-3	0.1930
9-3	0.1760	20-2	0.1576
10-2	0.1496	20-3	0.1937
10-3	0.1791	21-2	0.1579
11-2	0.1511	21-3	0.1944

**Tab. 6.19:** Ground state crossings for  $Z = 7 \dots 12$  and  $N = 4$ .

$Z-N$	$\bar{1}$	$\bar{0}$
7-4	0.0529	0.1766
8-4	0.0590	0.1828
9-4	0.0645	0.1879
10-4	0.0688	0.1921
11-4	0.0725	0.1956
12-4	0.0754	0.1984

**Tab. 6.20:** Ground state crossings for  $Z = 5 \dots 21$  and  $N = 4 \dots 5$ .

$Z-N$	$\bar{1}$	$\bar{0}$	1
5-5	0.0533	0.1584	0.1597
6-5	0.0806	0.1688	0.2019
7-5	0.1027	0.1766	0.2340
8-5	0.1194	0.1825	0.2595
9-5	0.1338	0.1871	0.2792
10-5	0.1458	0.1911	0.2961
11-5	0.1552	0.1943	0.3093
12-5	0.1628	0.1969	0.3203
13-4	0.0780	0.2007	0.2017
13-5	0.1707	0.1991	0.3298
14-4	0.0802	0.2026	0.2054
14-5	0.1764	0.2010	0.3382
15-4	0.0821	0.2042	0.2087
15-5	0.1824	0.2028	0.3463
16-4	0.0842	0.2058	0.2118
16-5	0.1871	0.2044	0.3527
17-4	0.0857	0.2071	0.2146
17-5	0.1910	0.2058	0.3583
18-4	0.0870	0.2082	0.2170
18-5	0.1937	0.2070	0.3633
19-4	0.0878	0.2092	0.2193
19-5	0.1973	0.2080	0.3678
20-4	0.0889	0.2101	0.2216
20-5	0.2004	0.2090	0.3719
21-4	0.0899	0.2109	0.2235
21-5	0.2029	0.2099	0.3749

**Tab. 6.21:** Ground state crossings for  $Z = 6, 7$  and  $N = 6$ .

$Z-N$	$\bar{21}$	$\bar{1}$	$\bar{0}$	1
6-6	0.0615	0.1118	0.1670	0.2590
7-6	0.0654	0.1519	0.1749	0.3108

**Tab. 6.22:** Ground state crossings for  $Z = 7 \dots 21$  and  $N = 6 \dots 9$ .

$Z-N$	$\bar{2}1$	$\bar{1}$	1
7-7	0.0780	0.1748	0.3743
8-6	0.0683	0.1811	0.3517
8-7	0.0822	0.1834	0.4333
8-8	0.0952	0.1845	0.5032
9-6	0.0709	0.1874	0.3852
9-7	0.0866	0.1905	0.4818
9-8	0.1009	0.1921	0.5699
9-9	0.1123	0.1929	0.6444
10-6	0.0728	0.1928	0.4101
10-7	0.0904	0.1963	0.5220
10-8	0.1054	0.1985	0.6251
10-9	0.1190	0.1997	0.7166
11-6	0.0745	0.1972	0.4333
11-7	0.0934	0.2014	0.5557
11-8	0.1097	0.2040	0.6722
12-6	0.0759	0.2010	0.4518
12-7	0.0961	0.2056	0.5834
12-8	0.1136	0.2086	0.7099
13-6	0.0772	0.2042	0.4685
13-7	0.0981	0.2092	0.6071
13-8	0.1170	0.2126	0.7453
14-6	0.0781	0.2069	0.4816
14-7	0.1004	0.2123	0.6284
14-8	0.1203	0.2160	0.7737
15-6	0.0792	0.2095	0.4935
15-7	0.1014	0.2152	0.6466
15-8	0.1225	0.2192	0.8006
16-6	0.0799	0.2116	0.5040
16-7	0.1032	0.2176	0.6642
17-6	0.0805	0.2137	0.5136
17-7	0.1045	0.2199	0.6784
18-6	0.0811	0.2154	0.5219
18-7	0.1057	0.2219	0.6912
19-6	0.0817	0.2169	0.5308
19-7	0.1068	0.2236	0.7028
20-6	0.0822	0.2184	0.5379
20-7	0.1078	0.2252	0.7131
21-6	0.0827	0.2196	0.5441
21-7	0.1087	0.2267	0.7213

**Tab. 6.23:** Ground state crossings for  $Z = 11, 12, 16 \dots 21$  and  $N = 8, 9$ .

$Z-N$	$\overline{31}$	$\overline{21}$	$\overline{1}$	1
11-9	0.0583	0.1254	0.2055	0.7765
12-9	0.0677	0.1307	0.2106	0.8295
16-8	0.0528	0.1249	0.2219	0.8220
17-8	0.0557	0.1268	0.2243	0.8416
18-8	0.0578	0.1287	0.2264	0.8598
19-8	0.0600	0.1303	0.2284	0.8760
20-8	0.0619	0.1314	0.2302	0.8908
21-8	0.0636	0.1327	0.2318	0.9044

**Tab. 6.24:** Ground state crossings for  $Z = 10, 11, 13$  and  $N = 9, 10$ .

$Z-N$	$\overline{31}$	$\overline{21}$	$\overline{1}$	2	1
10-10	0.0656	0.1328	0.2002	0.2013	0.7924
11-10	0.0830	0.1405	0.2053	0.2343	0.8702
13-9	0.0756	0.1353	0.2142	0.2258	0.8749

**Tab. 6.25:** Ground state crossings for  $Z = 11 \dots 21$  and  $N = 9 \dots 11$ .

$Z-N$	$\overline{31}$	$\overline{21}$	$\overline{2}$	$\overline{1}$	2	1
11-11	0.1081	0.1460	0.1695	0.2047	0.2752	0.9493
12-10	0.0976	0.1391	0.1595	0.2098	0.2619	0.9380
12-11	0.1284	0.1417	0.1936	0.2091	0.3099	1.0346
13-10	0.1104	0.1390	0.1782	0.2134	0.2859	0.9942
14-9	0.0831	0.1365	0.1430	0.2175	0.2391	0.9134
14-10	0.1219	0.1385	0.1948	0.2167	0.3070	1.0457
15-9	0.0893	0.1370	0.1533	0.2203	0.2538	0.9474
15-10	0.1330	0.1380	0.2097	0.2195	0.3257	1.0895
16-9	0.0927	0.1369	0.1621	0.2229	0.2642	0.9784
17-9	0.1001	0.1374	0.1693	0.2250	0.2759	1.0050
18-9	0.1045	0.1374	0.1772	0.2270	0.2855	1.0305
19-9	0.1090	0.1376	0.1833	0.2288	0.2940	1.0528
20-9	0.1126	0.1377	0.1884	0.2304	0.3017	1.0727
21-9	0.1164	0.1374	0.1952	0.2319	0.3087	1.0910

**Tab. 6.26:** Ground state crossings for  $Z = 16$  and  $N = 10$ .

$Z-N$	$\overline{31}$	$\overline{2}$	$\overline{1}$	2	1
16-10	0.1397	0.2207	0.2222	0.3424	1.1284



**Tab. 6.27:** Ground state crossings for  $Z = 12 \dots 21$  and  $N = 10 \dots 13$ .

$Z-N$	$\overline{31}$	$\overline{2}$	2	1
12-12	0.1480	0.2092	0.3536	1.1161
13-11	0.1427	0.2133	0.3438	1.1041
13-12	0.1562	0.2141	0.3960	1.2025
13-13	0.1734	0.2183	0.4560	1.3151
14-11	0.1483	0.2173	0.3717	1.1684
14-12	0.1635	0.2183	0.4317	1.2793
15-11	0.1532	0.2208	0.3973	1.2225
15-12	0.1697	0.2221	0.4644	1.3465
16-11	0.1582	0.2241	0.4198	1.2736
17-10	0.1418	0.2248	0.3569	1.1654
17-11	0.1625	0.2270	0.4403	1.3176
18-10	0.1510	0.2285	0.3711	1.1968
18-11	0.1656	0.2393	0.4775	1.3771
19-10	0.1482	0.2295	0.3835	1.2252
19-11	0.1689	0.2320	0.4754	1.3899
20-10	0.1503	0.2315	0.3946	1.2507
20-11	0.1719	0.2341	0.4907	1.4220
21-10	0.1521	0.2333	0.4045	1.2742
21-11	0.1745	0.2361	0.5042	1.4514

**Tab. 6.28:** Ground state crossings for  $Z = 16 \dots 20$  and  $N = 12$ .

$Z-N$	$\overline{41}$	$\overline{31}$	$\overline{2}$	2	1
16-12	0.0578	0.1765	0.2254	0.4952	1.4069
17-12	0.0634	0.1813	0.2286	0.5217	1.4595
18-12	0.0644	0.1858	0.2313	0.5460	1.5072
19-12	0.0738	0.1890	0.2338	0.5682	1.5505
20-12	0.0785	0.1936	0.2361	0.5866	1.5899

**Tab. 6.29:** Ground state crossings for  $Z = 14 \dots 21$  and  $N = 12 \dots 15$ .

$Z-N$	$\overline{41}$	$\overline{31}$	$\overline{2}$	31	2	1
14-13	0.0616	0.1774	0.2190	0.2192	0.4889	1.3780
14-14	0.0773	0.1910	0.2183	0.2354	0.5400	1.4621
15-13	0.0720	0.1846	0.2225	0.2279	0.5290	1.4595
15-14	0.0901	0.2012	0.2219	0.2454	0.5886	1.5570
15-15	0.1076	0.2154	0.2214	0.2603	0.6397	1.6431
16-13	0.0797	0.1936	0.2257	0.2354	0.5674	1.5287
16-14	0.1019	0.2098	0.2251	0.2546	0.6330	1.6409
17-13	0.0889	0.2001	0.2286	0.2421	0.6007	1.5934
17-14	0.1139	0.2183	0.2279	0.2626	0.6756	1.7164
18-13	0.0951	0.2052	0.2312	0.2493	0.6311	1.6504
19-13	0.1037	0.2106	0.2334	0.2550	0.6591	1.7337
20-13	0.1105	0.2154	0.2355	0.2597	0.6902	1.7530
21-12	0.0814	0.1972	0.2380	0.2393	0.6058	1.6289

**Tab. 6.30:** Ground state crossings for  $Z = 16, 18, 19, 21$  and  $N = 13 \dots 15$ .

$Z-N$	$\overline{41}$	$\overline{31}$	$\overline{2}$	31	3	2	1
16-15	0.1242	0.2244	0.2246	0.2679	0.2758	0.6944	1.7413
18-14	0.1258	0.2242	0.2306	0.2640	0.2793	0.7120	1.7850
19-14	0.1362	0.2309	0.2328	0.2660	0.2951	0.7472	1.8496
21-13	0.1167	0.2206	0.2374	0.2640	0.2655	0.7074	1.7968

**Tab. 6.31:** Ground state crossings for  $Z = 16 \dots 18, 20, 21$  and  $N = 14 \dots 16$ .

$Z-N$	$\overline{41}$	$\overline{31}$	31	3	2	1
16-16	0.1448	0.2251	0.2722	0.3096	0.7510	1.8285
17-15	0.1414	0.2280	0.2667	0.3022	0.7449	1.8303
18-15	0.1546	0.2310	0.2667	0.3259	0.7897	1.9117
20-14	0.1397	0.2351	0.2665	0.3104	0.7784	1.9060
21-14	0.1494	0.2373	0.2660	0.3225	0.8073	1.9574

**Tab. 6.32:** Ground state crossings for  $Z = 17 \dots 20$  and  $N = 15 \dots 17$ .

$Z-N$	$\overline{51}$	$\overline{41}$	$\overline{31}$	41	31	3	2	1
17-16	0.0562	0.1645	0.2281	0.2383	0.2704	0.3414	0.8092	1.9299
17-17	0.0688	0.1887	0.2278	0.2677	0.2744	0.3751	0.8611	2.0193
18-16	0.0640	0.1856	0.2307	0.2639	0.2694	0.3691	0.8621	2.0257
19-15	0.0531	0.1699	0.2334	0.2455	0.2689	0.3438	0.8313	1.9840
20-15	0.0580	0.1828	0.2354	0.2610	0.2691	0.3656	0.8691	2.0506

**Tab. 6.33:** Ground state crossings for  $Z = 18 \dots 21$  and  $N = 15 \dots 17$ .

$Z-N$	$\overline{51}$	$\overline{41}$	$\overline{31}$	41	3	2	1
18-17	0.0790	0.2119	0.2305	0.2840	0.4071	0.9259	2.1274
19-16	0.0712	0.2013	0.2330	0.2762	0.3954	0.9098	2.1079
20-16	0.0779	0.2205	0.2351	0.2855	0.4203	0.9551	2.1845
21-15	0.0611	0.1961	0.2373	0.2714	0.3834	0.9036	2.1106
21-16	0.0840	0.2364	0.2369	0.2930	0.4420	0.9960	2.2512

**Tab. 6.34:** Ground state crossings for  $Z = 18 \dots 21$  and  $N = 17 \dots 20$ .

$Z-N$	$\overline{62}$	$\overline{51}$	$\overline{41}$	41	3	2	1
18-18	0.0561	0.0929	0.2303	0.2976	0.4469	0.9845	2.2154
19-17	0.0539	0.0884	0.2328	0.2936	0.4426	0.9826	2.2197
19-18	0.0592	0.1051	0.2333	0.3103	0.4852	1.0495	2.3192
19-19	0.0646	0.1204	0.2336	0.3264	0.5236	1.1101	2.4090
20-17	0.0566	0.0964	0.2355	0.3050	0.4719	1.0362	2.3045
20-18	0.0626	0.1163	0.2360	0.3233	0.5208	1.1105	2.4174
20-19	0.0688	0.1377	0.2364	0.3404	0.5656	1.1793	2.5193
20-20	0.0744	0.1520	0.2366	0.3551	0.6295	1.2377	2.6102
21-17	0.0596	0.1044	0.2378	0.3138	0.4990	1.0837	2.3828
21-18	0.0657	0.1253	0.2386	0.3322	0.5527	1.1666	2.5070
21-19	0.0723	0.1494	0.2390	0.3509	0.6033	1.2427	2.6200
21-20	0.0791	0.1698	0.2394	0.3679	0.6478	1.3109	2.7258

**Tab. 6.35:** Ground state crossings for  $Z = 21$  and  $N = 21$ .

$Z-N$	$\overline{72}$	$\overline{62}$	$\overline{51}$	$\overline{41}$	51	41	3	2	1
21-21	0.0579	0.0850	0.1883	0.2392	0.2526	0.3826	0.6958	1.3754	2.8187



# Conclusion and outlook

## Conclusion

In the first part of this work we presented a fast and accurate method to calculate energies and wave functions for hydrogen in magnetic fields of arbitrary strength. We applied three different wave function expansions, using spherical harmonics, Landau orbitals and two-dimensional finite elements with  $B$ -splines. The latter proved to work best as it allows for an efficient description of the electronic wave function at any magnetic field strength. The iterative adaption of the expansion parameters enables the computation of hydrogen states with any energy precision demanded. Additionally, we implemented an automated magnetic field strength variation that allows for a compact description of the energy and wave function in dependence of the magnetic field strength. With the help of this program we investigated the lowest 30 states for each value of the magnetic quantum number  $m = 0, -1, \dots, -4$  and  $z$ -parity  $\pi_z = \pm 1$ , which emerge from the field-free states with principal quantum numbers up to  $n = 15$ , at magnetic fields from  $\beta = 0$  to  $\beta = 1000$ . However, the program is not restricted to these quantum numbers and can be readily applied to states with any magnetic quantum or excitation number, at any magnetic field strength. To facilitate further investigations in this field the program was modified for easy-to-use access and then published [113]. We calculated all dipole strengths and energies for transitions that involve the aforementioned states in the Lyman, Balmer, Paschen and Brackett series. These transition data are currently used by astrophysicists around the world to enhance spectral fits of magnetic white dwarf emission spectra [13].

In the second part of this work we switched our focus to the description of many-electron systems, i.e. heavier elements up to iron, in intermediate to strong magnetic fields by means of unrestricted Hartree-Fock methods. Here, we used two types of Landau orbital wave function expansions, a product ansatz and a full two-dimensional expansion, where we employed  $B$ -splines on finite elements to expand the longitudinal wave function components. Both types of expansion are realized in individual, highly speed-optimized programs. The first one of these programs, HFFER II, is based upon a previous implementation by Engel, with tremendous improvements with respect to convergence behavior and execution speed: We introduced individual finite element expansions for each orbital and used an optimal number of  $B$ -splines to balance the precision of our results and the computing effort. Additionally, we precalculated the interaction potentials for further runtime reduction. Together, these measures reduce the average runtime of this program by a factor of 80 compared to previous implementations. Again,

we published the program [92] to support future activities in this field of research.

The second one of these programs, 2DLHFR, features a full two-dimensional description of electronic wave functions using up to 31 Landau channels with individual longitudinal wave function components. This expands the region of accessible magnetic fields within our high-field ansatz down to  $\beta_Z \approx 0.1$  and enhances the accuracy of our results. In comparison to the highly precise FPDQMC algorithm the 2DLHFR energies usually deviate by about 0.5% to 1%, an extraordinary precision for Hartree-Fock methods. The 2DLHFR program has also been optimized for short runtimes: We reused the longitudinal finite element bases that were optimized by the HFFER II program. Additionally, we dropped electron-electron interaction terms of higher Landau channels, based upon the Landau channel occupation found by the HFFER II method. We implemented a simple quantum Monte Carlo algorithm to be able to compensate for these approximations and analyzed a huge number of states to ensure that this modification of the energy functional has negligible effects on the precision of our results. To calculate transition energies and oscillator strengths we created additional tools for both programs.

We compared our state energies, as well as transition energies and strengths with those of other methods. These comparisons prove the high accuracy of our results. Further, the combination of the HFFER II and 2DLHFR programs was used to analyze the ground state configurations of all atoms and ions from helium to scandium for magnetic field strengths  $\beta_Z \gtrsim 0.05$ . These findings can be applied directly to further investigations of these systems, e.g. the calculation of excitation energies and thus Boltzmann weights of excited states, as they are needed for the determination of ionization fractions or the thermal weighting of transition lines. All state energies and wave functions are stored in a uniform file format that allows further processing of our findings, i.e. as trial wave functions for the FPDQMC algorithm or for photoionization calculations. As a final remark we point out that the HFFER II plus 2DLHFR program package provides the long awaited efficient description of light to heavy atoms in intermediate to strong magnetic fields. Its power to quickly calculate all states relevant to the description of atoms in the atmosphere of neutron stars for the first time brings a comprehensive description of the atmospheres of these fascinating objects within reach.

## Outlook

We have achieved many objectives in this work, however, several open questions still remain. Most of these questions are connected to the approximations made in this work, i.e. regarding effects of the finite nuclear mass, the collective motion in magnetic fields or the effects of relativity in very strong fields. The first two effects are strongly correlated, as for the description of a moving atom or ion in a magnetic field the motions of the center of mass and the electronic shell are coupled. Then a pseudo-separation of internal and external degrees of freedom of such systems is no longer possible and, as we already mentioned, scaling relations of these systems from infinite to finite nuclear mass do not exist. It is important to overcome the approximations and to investigate these

---

motional Stark effects on the structure and energies of ions and atoms moving across the magnetic field, as these effects are expected to dominate the line profiles of bound-bound and bound-free transitions. This would also allow to treat additional external electric fields, which are expected to exist in a neutron star atmosphere. An integral description of these effects requires full three-dimensional calculations and should be applied to hydrogen first, for the reason of simplicity as well as with the intent to enhance the understanding of these effects on the spectra of hydrogen-rich magnetic white dwarfs. The consideration of relativistic effects could be relevant for heavier atoms, as they feature high binding energies of the inner electrons at strong magnetic fields, whereas for the lighter elements only small relativistic corrections below the Hartree-Fock energy resolution are to be expected.

The restriction to strong magnetic fields inherent to the Landau single-particle wave function expansion makes it clear that a more general ansatz based on the 2D  $B$ -spline expansion in Eq. (2.9) is likewise desirable for the wave function description in many-particle systems. These could then also be investigated at magnetic fields of arbitrary strength. Based upon our experience with this expansion for the description of hydrogen states we expect only a moderate increase in computing effort compared to the current implementation featuring the Landau expansion. In combination with a Hartree-Fock, a configuration interaction or a quantum Monte-Carlo algorithm, these single-particle wave function expansions would then represent the state of the art for atoms in magnetic fields for years to come.

To finally understand the absorption features in the thermal spectra of isolated neutron stars, the calculation of ionization equilibria that include effects of high temperature, mass density and fluctuating electric fields in NS atmospheres are necessary. In addition, one has to unite the bound-bound, bound-free and free-free photoabsorption cross sections and include thermal weights and ionization fractions as well as, yet unknown, line profiles, for the purpose of understanding the propagation of photons in the NS atmosphere. This tremendous effort, resulting in detailed predictions for neutron star spectra, will then justify further campaigns of astronomers to search for additional isolated neutron stars with thermal emission and to obtain high resolution spectra of these stellar remnants, to finally uncover their mysterious nature.





# Zusammenfassung in deutscher Sprache

Der Titel dieser Arbeit lautet: „2D Rechnungen für Atome und Ionen in den starken Magnetfeldern von Weißen Zwergen und Neutronensternen“.

## Einleitung

Auf der Oberfläche magnetischer Weißer Zwerge (MWZ) können starke Magnetfelder von bis zu  $10^5$  T gefunden werden. Noch wesentlich stärkere Magnetfelder von bis zu  $10^{11}$  T werden auf Neutronensternoberflächen vermutet. Der Einfluss solch starker Felder auf die Struktur von Atomen ist bereits seit einigen Jahrzehnten Gegenstand der Forschung. Dennoch sind insbesondere Mehrelektronensysteme in starken Feldern noch nicht völlig verstanden. Einer der Gründe für diesen langsamen Fortschritt ist, dass selbst das Wasserstoffatom in Magnetfeldern nicht mehr analytisch beschrieben werden kann, sondern über einen weiten Magnetfeldstärkebereich durch numerische Verfahren behandelt werden muss (siehe [3–6]). Ruder et al. [7] veröffentlichten für Magnetfeldstärken von  $B = 0$  T bis  $B \approx 5 \cdot 10^8$  T einen umfassenden Datensatz an Energieniveaus, Übergangsenergien und Oszillatorstärken für die 38 tieflegendsten Wasserstoffzustände, die sich aus den feldfreien Zuständen mit Hauptquantenzahlen  $n \leq 5$  entwickeln. Neue Ansätze von Kravchenko et al. [8, 9] und Stubbins et al. [10] erlauben die Berechnung von Energieniveaus mit bis zu 15 oder gar 30 Stellen Genauigkeit. Diese Arbeiten beschränken sich jedoch auf einige wenige, tiefliegende Zustände. Für eine kleine Auswahl an Magnetfeldstärken und Zuständen wurde auch eine relativistische Beschreibung des Wasserstoffproblems im Magnetfeld durch Lindgren und Virtamo [11] sowie Chen und Goldman [12] unternommen.

Mit Hilfe dieser atomaren Daten konnten Wasserstoffabsorptionsmerkmale in den Spektren von MWZs, beispielsweise GRW+70°8247, identifiziert werden [14]. Umfassende Modellatmosphären-Rechnungen von Euchner et al. [17–19] erlauben heute die Rekonstruktion der Magnetfeldtopologie von MWZs mit Wasserstoffatmosphäre, inklusive magnetischer Dipol- und Quadrupolmomente. Die Analyse von MWZs mit schwachen Feldern um 2 MG bleibt jedoch laut Kepler et al. [13] bisher verwehrt, da in diesem Bereich sehr wenige Daten für Wasserstoffzustände mit Hauptquantenzahl  $n > 5$  vorliegen. Der erste Teil dieser Arbeit schließt diese Lücke und präsentiert umfangreiche Liniendaten für Wasserstoff in beliebig starken Magnetfeldern für Zustände bis zu Hauptquantenzahlen  $n = 15$ .

Der zweite Teil dieser Arbeit widmet sich Mehrelektronensystemen in den starken Magnetfeldern auf der Oberfläche von Neutronensternen (NS). Die Spektren dieser Objekte sind noch nahezu unverstanden. Dies hat mehrere Gründe: Die Lösung von Mehrelektronenproblemen in starken Magnetfeldern ist von erheblicher Komplexität, da eine effiziente Beschreibung der Wellenfunktionen aufgrund struktureller Veränderungen derselben im Magnetfeld erschwert wird. Zugleich herrschen in einer Neutronensternatmosphäre extrem hohe Temperaturen von bis zu  $k_B T_{\text{eff}} = 200 \text{ eV}$  sowie Massendichten von bis zu  $100 \text{ g/cm}^3$  [47]. Das Magnetfeld bewirkt zudem eine Kopplung von inneren und äußeren atomaren Freiheitsgraden, sodass die Temperatur einen erheblich größeren Einfluss auf die spektralen Linienformen gewinnt, als durch die Dopplerverbreiterung zu erwarten wäre. Fluktuierende elektrische Felder erhöhen abermals den Komplexitätsgrad einer möglichen Atmosphärenmodellierung. Die Basis einer solchen ist jedoch eine umfassende Datenbank mit einem dichten Netz an Datenpunkten von atomaren Zuständen und Übergängen. Bisher sind lediglich für Helium umfangreiche Liniendaten (siehe beispielsweise Becken et al. [26–29, 85]) vorhanden. Für Lithium und Beryllium in starken Feldern liegen noch eine kleine Anzahl an Energiewerten (siehe Wang et al. [39], Al-Hujaj et al. [40]) vor, während für schwere Elemente nur für vier Magnetfeldstärken Grundzustandsenergien berechnet wurden (siehe Mori et al. [24, 42], Engel et al. [43], Bücheler et al. [44] und Meyer et al. [45]). Boblest [46] veröffentlichte erst kürzlich einen vollständigen Satz der Grundzustandsenergien für alle Atome und Ionen von Helium bis Neon in starken Magnetfeldern. Erst wenn diese atomaren Datenbanken komplettiert sind, kann die komplexe Aufgabe der Neutronensternatmosphärenmodellierung erfolgreich angegangen werden.

## Wasserstoff in Magnetfeldern beliebiger Stärke

Der nichtrelativistische Hamiltonoperator eines Elektrons im Coulombpotential der Ladung  $Z = 1$  und einem homogenen magnetischen Feld  $\mathbf{B} = B\mathbf{e}_z$  lautet

$$\hat{H} = -\Delta + 2\beta m + \beta^2 \rho^2 + 4\beta m_s - \frac{2}{|\mathbf{r}|}, \quad (1)$$

wobei wir hier und im Folgenden atomare Rydberg-Einheiten verwenden. Die Magnetfeldstärke  $\beta = B/B_0$  wird in Vielfachen der Referenzfeldstärke  $B_0 \approx 4.7 \times 10^5 \text{ T}$  angegeben. Die Symbole  $m$  und  $m_s$  bezeichnen die magnetische Quantenzahl und die  $z$ -Projektion des Elektronenspins. Des Weiteren verwenden wir die symmetrische Eichung  $\mathbf{A}(\mathbf{r}) = \frac{1}{2}\mathbf{B} \times \mathbf{r}$  des Vektorpotentials. Im Gegensatz zum bekannten Wasserstoffhamiltonoperator hat Gl. (1) zylindrische Symmetrie, und der Drehimpuls  $l$  ist keine gute Quantenzahl mehr. Es verbleibt daher, neben  $m$  und  $m_s$ , nur die  $z$ -Parität als gute Quantenzahl. Zusammen mit der Anregungszahl  $\nu$  können wir die Zustände in der Form  $(m, \pi_z, \nu, \{\uparrow\})$  darstellen, wobei die Spinausrichtung nur angegeben wird, falls der Spin parallel zum Magnetfeld, also nach “oben”, ausgerichtet ist.

Der obige Hamiltonoperator ist äquivalent zum Problem eines unbewegten Wasserstoffatoms im Magnetfeld mit unendlicher Protonenmasse  $m_p$ . Relationen zwischen den

Lösungen mit endlicher und unendlicher Kernmasse (siehe Pavlov-Verevkin et al. [58] sowie Refs. [7, 26]) erlauben diese Vereinfachung. Die Lösungen der Zustände mit positiver und negativer magnetischer Quantenzahl, bzw. mit Spinausrichtung “oben” und “unten” sind außerdem durch eine triviale Energieverschiebung von  $4m\beta$  bzw.  $4\beta$  miteinander verknüpft. Wir können uns daher auf die Berechnung von Zuständen mit  $m \leq 0$  und  $m_s = -\frac{1}{2}$  beschränken. Wir vernachlässigen in dieser Arbeit die Auswirkungen möglicher Schwerpunktsbewegungen oder relativistischer Effekte. Durch letztere sind gemäß Refs. [11, 12, 67] keine größeren Abweichungen unserer Ergebnisse zu erwarten. Die Beschreibung bewegter Atome in magnetischen und elektrischen Feldern ist an unserem Institut Gegenstand aktueller Forschung durch Kersting (siehe auch Refs. [60–65]).

## Darstellung der Wellenfunktionen

In schwachen Magnetfeldern dominiert die Coulomb-Wechselwirkung über das Magnetfeld und es bietet sich eine Entwicklung der Wellenfunktionen nach Kugelflächenfunktionen  $Y_{lm}$  in der Form

$$\psi(\mathbf{r}) = \sum_l^{l_{\max}} \frac{1}{r} f_l(r) Y_{lm}(\vartheta, \phi) \quad (2)$$

über verschiedene Drehimpulse  $l$  an (siehe Rösner et al. [6, 68]). Im Falle der Dominanz des Magnetfeldes für  $\beta \gtrsim 1$  ist eine Entwicklung nach Landauorbitalen  $\Phi_{nm}$  [70] in der Form

$$\psi(\mathbf{r}) = \sum_{n=0}^{N_L} P_n(z) \Phi_{nm}(\rho, \phi), \quad (3)$$

die geeignetere Wahl. Diese beschreiben die Bewegung eines freien geladenen Teilchens im Magnetfeld, wobei  $n$  die Landauquantenzahl angibt. In dem zwischenliegenden Bereich der Magnetfeldstärke jedoch konvergiert keine dieser beiden Entwicklungen hinreichend gut und ein allgemeinerer Ansatz (siehe Wang et al. [5])

$$\psi(\mathbf{r}) = \frac{e^{im\phi}}{\sqrt{2\pi}} \sum_{\mu\nu} \alpha_{\mu\nu} B_\mu(\rho) B_\nu(z) \quad (4)$$

ist notwendig. Hier werden die  $\rho$ - und  $z$ -Komponente mit Hilfe von  $B$ -splines [69] und deren Koeffizienten  $\alpha_{\mu\nu}$  auf finiten Elementen dargestellt. Diese Form wurde auch für die Radialfunktionen  $f_l(r)$  und die longitudinalen Funktionen  $P_n(z)$  in den Gleichungen (2) und (3) verwendet. Die Lösung der Schrödingergleichung ergibt sich dann aus der Variation des Energiefunktionals nach den  $B$ -spline-Koeffizienten, was auf ein verallgemeinertes Eigenwertproblem führt, zu dessen Lösung wir die Programmbibliothek LAPACK [72] verwenden.

Die Ergebnisse mehrerer umfangreicher Rechnungen für alle drei Wellenfunktionsentwicklungen in Abb. 2.3 zeigen, dass die 2D  $B$ -spline-Entwicklung (4) in Bereichen

niedriger und hoher Magnetfeldstärke zwar etwas langsamer zu hohen Genauigkeiten konvergiert als die jeweils symmetrieangepasste Wellenfunktionsentwicklung, jedoch bei mittlerem  $\beta$  überlegene Konvergenzeigenschaften aufweist. Die weiteren Wasserstoffergebnisse wurden daher ausschließlich mit Hilfe dieser Entwicklung gewonnen.

Die Wahl der finiten Elemente hat einen erheblichen Einfluss auf Konvergenzgeschwindigkeit und Ergebnisgenauigkeit. Die Basis wird durch die  $B$ -spline-Ordnung  $k$  und die Knotensequenz  $\{x_i\}$  gegeben, die wiederum durch einen Definitionsbereich  $[0, x_{\max}]$ , die Anzahl der finiten Elemente  $N_{\text{fem}}$  und eine Verteilungsfunktion bestimmt wird. Für die Verteilungsfunktion geben wir einen linearen Anstieg der Elementbreiten vor um eine höhere Dichte der finiten Elemente am Kern zu erhalten.  $N_{\text{fem}}$  und  $x_{\max}$  werden individuell für beide Richtungen  $\rho$  und  $z$  bestimmt. Dazu wird die Basislänge  $x_{\max}$  so gewählt, dass die Wellenfunktion bei  $x_{\max}$  in ihrer ausgedehntesten Schnittebene gerade auf  $10^{-6}$  ihres Maximalwertes abgefallen ist (siehe auch Abb. 2.4). Um diese Basislänge zu finden wird eine Vielzahl einzelner Schnitte der Wellenfunktion analysiert. Dies ist wichtig, da eine zu kleine Basis die Funktionswerte in Kernnähe, und damit die Bindungsenergie, überschätzt. Eine zu große Basis hingegen benötigt mehr finite Elemente um die gewünschte Energiepräzision der Ergebnisse zu erreichen. Sobald  $x_{\max}$  für beide Richtungen festgelegt ist, wird die Anzahl der finiten Elemente  $N_{\text{fem}}$  schrittweise erhöht, bis die gewünschte Präzision des Ergebnisses erreicht ist.

## Automatische Magnetfeldvariation

Der Bereich mittelstarker Magnetfeldstärken birgt neben der Herausforderung der Wellenfunktionsbeschreibung noch ein weiteres Problem. Vermiedene Kreuzungen von Zuständen innerhalb eines Symmetrieunterraumes [75] können eine dramatische Veränderung der elektronischen Struktur auf einem kurzen Intervall der Magnetfeldstärke bewirken. Die Anzahl an vermiedenen Kreuzungen steigt mit der Anregungszahl eines Zustandes, wie man in Abb. 2.5 erkennen kann. Darin erscheint die Energiefunktion  $E(\beta)$  des niedrig liegenden Zustandes (orange) glatt im Vergleich zu der durch vermiedene Kreuzungen geprägten Energiefunktion des hochangeregten Zustandes (blau). Um die schnellen Veränderungen bezüglich der Magnetfeldstärke von Energie und Wellenfunktion der Zustände adäquat zu berücksichtigen, ist eine angepasste Schrittweite im Magnetfeldparameter  $\beta$  notwendig. Abbildung 2.6 zeigt deutlich, dass eine äquidistante oder exponentielle Verteilung der Magnetfeldwerte zu großen Fehlern bei der Interpolation der Energiewerte führen kann. Wir haben daher eine automatische Magnetfeldvariation (AMV) implementiert, deren Ablauf in Abb. 2.7 skizziert ist. Die Magnetfeldpunkte werden dabei so bestimmt, dass eine Interpolation der Energiefunktion zwischen den Datenpunkten mit einer absoluten Genauigkeit von  $\epsilon_{\text{int}}$  gewährleistet ist. Dies erlaubt eine präzise Beschreibung der Energie und Wellenfunktion eines Zustandes über einen weiten Bereich der Magnetfeldstärke von  $\beta = 0$  bis  $\beta = 1000$  mit typischerweise 1000 Datenpunkten.

---

## Zustandsenergien

Wir haben jeweils die ersten 30 Anregungszustände aus den Symmetrieunterräumen zu  $m = 0, -1, \dots, -4$  und  $\pi_z = \pm 1$  für Magnetfelder von  $\beta = 0$  bis  $\beta = 1000$  mit einer absoluten Genauigkeit der Energie von  $10^{-7}$  Ry berechnet. Dies ist ausreichend genau um die spektrale Auflösung derzeitiger astronomischer Beobachtungen im Sloan Digital Sky Survey [76] zu übertreffen. Abbildung 2.8 zeigt einen Teil des Wasserstoffenergiespektrums über der magnetischen Feldstärke. Ausnahmsweise sind hier die Energiekorrekturen durch die finite Kernmasse ebenfalls berücksichtigt. Die blauen Beschriftungen bezeichnen Gruppen von Zuständen mit unterschiedlichen Energiefunktionen bezüglich der Magnetfeldstärke:

- A. Die eng gebundenen (engl. “tightly-bound” (tb)) Zustände haben die niedrigste Energie für  $\beta \gtrsim 1$ . Ihre Wellenfunktionen sind knotenfrei in  $z$ -Richtung. Ohne Kernmassenkorrektur divergieren die Energien der tb-Zustände logarithmisch gegen  $-\infty$ .
- B. Die angeregten Zustände bilden bei hoher Magnetfeldstärke wieder eine Rydbergserie aus (siehe Ref. [77]), die rechts durch rote Balken angezeigt ist. Sie werden daher wasserstoff-ähnlich (engl. “hydrogen-like” (hl)) genannt. Die Energie der Zustände mit  $m = 0$  behält diesen Charakter auch mit Korrekturen durch eine finite Kernmasse.
- C. Wasserstoff-ähnliche Zustände mit  $m < 0$  sind bei hohen Feldern durch die Kernmassenkorrektur betroffen. Diese Zustände werden sukzessive autoionisierend.
- D. Zustände mit  $m > 0$  sind um einen Betrag  $4\beta m$  energiewersoben zu denen mit  $m < 0$  und werden bereits bei mittelstarken Feldern autoionisierend. Selbiges trifft auch auf Zustände mit  $m_s = +\frac{1}{2}$  zu, welche um  $4\beta$  zu den spin-down Zuständen energiewersoben sind.

Abbildungen 2.9 und 2.10 zeigen die Energiefunktionen der ersten 30 Zustände der Symmetrieunterräume ( $m = 0, \pi_z = -1$ ) und ( $m = -1, \pi_z = +1$ ). Diese Abbildungen zeigen eindrucksvoll wie sich die vermiedenen Kreuzungen in einem schmalen Bereich der Magnetfeldstärke von Zustand zu Zustand fortsetzen. Ein Vergleich unserer Ergebnisse einiger Zustände mit den Ergebnissen aufwendiger Rechnungen von Kravchenko et al. [8] in den Tab. 2.1 und 2.2 und mit Zhao et al. [6] in Tab. 2.3 zeigt, dass unsere Ergebnisse durchweg die angegebene Präzision von 7 Nachkommastellen erreichen. Im Vergleich zu Wang et al. [5], die ebenfalls eine 2D  $B$ -spline-Basis verwendeten, sind unsere Ergebnisse bei hohen Magnetfeldstärken deutlich präziser, da Wang et al. die Anzahl der  $B$ -splines nicht an die Magnetfeldstärke anpassten.

## Übergänge

Ausschlaggebend für die Analyse von Spektren Weißer Zwerge sind Übergangsenergien und -wahrscheinlichkeiten. Die Übergangsenergie  $\Delta E$  ergibt sich aus der Energiedifferenz von Anfangszustand (i) und Endzustand (f). Zur Beschreibung der Übergangsstärke kann

entweder die Dipolstärke  $d$  oder die dimensionslose Oszillatorstärke  $f$  verwendet werden. Diese berechnen sich bekanntermaßen gemäß (siehe Ref. [7])

$$f = \Delta E_{\text{if}} d_{\text{if}}^q \qquad d_{\text{if}}^q = |p_{\text{if}}^q|^2, \qquad (5)$$

wobei  $\Delta E$  in Rydberg-Einheiten gegeben und  $q = \Delta m = m_f - m_i$  die Differenz der magnetischen Quantenzahl von End- und Anfangszustand ist. Das Dipolmatrixelement  $p_{\text{if}}^q$  wird mittels der Kugelflächenfunktionen  $Y_{1,q}$  dargestellt

$$p_{\text{if}}^q = \left\langle \psi_f \left| \sqrt{\frac{4\pi}{3}} r Y_{1,q}(\theta, \phi) \right| \psi_i \right\rangle, \qquad (6)$$

wobei  $r$  die radiale Komponente des Ortsvektors in atomaren Einheiten ist. Setzt man die 2D  $B$ -spline Darstellung  $\psi(\rho, z) = \sum_{\mu\nu} \alpha_{\mu\nu} B_\mu(\rho) B_\nu(z)$  der Wellenfunktionen (4) in Gl. (6) ein, werden die Dipolmatrixelemente durch die Ausdrücke

$$p_{\text{if}}^0 = 2 \int_0^\infty \int_0^\infty \psi_f(\rho, z) z \psi_i(\rho, z) \rho d\rho dz, \qquad (7)$$

$$p_{\text{if}}^{\pm 1} = \pm \sqrt{2} \int_0^\infty \int_0^\infty \psi_f(\rho, z) \rho \psi_i(\rho, z) \rho d\rho dz, \qquad (8)$$

beschrieben. Die Polarisation des beteiligten Photons hängt dabei direkt von  $q$  ab

$$q = \begin{cases} 0, & \text{lineare Polarisation} \\ \pm 1, & \text{zirkuläre Polarisation.} \end{cases} \qquad (9)$$

In Abb. 2.12 und 2.13 zeigen wir die Magnetfeldstärke über den Wellenlängen der Lyman- und Balmer Serie. Diese Anordnung der Achsen wurde gewählt um konform zu vorhergehenden Untersuchungen in der Literatur zu bleiben. Die wesentlich reichhaltigere Linienstruktur der zweiten Abbildung ist durch die höhere Anzahl an Ausgangszuständen (vier bei der Balmer Serie zu einem bei der Lyman Serie) sowie einer Mehrzahl an Kreuzungen und vermiedenen Kreuzungen der Balmer Serienzustände zu erklären. Eine Analyse der Wellenfunktionen in der Nähe von vermiedenen Kreuzungen in Abb. 2.15 zeigt die dramatischen Veränderungen der Wellenfunktionsstruktur an solchen Punkten.

Aufgrund der AMV müssen bei der Berechnung von Übergängen neben der Energiedifferenz  $\Delta E$  auch die Überlapp- und Dipolintegrale interpoliert werden, da Anfangs- und Endzustand an unterschiedlichen Magnetfeldstärken, bestimmt durch die AMV, berechnet wurden. Wir wählen daher die Magnetfeldstärke so, dass jeweils einer der beiden Zustände (Anfangs- oder Endzustand) exakt beschrieben ist, berechnen die Überlapp- oder Dipolintegrale mit den beiden nächstliegenden anderen Zuständen größerer und kleinerer Magnetfeldstärke, und interpolieren anschließend zwischen den Ergebnissen beider

---

Integrationen. Da die Datenpunktdichte in der Nähe von vermiedenen Kreuzungen eines Zustandes besonders hoch ist, können so auch vermiedene Kreuzungen mit extrem schwacher Wechselwirkung der Zustände, das heißt kurzem Wechselwirkungsbereich  $d\beta$ , sowie deren Auswirkungen auf Dipolübergänge adäquat untersucht werden.

Wir demonstrieren die Genauigkeit dieses Verfahrens in Abb. 2.16. Dort vergleichen wir die interpolierten Dipolstärken (blau) mit solchen bei denen Anfangs- und Endzustand bei gleichem  $\beta$  berechnet wurden (rot). Abweichungen ergeben sich nur in der siebten Nachkommastelle. Der Vergleich mit Literaturwerten von Baye et al. [78] in den Tabellen 2.4 bis 2.7 zeigt durchgehend eine Präzision unserer Dipolstärken von 6 bis 8 Stellen.

Im Anschluss untersuchen wir in Abb. 2.17 das qualitative Verhalten der Dipolstärken verschiedener Übergänge. Im Limes großer Feldstärken sinkt die Ausdehnung der Wellenfunktionen senkrecht zur Magnetfeldachse proportional zu  $1/\sqrt{\beta}$  und im selben Maße das Dipolmatrixelement von Übergängen zirkularer Polarisation  $q = \pm 1$ . Die Übergangsstärke von  $tb$ -Zuständen zu  $hl$ -Zuständen sinkt ebenfalls mit steigendem  $\beta$ , jedoch aufgrund der unterschiedlichen longitudinalen Ausdehnungen der Zustände. Lediglich Übergänge mit  $q = 0$  zwischen zwei  $hl$ -Zuständen können auch bei hohem  $\beta$  noch starke Dipolstärken aufweisen. Eine Besonderheit betrifft Übergänge von tiefliegenden Zuständen mit ungerader  $z$ -Parität zu höheren Zuständen mit gerader  $z$ -Parität. Für diese Übergänge wird die Dipolstärke in einigen Bereichen hoher Magnetfeldstärke erheblich unterdrückt. Dies wird, wie man in Abb. 2.18 sehen kann, durch gegenseitige Auslöschung der Dipolintegralbeiträge aufgrund der Knotenstruktur der beteiligten Wellenfunktionen verursacht.

In der Abb. 2.17 können bei der cyan-farbenen Linie außer diesen Dipolauslöschungsresonanzen auch solche beobachtet werden, die von vermiedene Kreuzungen verursacht werden. Jene Resonanzen betrachten wir genauer in Abb. 2.19, in welcher die Oszillatorstärken  $f$  zweier Übergänge ( $m = 0, \pi_z = -, \nu = 1$ ):( $m = 0, \pi_z = +, \nu = 6$ ) und ( $m = 0, \pi_z = -, \nu = 1$ ):( $m = 0, \pi_z = +, \nu = 7$ ) in der Umgebung einer vermiedenen Kreuzung der beiden Zustände ( $m = 0, \pi_z = +, \nu = 6$ ) und ( $m = 0, \pi_z = +, \nu = 7$ ) über  $\beta$  aufgetragen sind. Dabei stellen wir fest, dass die Summe der Oszillatorstärken näherungsweise erhalten bleibt, die beiden einzelnen Übergänge jedoch bei der vermiedenen Kreuzung entweder unterdrückt oder verstärkt werden. Sind höher angeregte Zustände an einem Übergang beteiligt, so ergibt sich aus der Vielzahl vermiedener Kreuzungen eine Serie abwechselnder Verstärkung und Unterdrückung der Übergangsstärke, wie sie in Abb. 2.20 gezeigt wird. Eine beeindruckende Demonstration für die Effizienz der automatischen Magnetfeldvariation in Kombination mit der Dipolstärkeinterpolation ist in Abb. 2.21 dargestellt. Dort wurden selbst feinste Details der Dipolstärkeverläufe aufgelöst (siehe Bildeinsätze).

Die Darstellung der Übergangswellenlängen in den Abb. 2.12 und 2.13 hat den Nachteil, dass Dipolstärken der Linien nicht berücksichtigt werden, d.h. es wird nicht zwischen wichtigen und unwichtigen Linienbeiträgen unterschieden. Um eine schnelle Identifizierung der wichtigen Linien zu ermöglichen haben wir in Abb. 2.22 den einzelnen Übergängen der Lyman-Serie ihre jeweiligen Dipolstärken, relativ zum stärksten abgebildeten

Übergang des gesamten Ausschnittes, mittels Farbwerten zugeordnet: dunkle Farben stehen für starke Übergänge, helle für weniger starke. Sofort stechen die Auswirkungen der vermiedenen Kreuzungen ins Auge (Beschriftungen “a” und “b”), die sich durch dunkle und helle Streifen im Bild bemerkbar machen. Bei Beschriftung “b” erkennt man die Signatur schwach gekoppelter vermiedener Kreuzungen: schmale dunkle Streifen, die abrupt an der Ionisationsschwelle des Symmetrieuntertraumes enden. Zum Ende dieses Abschnittes präsentieren wir in Abb. 2.23 ein vergleichbares Bild für die Balmer-Serie. In Abb. 2.24 kombinieren wir schließlich die Wellenlängen und Dipolstärken aller berechneten Übergänge der Lyman-, Balmer-, Paschen-, und Brackett-Serie und gewichten die Dipolstärken zusätzlich mit einem Boltzmannfaktor

$$w = e^{-(E_i - E_g)/(k_B T)}, \quad (10)$$

relativ zu Grundzustandsenergie  $E_g$  und Ausgangszustandsenergie  $E_i$  bei der jeweiligen Magnetfeldstärke. Die ausgewählte effektive Temperatur von 20.000 K ist typisch für weiße Zwerge [13]. Trotz dieses Boltzmannfaktors bleiben die Linien der Brackett-Serie bis hin zu etwa  $B = 250$  MG deutlich sichtbar. Oberhalb dieser Magnetfeldstärke dominieren vor allem Linien der Balmer- und Lyman-Serie. In Abb. 2.25 wurde der Bildausschnitt auf den im Rahmen des Sloan Digital Sky Survey beobachtbaren Wellenlängenbereich eingeschränkt. Ein breites Band von Übergängen der Paschen- und Brackett-Serie dominiert das Bild zwischen  $B = 10$  MG und  $B = 250$  MG. Da jedoch die Magnetfeldstärke auf der Oberfläche eines Weißen Zwerges wenigstens um einen Faktor 2 variiert und die Linien innerhalb dieses Bandes eine extrem starke Magnetfeldabhängigkeit aufweisen, ist ein Beitrag einzelner Linien solcher Bänder zum Absorptionsspektrum in der Form scharfer Absorptionsmerkmale nicht zu erwarten.

## Allgemeine Betrachtung von Mehrelektronensystemen in starken Magnetfeldern

Wir führen nun die notwendigen Begriffe zum Verständnis von Hartree-Fock-Rechnungen in starken Magnetfeldern ein. Bisher haben wir uns auf eine Kernladung von  $Z = 1$  beschränkt, und führen nun die Verallgemeinerung der effektiven Magnetfeldstärke auf  $\beta_Z = B/B_Z = \beta/Z^2$  durch. Für eine Magnetfeldstärke von  $\beta_Z = 1$  entspricht der kernladungsskalierte Bohrradius dem Larmorradius. Wir betrachten im Folgenden starke Magnetfelder  $\beta_Z \gtrsim 0.1$ . Der Hamiltonoperator eines Atoms mit  $N$  Elektronen im Magnetfeld ist durch den Ausdruck

$$\begin{aligned} \hat{H} = & \sum_{i=1}^N - \left( \frac{\partial^2}{\partial \rho_i^2} + \frac{1}{\rho_i} \frac{\partial}{\partial \rho_i} + \frac{1}{\rho_i^2} \frac{\partial^2}{\partial \phi_i^2} + \frac{\partial^2}{\partial z_i^2} \right) + 2\beta m_i + \beta^2 \rho_i^2 \\ & + \sum_{i=1}^N 4\beta m_s^i - \frac{2Z}{|\mathbf{r}_i|} + \sum_{\substack{i=1 \\ j=i+1}}^N \frac{2}{|\mathbf{r}_i - \mathbf{r}_j|} \end{aligned} \quad (11)$$



gegeben. Wir vernachlässigen weiterhin relativistische Effekte, Schwerpunktsbewegungen oder eine endliche Kernmasse. Im Gegensatz zum Wasserstoffatom gibt es allerdings keine exakte Skalierungsmöglichkeit für Ergebnisse aus Rechnungen mit unendlicher Kernmasse hin zu solchen mit endlicher Kernmasse. Für ungeladene Systeme  $Z = N$  kann jedoch eine genäherte Skalierungsregel angegeben werden (siehe [26, 84]). Für geladene Systeme  $Z \neq N$  können keine solchen Skalierungsgesetze gefunden werden [85].

Die Gesamtwellenfunktion  $\Psi$  wird mit Hilfe einer Slater-Determinanten aus Einteilchen-Spinorbitalen aufgebaut. Die Einteilchenquantenzahlen dieser Orbitale sind mit den Erhaltungsgrößen des Systems, den Vielteilchenquantenzahlen, über die Relationen

$$M = \sum_i^N m_i, \quad \Pi_z = \prod_i^N \pi_z^i, \quad S_z = \sum_i^N m_s^i, \quad (12)$$

verknüpft, wobei  $M$  die gesamte magnetische Quantenzahl,  $\Pi_z$  die  $z$ -Parität der Gesamtwellenfunktion und  $S_z$  die  $z$ -Projektion des Gesamtspins ist. Der Gesamtspin  $S^2$  wäre ebenso Erhaltungsgröße. Falls jedoch keine vollständige Spinpolarisation vorliegt ist der Gesamtspin aufgrund unseres uneingeschränkten Hartree-Fock-Ansatz keine Erhaltungsgröße mehr [88]. Die Gesamtanregungszahl kann aus den Einteilchenorbitalen nicht sicher vorhergesagt werden. Um die Zustände eindeutig zu benennen, verwenden wir daher die Einteilchenquantenzahlen in der Kurznotation  $(-m)_{\uparrow}^{\nu'}$ , wobei der Spinausrichtungspfeil nur angegeben wird im Falle der Ausrichtung "oben". Für sehr starke Magnetfelder ist der Grundzustand der Atome durch die Hochfeldgrundzustandskonfiguration

$$\underline{0}_N = 0^0 1^0 2^0 \dots (N-1)^0 \quad (13)$$

gegeben. Hier besetzen die Elektronen ausschließlich die energetisch tiefliegenden  $t_b$ -Orbitale, beginnend bei  $m = 0$  und bis  $m = -(N-1)$ . Falls nur wenige Elektronen von dieser Konfiguration abweichen, werden deren Quantenzahlen angefügt. So können auch Zustände mit vielen Elektronen platzsparend notiert werden.

## Entwicklung der Einteilchenwellenfunktionen

In sehr starken Magnetfeldern  $\beta_Z \gtrsim 0.1$  können wir uns auf die Landauentwicklung der Einteilchenwellenfunktionen aus Gl. (3) beschränken. In noch stärkeren Feldern  $\beta_Z > 1$  sind die longitudinalen Wellenfunktionskomponenten

$$P^i(z) = \sum_{\mu} \alpha_{\mu}^i B_{\mu}^i(z), \quad (14)$$

welche wir erneut mit  $B$ -splines und finiten Elementen entwickeln, für verschiedene Landauorbitale annähernd gleich in der Form [43] und unterscheiden sich nur durch einen Vorfaktor. Diese lassen sich dann zu einer einzelnen longitudinalen Funktion zusammenfassen und gehen nur noch als Landau-Gewichte  $t_n$  in einen Produktansatz für

die Wellenfunktion der Form

$$\psi(\mathbf{r}) = P(z)\Phi(\rho, \phi) = \sum_{\mu} \alpha_{\mu} B_{\mu}(z) \sum_n t_n \Phi_{nm}(\rho, \phi) \quad (15)$$

ein (siehe Engel et al. [43, 54]). Für noch stärkere Felder  $\beta_Z \gg 1$  können die Beiträge der höheren Landaukanäle vernachlässigt werden, was als adiabatische Näherung bezeichnet wird, und es ergibt sich die Form

$$\psi(\mathbf{r}) = \sum_{\mu} \alpha_{\mu} B_{\mu}(z) \Phi_{0m}(\rho, \phi), \quad (16)$$

die bereits vielfach in der Literatur zur Anwendung kam (siehe, z.B. [7, 52, 53]).

Die Beschreibung mehrerer Elektronen eines Atoms in starken Magnetfeldern ist von hoher Komplexität, da die Ausdehnung der Wellenfunktionen von Orbitalen mit verschiedenen Anregungszahlen extrem unterschiedlich sein kann. Als Beispiel seien die drei Orbitale in Abb. 3.1 genannt, deren Breiten sich um bis zu einen Faktor 50 unterscheiden. Um dennoch eine adäquate Beschreibung aller Orbitale zu gewährleisten, bei gleichzeitiger Minimierung der Anzahl an finiten Elementen, wurde eine "schlanke"  $B$ -spline-Basis entwickelt. Diese nutzt für jedes Orbital eine individuelle Anzahl an finiten Elementen und passt deren Verteilung an die Wellenfunktionsform an. Wir zeigen anhand umfangreicher Testrechnungen und Vergleiche in den Abschnitten 3.3.1 und 3.3.2, dass diese von uns entwickelte  $B$ -spline-Basis gerade so exakt ist, dass die durch sie bedingten zusätzlichen Fehler unterhalb derer liegen, die durch vernachlässigte Korrelationen des Hartree-Fock-Verfahrens typischerweise verursacht werden, wenigstens jedoch unterhalb jener Fehler, die der Landau-Entwicklung zuzuordnen sind.

## Das beschleunigte doppelt selbstkonsistente Hartree-Fock-Roothaan Verfahren

Das nachstehende Verfahren wurde ursprünglich von Klews [52, 53] entwickelt und bediente sich der adiabatischen Näherung (16). Engel [43, 54] erweiterte das Programm mit Hilfe des Produktansatzes (15). In der vorliegenden Arbeit wurde das Programm vollständig überarbeitet, die Ausführungszeit erheblich reduziert, die Bedienung vereinfacht [92] und das Konvergenzverhalten verbessert. Diese beschleunigte Implementation des doppelt selbstkonsistenten Hartree-Fock-Roothaan Verfahrens bezeichnen wir mit HFFER II. Obwohl wir um die Einschränkungen des Produktansatzes im Vergleich zur vollen Entwicklung (3) wissen, ist er doch keinesfalls obsolet. Durch den Produktansatz kann das Lösen der longitudinalen und transversalen Anteile der Wellenfunktion getrennt implementiert werden, was einen erheblichen Geschwindigkeitsvorteil bedeutet. Wir nutzen dies um die  $B$ -spline-Basisparameter zu optimieren, sodass nachfolgende Rechnungen in voller Landauentwicklung wesentlich effizienter ablaufen können.

---

Die Variation des Energiefunktionals zum Hamiltonoperator (11) bezüglich der  $B$ -spline-Koeffizienten  $\alpha_\mu^i$  bei festgehaltenen Landaugewichten  $t_n^i$  führt auf  $N$  verallgemeinerte Eigenwertprobleme der Form

$$\sum_{\mu} F_{\mu\nu}^i \alpha_{\mu}^i = \varepsilon_i \sum_{\mu} S_{\mu\nu}^i \alpha_{\mu}^i, \quad i = 1, \dots, N, \quad (17)$$

wobei die Matrix  $S_{\mu\nu}^i = \int B_{\mu}^i(z) B_{\nu}^i(z) dz$  auf der rechten Seite der Gleichung die Überlappmatrix, und diejenige auf der linken Gleichungsseite die Fockmatrix ist. Letztere setzt sich aus den Beiträgen der kinetischen und Spin-Energie, dem Kernpotential und den Wechselwirkungspotentialen (direkt und Austausch) der Elektronen zusammen (siehe Gl. (4.2) bis (4.6)). Ein ähnliches Gleichungssystem lässt sich auch für die Landaugewichte aufstellen, diesmal bei festgehaltenen  $B$ -spline-Koeffizienten:

$$\sum_{n=0}^{N_L} \tilde{F}_{nn'}^i t_n^i = \varepsilon_i t_{n'}^i \quad i = 1, \dots, N. \quad (18)$$

Wegen der Orthonormalität der Landaubasis wird die Überlappmatrix diagonal und es liegt ein gewöhnliches Eigenwertproblem vor. Die Beiträge zur Fockmatrix liefern die Terme in Gleichungen (4.14) bis (4.18). Zur Lösung der Gleichungen (17) und (18) wird ein iteratives Vorgehen angewandt. Die Startwellenfunktionen hierfür können als Einteilchenprobleme leicht berechnet werden, indem die Elektron-Elektron-Wechselwirkungen durch eine Abschirmung (siehe Gl. (4.19) oder Ref. [91, 92]) abgeschätzt werden. Anschließend werden abwechselnd und doppelt selbstkonsistent longitudinale und transversale Lösungen bestimmt bis Konvergenz erzielt wurde. Eine Skizze des gesamten HFFER II-Verfahrens ist in Abb. 4.1 dargestellt.

Die wesentlichen Neuerungen dieser Implementation betreffen Geschwindigkeits- und Konvergenzoptimierungen: Neben der Einführung einer individuellen  $B$ -spline-Basis für jedes Einteilchenorbital haben wir außerdem die Berechnung der Kern- und Wechselwirkungspotentiale ausgelagert. Diese Potentiale liegen vorberechnet und tabelliert vor. Beide Maßnahmen zusammen ergaben eine dramatischen Beschleunigung des Programms im Vergleich zur vorherigen Implementation von im Mittel einem Faktor 83, wie in Abb. 4.2 dargestellt. Die Maßnahmen zur Konvergenzverbesserung umfassen unter anderem einen komplexen Algorithmus zur Bestimmung optimaler Basislänge sowie ein Schritt-für-Schritt-Verfahren, bei dem jedes Elektron *nacheinander* (nicht wie sonst üblich gleichzeitig) variiert wird, um periodische Iterationszyklen, wie sie in Abb. 4.3 schematisch dargestellt sind, zu durchbrechen. Dieses Verfahren ist zwar erheblich langsamer, da die ansonsten hocheffiziente Parallelisierung der Rechnungen umgangen wird, kommt aber nur im Falle langsamer oder fehlender Konvergenz des gleichzeitigen Lösungsverfahrens zum Einsatz.

## Die zweidimensionale Landau-Hartree-Fock-Roothaan Methode

Der im HFFER II-Programm verwendete Produktansatz (15) für die Einteilchenwellenfunktionen führt ab  $\beta_Z \gtrsim 1$  zu Ergebnissen mit guter Präzision. Die innersten Orbitale  $|m| < 5$  lassen sich jedoch selbst bei diesen Magnetfeldstärken nur unzureichend genau beschreiben, wie wir in Abb. 3.2 gezeigt haben. Die allgemeinere zweidimensionale Landau Entwicklung (2.6) mit unterschiedlichen longitudinalen Komponenten  $P_n(z)$  für jeden der  $n$  Landaukanäle ermöglicht es nun aber, zu noch tieferen Magnetfeldstärken bis  $\beta_Z \approx 0.1$  vorzudringen. Obwohl diese Entwicklung der Wellenfunktion im Prinzip vollständig ist, stoßen wir dennoch auf diese Grenze, da die Landauentwicklung, wie man in Abb. 2.1 sehen kann, für niedrige  $\beta$  nur langsam konvergiert.

Bei der Berechnung der Energien und Wellenfunktionen gehen wir analog zum vorigen Abschnitt vor. Wir variieren das Energiefunktional bezüglich der  $B$ -spline-Koeffizienten und erhalten das verallgemeinerte Eigenwertproblem

$$\sum_{n'\mu} F_{n\nu n'\mu}^i \alpha_{n'\mu}^i = \varepsilon_i \sum_{n'\mu} S_{n\nu n'\mu}^i \alpha_{n'\mu}^i, \quad (19)$$

mit den Überlappmatrizen  $S_{n\nu n'\mu}^i$  und den Fock-Matrizen  $F_{n\nu n'\mu}^i$ . Letztere sind die Summe der Beiträge von kinetischer und Spin-Energie, sowie Kern- und Wechselwirkungspotentialen der Gleichungen (5.2) bis (5.6). Da nun über verschiedene Kombinationen von Landauniveaus mit unterschiedlichen  $z$ -Komponenten integriert werden muss, wurden die effektiven Potentiale neu berechnet. Eine kurze Beschreibung hierzu findet sich im Anhang B. Das zugehörige Programm zur Lösung der Gleichungen (19) nennen wir 2DLHFR. Das wesentliche Merkmal dieser Implementation ist, dass ausschließlich bei der Berechnung der Wechselwirkungsterme nicht alle  $N_L + 1$  Landaukanäle berücksichtigt werden, sondern lediglich die niedrigsten  $N_{\text{int}}^i + 1$  Kanäle. Für die Berechnung der Einteilchenpotentiale und der kinetischen Anteile werden jedoch alle  $N_L + 1$  Landaukanäle eingebunden. Diese Modifikation des Energiefunktionals, bei der die hauptsächlich abstoßenden Elektron-Elektron-Wechselwirkungen reduziert werden, führt zu einer Absenkung des Energiefunktionals und beraubt uns der Variationalität des Verfahrens. Wir können jedoch den Verlust höherer Abstoßungsterme durch eine Renormalisierung mit dem Faktor

$$\xi^j = \sum_{k=0}^{N_{\text{int}}^j} \int_{-\infty}^{\infty} |P_k^j(z)|^2 dz \quad (20)$$

der Wechselwirkung der unteren Landauniveaus in Gleichungen (5.5) und (5.6) teilweise kompensieren. Ist zudem die Besetzung der unberücksichtigten Landaukanäle nur sehr gering, so ergibt sich ein vernachlässigbarer Energie- und Wellenfunktionsfehler. Wir bestimmen die individuellen Abschneideparameter  $N_{\text{int}}^i$  anhand der gespeicherten

---

Landaugewichte  $t_n^i$  der HFFER II-Rechnungen mit Hilfe der Beziehung

$$\left(t_{N_{\text{int}}^i}^i\right)^2 \geq t_{\text{min}}, \quad (21)$$

wobei  $t_{\text{min}}$  ein zu optimierender Parameter ist. Das letzte in Wechselwirkungen berücksichtigte Landauniveau eines Orbitals ist nach Gl. (21) also jenes, welches gerade noch einen Anteil an der Wellenfunktion größer als  $t_{\text{min}}$  aufweist.

In Abb. 5.1 zeigen wir eine erste Abschätzung der induzierten Fehler durch das wechselwirkungsmodifizierte Energiefunktional und zeigen, dass durch die Renormalisierung der Wechselwirkungen die Energieergebnisse auch bei signifikanter Reduktion der berücksichtigten Landaukanäle stabil bleiben, sofern  $t_{\text{min}} \lesssim 10^{-6}$ . Für diese Untersuchung beschränkten wir uns noch auf  $N_L = 7$ , da so die Wechselwirkungen aller Landaukanäle berechnet werden konnten und ein Vergleich zum unmodifizierten Energiefunktional möglich war. Die Wechselwirkungspotentiale höherer Landaukanäle können jedoch aufgrund der zugehörigen riesigen Datenmenge nicht im Arbeitsspeicher zwischengespeichert werden, sodass wir auf die Vernachlässigung höherer Wechselwirkungspotentiale schon aus technischen Gründen angewiesen sind. Um das Energiefunktional zu Gleichung (19) dennoch auch für  $N_L = 30$  genau auswerten zu können, haben wir einen einfachen Monte-Carlo-Algorithmus implementiert. Dieser berechnet die Wechselwirkungsenergien des *unmodifizierten* Energiefunktionals (d.h.  $N_{\text{int}}^i = N_L$  und  $\xi^j = 1$ ) und erlaubt so eine Abschätzung der Energie- und Wellenfunktionsfehler durch das vorgestellte, modifizierte Energiefunktional. Da das Monte-Carlo-Verfahren jedoch numerisch sehr aufwendig ist, kann es nicht standardmäßig, sondern nur für ausgewählte Untersuchungen zum Einsatz kommen.

Mit Hilfe des Monte-Carlo-Verfahrens wurden umfangreiche Fehlerbetrachtungen anhand verschiedener Zustände durchgeführt, deren Ergebnisse in den Abb. 5.2 bis 5.6 festgehalten sind. Zusammenfassend lässt sich sagen, dass sich nahezu unabhängig von elektronischer Konfiguration, Magnetfeldstärke oder Kernladungszahl ein minimaler Landau-Besetzungsparameter  $t_{\text{min}} = 10^{-6}$  als optimal erwiesen hat. Hiermit lassen sich verlässlich zusätzliche Fehler durch ein Vernachlässigen wichtiger Wechselwirkungsbeiträge höherer Landauniveaus verhindern, und gleichzeitig der Berechnungsaufwand minimieren. Die bereits genannte untere Grenze der Magnetfeldstärke  $\beta_Z \gtrsim 0.1$  wurde ebenfalls als für dieses Programm geeignete Schranke bestätigt. In Abb. 5.7 zeigen wir schließlich das gute Konvergenzverhalten des Algorithmus anhand eines Eisengrundzustandes bei einer effektiven Magnetfeldstärke nahe der unteren Schranke. Im Vergleich zum HFFER II-Verfahren konnte der Energiefehler zum hoch präzisen FPDQMC-Algorithmus [45, 46] um einen Faktor 8 gesenkt werden. Der verbleibende relative Energiefehler beträgt lediglich 0.65%.

Wir stellen das Programmschema des 2DLHFR-Verfahrens in Abb. 5.8 vor. Die berechneten Ergebnisse werden zur späteren Weiterverwendung in einem standardisierten Dateiformat abgespeichert. Sie dienen zum einen als Führungswellenfunktionen für den wesentlich aufwendigeren FPDQMC-Algorithmus und werden außerdem zur Berechnung von Übergangsenergien und Oszillatorstärken verwendet. Letztere können mit Hilfe der

Gl. (5.11) bis (5.14) gewonnen werden. Die Herleitung selbiger Gleichungen erfolgt unter Verwendung der Wellenfunktionsentwicklung aus Gleichungen (2.6) und (3.3) analog zu Kap. 2.4.

## Ergebnisse

In diesem Abschnitt spielen wir die Stärken des neuen 2DLHFR-Verfahrens voll aus und vergleichen Energien, Übergangsennergien und Dipolstärken mit Literaturwerten sowie zwischen beiden Implementationen HFFER II und 2DLHFR. Des Weiteren präsentieren wir eine neue, aufwendige Untersuchung der Grundzustandsenergien und Konfigurationen aller Atome mit  $2 \leq Z \leq 21$  für alle Magnetfeldstärken in dem uns zugänglichen Bereich.

In den Tabellen 6.1 und 6.2 vergleichen wir unsere HFFER II und 2DLHFR Bindungsenergien für *tb*-Heliumzustände mit den Ergebnissen anderer Hartree-Fock-Verfahren von Jones et al. [31] und Thirumalai et al. [38] sowie mit FPDQMC-Ergebnissen von Boblest [46]. Es zeigt sich, dass das 2DLHFR-Verfahren bei niedrigem  $\beta_Z$  eine Verbesserung der HFFER II-Energiewerte um bis zu 10% erreicht. Bei hohem  $\beta_Z$  wird der verbleibende HFFER II-Fehler zu den hoch präzisen FPDQMC-Energiewerten immerhin noch etwa gedrittelt. Das 2DLHFR-Verfahren übertrifft die Genauigkeit der konkurrierenden Hartree-Fock-Verfahren ab  $\beta_Z \geq 10$ . In den Tabellen 6.3 bis 6.5 vergleichen wir unsere Energiewerte angeregter Heliumzustände für niedrigere Magnetfeldstärken mit denen des Full-CI Verfahrens von Becken et al. [26–28]. Für  $\beta_Z = 0.125$  ergeben sich hier noch Energieunterschiede von etwa 2%, die jedoch bei  $\beta_Z = 1.25$  bereits auf den, der Hartree-Fock-Näherung immer innewohnenden Korrelationsfehler von etwa 0.2%-0.4% abgefallen sind.

In Tabelle 6.6 stellen wir eine neue, eindeutige Notation der elektronischen Konfiguration möglicher Grundzustände vor, die die bereits bekannte Notation aus Gl. (13) noch einmal verkürzt. Diese kommt u.a. in den Tabellen 6.7 bis 6.10 zur Anwendung, in welchen wir die Grundzustände und zugehörigen Energien aller neutralen Atome von Helium bis Eisen (in Tab. 6.7 bis Silizium) bei vier Magnetfeldstärken von  $B = 10^7$  T bis  $B = 5 \cdot 10^8$  T angeben. Im Vergleich zu den Referenzwerten von Mori et al. [42] erhalten wir wesentlich genauere Ergebnisse. Durch die Betrachtung nicht voll spinpolarisierter Zustände konnten zudem für schwere Atome neue Grundzustandskonfigurationen gefunden werden, die die Grundzustandsenergien um bis zu 6% unterhalb derjenigen voll spinpolarisierter Konfigurationen absenken.

Der Vergleich von Dipolstärken und Übergangsennergien für leichte Elemente erfolgt in den Tabellen 6.11 und 6.12 wieder mit den Full-CI-Ergebnissen von Becken et al. [29]. Die großen relativen Unterschiede zwischen den Übergangsennergien des 2DLHFR- und CI-Verfahrens von 3% sind aufgrund der in absoluten Zahlen geringen Übergangsennergien nicht maßgeblich. Ähnliche Unterschiede von  $-2\%$  bis  $+5\%$  erhalten wir auch für die Dipolstärken. Energien und Dipolstärken für Übergänge zu hochangeregten Endzuständen präsentieren wir in grafischer Form in den Abb. 6.1 und 6.2. Insbesondere

---

fällt in der zweiten Abbildung auf, dass die Dipolstärken des CI-Verfahrens für den Übergang zum höchstangeregten Zustand stark fluktuieren und offensichtlich nicht konvergieren sind. Beim Vergleich der Oszillatorstärken in Kohlenstoff mit Referenzwerten von Mori et al. [42] in Tab. 6.13 fanden wir erhebliche Abweichungen von bis zu 27% zu den 2DLHFR-Werten. Da jedoch die HFFER-II-Energien und Oszillatorstärken erheblich kleinere Abweichungen zu den 2DLHFR-Werten aufweisen, können wir annehmen, dass unsere Oszillatorstärken der Wahrheit näher sind.

Im Abschnitt 6.4 betrachten wir die Abhängigkeit der Grundzustandskonfigurationen von der Magnetfeldstärke. Mit steigender Magnetfeldstärke unterscheiden wir vier Grundzustandsdomänen: Die Schwachfelddomäne um  $B \approx 0$ , die Domäne der magnetischen Polarisierung, der Spinpolarisierung und schließlich die Domäne des Hochfeldgrundzustandes. In der ersten Domäne ist der Grundzustand aus der Literatur bekannt. Im Bereich der magnetischen Polarisierung ab  $\beta_Z \gtrsim 10^{-2}$  sind in der Grundzustandskonfiguration keine Orbitale mit positiver magnetischer Quantenzahl mehr enthalten. Für  $\beta_Z \gtrsim 0.1$  sind alle Spins antiparallel zum Magnetfeld orientiert und die Domäne der vollständigen Spinpolarisierung ist erreicht. Schließlich ist bei Magnetfeldern  $\beta_Z \gtrsim Z$  [66] die Grundzustandskonfiguration durch den Hochfeldgrundzustand aus Gl. (13) gegeben. In den Abb. 6.3 und 6.4 zeigen wir die Energie des Grundzustandes von neutralem Neon und Chlor als Funktion der Magnetfeldstärke. Die jeweils gültige Grundzustandskonfiguration ist durch farbige Abschnitte markiert. Beide Abbildungen enthalten eine Vergrößerung auf den jeweils bezüglich der Magnetfeldstärke kürzesten Grundzustandskonfigurationsabschnitt. Dies zeigt, dass viele elektronische Konfigurationen zum Grundzustand beitragen können, wenngleich auch nur für kleine Bereiche der Magnetfeldstärke.

In den Tab. 6.14 bis 6.17 vergleichen wir unsere 2DLHFR-Ergebnisse für die Magnetfeldstärken an Grundzustandskreuzungen von Helium bis Neon mit den FPDQMC-Ergebnissen von Boblest [105]. Die ersten beiden Tabellen beziehen sich auf den Übergang von teilweiser Spinpolarisierung zu vollständiger Spinpolarisierung, wohingegen die letzten beiden Tabellen den Vergleich bezüglich des ersten Auftretens des Hochfeldgrundzustandes ermöglichen. Die Übereinstimmung zwischen beiden Verfahren ist beeindruckend. Unsere Ergebnisse weichen um maximal 4% von den hochpräzisen FPDQMC-Vergleichsrechnungen ab. Im Anschluss finden sich umfassende Tabellen aller Grundzustandskonfigurationen, ihrer Gültigkeitsbereiche sowie Abfolge mit steigender Magnetfeldstärke für alle Atome  $2 \leq Z \leq 21$  samt ihrer positiven Ionen für Magnetfeldstärken  $\beta_Z \gtrsim 0.05$ .

## Ausblick

In dieser Arbeit wurden bereits viele Ziele erreicht. Es verbleiben dennoch einige offene Fragen zu Atomen in Magnetfeldern. Die meisten dieser Fragen betreffen die Aufhebung der in dieser Arbeit verwendeten Näherungen. Die vollständige Analyse von Atomspektren unter Berücksichtigung der endlichen Kernmasse, einer Schwerpunktsbewegung und zusätzlichen äußeren elektrischen Feldern bleibt eine wichtige Aufgabe, da erwartet wird,

dass der (bewegungsinduzierte) Starkeffekt die Linienform maßgeblich bestimmt und erheblichen Einfluss auf die Ionisationsgleichgewichte in der Atmosphärenmodellierung hat [24]. Aufgrund der hohen Bindungsenergien in schweren Atomen könnte außerdem die Berücksichtigung relativistischer Effekte in solchen Systemen notwendig werden. Für leichte Elemente erwarten wir jedoch nur kleine relativistische Einflüsse auf die Energieniveaus [12].

Viel drängender ist jedoch die Implementierung des allgemeineren zweidimensionalen  $B$ -spline-Ansatzes (2.9) für Mehrelektronensysteme, da hiermit die generelle Beschränkung auf ein Magnetfeldintervall entfallen und gleichzeitig eine optimale Beschreibung der Einteilchenwellenfunktionen zu jeder Magnetfeldstärke erreicht würde. Den damit verbundenen Anstieg im Rechenaufwand schätzen wir aufgrund unserer Erfahrungen mit Wasserstoffwellenfunktionen in dieser Darstellung als eher moderat ein. In Verbindung mit einem Hartree-Fock-, Configuration-Interaction- oder Quanten-Monte-Carlo-Ansatz könnte diese Wellenfunktionsentwicklung zu einem Standard der Beschreibung atomarer Zustände in Magnetfeldern beliebiger Stärke avancieren.

Die in dieser Arbeit gefundenen Ergebnisse und enthaltenen Algorithmen ermöglichen nun erstmals eine präzise und zugleich schnelle Berechnung von Atomen und Ionen in starken Magnetfeldern. Dem Aufbau einer umfassenden Datenbank von Zuständen und Übergängen, wie er in dieser Arbeit in beispiellosem Umfang für Wasserstoff durchgeführt wurde, steht nun auch für schwerere Atome bis hin zu Eisen nichts mehr entgegen. Damit ist der Weg für die Modellierung der Atmosphären von Neutronensternen geebnet und somit auch für das Verständnis der Physik auf der Oberfläche wie im Inneren dieser faszinierenden Objekte.



# A Atomic units

This work uses atomic Rydberg units (a.u.), which are defined by the following set of equations

$$2m_e = 4\pi\epsilon_0 = \hbar = e^2/2 = 1 \text{ a.u.} \quad (\text{A.1})$$

Physical quantities and constants used in this work are provided in Tab. A.1, using latest values for the fundamental physical constants from Mohr et al. [114] and relations from [7].

**Tab. A.1:** Units and constants in atomic Rydberg units

Symbol	Expression	Reference value	Quantity
$a_0$	$\hbar/(\alpha m_e c)$	$5.2917721092(17) \times 10^{-11} \text{ m}$	length
$E_\infty$	$\alpha^2 m_e c^2 / 2$	$13.6056925(9) \text{ eV}$	energy
	$2m_e$	$1.82187658(8) \times 10^{-30} \text{ kg}$	mass
	$\hbar/E_\infty$	$4.83776865(44) \times 10^{-17} \text{ s}$	time
	$\alpha c/2$	$1.0938456319(4) \times 10^6 \text{ m/s}$	speed
$\hbar$		$1.054571726(47) \times 10^{-34} \text{ Js}$	angular momentum
	$e/\sqrt{2}$	$1.132909913(25) \times 10^{-19} \text{ C}$	charge
Symbol	in a.u.	Reference value	Name
$c$	$2/\alpha$	$299792458 \text{ m/s}$	speed of light
$B_0$	$\sqrt{2}$	$4.7010349(8) \times 10^5 \text{ T}$	reference mfs
$a_L$	$1/\sqrt{\beta}$		Larmor length
$\hbar\omega_c$	$4\beta$		cyclotron energy
$B_{\text{crit}}$	$1/(\sqrt{2}\alpha^2)$	$4.4140050(7) \times 10^9 \text{ T}$	quantum critical mfs
$\lambda_m$		$1.000544617022(1)$	finite mass correction
$\gamma_{\text{AE}}$		$911.267050(6) \text{ \AA}$	Rydberg wavelength
$k_B$		$1.3806488(13) \times 10^{-23} \text{ J/K}$	Boltzmann constant
$m_p$		$1.672621777(74) \times 10^{-27} \text{ kg}$	proton mass



## B Landau averaged potentials

The Landau averaged potentials  $V$ ,  $U$  and  $A$  in Eqs. (4.8), (4.11) and (4.12) are essential for the evaluation of the energy functional with any of the three wave function expansions given in Eqs. (2.6), (2.7) or (2.8). Pröschel et al. [71] and Engel [54] showed that all of these potentials can be traced back to sums of adiabatic approximation potentials

$$V_s(z) := V_s^{00}(z) = 2 \int \frac{\Phi_{0s}^*(\mathbf{r}^\perp) \Phi_{0s}(\mathbf{r}^\perp)}{|\mathbf{r}^\perp|} d\mathbf{r}^\perp, \quad (\text{B.1})$$

which results in the following relations [54, 71] for the Landau averaged potentials

$$V_m^{nn'}(z) = -Z \sqrt{\beta} \sum_{k=|m|}^{n+n'-m} b(ss', nn'; k) V_k(\sqrt{\beta}z), \quad (\text{B.2})$$

$$U_{m_i m_j}^{n_i n_j n'_i n'_j}(z_i, z_j) = \sqrt{\frac{\beta}{2}} \sum_{k=0}^{n_i+n_j+n'_i+n'_j-m_i-m_j} c(s_i s_j s'_i s'_j, n_i n_j n'_i n'_j; k) V_k \left( \sqrt{\frac{\beta}{2}} |z_i - z_j| \right), \quad (\text{B.3})$$

$$A_{m_i m_j}^{n_i n_j n'_i n'_j}(z_i, z_j) = \sqrt{\frac{\beta}{2}} \sum_{k=0}^{n_i+n_j+n'_i+n'_j-m_i-m_j} d(s_i s_j s'_i s'_j, n_i n_j n'_i n'_j; k) V_k \left( \sqrt{\frac{\beta}{2}} |z_i - z_j| \right). \quad (\text{B.4})$$

Here we used  $s_i = n_i - m_i$  and  $s'_i = n'_i - m_i$ . The calculations of the coefficients  $b$ ,  $c$  and  $d$  is given in Ref. [71] but is numerically challenging for larger  $m$  or  $n$ . Each coefficient has to be obtained from quadruple sums with alternating sign, containing products of binomial coefficients. However, despite the large number of terms involved in their calculation the coefficients stay in the order of 1. On a computing machine with e.g. 15 significant digits for each number, the evaluation of these sums fails due to loss of significance. Therefore, all coefficients must be evaluated with arbitrary precision software (we use the ARPREC software package [115]), which is of course numerically very expensive. The calculation of the adiabatic potentials  $V_s$  is likewise intricate, as it also involves large sums with alternating signs that include factorials and binomial coefficients. On top of that, the coefficients and adiabatic potentials are then combined in Eqs. (B.2), (B.3) and (B.4) in such a sum, which means one has to calculate *all* coefficients and adiabatic potentials to very high accuracy. In our calculations we employed 65.000 digits accuracy for the coefficients and adiabatic potentials to achieve an overall 8-digit precision for the potentials  $V$ ,  $U$  and  $A$  on the full range of  $z$  with  $n \in [0, 30]$  and  $m \in [0, -200]$ .

In the HFFER II program the coefficients  $b$ ,  $c$  and  $d$  are directly combined with the Landau channel weights  $t_n^i$  and the adiabatic potentials (B.1) to obtain the effective

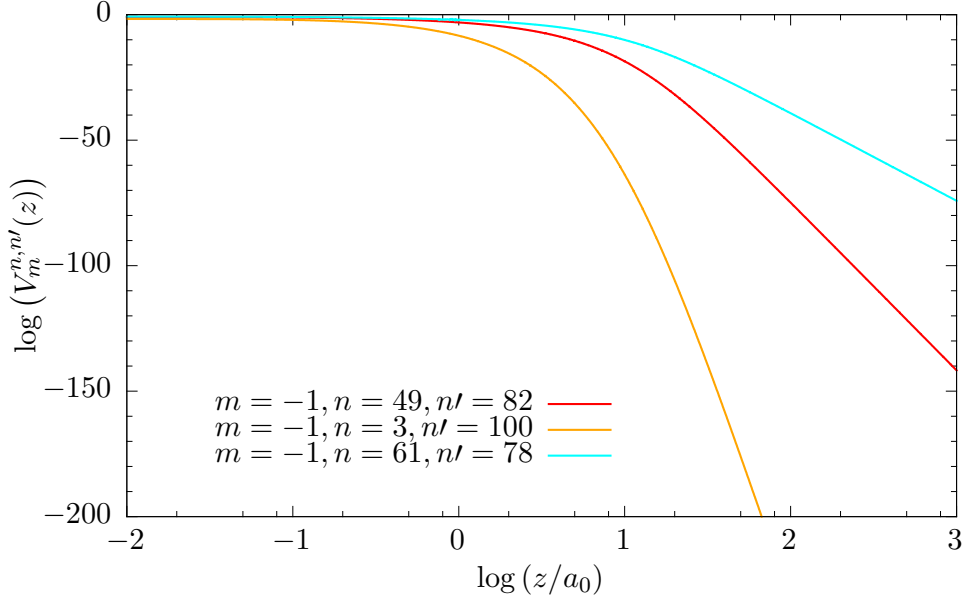


**Fig. B.1:** Values of the electron-core potentials  $V_{-1}^{49,82}$ ,  $V_{-1}^{3,100}$ , &  $V_{-1}^{61,78}$  as function of  $z$ .

potentials given in Eqs. (4.7), (4.9) and (4.10). Both, the coefficients and the adiabatic potentials are stored in external files and are loaded at program startup. Each time the Landau channel coefficients change, namely after completing the transversal iterations, the effective potentials must be updated. However, this scheme is not applicable for the 2DLHFR program. Here, we need explicitly every potential  $V_m^{nn'}(z)$ ,  $U_{m_i m_j}^{n_i n_j n'_i n'_j}(z_i, z_j)$  and  $A_{m_i m_j}^{n_i n_j n'_i n'_j}(z_i, z_j)$ . It would be very inefficient to evaluate the sums (B.2), (B.3) and (B.4) during runtime. Instead, we want to store the Landau averaged potentials separately and are in need of a subtle storage scheme that allows for a fast interpolation of the potentials but is economical in memory.

Therefore, we analyze the structure of the Landau averaged potentials in Fig. B.1, which shows a selection of electron-core potentials on log-log scales. All three potentials converge to a fixed value at  $z \rightarrow 0$  and exhibit a polynomial decline in the limit  $z \rightarrow \infty$ . This has been reported in the literature [74] for the potentials  $V$  but applies to the potentials  $U_{m_i m_j}^{n_i n_j n'_i n'_j}(z)$  and  $A_{m_i m_j}^{n_i n_j n'_i n'_j}(z_i, z_j)$  as well. The leading order  $w$  of the polynomial decline  $z^{-w}$  solely depends on the quantum numbers of the involved Landau states and the type of potential

$$w_V = 2|n - n'| + 1 \quad (\text{B.5})$$

$$w_U = 2|n_i - n'_i| + 2|n_j - n'_j| + 1 \quad (\text{B.6})$$

$$w_A = |n_i - n'_j| + |n_j - n'_i| + |n_i - n'_j + m_j - m_i| + |n_j - n'_i + m_i - m_j| + 1. \quad (\text{B.7})$$

Over the relevant interval of the  $z$ -coordinate, each Landau averaged potential covers a large number of magnitudes, mainly due to the polynomial decline. This makes a direct interpolation numerically unstable and one has to reduce the codomain of each potential

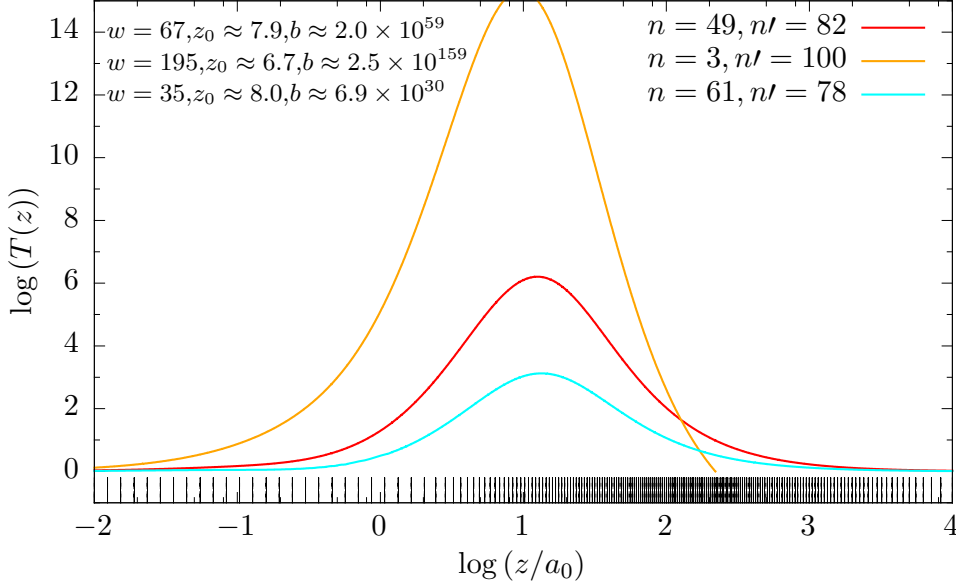


**Fig. B.2:** Transformed form  $T(z)$  of the three Landau averaged potentials presented in Fig. B.1 in corresponding colors. The used transformation parameters are given in the plot. The  $n = 3, n' = 100$  curve ends early at  $z \approx 220$  as the affiliated Landau potential  $V(z)$  falls below  $10^{-300}$  and thus can be safely ignored. Lines at the bottom indicate the positions of finite element borders of the potential  $B$ -spline basis.

by removing its polynomial tail. Therefore, we divide the potentials by a function

$$f(z) = \frac{b}{(z + z_0)^w}, \quad (\text{B.8})$$

resulting in a well-behaved, transformed form  $T(z) = V(z)/f(z)$  of the potentials. The parameters  $b$  and  $z_0$  are chosen such that the transformed potential function approaches unity for  $z \rightarrow 0$  and  $z \rightarrow \infty$ . In practice, this can be achieved with

$$z_0 = \frac{z_r}{(|V(z_1)|/|V(z_r)|)^{\frac{1}{w}} - 1} \quad \text{and} \quad b = (z_r + z_0)^w V(z_r), \quad (\text{B.9})$$

where  $z_1$  and  $z_r$  are sufficiently low and high values of  $z$ . We chose  $z_1 = 10^{-8}$  and  $z_r = 10^5$ , which worked well for all potentials considered.

Figure B.2 shows the transformed forms  $T(z)$  of the potentials shown in Fig. B.1, as well as the employed transformation parameters obtained with Eqs. (B.5) and (B.9). Please note that the high values of the parameter  $b$  constitute no numerical problem, as they are involved in the transformation as mere factors. The simple form of the transformed potentials allows us to interpolate them with reliable accuracy using a set of  $B$ -splines, specially adapted to the form of the transformed potentials. These are featureless up to  $z = 10^{-3}$ , therefore we use only 5 finite elements per decade at the lower end of  $z$ . In the central, more structured region of  $T(z)$  from  $z = 10^{-3}$  to  $z = 10^1$  we

use an increased finite element density. In total we use 195 finite elements to interpolate any of the potentials  $V$ ,  $U$  or  $A$ .

We give an impression of the node distribution at the bottom of Fig. B.2. Note that it is not reasonable to sample the transformed potentials at  $z < 10^{-8}$  or  $z > 10^5$ , as they approach unity. The first or last sampled value of the potentials can safely be used to calculate the true Landau averaged potentials at any  $z$  out of the sampled range with adequate precision. Therefore, we can store the Landau averaged potentials on the semi-infinite interval  $z \in [0, \infty]$  with a finite set of interpolation parameters. As each magnetic quantum number corresponds to different Landau averaged potentials, we have to make a selection of quantum numbers that we want to include into our calculations. Previously, we were restricted to a maximum absolute magnetic quantum number of  $|m| = 25$ . In the process of pre-calculating the Landau averaged potentials, we also expanded the range of accessible magnetic quantum numbers to  $m = -200$  in adiabatic approximation.

The electron interaction potentials  $U$  and  $A$  can be transformed in the same way and behave as good as the electron-core potentials, with the difference of possible nodes of  $T(z)$ . In order to ensure a high precision for all the potentials and possible quantum numbers, we leave the  $B$ -spline order  $k_{\text{pot}}$  of the finite element interpolation of the potentials variable, allowing values  $3 \leq k_{\text{pot}} \leq 12$ . Lower  $B$ -spline orders allow for a faster evaluation of the transfer potentials, thus we choose  $k_{\text{pot}}$  as low as possible, while guaranteeing a relative interpolation error below  $10^{-6}$ , typically resulting in  $\langle k_{\text{pot}} \rangle \approx 7$ . In the main program, we secure a fast evaluation of the transformed potentials by pre-calculating all possible spline values of the different orders  $k_{\text{pot}}$  at the integration points.

# Bibliography

- [1] E. Hog, C. Fabricius, V.V. Makarov, S. Urban, T. Corbin, G. Wycoff, U. Bastian, P. Schwekendiek, and A. Wicenec. The Tycho-2 catalogue of the 2.5 million brightest stars. *A&A* 355, L27–L30.
- [2] V. Canuto and D. Kelly. Hydrogen atom in intense magnetic field. *Astrophys. Space Sci.* 17, 277–291 (1972).
- [3] J. Shertzer, L. R. Ram-Mohan, and D. Dossa. Finite-element calculation of low-lying states of hydrogen in a superstrong magnetic field. *Phys. Rev. A* 40, 4777–4780 (1989).
- [4] Jinhua Xi, Xinghong He, and Baiwen Li. Energy levels of the hydrogen atom in arbitrary magnetic fields obtained by using  $B$ -spline basis sets. *Phys. Rev. A* 46, 5806–5811 (1992).
- [5] Jang-Haur Wang and Chen-Shiung Hsue. Calculation of the energy levels of a hydrogen atom in a magnetic field of arbitrary strength by using  $B$  splines. *Phys. Rev. A* 52, 4508–4514 (1995).
- [6] L. B. Zhao and P. C. Stancil. Calculation of low-lying levels of atomic hydrogen in a magnetic field with a finite basis set from B-splines. *J. Phys. B* 40, 4347 (2007).
- [7] H. Ruder, Günter Wunner, H. Herold, and F. Geyer. *Atoms in Strong Magnetic Fields*. A&A Library. Springer-Verlag (1994).
- [8] Yu. P. Kravchenko, M. A. Liberman, and B. Johansson. Exact solution for a hydrogen atom in a magnetic field of arbitrary strength. *Phys. Rev. A* 54, 287–305 (1996).
- [9] Yu. P. Kravchenko, M. A. Liberman, and B. Johansson. Highly Accurate Solution for a Hydrogen Atom in a Uniform Magnetic Field. *Phys. Rev. Lett.* 77, 619–622 (1996).
- [10] Calvin Stubbins, Kunal Das, and Yohannes Shiferaw. Low-lying energy levels of the hydrogen atom in a strong magnetic field. *J. Phys. B* 37, 2201 (2004).
- [11] K A U Lindgren and J. T. Virtamo. Relativistic hydrogen atom in a strong magnetic field. *J. Phys. B* 12, 3465 (1979).

- [12] Zonghua Chen and S. P. Goldman. Relativistic and nonrelativistic finite-basis-set calculations of low-lying levels of hydrogenic atoms in intense magnetic fields. *Phys. Rev. A* 45, 1722–1731 (1992).
- [13] S. O. Kepler, I. Pelisoli, S. Jordan, S. J. Kleinman, D. Koester, B. Külebi, V. Peçanha, B. G. Castanheira, A. Nitta, J. E. S. Costa, D. E. Winget, A. Kanaan, and L. Fraga. Magnetic white dwarf stars in the Sloan Digital Sky Survey. *MNRAS* 429, 2934–2944 (2013).
- [14] J. R. P. Angel, J. Liebert, and H. S. Stockman. The optical spectrum of hydrogen at 160-350 million gauss in the white dwarf GRW +70 deg 8247. *ApJ* 292, 260–266 (1985).
- [15] S. Jordan. Models of white dwarfs with high magnetic fields. *A&A* 265, 570–576 (1992).
- [16] S. Friedrich, R. Ostreicher, H. Ruder, and G. Zeller. Line broadening in the presence of strong magnetic fields. *A&A* 282, 179–189 (1994).
- [17] F. Euchner, S. Jordan, K. Beuermann, B. T. Gänsicke, and F. V. Hessman. Zeeman tomography of magnetic white dwarfs. *A&A* 390, 633–647 (2002).
- [18] F. Euchner, K. Reinsch, S. Jordan, K. Beuermann, and B. T. Gänsicke. Zeeman tomography of magnetic white dwarfs II. *A&A* 442, 651–660 (2005).
- [19] F. Euchner, S. Jordan, K. Beuermann, K. Reinsch, and B. T. Gänsicke. Zeeman tomography of magnetic white dwarfs III. *A&A* 451, 671–681 (2006).
- [20] B. Külebi, S. Jordan, F. Euchner, B. T. Gänsicke, and H. Hirsch. Analysis of hydrogen-rich magnetic white dwarfs detected in the Sloan Digital Sky Survey. *A&A* 506, 1341–1350 (2009).
- [21] G. F. Bignami, A. De Luca, P. A. Caraveo, S. Mereghetti, M. Moroni, R. P. Mignani, and M. Marconi. 1E1207.4-5209 - a Unique Object. *Mem. S.A.It.* 75, 448 (2004).
- [22] J. Trümper, W. Pietsch, C. Reppin, B. Sacco, E. Kendziorra, and R. Staubert. Evidence for strong cyclotron emission in the hard X-ray spectrum of HER X-1. *Annals of the New York Academy of Sciences* 302, 538–544 (1977).
- [23] V. Hambaryan, V. Suleimanov, A. D. Schwöpe, R. Neuhäuser, K. Werner, and A. Y. Potekhin. Phase-resolved spectroscopic study of the isolated neutron star RBS 1223 (1RXS0848.6+212708). *A&A* 534, A74 (2011).
- [24] K. Mori and C. J. Hailey. Detailed Atmosphere Modeling for the Neutron Star 1E1207.4-5209: Evidence of Oxygen/Neon Atmosphere. *ApJ* 648, 1139–1155 (2006).



- 
- [25] J. M. Lattimer and M. Prakash. The Physics of Neutron Stars. *Science* 304, 536–542 (2004).
- [26] W. Becken, P. Schmelcher, and F. K. Diakonov. The helium atom in a strong magnetic field. *J. Phys. B* 32, 1557 – 1584 (1999).
- [27] W. Becken and P. Schmelcher. Non-zero angular momentum states of the helium atom in a strong magnetic field. *J. Phys. B* 33, 545 (2000).
- [28] W. Becken and P. Schmelcher. Higher-angular-momentum states of the helium atom in a strong magnetic field. *Phys. Rev. A* 63, 053412 (2001).
- [29] W. Becken and P. Schmelcher. Electromagnetic transitions of the helium atom in a strong magnetic field. *Phys. Rev. A* 65, 033416 (2002).
- [30] M. D. Jones, G. Ortiz, and D. M. Ceperley. Released-phase quantum Monte Carlo method. *Phys. Rev. E* 55, 6202–6210 (1997).
- [31] M. D. Jones, G. Ortiz, and D. M. Ceperley. Spectrum of neutral helium in strong magnetic fields. *Phys. Rev. A* 59, 2875–2885 (1999).
- [32] M. V. Ivanov. Hartree-Fock mesh calculations of the energy levels of the helium atom in magnetic fields. *J. Phys. B* 27, 4513–4521 (1994).
- [33] Armin Scrinzi. Accurate bound-state energies of helium in a strong magnetic field. *Phys. Rev. A* 58, 3879–3883 (1998).
- [34] O. A. Al-Hujaj and P. Schmelcher. Helium in superstrong magnetic fields. *Phys. Rev. A* 67, 023403 (2003).
- [35] M. Hesse and D. Baye. Helium atoms in a strong magnetic field studied with the Lagrange-mesh method. *J. Phys. B* 377, 3937 – 3946 (2004).
- [36] Xiaofeng Wang and Haoxue Qiao. Configuration-interaction method with Hylleraas-Gaussian-type basis functions in cylindrical coordinates: Helium atom in a strong magnetic field. *Phys. Rev. A* 77, 043414 (2008).
- [37] Xiaofeng Wang, Jijun Zhao, and Haoxue Qiao. Helium atom in strong magnetic fields: An application of the configuration-interaction method with Hylleraas-Gaussian basis. *Phys. Rev. A* 80, 053425 (2009).
- [38] A. Thirumalai and J. S. Heyl. Hydrogen and helium atoms in strong magnetic fields. *Phys. Rev. A* 79, 012514 (2009).
- [39] X. Wang and H. Qiao. Full-core-plus-correlation method in cylindrical coordinates: Lithium atom in strong magnetic fields. *Phys. Rev. A* 75, 033421 (2007).

- [40] O. A. Al-Hujaj and P. Schmelcher. Lithium in strong magnetic fields. *Phys. Rev. A* 70, 033411 (2004).
- [41] O. A. Al-Hujaj and P. Schmelcher. Beryllium in strong magnetic fields. *Phys. Rev. A* 70, 023411 (2004).
- [42] K. Mori and C. J. Hailey. Atomic Calculation for the Atmospheres of strongly magnetized neutron stars. *ApJ* 564, 914 – 929 (2002).
- [43] D. Engel and Günter Wunner. Hartree-Fock-Roothaan calculations for many-electron atoms and ions in neutron-star magnetic fields. *Phys. Rev. A* 78, 032515 (2008).
- [44] S. Bücheler, D. Engel, J. Main, and Günter Wunner. Quantum Monte Carlo studies of the ground states of heavy atoms in neutron-star magnetic fields. *Phys. Rev. A* 76, 032501 (2007).
- [45] D. Meyer. *Korrelationsfunktions-Quanten-Monte-Carlo- Methode zur Berechnung von angeregten Zuständen von Mehrelektronen-Atomen in Neutronensternmagnetfeldern*. Ph.D. thesis, Uni Stuttgart (2012).
- [46] Sebastian Boblest. *Monte-Carlo-Studien für neutrale Atome und Ionen in starken Magnetfeldern*. Ph.D. thesis, Uni Stuttgart (2013).
- [47] M. C. Miller. Model atmospheres for neutron stars. *MNRAS* 255, 129–145 (1992).
- [48] S. Mereghetti, A. De Luca, P. A. Caraveo, W. Becker, R. Mignani, and G. F. Bignami. Pulse Phase Variations of the X-Ray Spectral Features in the Radioquiet Neutron Star 1E 1207-5209. *ApJ* 581, 1280–1285 (2002).
- [49] D. Sanwal, G. G. Pavlov, V. E. Zavlin, and M. A. Teter. Discovery of Absorption Features in the X-Ray Spectrum of an Isolated Neutron Star. *ApJ Letters* 574, L61–L64 (2002).
- [50] James M. Lattimer and Madappa Prakash. Neutron star observations: Prognosis for equation of state constraints. *Phys. Rep.* 442, 109 – 165 (2007).
- [51] W. C. G. Ho and C. O. Heinke. A neutron star with a carbon atmosphere in the Cassiopeia A supernova remnant. *Nature* 462, 71–73 (2009).
- [52] M. Klews. *Diskretisierungsverfahren zur Untersuchung von Atomen in zeitabhängigen elektrischen Feldern und in extrem starken Magnetfeldern*. Ph.D. thesis, Universität Tübingen (2003).
- [53] D. Engel, M. Klews, and Günter Wunner. A fast parallel code for calculating energies and oscillator strengths of many-electron atoms at neutron star magnetic field strengths in adiabatic approximation. *Comp. Phys. Comm.* 180, 302 – 311 (2009).

- 
- [54] D. Engel. *Hartree-Fock-Roothaan-Rechnungen für Vielelektronen-Atome in Neutronenstern-Magnetfeldern*. Ph.D. thesis, Universität Stuttgart (2007).
- [55] bwGRiD (<http://www.bw-grid.de/>). Member of the German D-Grid initiative, funded by the Ministry of Education and Research (Bundesministerium für Bildung und Forschung) and the Ministry for Science, Research and Arts Baden-Wuerttemberg (Ministerium für Wissenschaft, Forschung und Kunst Baden-Württemberg). Technical report, Universities of Baden-Württemberg (2007-2013).
- [56] J. D. Landstreet, S. Bagnulo, G. G. Valyavin, L. Fossati, S. Jordan, D. Monin, and G. A. Wade. On the incidence of weak magnetic fields in DA white dwarfs. *A&A* 545, A30 (2012).
- [57] Werner Becker (editor). *Neutron Stars and Pulsars*, volume 357 of *Astrophysics and Space Science Library*. Springer, Berlin (2009).
- [58] V. B. Pavlov-Verevkin and B. I. Zhilinskii. Neutral hydrogen-like system in a magnetic field. *Phys. Lett. A* 78, 244 – 245 (1980).
- [59] G. Wunner, H. Ruder, and H. Herold. Comment on the effect of the proton mass on the spectrum of the hydrogen atom in a very strong magnetic field. *Phys. Lett. A* 79, 159 – 161 (1980).
- [60] A. Y. Potekhin. Structure and radiative transitions of the hydrogen atom moving in a strong magnetic field. *J. Phys. B* 27, 1073 (1994).
- [61] Yu. E. Lozovik and S. Yu. Volkov. Hydrogen atom moving across a magnetic field. *Phys. Rev. A* 70, 023410 (2004).
- [62] M Vincke, M Le Dourneuf, and D. Baye. Hydrogen atom in crossed electric and magnetic fields: transition from weak to strong electron-proton decentring. *J. Phys. B* 25, 2787 (1992).
- [63] P. Faßbinder and W. Schweizer. Atomic Data of the Hydrogen Atom in Magnetic and Electric Fields Relevant to White Dwarf Stars. *Astron. Soc. Pac. Conf. Ser.* 81, 220 (1995).
- [64] Jochen Garcke and Michael Griebel. On the Computation of the Eigenproblems of Hydrogen and Helium in Strong Magnetic and Electric Fields with the Sparse Grid Combination Technique. *J. Comp. Phys.* 165, 694 – 716 (2000).
- [65] Xiaoxu Guan. Oscillator strength spectrum of hydrogen in strong magnetic and electric fields with arbitrary mutual orientation. *Phys. Rev. A* 74, 023413 (2006).
- [66] Alice K Harding and Dong Lai. Physics of strongly magnetized neutron stars. *Rep. Prog. Phys.* 69, 2631 (2006).

- [67] A. Poszwa and A. Rutkowski. Hydrogen atom in a strong magnetic field. II. Relativistic corrections for low-lying excited states. *Phys. Rev. A* 69, 023403 (2004).
- [68] W. Rösner, G. Wunner, H. Herold, and H. Ruder. Hydrogen atoms in arbitrary magnetic fields. I. Energy levels and wavefunctions. *J. Phys. B* 17, 29 (1984).
- [69] Carl de Boor. On calculating with B-splines. *J. Approx. Theory* 6, 50 – 62 (1972).
- [70] V. Canuto and J. Ventura. Quantizing Magnetic Fields in Astrophysics. *Fund. Cosm. Phys.* 2, 203–353 (1977).
- [71] P. Pröschel, W. Rösner, Günter Wunner, H. Ruder, and H. Herold. Hartree-Fock calculations for atoms in strong magnetic fields. I. Energy levels of two-electron systems. *J. Phys. B* 15, 1959–1976 (1982).
- [72] E. Anderson, Z. Bai, C. Bischof, S. Blackford, J. Demmel, J. Dongarra, J. Du Croz, A. Greenbaum, S. Hammarling, A. McKenney, and D. Sorensen. *LAPACK Users' Guide*. Philadelphia, PA, third edition (1999).
- [73] Harald Friedrich and Dieter Wintgen. The hydrogen atom in a uniform magnetic field — An example of chaos. *Phys. Rep.* 183, 37 – 79 (1989).
- [74] J Simola and J Virtamo. Energy levels of hydrogen atoms in a strong magnetic field. *J. Phys. B* 11, 3309 (1978).
- [75] J. von Neumann and E. P. Wigner. Über das Verhalten von Eigenwerten bei adiabatischen Prozessen. *Z. Physik* 30, 467 (1929).
- [76] Donald G. York et al. The Sloan Digital Sky Survey: Technical Summary. *Astron. J.* 120, 1579 (2000).
- [77] R. Loudon. One-Dimensional Hydrogen Atom. *Am. J. Phys.* 27, 649 – 655 (1959).
- [78] D. Baye, M Vincke, and M. Hesse. Simple and accurate calculations on a Lagrange mesh of the hydrogen atom in a magnetic field. *J. Phys. B* 41, 055005 (2008).
- [79] H Forster, W Strupat, W. Rösner, G. Wunner, H. Ruder, and H. Herold. Hydrogen atoms in arbitrary magnetic fields. II. Bound-bound transitions. *J. Phys. B* 17, 1301 (1984).
- [80] P. Diemand. *Hartree-Fock-Rechnungen zur Photoionisation von leichten bis mittelschweren Atomen und Ionen in Neutronenstern-Magnetfeldern*. Ph.D. thesis, Universität Stuttgart (2012).
- [81] M J Seaton. Atomic data for opacity calculations. I. General description. *J. Phys. B* 20, 6363 (1987).

- 
- [82] Baybars Külebi, Stefan Jordan, Fabian Euchner, Heiko Hirsch, and Wolfgang Löffler. Analysis of the hydrogen-rich magnetic white dwarfs in the SDSS. *J. Phys.: Conf. Ser.* 172, 012047 (2009).
- [83] O. Kepler (2013). Private communication.
- [84] P. Schmelcher and L. S. Cederbaum. Interaction of the Landau orbitals of atomic ions in a magnetic field with electronic motion. *Phys. Rev. A* 43, 287–293 (1991).
- [85] W. Becken. *Elektronische Struktur des Helium-Atoms im starken Magnetfeld*. Ph.D. thesis, Universität Heidelberg (2000).
- [86] B. L. Hammond, W. A. Lester, jr., and P. J. Reynolds. *Monte Carlo Methods in ab initio quantum chemistry*. World Scientific Lecture and Course Notes in Chemistry. World Scientific Publishing Co. Pte. Ltd., Singapur (1994).
- [87] T. Bouabca, B. Braïda, and M. Caffarel. Multi-Jastrow trial wavefunctions for electronic structure calculations with quantum Monte Carlo. *J. Chem. Phys.* 133, 044111 (2010).
- [88] M. D. Jones, G. Ortiz, and D. M. Ceperley. Many-Body Approaches to Atoms and Molecules in External Magnetic Fields. *Int. J. Quant. Chem.* 648, 523 – 552 (1997).
- [89] S. Bücheler. *Diffusions-Quanten-Monte-Carlo-Simulationen für Vielelektronen-Atome in Neutronensternmagnetfeldern*. Ph.D. thesis, Universität Stuttgart (2007).
- [90] M. V. Ivanov and P. Schmelcher. Ground states of H, He, . . . , Ne, and their singly positive ions in strong magnetic fields: The high-field regime. *Phys. Rev. A* 61, 022505 (2000).
- [91] C. Schimeczek. *Startwellenfunktionen für Hartree-Fock-Roothaan-Rechnungen für Mehrelektronenatome in Neutronensternmagnetfeldern*. Diplomarbeit, Universität Stuttgart (2010).
- [92] C. Schimeczek, D. Engel, and Günter Wunner. A highly optimized code for calculating atomic data at neutron star magnetic field strengths using a doubly self-consistent Hartree–Fock–Roothaan method. *Comp. Phys. Comm.* 183, 1502 – 1510 (2012).
- [93] Damir Zajec. *Selbstkonsistente Berechnungen von gebunden-frei Übergängen bei leichten bis mittelschweren Mehrelektronenatomen in superstarken Magnetfeldern*. Diplomarbeit, Universität Stuttgart (2011).

- [94] T. Kersting. *Hartree-Fock Rechnungen zur Photoionisation von schweren Mehrelektronenatomen in Neutronensternmagnetfeldern*. Diplomarbeit, Universität Stuttgart (2011).
- [95] Dirk Meyer, Sebastian Boblest, and Günter Wunner. Fixed-phase correlation-function quantum Monte Carlo calculations for ground and excited states of helium in neutron-star magnetic fields. *Phys. Rev. A* 87, 032515 (2013).
- [96] Alexander Y. Potekhin. Cyclotron harmonics in opacities of isolated neutron star atmospheres. *A&A* 518, A24 (2010).
- [97] Alejandro J. Garza and Gustavo E. Scuseria. Comparison of self-consistent field convergence acceleration techniques. *J. Chem. Phys.* 137, 054110 (2012).
- [98] D. M. Larsen. Variational studies of bound states of the  $H^-$  ion in a magnetic field. *Phys. Rev. B* 20, 5217 – 5227 (1979).
- [99] O. A. Al-Hujaj and P. Schmelcher. Ground and excited states of the hydrogen negative ion in strong magnetic fields. *Phys. Rev. A* 61, 063413 (2000).
- [100] Zhao Ji-Jun, Wang Xiao-Feng, and Qiao Hao-Xue. High accuracy calculation of the hydrogen negative ion in strong magnetic fields. *Chin. Phys. B* 20, 053101 (2011).
- [101] G. Ortiz, D. M. Ceperley, and R. M. Martin. New Stochastic Method for Systems with Broken Time-Reversal Symmetry: 2D Fermions in a Magnetic Field. *Phys. Rev. Lett.* 71, 2777 – 2780 (1993).
- [102] M. D. Jones. *Physics under extreme conditions: Magnetized atoms and hot dense plasmas*. Ph.D. thesis, University of Illinois at Urbana-Champaign (1996).
- [103] D. M. Ceperley and B. Bernu. The calculation of excited state properties with quantum Monte Carlo. *J. Chem. Phys.* 89, 6316–6328 (1988).
- [104] Christoph Schimeczek, Sebastian Boblest, Dirk Meyer, and Günter Wunner. Atomic ground states in strong magnetic fields: Electron configurations and energy levels. *Phys. Rev. A* 88, 012509 (2013).
- [105] S. Boblest, C. Schimeczek, and G. Wunner. Ground states of He-Ne and their ions in strong magnetic fields. (2013). Submitted to *Phys. Rev. A*.
- [106] M. V. Ivanov and P. Schmelcher. Ground state of the lithium atom in strong magnetic fields. *Phys. Rev. A* 57, 3793–3800 (1998).
- [107] M. V. Ivanov and P. Schmelcher. Ground state of the carbon atom in strong magnetic fields. *Phys. Rev. A* 60, 3558–3568 (1999).

- [108] M. V. Ivanov and P. Schmelcher. The boron atom and boron positive ion in strong magnetic fields. *J. Phys. B* 34, 2031 (2001).
- [109] M. D. Jones, G. Ortiz, and D. M. Ceperley. Hartree-Fock studies of atoms in strong magnetic fields. *Phys. Rev. A* 54, 219 – 231 (1996).
- [110] P. J. Knowles and N. C. Handy. A new determinant-based full configuration interaction method. *Chem. Phys. Lett.* 111, 315 – 321 (1984).
- [111] Yin Tang, Liming Wang, Xuanyu Song, Xiaofeng Wang, Z. C. Yan, and Haoxue Qiao. Bound-state energies of lithium in magnetic fields using Hylleraas basis functions. *Phys. Rev. A* 87, 042518 (2013).
- [112] Xiaofeng Wang and H. X. Qiao. Beryllium Atom from Weak to Strong Magnetic Fields. *Few-Body Systems* 53, 453–459 (2012).
- [113] C. Schimeczek and Günter Wunner. Accurate 2d finite element calculations for hydrogen in magnetic fields of arbitrary strength. *Comp. Phys. Comm.* 185, 614–621 (2014).
- [114] Peter J. Mohr, Barry N. Taylor, and David B. Newell. CODATA recommended values of the fundamental physical constants: 2010. *Rev. Mod. Phys.* 84, 1527–1605 (2012).
- [115] *ARbitrary PRECISION Computation Package*. <http://crd-legacy.lbl.gov/dhbailey/mpdist/> (2003-2013).





# Danksagung

Im Zusammenhang der Entstehung dieser Arbeit möchte ich folgenden Personen meinen Dank aussprechen:

- Prof. Dr. Wunner für das mir entgegengebrachte Vertrauen in meine Arbeit, sowie viele gleichermaßen aufschlussreiche wie elegante Formulierungen physikalischer Sachverhalte in englischer Sprache;
- Junior Prof. Dr. Maria Fyta für die freundliche Übernahme des Mitberichtes;
- meinen Zimmernachbarn Sebastian Boblest und Patrick Köberle, für Rat und Tat, Ablenkung von – sowie Hilfe bei – Fragen zur Physik, gute Zusammenarbeit, und ihre starken Nerven;
- Rüdiger Fortanier und Sebastian Boblest für beharrliches Korrekturlesen dieser Arbeit und viele hilfreiche Hinweise zu Form und Stil der solchen;
- Holger Cartarius für seine Bereitschaft *jederzeit* alles liegen zu lassen um mir die eine oder andere physikalische Frage zu beantworten, seine herausragenden Kuchen, seine PC-Administration, sowie sein stetes Engagement für alle Belange rund um den Arbeitsalltag;
- den Kollegen, die mich stets an ihrem reichhaltigen Wissen teilhaben ließen, namentlich Andrej Junginger, Manuel Kreibich, Robin Gutöhrlein und Apl. Prof. Dr. Jörg Main;
- den freundlichen Kollegen am ITP1, die einen großen Anteil daran hatten oder haben, dass ich jeden Morgen gerne zur Arbeit komme, besonders Sebastian Boblest, Andrej Junginger, Rüdiger Fortanier, Dirk Meyer, Patrick Köberle, Florian Rempp;
- allen Trekkies am Institut für die Raumschiff-Romantik, allen Rollenspielern für heldenhafte Fantasiereisen, allen Atheisten für gottloses Treiben in der Kaffeerrunde und allen, die mich und meine Kommentare zum (Welt-) Geschehen (stillschweigend) ertragen haben.



# christoph schimeczek

---

Geboren am 21. Juni 1983 in München

## Schulausbildung

- Sept. 1989 – Juli 1993 **Grundschule Münsing.**
- Sept. 1993 – Juli 1996 **Landschulheim Kempfenhausen.**
- Sept. 1996 – Juni 2002 **Paracelsus-Gymnasium Hohenheim.**
18. Juni 2002 **Abschluss: Abitur.**

## Zivildienst

- Juli 2002 – April 2003 **Kliniken Schmieder, Stuttgart Gerlingen.**

## Studium

- Okt. 2003 – März 2010 **Diplomstudiengang Physik.**  
Universität Stuttgart
26. April 2006 **Vordiplom in Physik.**
- März 2009 – Februar 2010 **Diplomarbeit, Startwellenfunktionen für Hartree-Fock-Roothaan-Rechnungen für Mehr-elektronenatome in Neutronensternmagnetfeldern**, unter der Betreuung von Prof. Dr. Günter Wunner.  
1. Institut für Theoretische Physik der Universität Stuttgart
2. März 2010 **Abschluss: Diplom-Physiker (Dipl.-Phys.).**

## Wissenschaftliche Tätigkeiten

- 2010–2013 **Wissenschaftlicher Mitarbeiter.**
12. März 2010 **DPG-Frühjahrstagung, A database for bound-bound transitions using a Hartree-Fock-Roothaan method for atoms and ions in neutron star magnetic fields**, Hannover.  
Vortrag
16. März 2011 **DPG-Frühjahrstagung, Ultra-fast calculation of bound atomic states and transitions in neutron star atmospheres with very strong magnetic fields**, Dresden.  
Vortrag
13. März 2012 **DPG-Frühjahrstagung, Advanced Landau expansion of atoms in neutron star magnetic fields**, Stuttgart.  
Vortrag
26. Februar 2013 **DPG-Frühjahrstagung, Atoms in the strong magnetic fields of magnetic white dwarfs and neutron stars**, Jena.  
Vortrag

## Publikationen

- 2012 C. Schimeczek and D. Engel and G. Wunner. A highly optimized code for calculating atomic data at neutron star magnetic field strengths using a doubly self-consistent Hartree-Fock-Roothaan method. *Comp. Phys. Comm.* **183**, 1502 - 1510.
- 2013 C. Schimeczek and S. Boblest D. and Meyer and G. Wunner. Atomic ground states in strong magnetic fields: Electron configurations and energy levels. *Phys. Rev. A* **88**, 012509.
- 2013 C. Schimeczek and G. Wunner. Accurate 2d finite element calculations for hydrogen in magnetic fields of arbitrary strength. *Comp. Phys. Comm.* pp.



### **Ehrenwörtliche Erklärung**

Ich erkläre, dass ich diese Dissertation, abgesehen von den ausdrücklich bezeichneten Hilfsmitteln und den Ratschlägen von den jeweils namentlich aufgeführten Personen, selbständig verfasst habe.

Stuttgart, 27. Januar 2014

*Christoph Schimeczek*